Portable Ultrasound Imaging

di Ianni, Tommaso

Publication date:
2017

Document Version
Publisher's PDF, also known as Version of record

PhD Thesis

Portable Ultrasound Imaging

Tommaso Di Ianni

Supervised by: Prof. Jørgen Arendt Jensen, PhD, Dr. Techn.

Co-supervised by: Carlos Armando Villagómez Hoyos, PhD
Martin Christian Hemmsen, PhD

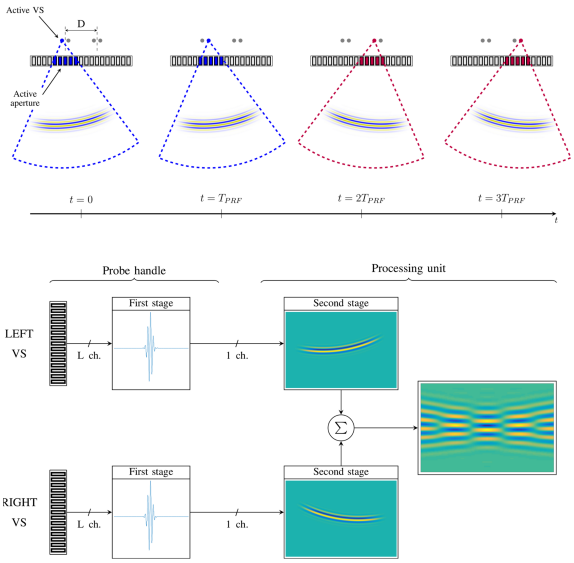

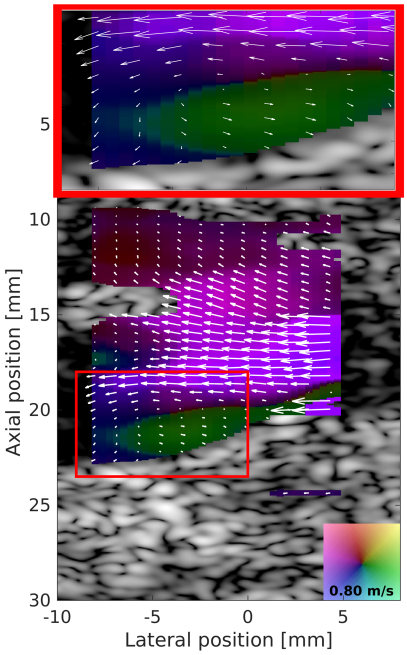

Technical University of Denmark
Kgs. Lyngby, Denmark 2017

Cover image:
Left: Imaging sequence and dual-stage beamforming involved in the vector flow imaging method developed in this thesis for a hand-held ultrasound scanner.

Right: Vector flow image of a carotid bifurcation measured *in vivo*. A vortex can be detected in the internal carotid artery due to the high frame rate.

Technical University of Denmark

Department of Electrical Engineering

Center for Fast Ultrasound Imaging (CFU)

Ørsteds Plads 349

2800 Kgs. Lyngby

DENMARK

Tel: (+45) 4525 3898

Web: www.bme.elektro.dtu.dk

Author e-mail: todiian@elektro.dtu.dk

Contents

Preface

This PhD thesis has been submitted to the Department of Electrical Engineering at the Technical University of Denmark (DTU) in partial fulfilment of the requirements for acquiring the PhD degree. The research providing the foundation for the thesis has been conducted over a period of three years from August 15, 2015, to August 14, 2017, at the Center for Fast Ultrasound Imaging (CFU), Department of Electrical Engineering. The project has been supervised by Prof. Jørgen Arendt Jensen, PhD, Dr. Techn., and co-supervised by Carlos Armando Villagómez Hoyos, PhD, and Martin Christian Hemmsen, PhD. The project was financially supported by grant 82-2012-4 from the Danish National Advanced Technology Foundation and by BK Ultrasound, Herlev, Denmark.

During the three years, I had the opportunity to attend the IEEE International Ultrasonics Symposium in Chicago, IL, USA, Taipei, Taiwan, and Tours, France, the SPIE Medical Imaging in San Diego, CA, USA, the AIUM Convention in Orlando, FL, USA, and the Artimino Ultrasound Conference in Helsinborg, Sweden, and Florence, Italy. In addition, I had the privilege to participate in the International Summer School on Advanced Ultrasound Imaging in Lyngby, and the 8^{th} International Summer School on Radar/SAR at the Fraunhofer Institute for High Frequency Physics and Radar Techniques FHR, Bonn, Germany. These experiences gave me the unique opportunity to deepen and broaden my knowledge in the fields of medical ultrasound and array signal processing, and to meet an incredible number of very valuable fellow researchers with whom I had the pleasure to share a great deal of interesting discussions.

During the Spring Semesters 2015 and 2016, I have gladly assisted Associate Professor Sadasivan (Sada) Puthusserypady, PhD, in teaching the course Applied Signal Processing, together with my fellows Simon Holbek, PhD, and Cristina Pasquinelli. This gave me the chance to find new ways of explaining concepts that are taken for granted in my mind, and it was a very good exercise to let them come out with the simplest words possible. Furthermore, I had the pleasure to co-supervise Mikkel Schou, MSc, during his master

project “Spatial matched filter focusing in medical ultrasound”.

I was granted financial support by the Otto Mønsteds Fond, Copenhagen, Denmark, for the IEEE International Ultrasonics Symposium in 2016 and 2017, and I was assigned the New Investigator Award for Basic Science at the 2017 AIUM Convention for the presentation “In vivo Vector Flow Imaging for a Portable Ultrasound Scanner”.

Tommaso Di Ianni
Kgs. Lyngby, Denmark
August 2017

Summary

This PhD project investigates hardware strategies and imaging methods for hand-held ultrasound systems. The overall idea is to use a wireless ultrasound probe linked to general-purpose mobile devices for the processing and visualization. The approach has the potential to reduce the upfront costs of the ultrasound system and, consequently, to allow for a wide-scale utilization of diagnostic ultrasound in any medical specialties and out of the radiology department.

The first part of the contribution deals with the study of hardware solutions for the reduction of the system complexity. Analog and digital beamforming strategies are simulated from a system-level perspective. The quality of the B-mode image is evaluated and the minimum specifications are derived for the design of a portable probe with integrated electronics in-handle. The system is based on a synthetic aperture sequential beamforming approach that allows to significantly reduce the data rate between the probe and processing unit.

The second part investigates the feasibility of vector flow imaging in a hand-held ultrasound system. Vector flow imaging overcomes the limitations of conventional imaging methods in terms of flow angle compensation. Furthermore, high frame rate can be obtained by using synthetic aperture focusing techniques. A method is developed combining synthetic aperture sequential beamforming and directional transverse oscillation to achieve the wireless transmission of the data along with a relatively inexpensive 2-D velocity estimation. The performance of the method is thoroughly assessed through simulations and measurements, and *in vivo* investigations are carried out to show its potential in presence of complex flow dynamics. A sufficient frame rate is achieved to allow for the visualization of vortices in the carotid bifurcation. Furthermore, the method is implemented on a commercially available tablet to evaluate the real-time processing performance in the built-in GPU with concurrent wireless transmission of the data.

Based on the demonstrations in this thesis, a flexible framework can be implemented with performance that can be scaled to the needs of the user and according to the computing resources available. The integration of high-frame-rate vector flow imaging in a hand-held ultrasound scanner, in addition, has the potential to improve the operator's workflow and opens the way to new possibilities in the clinical practice.

x

Resumé

Dette ph.d.-projekt undersøger hardwarestrategier og billeddannelsesmetoder til håndholdte ultralydssystemer. Den overordnede idé er at opsamle data med en ultralydsprobe, der er trådløst forbundet til en off-the-shelf mobiltelefon eller tablet, som står for dataprocessering og visualisering. Ideen om at kunne sende ultralydsdata trådløst til eksempelvis en mobiltelefon vil kunne føre til en betragtelig reduktion i hardwareomkostninger, samt muliggøre en bred udnyttelse af diagnostisk ultralyd i ethvert medicinsk speciale.

Første del af dette projekt undersøger forskellige hardware løsninger til reduktion af systemkompleksiteten. Analog og digital beamforming strategier er simuleret fra et systemniveau perspektiv. Kvaliteten af ultralydsbilleder evalueres, hvorfra designspecifikationerne bestemmes således, at vi udvikler en bærbar ultralydsprobe med integreret elektronik i håndtag. Systemet er baseret på synthetic aperture sequential beamforming, hvilket muliggør en markant reduktion i datamængden sendt mellem probe og tablet.

Anden del af projektet undersøger muligheden for vektor blod flow billeddannelse med et håndholdt ultralydssystem. Vektor flow overvinder grænserne for konventionel billeddannelse metoder i form af flowvinkel kompensation. Desuden kan høj billedhastighed opnås ved anvendelse af synthetic aperture fokuseringsteknikker.

En metode er udviklet i projektet, som kombinerer synthetic aperture sequential beamforming og directional transverse oscillation, hvorfra vi opnår trådløse dataoverførelser som trods datareduktion kan benyttes til 2-D vektor flow estimering. Metoden er valideret igennem simuleringer, eksperimentelle målinger, og *in vivo* undersøgelser. *In vivo* målinger over halspulsåren viste, at den udviklede teknik er i stand at fange selv komplekse flowfænomener.

Baseret på resultaterne opnået i denne afhandling, kan en fleksibel ramme implementeres med ydeevne, der kan skaleres til brugernes behov og i overensstemmelse med computeren tilgængelige ressourcer. Integrationen af high-frame-rate vektor flow billeddannelse i en håndholdt ultralydsscanner har desuden potentiale til at forbedre operatørens workflow og åbner vejen for nye muligheder i den kliniske praksis.

Acknowledgements

First of all, I would like to sincerely thank my main supervisor, Prof. Jørgen Arendt Jensen, for giving me the opportunity to work on this exciting project. You have been an excellent guide and it was a great pleasure to share with you interesting discussions that helped me shape my future career directions. Special thanks to my co-supervisors Martin Christian Hemmsen, for all the support during the start of the PhD project, and Carlos Armando Villagòmez Hoyos, for sharing with me your broad knowledge about flow imaging and ultrasound, as well as a great deal of drinks and hotel rooms.

I would like to express my most sincere gratefulness to all my current and former fellow colleagues at the Center for Fast Ultrasound Imaging, DTU Nanotech, and Rigshospitalet. You have made these years exceptional and it was great fun to work and travel with you. A warm thank you to Ramin Moshavegh, Mathias Engholm, and Thomas Lehrmann Christiansen, with whom I have shared the office and spent long hours staring out of the window. Thank you also to Jacob Bjerring Olesen for translating the summary to Danish. I would like to thank, in addition, Thomas Kim Kjeldsen for making our collaboration so smooth and productive. Particular appreciation goes to them who helped me settle down in Copenhagen, in particular David Pierson Bradway for handing over his furniture.

Special thanks to Nina Kjærgaard for taking the time to proof-read this thesis, and to Elna Sørensen and Henrik Laursen for their administrative and technical support. Further, thanks to Borislav Gueorguiev Tomov for the help with SARUS.

A warm, huge thank you goes to my family for understanding the reasons that pushed me to leave and follow my dreams. To my parents Michelangelo and Marianna, who handed down to me all their passion and commitment towards making projects come true, and my siblings Emilio, Marco, Luca, and Annamaria for always making me feel loved no matter where I am. Thanks to all the friends I have left for still having the patience to keep in touch.

Finally, all my recognition and gratitude go to Nora for the unconditional love and understanding you have shown in these years. Thank you for always supporting my projects, even when they involve moving to the other side of the world. I hope one day to have the possibility to give back everything you have done for me.

Thank you all, for making all this possible!

List of Figures

List of Tables

Symbols

c	Speed of sound
C	Contrast
dt	Gradient delay quantization step
D	Lateral distance between VAs
f_0	Center frequency
f_N	Nyquist sampling frequency
f_s	Sampling frequency
$F_\#$	F-number
j	Imaginary unit equal to $\sqrt{-1}$
K	Number of flow VSs
l	Oversampling ratio
L	Number of active elements - Aperture length
M	Length of the lateral signal
N	Sub-aperture length
N_e	Number of emissions/HRIs used for the velocity/frequency estimation
R	Correlation function
t_s	Time shift of consecutively received signals
T_0	Pulse period
T_s	Sampling period
$\vec{v}$	Blood velocity vector
v_x	Lateral velocity component
v_z	Axial velocity component
α	Attenuation factor
Δx	Lateral sampling interval
$\lambda = c/f_0$	Axial wavelength
λ_x	Lateral wavelength
σ	Width of a Gaussian apodization function
σ_e	Power of the noise
σ_s	Power of a signal
θ	Beam-to-flow angle

Abbreviations

1-D	One-Dimensional
2-D	Two-dimensional
3-D	Three-dimensional
ADC	Analog-to-digital converter
AFE	Analog front end
ASIC	Application-specific integrated circuit
CFM	Color flow mapping
CFU	Center for fast ultrasound imaging
CR	Cystic resolution
CW	Continuous wave
DAS	Delay-and-sum
DB	Directional beamforming
DR	Dynamic range
DRF	Dynamic receive focusing
DTO	Directional transverse oscillation
DTU	Danmarks Tekniske Universitet (Technical University of Denmark)
EDV	End diastolic velocity
FIR	Finite impulse response
FDA	Food and Drug Administration
FFT	Fast Fourier transform
FPGA	Field-programmable gate array
FPS	Frames per second
FSB	First-stage beamformer
FWHM	Full-width at half-maximum
GPU	Graphics processing unit
HRI	High-resolution image
IC	Integrated circuit
ICA	Internal carotid artery
IEC	International Electrotechnical Commission
I/Q	In-phase/Quadrature
LNA	Low noise amplifier

LRI	Low-resolution image
LRL	Low-resolution line
PD	Power dissipation
PDSNR	SNR at penetration depth
PG	Pressure gradient
PIV	Particle imaging velocimetry
PRF	Pulse repetition frequency
PSF	Point spread function
PSV	Peak-systolic velocity
PW	Plane wave
RF	Radio frequency
RT	Residence time
Rx	Receive
SA	Synthetic aperture
SARUS	Synthetic aperture real-time ultrasound system
SASB	Synthetic aperture sequential beamforming
SD	Standard deviation
SDM	Sigma-delta modulator
SNR	Signal-to-noise ratio
SQNR	Signal-to-quantization-noise ratio
SSB	Second-stage beamformer
TGC	Time gain comensation
TO	Transverse oscillation
Tx	Transmit
US	Ultrasound
VA	Virtual aperture
VE	Virtual element
VFI	Vector flow imaging
VGA	Variable-gain amplifier
VLSI	Very-large-scale integration
VR	Virtual receiver
VS	Virtual source
WSS	Wall shear stress

CHAPTER 1

Introduction

1.1 Motivation

Since the 1950s, when researchers from universities around the world started experimenting with ultrasound waves for medical imaging purposes (Edler and Hertz 1954; Ludwig and Struthers 1949; Wild 1950), ever more sophisticated ultrasound scanners have been developed in a continuous effort of the scientific and medical communities, hand-in-hand with industrial technological development. The imaging of soft tissue with high spatial resolution and the quantitative estimation of blood velocity and tissue elasticity are only few examples of the wide spectrum of diagnostic applications currently available in a conventional ultrasound scanner (Jensen 1996; Szabo 2014). In reflection of this exceptional technological evolution, it is often said that the complexity (and cost) of ultrasound systems scales with the Moore's law (Szabo 2014), contrary to other medical imaging methods which are costly to purchase and often set tight infrastructural demands.

In parallel, the miniaturization of integrated electronics and the advent of digital beamforming techniques allowed for the introduction of ultra-compact systems, and a number of pocket-size devices are today available on the market (Figure 2.1). These scanners incorporate anatomical and functional imaging capabilities in a form factor such as to fit in a lab coat pocket and can be used anywhere like a conventional stethoscope, as pointed out as early as 2002 by J. Roelandt (Roelandt 2002). In this regard, hand-held systems were also named *sonoscopes* in an editorial by L.D. Greenbaum on the journal *Heart* calling attention to the similarities with the long-time friend of every physician (Greenbaum 2003). The parallel Roelandt and Greenbaum, among others, draw is nevertheless not limited to portability considerations and brings about concerns regarding the clinical use of the equipment as well as the training of healthcare providers and the cost of the system, which is certainly higher than that of a stethoscope [see also the counterpoint to Greenbaum's editorial by R.A. Filly (Filly 2003)]. Concerns apart, it is safe to say that hand-held devices have greatly expanded the use of ultrasound with benefit for both the physician and the patient and have made feasible to perform diagnostic imaging at the point of care, opening a wide range of new possibilities.

It is important to specify that portable devices are not aimed to substitute state-of-the-art, high-end scanners. They are rather intended to complement them in a number of more specific scenarios. The American Society of Echocardiography and the European Association of Echocardiography, for instance, suggest that such devices be employed to complement and improve the accuracy of the physical examination allowing a more rapid

assessment of the patient's condition (Seward et al. 2002; Sicari et al. 2011). Nevertheless, hand-held systems have become continuously more advanced and their usefulness spans an increasing number of medical fields.

Portable scanners have shown great potential in assisting the diagnosis in situations where a prompt decision is of vital importance, as in presence of life-threatening conditions. Examples include intensive care and emergency medicine. In a number of studies, the devices have proven beneficial during the examination of haemodynamically unstable trauma patients (Kirkpatrick et al. 2004; Liu et al. 2005; Schleder et al. 2013). Lapostolle *et al.* demonstrated the usefulness of hand-held ultrasound provided by emergency physicians in an ambulance setting for the early diagnosis of pleural, peritoneal and pericardial effusion as well as vascular diseases like thrombosis and ischemia (Lapostolle et al. 2006).

Similar studies have been conducted in echocardiography (Lafitte et al. 2011; Mehta et al. 2014; Razi et al. 2011). Pinz and Voigt investigated the diagnostic agreement between a portable device (Vscan, GE Vingmed Ultrasound AS, Horten, Norway) and high-end scanners (Vivid 7 or E; GE Vingmed Ultrasound AS) in the examination of the left ventricular function (Prinz and Voigt 2011). The hand-held scanner measured 135 mm × 73 mm × 28 mm and the probe 120 mm × 33 mm × 26 mm, for a total weight of 390 g. The rechargeable battery allowed for a scanning time of approximately 70 min.

In addition, owing to their increased affordability, portable devices represent an effective help to provide basic healthcare in rural and remote districts of low and middle-income countries, where the access to other imaging technologies is nearly absent (Harris and Marks 2009; Sippel et al. 2011).

Despite their clinical potential, however, the price of hand-held systems is still a major limitation. Nevertheless, significant cost reductions have been registered in the last few years. One factor driving this trend is certainly the result of system simplification and optimization of the production processes, but a paradigm shift was seen with the introduction of the so-called *app-based* ultrasound devices. These systems consist of a compact probe with electronics integrated in-handle, linked to a general-purpose, mobile device like a laptop, tablet, or smartphone. The processing and visualization of the ultrasound images are performed through an application that can be downloaded from an app-store, allowing quick support and development of new features.

This new framework breaks the barriers of conventional, closed ultrasound systems providing full adaptability of the algorithm complexity and performance, which can be scaled up or down to the needs of the operator and according to the resources available. On this purpose, infinite processing resources may be obtained on-demand by exploiting cloud computing. In a not-too-far future, the clinician can be envisioned to have an ultrasound device in his or her pocket, scan patients with very little manual interaction with the device, visualize a preview on the same mobile device used to read emails between scans, and send the data to the cloud whenever a suspicious finding requires further investigation. The data will be dispatched to clusters of computers performing computational tasks for the most varied clients, and the results will be returned a few seconds later to the same clinician, who can promptly decide on the diagnosis, perhaps

with the support of a specialized fellow. It can be said, in a nutshell, that these systems bring the concept of *ultrasound-as-a-service* to its highest and most powerful realization.

Research in the ultrasound community is currently ongoing to address the design of simplified electronics necessary to fit the device miniaturization requirements, on the one hand, and to develop imaging modalities and algorithms that suit this new pattern of diagnostic ultrasound on the other. This thesis deals with both areas of concern, towards the development of a fully-scalable wireless ultrasound system.

1.2 Scientific contributions

In this manuscript, imaging strategies and hardware optimization problems are studied towards the development of a wireless ultrasound probe, and a blood flow imaging algorithm is developed and tested. The method provides operator-independent flow measurements with the potential to improve the clinical workflow and enables the possibility of wireless transmission of the flow data.

The research object of the thesis includes contributions published or accepted for publication in International Scientific Impact journals and a patent application filed to the United States Patent and Trademark Office. In addition, four proceedings papers have been published after presentation at international conferences.

1.2.1 Journal papers

I **T. Di Ianni**, C.A. Villagómez-Hoyos, C. Ewertsen, T.K. Kjeldsen, J. Mosegaard, M. Bachmann Nielsen, and J.A. Jensen
"A Vector Flow Imaging Method for Portable Ultrasound using Synthetic Aperture Sequential Beamforming"
Accepted for publication after minor revisions in *IEEE Trans. Ultrasons., Ferroelec., Freq. Contr.*.

II **T. Di Ianni**, M.C. Hemmsen, P. Llimós Muntal, I.H.H. Jørgensen, and J.A. Jensen
"System-level Design of an Integrated Receiver Front-end for a Wireless Ultrasound Probe"
In *IEEE Trans. Ultrasons., Ferroelec., Freq. Contr.*, vol. 63, no. 11, pp. 1935-1946, Nov. 2016.

1.2.2 Conference papers

III **T. Di Ianni**, T.K. Kjeldsen, C.A. Villagómez-Hoyos, J. Mosegaard, and J.A. Jensen
"Real-time implementation of synthetic aperture vector flow imaging in a consumer-level tablet"
To be published in *Proc. IEEE Ultrasons. Symp.*, 2017.

IV **T. Di Ianni**, C.A. Villagómez-Hoyos, C. Ewertsen, M. Bachmann Nielsen, and J.A. Jensen
"High-frame-rate imaging of a carotid bifurcation using a low-complexity velocity estimation approach"
To be published in *Proc. IEEE Ultrasons. Symp.*, 2017.

V **T. Di Ianni**, M.C. Hemmsen, and J.A. Jensen
"Vector Velocity Estimation for Portable Ultrasound using Directional Transverse Oscillation and Synhtetic Aperture Sequential Beamforming"
In *Proc. IEEE Ultrasons. Symp.*, pp. 1-4, 2016.

VI **T. Di Ianni**, M.C. Hemmsen, J.P. Bagge, H. Jensen, N. Vardi, and J.A. Jensen
"Analog Gradient Beamformer for a Wireless Ultrasound Scanner" In *Proc. SPIE Ultrasound Imaging. Symp.*, vol. 9790, 2016.

1.2.3 Patent applications

I **T. Di Ianni**, M.C. Hemmsen, and J.A. Jensen
"Vector Velocity Estimation using Transverse Oscillation (TO) and Synthetic Aperture Sequential Beamforming (SASB)"
International Patent Application, August 31, 2016, number: ANA1310-US (BKM-10-7988).

1.2.4 Publications not included in the thesis

- M. Schou, **T. Di Ianni**, and J.A. Jensen
"Improved Synthetic Aperture Sequential Beamforming using Spatial Matched Filtering"
To be published in *Proc. IEEE Ultrasons. Symp.*, 2017.

- M.B. Stuart, J. Jensen, **T. Di Ianni**, and J.A. Jensen
"Image quality degradation from transmit delay profile quantization"
In *Proc. IEEE Ultrasons. Symp.*, pp. 1-4, 2015.

1.3 Structure of the thesis

The thesis is organized as follows. After introducing the portable systems and the methods published in literature in an historical perspective, the remaining chapters are divided into two parts. The first part deals with the study of imaging strategies and hardware optimization to simplify the architecture of the system while maintaining the quality of the B-mode image. In the second part, a vector flow imaging method is developed and validated through simulations and measurements. The method allows for the estimation

of quantitative velocities and fits the data throughput and computational requirements of a wireless scanner. The thesis is intended to be read as a whole. The reader is occasionally referred to the appended papers whenever details have been omitted to improve the flow of the text.

Chapter 2 reviews the portable ultrasound devices presented in literature, along with the technical challenges encountered in the design of a hand-held system and some of the strategies proposed to simplify the system architecture.

PART I:

Chapter 3 introduces synthetic aperture focusing techniques and, in particular, synthetic aperture sequential beamforming (SASB). This focusing approach is used in all the experimental studies concerning the system-level design of the probe as well as the estimation of blood velocities.

Chapter 4 addresses the problem of the reduction of the hardware complexity by presenting an analog beamforming approach. The method reduces the number of A/D converters (ADCs), and provides a significantly simplified architecture. Simulations of the point spread function (PSF) are used to derive the minimum requirements needed to maintain an acceptable image quality.

Chapter 5 presents a system-level design of a digital wireless probe. Several strategies are analyzed for the ADCs and beamformer to minimize the system complexity. The PSF is simulated as a function of the depth to obtain the design specification for the development of an integrated receiver front-end circuit.

PART II:

Chapter 6 reviews the state-of-the-art of vector flow imaging (VFI) techniques by proving an overview of the methods published in literature. The time and phase-shift approaches are introduced, and studies addressing the clinical validation of VFI and its possible applications are reported.

Chapter 7 introduces the basic concepts of the transverse oscillation (TO) approach, which allows for the estimation of blood velocities in 2-D, and its combination with directional beamforming. The TO approach is used for the development of a 2-D VFI method in the following chapters.

Chapter 8 presents a 2-D VFI method developed combining SASB and directional TO. The method suits the requirement of a wireless ultrasound system while providing quantitative velocity estimation. The use of a sequential beamforming approach allows for a

data reduction that enables the wireless transmission, and a relatively inexpensive velocity estimator can be used. Simulations are performed to validate the method using a linear and a convex array of transducers.

Chapter 9 continues the investigations in Ch. 8 including measurements of a straight vessel with constant as well as pulsatile flow. *In vivo* measurements are reported from a common carotid artery and a carotid bifurcation. The implementation on a commercially available tablet is presented to evaluate the feasibility of the real-time processing with concurrent transmission of the data via Wi-Fi link. Finally, the limitations of the method are discussed.

Chapter 10 draws the conclusion to the study by summarizing the major results and identifying the future research perspectives.

CHAPTER 2

Portable ultrasound

Summary *The continuous advancements of the semiconductor technology and the progress of innovative digital beamforming techniques have pushed forward the development of miniaturized ultrasound scanners. Hand-carried devices are currently experiencing a broad utilization in medical fields such as radiology, cardiology and emergency medicine. In this chapter, some of the point-of-care systems published in literature are reviewed in an historical perspective. In addition, the technical challenges encountered in the design of portable scanners are discussed, along with some of the strategies suggested to deal with their limited resources.*

2.1 Historical perspective

In the wake of the continuous advancements of the semiconductor technology and the progress of digital beamforming techniques, the study and development of miniaturized ultrasound scanners has evoked increasing interest. Major ultrasound companies such as Siemens, GE, Philips and Mindray have in recent years introduced devices with the form factor of a laptop or smaller. Companies like SonoSite have made of the production of point-of-care devices their primary expertise, and a number of new companies emerged like, among others, Mobisante and Clarius, which are solely dedicated to the development of such machines (Figure 2.1). The idea of a hand-carried ultrasound imaging device, however, came into being back in the 1970s. To the best of the author's knowledge, the first battery-powered ultrasound scanner was built in 1978 at the Thoraxcentre, Erasmus University, Rotterdam, The Netherlands (Ligtvoet et al. 1978; Roelandt, Wladimiroff, and Baars 1978). The Minivisor weighed 1.4 kg and measured 10 cm $\times$ 25 cm (Figure 2.2). It included a built-in linear array, a battery capable of providing continuous operation during 1.5 h, and a 2 cm $\times$ 4 cm display. Its capabilities were demonstrated in the clinic for cardiological, obstetrical, and gynaecological scans. Due to its unsatisfactory resolution and very restricted user control over the imaging settings, no great popularity was ever achieved by this system, but it was without doubt groundbreaking for the time.

The prototype of an experimental C-scan scanner was developed at the University of Virginia, Charlottesville, VA, in collaboration with PocketSonics, Inc., Charlottesville, VA. The Sonic Window (Figure 2.1(b)) was presented by Fuller *et al.* targeting applications such as needle and catheter tracking, internal bleeding identification, and support to routine physical examination (Fuller, Owen, et al. 2009; Fuller, Ranganathan, et al. 2008). The system was a good example of a fully integrated design, resulting from the collaboration

(a)

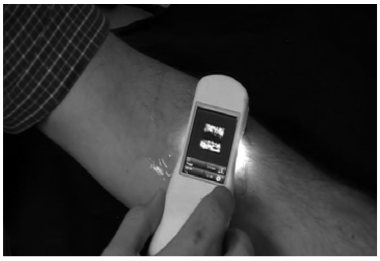

(b)

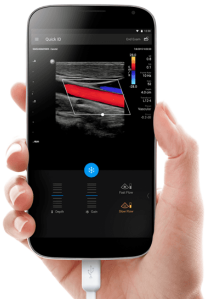

(c)

(d)

(e)

Figure 2.1: Pocket-size ultrasound systems: (a) Vscan, GE Vingmed Ultrasound AS, Horten, Norway; (b) Sonic Window - image from (Fuller, Owen, et al. 2009; Fuller, Ranganathan, et al. 2008); (c) Lumify, Philips Ultrasound, Inc., Bothell, WA, USA; (d) MobiUS SP1, Mobisante, Inc., Redmond, WA, USA; (e) Clarius, Clarius Mobile Health Corp., Burnaby, BC, Canada. The Lumify, SP1 and Clarius represent the newest generation of scanners using general purpose mobile devices.

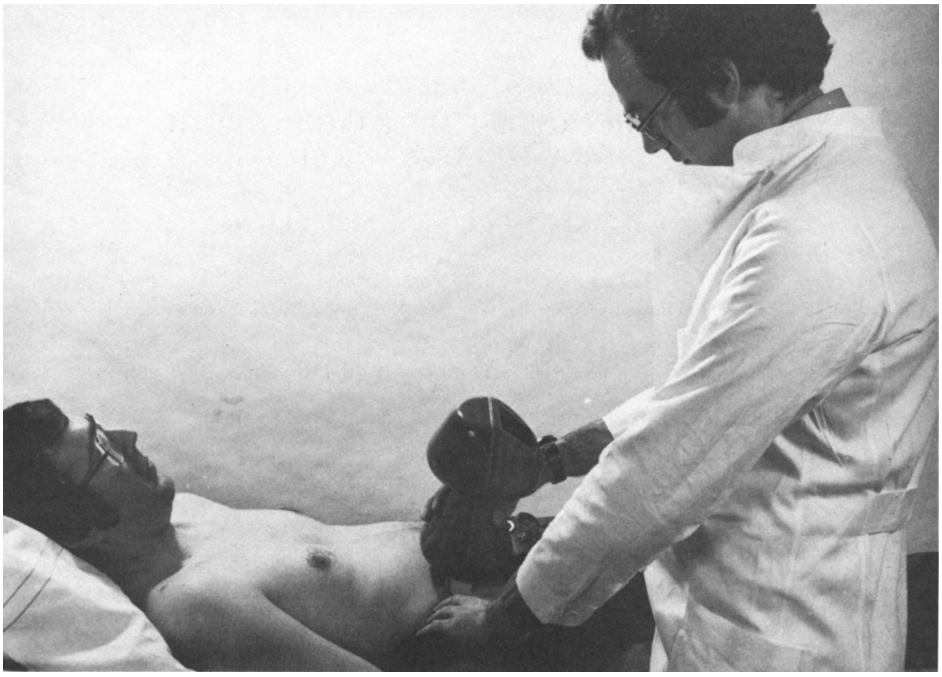

Figure 2.2: The Minivisor developed in 1978 at the Thoraxcentre, Erasmus University, Rotterdam, The Netherlands. Image from (Ligtvoet et al. 1978).

between transducer, electronics, and algorithm developers. The device consists of a fully sampled, 60 x 60 elements transducer array, front-end integrated circuits (ICs) for each receiving channel, transmit (Tx) circuitry, a digital signal processor for beamforming, and a liquid crystal display. Significant savings in circuit complexity were achieved by using direct sampled in-phase/quadrature (DSIQ) beamforming, which allowed sampling rates as low as 10 kHz (Ranganathan, Santy, et al. 2004). The system was capable of imaging with a frame rate of 43 frames per second (FPS) for a scan time of 2 h; it measured 6 cm $\times$ 15 cm $\times$ 3.5 cm and weighed 170 g. The promising results of the prototype drove the consequent development and commercialization of the system.

A wireless battery-powered ultrasound probe was proposed in 2010 in a patent by Poland and Wilson (Poland and Wilson 2010). The solution was intended for general-purpose ultrasound imaging, and was proposed to tackle the disadvantages of having a cabled connection between the probe and the central processing unit. The cable is usually bulky and heavy, as it contains a high number of coaxial wires. It creates contaminating sources in sterile fields such as ultrasound-guided surgery and anaesthesiology, and it is usually expensive. The proposed probe was based on micro-beamforming focusing

(Larson 1993) and included an array of transducers, receivers and beamforming circuits, as well as antennas for the data transfer. The battery-powered feature raises concerns about the power consumption of the probe, that has to be carefully controlled to achieve a reasonable scan time and to keep the thermal heating within the safety limits. A number of measures were discussed in (Poland and Wilson 2010) to deal with thermal heating issues.

Kim *et al.* designed a prototype of a low-cost standalone scanner with the form-factor of a laptop (Kim et al. 2012). The system consisted of only 16 channels, and an extended aperture was emulated by transmitting twice in the same direction while receiving with adjacent sub-apertures. This improved the lateral resolution without increasing the system complexity at the expense of the frame rate. The processing was performed in a single field-programmable gate array (FPGA), and further simplification was accomplished by means of beamforming strategies that reduced the delay calculation and storage requirements. The same group designed in 2016 a system-on-chip architecture integrating beamformers and signal processors for B-mode and flow imaging (Kang et al. 2016). The fabricated application-specific integrated circuit (ASIC) allowed the development of a hand-held system consisting of a probe and an FPGA-based back-end processor. The system measures 20 cm $\times$ 12 cm $\times$ 4.5 cm and weighs approximately 700 g. The probe has also been used coupled to a smartphone for B-mode and flow imaging (Ahn et al. 2015; Jeong et al. 2015). The use of general-purpose mobile devices as smartphones or tablets has the advantage of improving the cost-effectiveness of the ultrasound system by cutting down significantly the cost of the processing unit.

In 2014, Hemmsen *et al.* presented a proof-of-concept implementation of a scanner based on consumer-level mobile devices linked via Wi-Fi to an ultrasound probe (Hemmsen, Kjeldsen, et al. 2014). The system was based on synthetic aperture sequential beamforming (SASB) (Kortbek, Jensen, and Gammelmark 2013). The approach reduces the data rate between the probe and the processing unit by dividing the focusing between a first-stage beamformer (FSB) integrated into the probe handle, and a second, software-based beamformer implemented in the mobile device. The necessary data throughput was achieved in a realistic noisy usage situation (office environment), and the processing time was suitable for real-time performance. The implementation was extended to a duplex sequence including color flow mapping (CFM) executed in the tablet's graphics processing unit (GPU) (Hemmsen, Lassen, et al. 2015). The studies showed that a complete wireless system can be obtained by using general-purpose mobile devices with imaging performance comparable with conventional system.

The prototype of a ultra-low-cost ultrasound scanner has been developed in 2017 by van den Heuvel *et al.* (Heuvel et al. 2017). The system is intended for low-resource settings and uses a single-element transducer mechanically swept across a convex image geometry. The probe is connected through a USB link to a general-purpose processing device, where a synthetic aperture (SA) beamformer is employed to improve the image quality. Due to the monostatic approach, a limited frame rate could be achieved (reported to be 4 FPS for a conventional imaging sequence), and the signal-to-noise ratio (SNR)

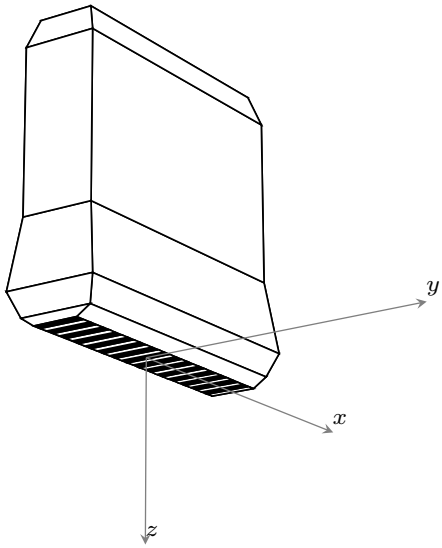

Figure 2.3: Cartesian frame of reference with respect to the position of the transducer.

and penetration depth are reduced. However, the authors claim production costs in the order of $100 that would allow the system to experience a widespread use in developing countries.

2.2 Image quality metrics

A number of metrics and procedures have been proposed for the quantification of the image quality of an ultrasound system or method (AIUM 1995; Thijssen, Weijers, and Korte 2007). Some metrics are introduced in this section to allow for a technical evaluation of the point spread function (PSF). In the remainder of this dissertation, the Cartesian coordinate system in Fig. 2.3 is considered the standard frame of reference.

2.2.1 SNR and depth of penetration

The SNR is defined as

$$SNR = \frac{\sigma_s}{\sigma_n}, \tag{2.1}$$

where σ_s and σ_n are the standard deviations of the signal and the noise, respectively. The standard deviations are calculated from an ensemble of signals.

During the propagation in the tissue, the ultrasonic signals are gradually attenuated, while the level of the noise coming from the receiving electronics remains constant. As

a result, the SNR decreases as a function of the depth. The power of the signal equals that of the noise, i.e. SNR = 0 dB, at the penetration depth, beyond which the image is dominated by the noise.

2.2.2 Spatial resolution

The spatial resolution is the ability of an imaging system to discriminate between two distinct objects in the field of view. More specifically, it is the minimum distance between two details necessary to resolve them as separated, and it is formally measured by the full-width at half-maximum (FWHM), i.e. the −6-dB beamwidth. In the axial direction, the resolution depends upon the center frequency f_0 and the bandwidth of the ultrasonic pulse. The lateral resolution is a function of the shape of the pulse-echo beam and can be altered through the focusing and apodization functions. In general, the lateral resolution is optimal at the focal position, where the following relation is verified

$$FWHM \sim \lambda F_{\#} = \lambda \frac{z}{L} = \frac{c}{f_0} \frac{z}{L}, \tag{2.2}$$

and decreases away from this point because of diffraction effects. In (2.2), $\lambda = c/f_0$ is the pulse wavelength, c the speed of sound, $F_{\#} = z/L$ the F-number of the system, z the depth of focus, and L the length of the aperture.

The spatial resolution is influenced by all the stages in the signal processing chain as well as the physics of the propagation of the ultrasonic pulse in the tissue. For example, the frequency-dependent attenuation lowers the center frequency, therefore increasing the FWHM. Errors in the beamforming can also degrade the spatial resolution.

2.2.3 Contrast

Differently from radar and sonar, in medical ultrasound imaging the “targets” of the imaging system are embedded in a continuous backscattering medium. It is, therefore, important to be able to separate different objects given their reflectivity, i.e. the strength of the backscattered signal that they generate. Hypoechoic regions can be, for example, interpreted as lesions, blood vessels, or other fluid-filled structures as bladders, and their detectability is measured by the contrast. This characteristic is a function of the sidelobe and grating lobe levels and can be quantified by metrics as the cystic resolution (CR).

The CR is a PSF metric that is defined as the radius r of the smallest void that can be resolved with a contrast

$$C(r) = \sqrt{\frac{1 + SNR^2 \left(1 - \frac{E_{in}(r)}{E_{tot}}\right)}{1 + SNR^2}}, \tag{2.3}$$

where E_{in} is the PSF energy inside the void, and E_{tot} is the total energy of the PSF (Ranganathan and Walker 2007; Vilkomerson, Greenleaf, and Dutt 1995). An example

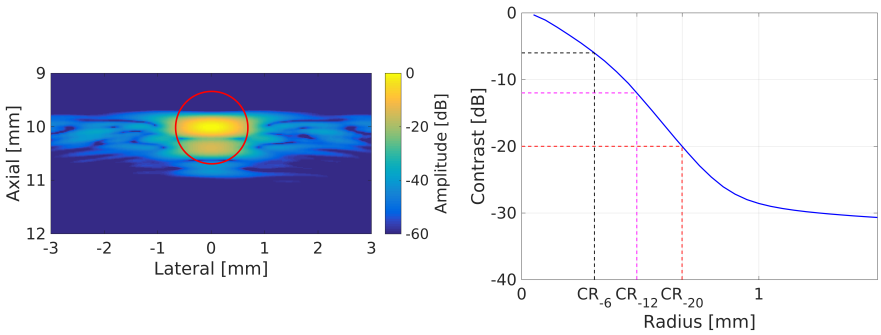

(a) (b)

Figure 2.4: (a) PSF at a depth of 10 mm displayed with a DR of 60 dB; (b) contrast $C(r)$ calculated for increasing values of r. The values for the CR at -6, -12 and -20 dB are shown in black, magenta and red. For this PSF, the smallest void that can be resolved with a contrast of 20 dB has a radius $C_{-20} = 0.68$ mm; a red circle with the same radius is superimposed on the PSF in (a).

of a PSF at a depth of 10 mm displayed with a DR of 60 dB is shown in Fig. 2.4(a). The contrast $C(r)$ calculated using (2.3) for increasing values of r is plotted in Fig. 2.4(b). The values for the CR at −6 , −12 , and −20 dB are shown in black, magenta and red. For this PSF, the smallest void that can be resolved with a contrast of 20 dB has a radius C_{-20} = 0.68 mm. A red circle with the same radius is superimposed on the left plot to give an indication of the void's dimensions relative to those of the PSF. The advantage of the CR is that it provides a quantification of the contrast directly from the PSF without requiring a complete image, and it is therefore a valuable and helpful tool for the design of a new imaging method.

It must be noted that the contrast of a system is a function of its dynamic range (DR), i.e. the ratio between the maximum and minimum amplitudes resolvable by the system, and it is therefore important to specify the DR for the correct evaluation of the contrast.

2.3 Challenges in the design of a portable ultrasound system

In a conventional cart-based scanner, only the transducers and the early conditioning circuitry are integrated in-handle, and most of the computational effort is taken care of by the central processing unit. On the contrary, the signal processing burden must be shared between the probe and the console in portable systems, and more challenging demands arise for the power dissipation in the probe handle. The problem of the minimization of

the system complexity has been addressed over the years with the design of innovative imaging algorithms and electronic strategies that attempt to limit the power consumption. Some of the possible solutions are reviewed in this section focusing on the receiving portion of the system.

2.3.1 Transducer

Arrays of transducers are commonly used in ultrasound scanners. These can be arranged in a number of geometries to address different clinical needs, e.g. linear arrays for small and shallow parts, convex arrays for abdominal scans, small-footprint, phased-arrays for cardiac scans. The array consists of a series of ultrasonic transducers that can be individually controlled to electronically shape and steer the beam.

The lateral resolution and the amplitude of the side-lobes can be adjusted by controlling the width and apodization window of the active aperture. In general, larger apertures provide better resolution.

A first and straightforward solution to reduce the number of channels is the undersampling of the spatial aperture. In this case, the transducer element layout must be carefully optimized to attenuate the influence of the grating lobes while maintaining reasonable the number of channels. The problem has been addressed by several groups (Austeng and Holm 2002; Lockwood, P.-C. Li, et al. 1996; Lockwook and Foster 1996). More recently, alternative strategies as row-column addressed arrays have also been proposed (Rasmussen et al. 2015). However, these solutions are mainly for 3-D ultrasound imaging, where the sampling of 2-D arrays and the necessity for beam-steering can easily result in thousands of channels.

2.3.2 Receiver front-end

The receiver analog front-end (AFE), i.e. the receiving electronics directly connected to the transducer elements, is critical to any ultrasound system (Schafer and Lewin 1984). Modern scanners largely rely on digital signal processing, and it is, therefore, convenient to convert the signal to the digital domain as early as possible in the processing path. However, an earlier amplification by means of analog low-noise amplifiers (LNAs) is required to fulfil the DR, bandwidth, and SNR demands while reducing the complexity of the analog/digital converter (ADC). An optimized design of these components is paramount for achieving an adequate image quality, and it has a critical impact on the system complexity and power consumption. Therefore, careful attention must be paid especially in the case of resource-limited designs.

Schafer and Lewin (Schafer and Lewin 1984) stressed the necessity of an integrated design for optimal performance. Integrated AFE solutions have the advantage of minimizing the number of interconnections, which represent a major source of noise and power dissipation. Examples of integrated Tx and receive (Rx) front-ends can be found in (Sawan, Chebli, and Kassem 2003) and (Chebli and Sawan 2007), and in the system description section of (Fuller, Ranganathan, et al. 2008).

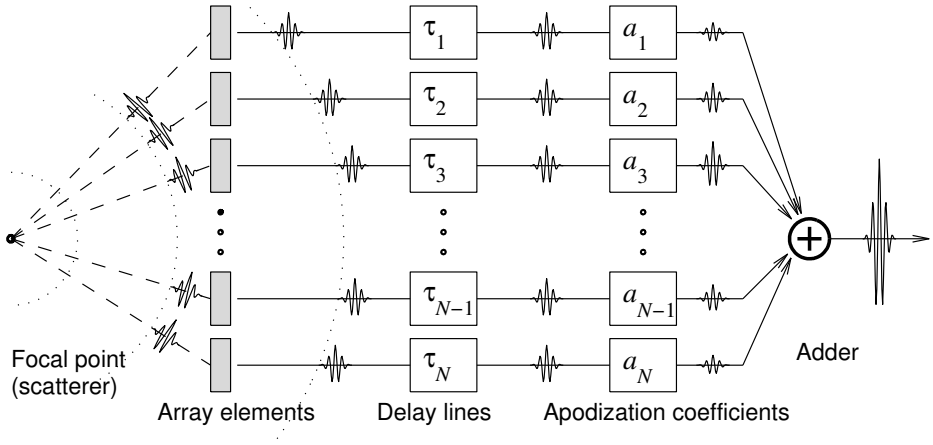

Figure 2.5: Delay-and-sum beamformer. Image from (Nikolov 2001).

2.3.3 Beamformer

A comprehensive review of digital beamforming approaches was published by Mucci (Mucci 1984). The beamformer allows to coherently process the data collected with an array of sensors. The purpose of this component is to emulate an aperture of a certain width, oriented in a specific direction, and focused at a given range. The aperture width, direction, and focus position can be dynamically changed during reception by delaying and summing the weighted sensor data (Fig. 2.5), and this defines the epithet delay-and-sum (DAS) commonly used for this family of beamformers.

The quantization of the delays in a digital DAS beamformer hinders the optimality of the focusing, introducing artefacts in the final image. This problem and its effect on the shape of the ultrasound beam has been object of study by Peterson and Kino (Peterson and Kino 1984), who generalized to the near field the radar's theory for delay quantization errors. In the far field, the delay quantization gives rise to lobes similar in appearance to grating lobes. In the near field, the beam is a superposition of an infinite number of focused beams, the amplitude of which decreases as a function of the number of quantization levels. However, when focusing is utilized, the effects in the near field can be considered to have a limited impact on the final image. The authors also demonstrated that the contribution from amplitude quantization errors is reasonably below the level of other quantization errors.

Holm and Kristoffersen (Holm and Kristoffersen 1992) studied the effect of random and periodic errors in a focused and steered imaging system. The periodic nature of the delay quantization error in an unfocused beamformer gives rise to discrete sidelobes exhibiting maxima in a number of directions. These errors are deterministic, and the beamformer can be designed to avoid that the directions of maximum are in the image

field of view. The focusing, on the other hand, provides uncorrelated errors that can be characterized statistically, and cause effects similar to those of other random variations, e.g. gain uncertainties and amplitude quantization.

2.3.4 Influence of the beamformer on the system complexity

The delay resolution is, in general, a function of the sampling rate, which must be high enough to ensure a proper image quality. Therefore, the image quality requirements affect the ADC and memory specifications, and the optimization of the signal processing involved in the beamforming can yield considerable savings in terms of power consumption and circuit area (Mucci 1984).

One possible approach relies on summing digital samples directly read from the memory, where the digitized signals are buffered prior to beamforming. The memory addresses encode the time delays stored in a look-up table, and the computational complexity of this beamformer is essentially limited to one single adder. However, it requires high sampling rates and large amounts of memory.

It is possible to relax the requirements on the ADC if temporal interpolation of the sensor data is available. The required delay resolution can be achieved at the cost of the additional circuitry required for the interpolator. Temporal interpolation can be efficiently realized by finite impulse response (FIR) low-pass filters, and usually this approach provides a less expensive solution than oversampling.

The delays can be approximated by a phase shift at the center frequency of the received signal. In this case, the delay resolution is not dependent upon the sampling rate. However, the assumption of narrowband signals is made, and this is an approximation in realistic situations.

2.4 Beamforming methods for miniaturized systems

The challenging demands raised by the increased power density of miniaturized ultrasound systems promoted the design of innovative imaging algorithms to care of the limited power budget. In the past decades, the research community has supplied a number of intelligent ideas taking advantage of the newest developments of the semiconductor technology. Some of the proposed solutions are reviewed in this section.

2.4.1 Early solutions

In 1984, Peterson and Kino (Peterson and Kino 1984) presented a system based on a back-projection algorithm showing how the complexity can be effectively reduced by taking into account features of the system such as the symmetry of the apertures.

Digital beamforming can be efficiently integrated in compact digital circuits taking advantage of very-large-scale integration (VLSI) technology (O'Donnel 1988). A VLSI beamformer has been presented by Karaman *et al.* (Karaman, Atalar, and Köymen 1993)

and included a linear interpolator for upsampling the digital signals and circuits for the phase aberration correction.

2.4.2 FPGA-based beamforming

Tomov and Jensen (Tomov and Jensen 2005) presented a compact beamformer based on oversampling sigma-delta modulator (SDM) ADCs. SDMs offer a high degree of integration due to the fact that only single-bit sequences need to be handled. Furthermore, due to the inherently high sampling frequency, high delay resolution is achieved without the need for interpolation. The reconstruction of the modulated signals is combined in this approach with the beam formation, i.e. only the samples used by the beamformer are demodulated in a sparse manner by means of a pair of FIR filters for the in-phase/quadrature (I/Q) components. The method was tested through simulations of the PSF and blood flow estimation, and the architecture was successfully implemented on FPGA. The image quality was slightly lower compared with conventional beamforming; however, the authors state this could be improved by using a higher oversampling ratio.

An FPGA-based beamformer was also proposed for the portable system in (Kim et al. 2012). Pseudo-dynamic Rx beamforming was used to simplify the system architecture, i.e the range was divided into a number of focal zones, and fixed delay profiles were used in each zone. On the one hand, this focusing method significantly reduces the delay calculation and storage requirements. On the other hand, it introduces delay errors with consequent degradation of the image quality.

2.4.3 Direct sampled in-phase/quadrature beamforming

The DSIQ beamforming (Ranganathan, Santy, et al. 2004) saves system resources by implementing the focusing through a complex phase rotation of the digital I/Q data. The I and Q components are directly sampled for each receiving element by two sample/hold circuits. The clock signals for the I and Q channels have the same frequency, but the Q channel is shifted by $T_0/4$, with $T_0 = 1/f_0$ the pulse period. The knowledge of the center frequency is therefore critical for the correct calculation of the phase shift, and this poses a first limitation due to the frequency shift induced by the frequency-dependent attenuation. Furthermore, the beamformer assumes narrowband signals, and this is an approximation in realistic situations.

Images of wire targets and anechoic cysts are shown in (Ranganathan, Santy, et al. 2004) for comparison with non-quantized DAS beamforming with a DR of 20 and 40 dB, which is not sufficient for general purpose imaging, where 60 to 80 dB are usually required. However, the beamformer has been successfully integrated in the Sonic Window system introduced in Sec. 2.1.

2.4.4 Sub-array beamforming

A parallel processing system called Explososcan was developed at Duke University by Shattuck *et al.* (Shattuck et al. 1984). The system was capable of dynamically focusing

four simultaneous channels in Rx (Explosolines). The delays required for each line are divided into focusing and steering contributions. The focusing delays are shared by all the receiving channels while the steering is realized by addition of small tapped delay lines cascaded with the focusing circuits of each channel. The method has been extended to 3-D imaging with 2-D linear phased arrays (Ramm, Smith, and Pavy 1991).

A similar approach was developed at Hewlett-Packard, Palo Alto, CA, by J. D. Larson, III (Larson 1993) to reduce the number of lines transmitted from the probe to the central unit. The receiving elements are grouped in clusters, each of which is independently pre-processed in the probe. One partially beamformed signal is then sent to the base unit for each cluster of receivers. The delays for steering and focusing are distributed between a pre-beamformer implemented into the probe, which introduces intra-group delays, and a post-processor in the host unit for inter-group delays. For a 100 x 100-element transducer, for example, the number of lines can be reduced from 10000 to 400 by grouping the receivers in sub-arrays of 5 x 5 elements.

The proximity of receiving elements in the same cluster makes the intra-group delay network easy to implement, since only short delays are needed for signals in the same group (B. J. Savord 2000; B. Savord and Solomon 2003). The method has been successfully employed in 3-D ultrasound systems (B. Savord and Solomon 2003). Chen *et al.* have developed an ASIC AFE with integrated beamformer for a 32x32 element transesophageal probe with a total area of $6.1\,\mathrm{mm}^2 \times 6.1\,\mathrm{mm}^2$. The same approach can be used with 1-D arrays for reducing the data bandwidth of the communication link.

2.4.5 Synthetic aperture for small-scale devices

SA focusing is based on the use of defocused spherical waves to collect information from a whole image sector at once and obtain dynamic focus in both Tx and Rx (Jensen et al. 2006). Although SA techniques were originally developed for improving the image quality of high channel count scanners, in 1995 Karaman *et al.* (Karaman, P. C. Li, and O'Donnell 1995) suggested their use to reduce the size and cost of the ultrasound systems. The authors stated that image quality comparable with that of a conventional phased array scanner can be achieved by using a SA with about 10 active channels in Tx and Rx. The result comes at the expense of a reduced SNR due to the lower acoustic power emitted by the active sub-aperture.

SA was also used by (Lockwood, Talman, and Brunke 1998) with sparse arrays to minimize the channel count for real-time 3-D imaging. Van den Heuvel *et al.* have recently presented the prototype of a low-cost system based on SA focusing (Heuvel et al. 2017).

Part I

Imaging strategies and hardware optimization

CHAPTER 3

Synthetic aperture sequential beamforming

3.1 Introduction to synthetic aperture focusing

In conventional ultrasound imaging, a sector is scanned by sequentially sweeping a narrow beam in a number of directions. For a given imaging depth and speed of sound, there exists a trade-off between the image quality and the frame rate imposed by the number of lines that have to be acquired per frame to satisfy the Nyquist sampling criterion. The minimum amount of lines is a function of the lateral resolution, and the frame rate is often unacceptable if a reasonable image quality must be achieved (Jensen, S. Nikolov, et al. 2006; Karaman, P. C. Li, and O'Donnell 1995). The problem is worsened in the case of flow imaging, where a number of acquisitions in the same direction must be performed for the detection of the velocity (S. I. Nikolov 2001). In addition, the image is, in general, optimally focused only at one depth, if a single focused emission is used per direction.

Starting from the late 1960s, SA techniques have been introduced (Flaherty, Erikson, and Lund 1967; Prine 1972) to overcome these limitations and achieve improved lateral resolution, while paving the way to high-frame-rate ultrasound imaging. The overall idea is to emit wide diverging beams to insonify significant portions of the image. The received ultrasound signals collected from a number of emission angles and carrying information from the whole insonified area are then coherently combined to obtain a high-resolution image (HRI) with ideally uniform Tx and Rx dynamic focus.

Early SA systems used single pulsed ultrasonic transducers mechanically swept in the lateral direction (Burckhardt, Grandchamp, and Hoffmann 1974) or multiplexed single elements of transducer arrays to emit a wide beam (Corl, Grant, and Kino 1978). This approach is referred to as monostatic. By using one element in Tx and Rx, these systems required only a single AFE and were, therefore, inherently simple. They suffered, however, from low SNR due to the low emitted pressure and sensitivity of the small active aperture. The full array has also been used in Rx for improved resolution and sensitivity at the cost of increased system complexity (Karaman and O'Donnell 1998; Lockwood, Talman, and Brunke 1998).

The problem of the reduced SNR of SA systems has been addressed by several researchers. O'Donnell and Thomas used multiple transducer elements that were short-circuited to increase the emitted pressure and reduce the impedance seen by the electronics.

The method has been implemented in a circular array for intravascular imaging (O'Donnell and Thomas 1992). Ylitalo and Ermert proposed the simultaneous excitation of several elements in a monostatic approach to increase the DR by almost 20 dB compared with the single element transmission (Ylitalo and Ermert 1994). The resolution was, however, lowered by the narrower beam. A wide beam is necessary in order to look at a given object from a large range of angles and achieve high lateral resolution. Karaman *et al.* used defocused sub-apertures to restore the beam width (Karaman, P. C. Li, and O'Donnell 1995) and, in turn, the resolution and contrast.

The drawback of SA imaging with transducer arrays is the high demand in terms of data sampling, transport, and storage. For this reason, only few systems have been developed to allow fully parallel acquisition of the channel data from multiple transducer elements (Jensen, Holm, et al. 2005; Jensen, Holten-Lund, et al. 2013; Lu, Cheng, and Wang 2006; Sandrin et al. 1999; Tortoli et al. 2009). Furthermore, the high processing requirements given by the necessity to beamform a whole image after each emission make it challenging to achieve real-time imaging performance (Amaro et al. 2015; Boni et al. 2016).

3.2 Virtual source focusing

The concept of virtual source (VS) was introduced by Passman and Ermert in 1996 to address the problem of the limited depth of field of strongly focused transducers (Passmann and Ermert 1996). The authors obtained more uniform lateral resolution using SA and assuming the focal region to be a source of spherical waves (Fig. 3.1). The use of VSs has been also studied by other research groups employing focused transducers or focused sub-apertures of transducer arrays (Bae and Jeong 2000; Frazier and O'Brien 1998; S. I. Nikolov and Jensen 2002).

The wave propagation path in the case of VS focusing with an array of transducers is shown in Fig. 3.2(a). A pulse is emitted by an active sub-aperture with Tx origin in $\vec{r}_e$ and electronically focused at $\vec{r}_{vs}$. The insonified region can be approximated as the area covered by the arcs. After passing through the focus point, the pulse travels to the image point $\vec{r}_{ip}$, and the backscattered wave is then detected by the receiver element $\vec{r}_r$. The point $\vec{r}_{ip}$ is insonified in several consecutive emissions, and this information can be used to apply SA focusing. The data from each element in the active sub-aperture has to be saved for each emission in order to apply the focusing retrospectively, therefore the data sampling and storage requirements are similar to those of multistatic SA.

3.3 Sequential beamforming approach

The SASB approach has been proposed by Kortbeck *et al.* to loosen the high requirements on the ultrasound system of a full SA focusing scheme (Kortbek, Jensen, and Gammelmark 2013). In SASB, the concept of VS is used in both Tx and Rx, i.e. the focal position is

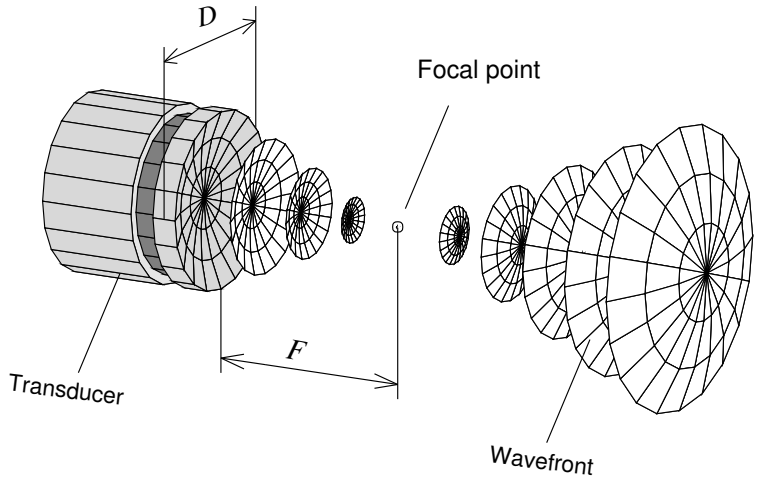

Figure 3.1: Wavefront of a concave transducer with an aperture diameter D and focused at a distance F. The focal region can be considered to be a source of spherical waves. Image from (S. I. Nikolov 2001).

also considered a virtual receiver (VR). A first beamformer is used to focus the signals received by the active sub-aperture in a point coincident with the VS, and a line is obtained, which is referred to as low-resolution line (LRL). The situation is depicted in Fig. 3.2(b), showing that the backscattered pulse is assumed to travel back to the VR before hitting the receiving aperture. As a result of the first beamformer, only one LRL needs to be stored after each emission.

The focused emissions create a virtual aperture (VA), and a HRI is reconstructed by a second-stage beamformer (SSB) using a set of LRLs from the entire VA. The assumption is that each sample in the LRL carries information from the arc of a circle crossing the corresponding point and centred at $\vec{r}_{vs}$, as illustrated in Fig. 3.3. The FSB can thus be seen as an integrator that operates along these arcs. This is exploited to obtain high resolution by coherently adding in a tomographic manner the representations of a point from all the VSs that *see* that point. In Fig. 3.3, for example, the point $\vec{r}_{ip}$ lies on the red, black, and blue arcs. The information on $\vec{r}_{ip}$, therefore, can be found in the respective LRLs at the samples corresponding to these arcs.

The opening angle α of a VS is determined as shown in Fig. 3.4, and is equal to

$$\alpha = 2 \arctan \frac{1}{2F_{\#}}, \tag{3.1}$$

where $F_{\#}$ is the F-number of the emission equal to z_f/L_A, with $z_f = |\vec{r}_{vs} - \vec{r}_e|$ denoting the distance of the VS from the aperture and L_A the aperture width. Similar considerations

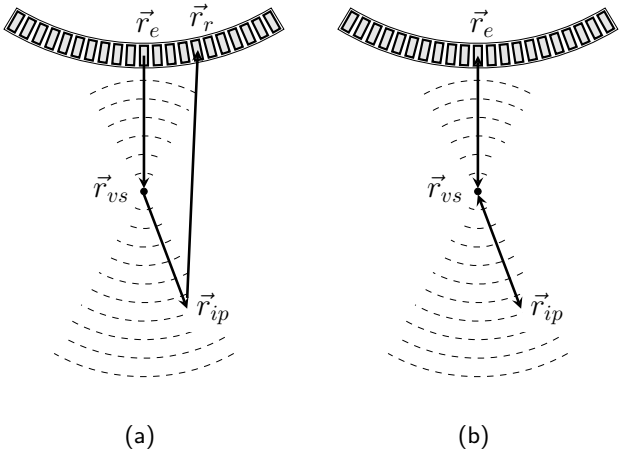

Figure 3.2: Wave propagation path for conventional VS focusing with an array of transducers (a); and in case of sequential beamforming approach (b). In (b), the backscattered pulse travels back to the VS before hitting the receiving aperture.

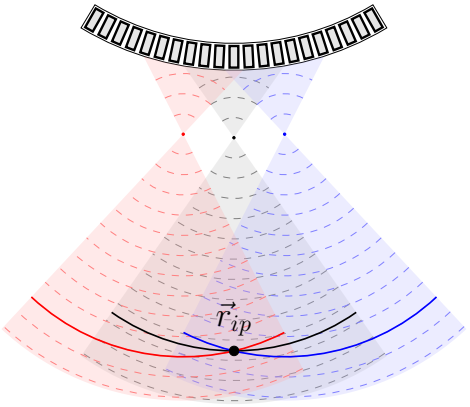

Figure 3.3: Second stage beamforming: each point in the LRL carries information from the arc of a circle crossing that point and centred on the VS. The information on $\vec{r}_{ip}$ can be found in the samples relative to the red, black, and blue arcs in the LRLs of the respective VS.

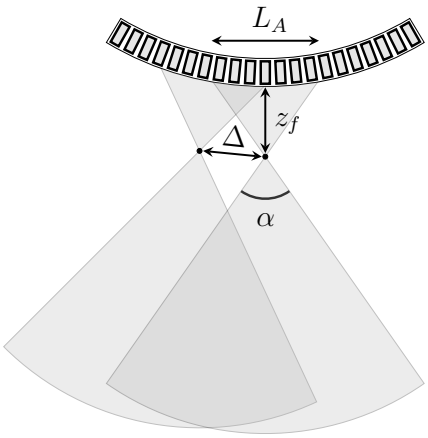

Figure 3.4: Geometrical description of the aperture angle α and pitch Δ of the VSs.

to conventional SA apply to SASB in terms of the relation between the beam angle and the resolution of the system, i.e. wider beams provide improved lateral resolution. The lateral distance between the VSs gives the pitch Δ, which plays a similar role to that of the pitch of the physical aperture.

The processing requirements of the SSB equal those of a monostatic SA beamformer where the LRLs are used in place of the transducer signals. A frequency-wavenumber approach has been proposed by Vos *et al.* for the SSB to further lower the computational complexity (Vos et al. 2016). An additional cost must be paid for the FSB, which is, nevertheless, very simple to realize and can be integrated in the probe handle to lower the data throughput between the transducer array and the processing unit. If an aperture of L transducer elements is used in Rx, for example, the data rate is reduced by a factor L by using the sequential beamforming approach. Finally, SASB enables the possibility to obtain SA focusing without the need for storing the complete channel dataset as in multistatic techniques, while the SNR of the VS approach and the flexibility of the electronic focusing are maintained. The data rate is also reduced compared with conventional dynamic receive focusing (DRF), where the complete channel dataset is saved prior to the focusing of an image line. This data reduction opens the way to the wireless transmission of the ultrasound data from the probe to the processing unit.

3.3.1 Method validation and applications

SASB has been demonstrated to provide improved lateral resolution compared with conventional DRF in phantom meaurements (Kortbek, Jensen, and Gammelmark 2013). Hemmsen *et al.* evaluated the performance of the method in terms of penetration depth,

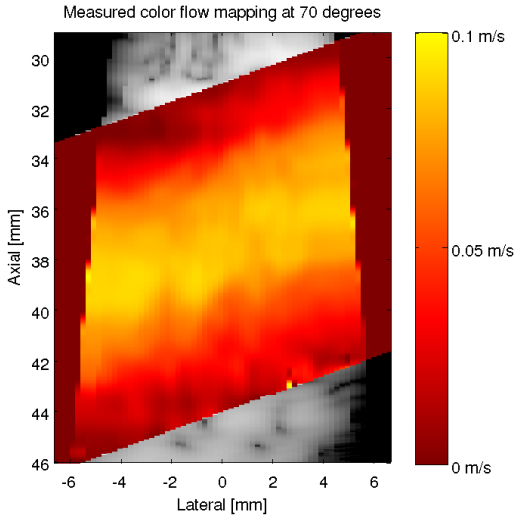

Figure 3.5: SASB color flow mapping of a straight vessel in a flow rig system with a parabolic flow profile. Image from (Y. Li and Jensen 2013).

resolution, and contrast in a pre-clinical study (Hemmsen, Hansen, et al. 2012). Abdominal scans from eighteen volunteers were independently examined by five experienced radiologists, and the images obtained with SASB were evaluated against those obtained with DRF. The clinical evaluation demonstrated that SASB provides image quality comparable with that of DRF, while the data storage and transmission requirements on the system are lowered.

The use of SASB was also investigated for tissue harmonic imaging (Brandt et al. 2014; Hemmsen, J. Rasmussen, and Jensen 2014) and for 3-D imaging (Hemmsen, M. F. Rasmussen, et al. 2014). The feasibility of the wireless transmission has been proven using commercial, general purpose mobile devices (Hemmsen, Kjeldsen, et al. 2014). A data throughput of 25.3 MB/s was demonstrated to be sufficient for achieving real-time performance.

A CFM imaging scheme has been proposed by Li and Jensen based on SASB (Y. Li and Jensen 2013). The method was tested on a flow phantom using a time shift estimator for the detection of the velocities. Due to the SA focusing, the method allows for the continuous acquisition of the flow data, which makes the velocities available at any time everywhere in the image. In addition, the clutter filter is simplified compared with the case of time-limited acquisition sequences. The SASB CFM approach has been successfully implemented in a commercial tablet (Hemmsen, Lassen, et al. 2015).

CHAPTER 4

System-level design of a wireless ultrasound probe: analog gradient beamformer

Summary *Having demonstrated that the wireless transmission of the data is feasible, a suitable hardware implementation must be found for the probe to comply with the thermal regulations. Compromises have to be made to reduce the power consumption while obtaining an acceptable image quality. Several system-level strategies for the receiver AFE and FSB have been investigated with simulations to study the effect of design choices on the quality of the B-mode image. In this chapter, an analog beamforming approach is introduced, which allows to significantly reduce the system complexity. The study is object of Paper VI in appendix.*

Having demonstrated that the wireless transmission of the data is feasible using SASB, a number of challenges must be faced to find a suitable hardware implementation of the probe. Due to the necessity of integrating the AFEs into the probe handle, and in particular the LNAs and ADCs, a significant amount of power is dissipated in a small area. Therefore, particular attention must be paid to optimize the thermal design of the system to comply with the thermal regulations of the Food and Drug Administration (FDA) (FDA 2008) and International Electrotechnical Commission (IEC) (IEC 2015).

The thermal regulations translate into limits for the maximum power dissipated by the circuitries. To have an idea of the power budget for such system, an analogy can be made with a smartphone, which encounters the same thermal design challenges given the small form-factor and the impossibility of using active cooling strategies. The power dissipation in a normal usage modality (phone call) for an average device is reported to be between 0.75 and 1.1 W (Carroll and Heiser 2010). Taking into account a larger contact area of the probe compared with conventional smartphones, the ideal target power consumption for this system can be guessed to be about 2.2 W and should certainly not exceed 3 W for comfortable use. Compromises have to be made, therefore, at every stage of the design process to reduce the power consumption while obtaining an acceptable

image quality, and state-of-the-art commercial ICs are overdesigned for the purposes of a portable scanner.

Several system-level strategies for the receiver AFE and FSB have been investigated with simulations to study the effect of design choices on the quality of the B-mode image, and the results are reported in the following sections. The work was a collaboration with the Department of Electrical Electrical Engineering at DTU and BK Ultrasound, Herlev, Denmark. The objective of the study was to provide the IC designers with the minimum specifications necessary to meet the image quality requirements. In this chapter, an analog beamforming approach is introduced, which allows to significantly reduce the system complexity.

4.1 Analog gradient beamformer

In the gradient beamformer, the transducer elements are grouped into sub-apertures of N receiving channels as illustrated in Fig. 4.1. For each channel, the delay is divided into a coarse group delay T_g applied to the entire sub-aperture and a fine, element-dependent delay t. The signals in the sub-aperture are gradually delayed and summed in the analog domain, and one single ADC is needed for each sub-aperture, obtaining an N-fold reduction of the number of ADCs compared with a fully digital approach.

The schematic representation of the system is displayed in Fig. 4.2. The received signals are fed to a cascade of analog amplifiers for time-gain compensation (TGC) and apodization, and partially beamformed in the analog domain before A/D conversion. The group delay T_g is applied to the digital signal and is a multiple of the sampling period. The pre-beamformed signals are finally summed together before transmission to the processing unit, where the HRIs are created by the SSB.

Each signal in Fig. 4.2 is delayed by an amount ∇t_i, referred to as gradient delay. This delay is equal to the difference between the fine delays of the two adjacent elements, i.e. $\nabla t_i = t_i - t_{i+1}$. In other words, the fine delay t_i is obtained through an integration of N-i+1 gradients. For example, channel 1 in Fig. 4.2 is the one to be delayed the most in the sub-aperture, therefore is the first in the chain. The signal is delayed by an amount $\nabla t_1 = t_1 - t_2$ and then summed with the signal from channel 2. The result is then delayed by $\nabla t_2 = t_2 - t_3$ and summed to the signal from channel 3, and so on. To further simplify the architecture, the delays ∇t are obtained by using a variable-length bank of elemental delays dt as shown in Fig. 4.3, therefore the resulting ∇t is quantized to the value dt.

The elemental delays dt can be realized by means of a network of simple phase shifting all-pass filters, and this simplifies a single-chip implementation of the beamformer. Compared with a micro-beamformer, the approach presented here provides a more simple architecture, since a fixed-focus is used in the FSB and the delay profile is not updated during reception, while a dynamic Tx and Rx focus is obtained in the SSB.

The sub-aperture size N and the quantization step dt have an impact on the system complexity. It is desirable to maximize N to lower the amount of ADCs, while a greater

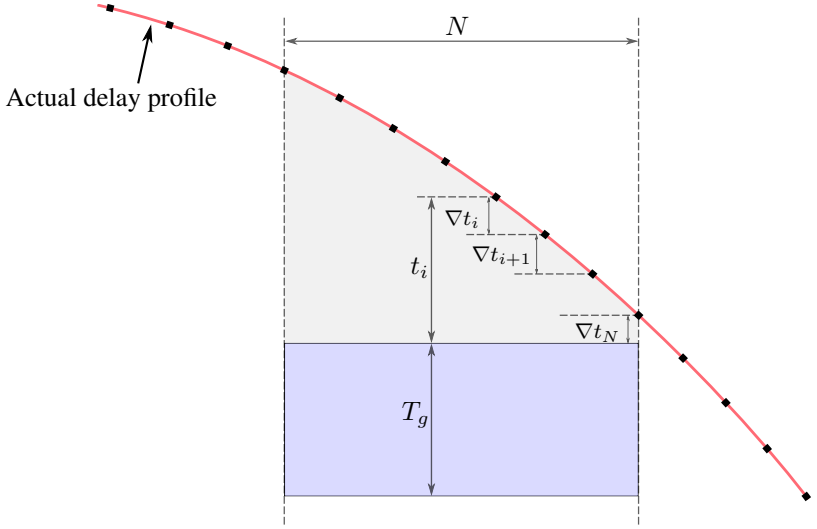

Figure 4.1: Gradient beamforming delay profile integration. The transducer elements are grouped into sub-apertures of N receiving channels. For each channel, the delay is divided into a coarse group delay T_g applied to the entire sub-aperture and a fine, element-dependent delay t.

dt allows to lower the number of delay blocks. On the other hand, artefacts appear in the images due to the grouping and quantization. The approach was simulated with varying N and dt to study the impact of these parameters on the image quality.

4.2 Simulation setup

Simulations were carried out in Field II (Jensen 1996; Jensen and Svendsen 1992) to evaluate the image quality as a function of N and dt. The PSF was simulated in a range from 10 to 130 mm using a convex array transducer with a fixed Tx/Rx focus in 70 mm. The parameters are reported in Table 4.1 for the transducer and Table 4.2 for the imaging setup. The quantization step size was swept from 2 to 50 ns in steps of 2 ns with the values of N in Table 4.3. A sampling frequency of 60 MHz was used for the calculation of the group delay T_g. The ideal and quantized delay profiles with $N = 32$ and dt =12 and 30 ns are shown in Fig. 4.4.

A model of the gradient beamformer was built in MATLAB (The MathWorks Inc., Natick, MA), and the SSB was implemented using the BFT3 toolbox (Hansen, Hemmsen, and Jensen 2011). The HRIs were log-compressed after envelope detection, and displayed with a DR of 60 dB. The B-mode image quality was evaluated in terms of lateral FWHM

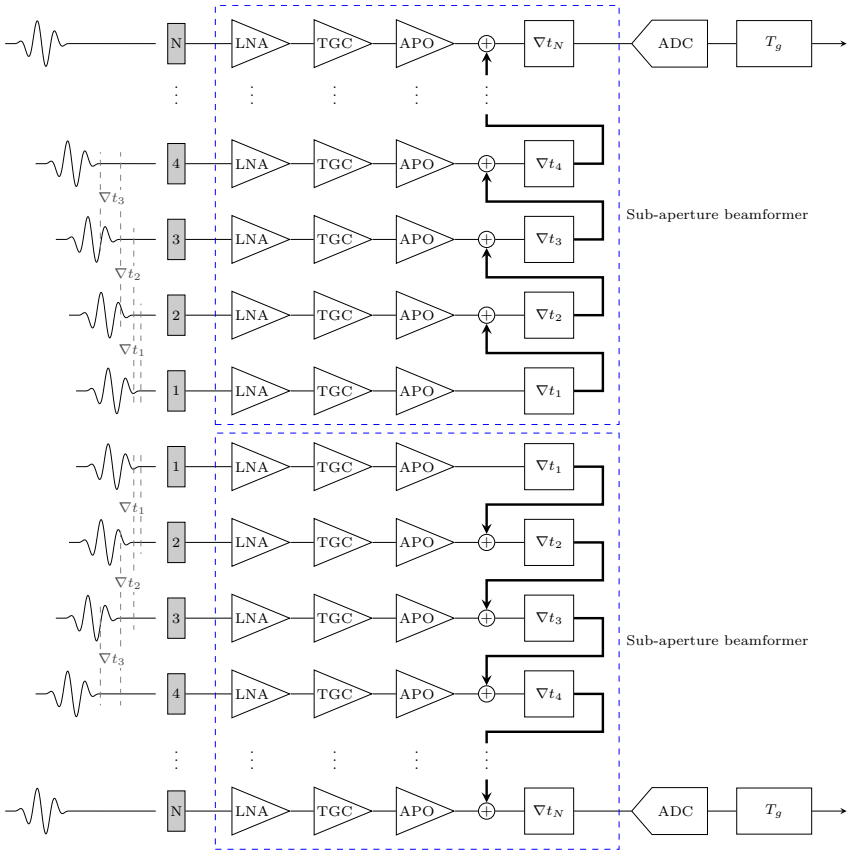

Figure 4.2: Schematic representation of the gradient delay beamformer system. The received signals are amplified and partially beamformed in the analog domain before A/D conversion. The group delay T_g is applied to the digital signal and is a multiple of the sampling period. The individual signals are delayed by an amount ∇t_i referred to as gradient delay. This is equal to the difference between the fine delays of the two adjacent elements, i.e. $\nabla t_i = t_i - t_{i+1}$.

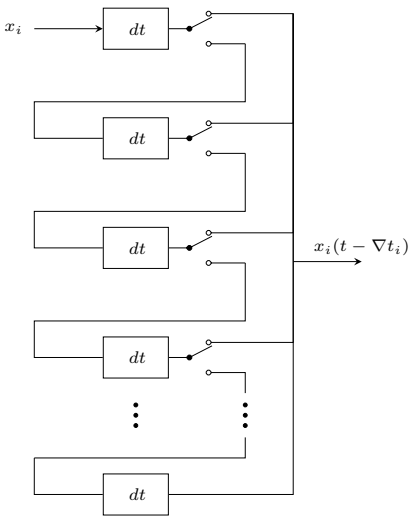

Figure 4.3: Schematic representation of the gradient delay block. The gradients ∇t are obtained by using a variable-length bank of elemental delays dt.

Table 4.1: Convex array parameters

Parameter	Symbol	Value	Unit
Array type	-	Convex	-
Element pitch	p	0.33	mm
Element height	-	13	mm
Number of elements	-	192	-
Elevation focus	-	65	mm
Radius of curvature	-	61	mm
Center frequency	-	3.75	MHz

and −20 dB CR calculated as in (2.3). FWHM and CR were averaged over all the simulated depths and compared with the ideal, non-quantized setup.

4.3 Results

The average FWHM is shown in Fig. 4.5(a). The resolution is close to that of the ideal beamformer for quantization steps lower than 26 ns, with losses limited to 3.2% with respect to the reference. For greater values of dt, the resolution drops and the FWHM increases for all the values of N.

The beamforming errors introduced by the delay quantization mostly affect the ampli-

Table 4.2: Simulation parameters

Parameter	Symbol	Value	Unit
Speed of sound	c	1490	$\mathrm{m\,s^{-1}}$
Attenuation	α	0.5	$\mathrm{dB\,cm^{-1}\,MHz^{-1}}$
Imaging setup			
Excitation	-	2 cycles	-
Center frequency	f_0	3.75	MHz
Tx apodization	-	Rectangular	-
Rx apodization	-	Hamming	-
VS axial position	-	70	mm
Active elements	L	64	-
f-number	$F_\#$	3.3	-
Number of VSs	-	269	-
Distance between VSs	-	3.9	mrad
Processing			
Sampling frequency	f_s	60	MHz
SSB apodization	-	Hamming	-

Table 4.3: Varied simulation parameters

Parameter	Symbol	Value	Unit
Quantization step	dt	2 to 50 in steps of 2	ns
Sub-aperture size	N	2 - 4 - 8 16 - 32	samples

tude of the sidelobes and, in turn, the contrast of the system. This can be seen from the −20 dB CR in Fig. 4.5(b). The CR is close to the reference for $dt < 12$ ns. Therefore, this point represents the quantization limit if ideal image quality is to be maintained.

Examples of the simulated PSFs in 20 mm, 70 mm, and 120 mm are shown in Fig. 4.6, 4.7, and 4.8 for the ideal case (a), and using the gradient beamforming approach with $N = 32$ and dt =12 ns (b) and dt =30 ns (c). The effects of the beamforming errors are more evident in the close field, in particular with regard to the amplitude and spatial extension of the sidelobes. With $N = 32$ and dt =12 ns, however, the average FWHM drops by 0.25% and the average CR by less then 8.70%, while only two ADCs are used for a 64-element active aperture.

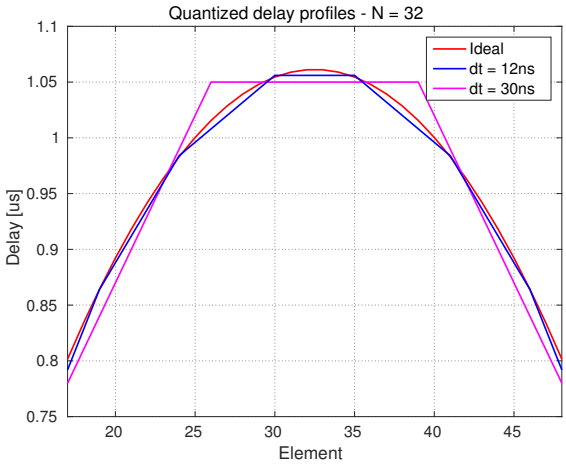

Figure 4.4: Examples of ideal and quantized delay profiles with $N = 32$ and dt =12 and 30 ns.

4.4 Discussion

An analog gradient beamforming approach was presented in this chapter and its performance investigated through simulations of the PSF. The method allows for a simplification of the system architecture by significantly reducing the amount of ADCs. The active aperture is divided in sub-apertures, and the delays are divided into a coarse and a fine components. The signals in each sub-aperture are pre-beamformed using the fine delays, and a single signal is obtained for each sub-aperture after summation. This is A/D converted, and the coarse delay is applied in the digital domain. To further simplify the system, the fine delays are quantized.

The image quality was evaluated for this beamformer and compared with the ideal case to derive the specifications for the size of the sub-aperture and the quantization step to maintain acceptable lateral resolution and contrast. Images of the PSF were shown for the design using as few as two ADCs for an active aperture of 64 transducers.

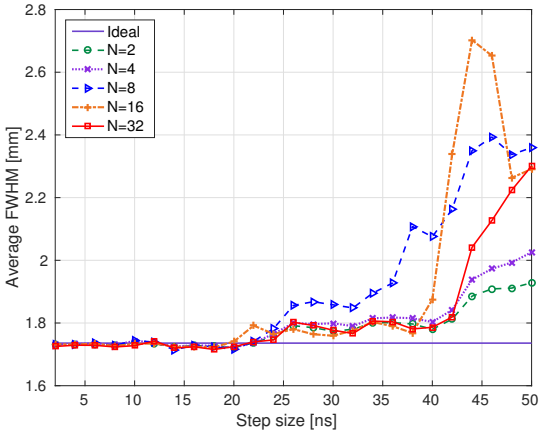

(a)

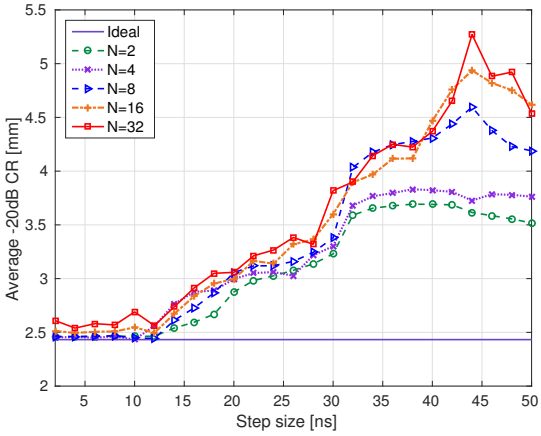

(b)

Figure 4.5: Average FWHM (a) and -20 dB CR (b) as a function of the quantization step dt for the simulated PSF obtained with the gradient beamformer approach using sub-aperture sizes $N = 2, 4, 8, 16, 32$ and compared with the ideal setup.

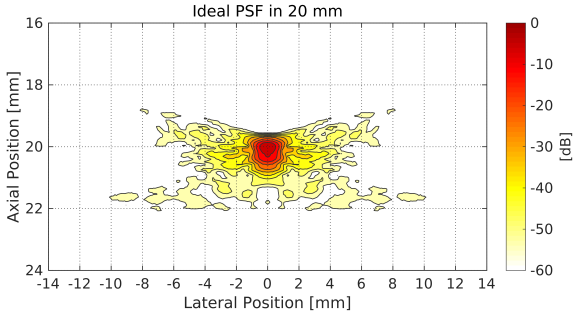

(a)

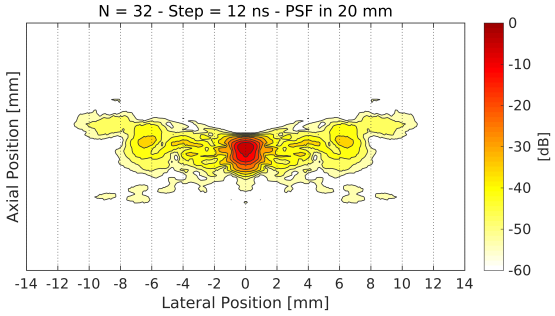

(b)

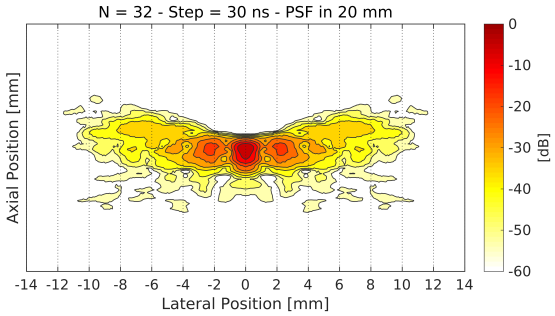

(c)

Figure 4.6: Simulated PSF at 20 mm for the ideal beamformer (a); gradient beamformer with $N = 32, dt$ =12 ns (b); and gradient beamformer with $N = 32, dt$ =30 ns (c).

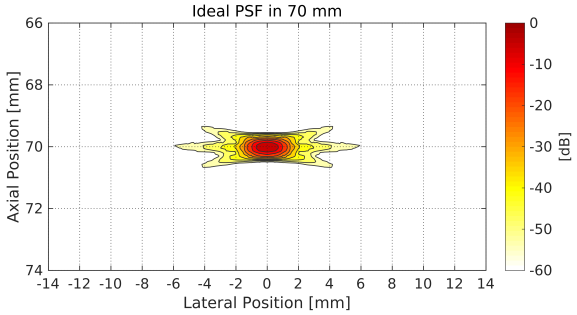

(a)

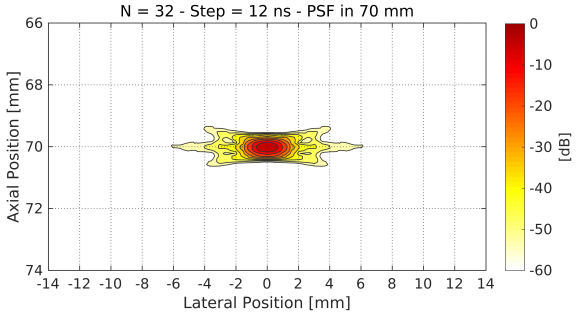

(b)

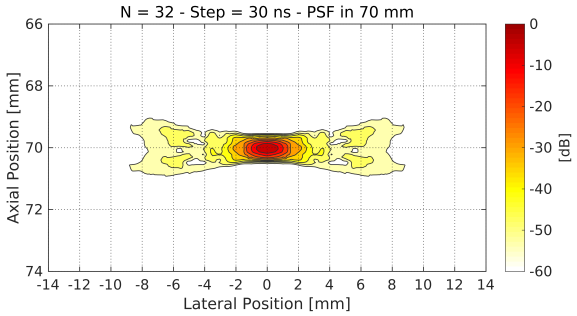

(c)

Figure 4.7: Simulated PSF at 70 mm for the ideal beamformer (a); gradient beamformer with $N = 32, dt =$12 ns (b); and gradient beamformer with $N = 32, dt =$30 ns (c).

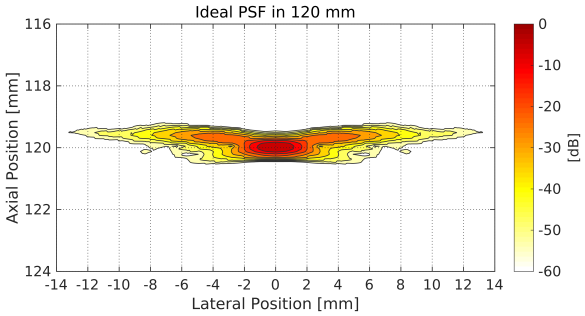

(a)

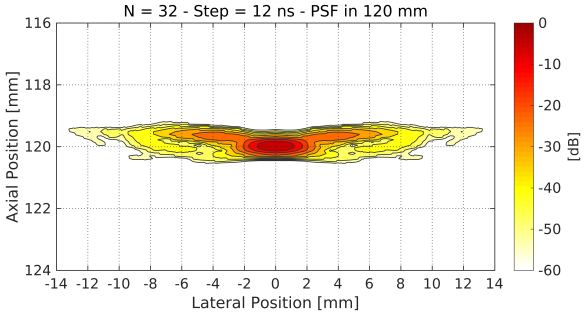

(b)

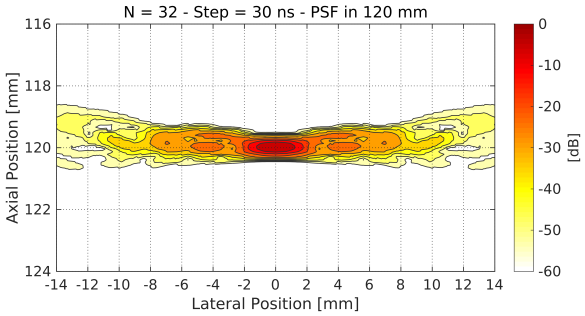

(c)

Figure 4.8: Simulated PSF at 120 mm for the ideal beamformer (a); gradient beamformer with $N = 32, dt$ =12 ns (b); and gradient beamformer with $N = 32, dt$ =30 ns (c).

CHAPTER 5

System-level design of a wireless ultrasound probe: digital beamforming

Summary *In this chapter, system-level strategies are presented and investigated for the design of a fully digital probe. The digital design represents a flexible and robust alternative and is an attractive choice towards the implementation of a versatile system integrating a wide spectrum of imaging modalities. The methods and results presented in this chapter are object of Paper II in appendix. This work has led to the fabrication of an integrated ADC at the Department of Electrical Engineering at DTU, and to the development at BK Ultrasound of the ATLAS probe, the prototype of a hand-held ultrasound device.*

5.1 Architecture overview

A schematic plot of the SASB wireless digital system investigated in this chapter is displayed in Fig. 5.1. In particular, Fig. 5.1(a) shows the receiver AFE. Sixty-four channels consisting of analog pre-amplifiers, ADCs, and DAS beamforming modules process the signals received by L transducers. The beamformed LRLs are first downsampled to the Nyquist rate f_N and Hilbert transformed to obtain the I/Q components. These are sent via wireless link to the external processing unit (Fig. 5.1(b)) and stored in the device memory. An HRI is finally created by the SSB, and envelope detection, log-compression, and scan-conversion are performed before the image is displayed.

5.1.1 Noise models

The models used in this study are introduced in this section. Time and depth are used interchangeably here, being the quantities related by a direct proportionality in case of constant speed of sound.

In the AFE in Fig. 5.1(a), the received signals are first amplified by the LNAs located close to the transducers, and a time-dependent gain is introduced by the variable-gain amplifiers (VGAs) for the compensation of the attenuation. An apodization is finally used to lower the sidelobes in the LRLs.

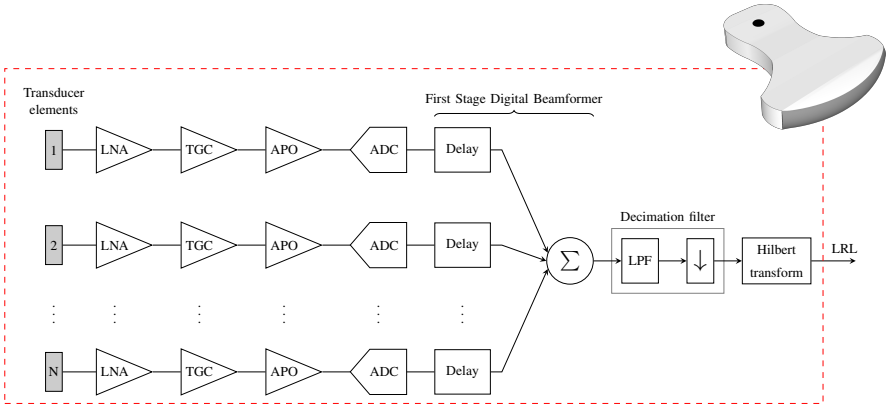

(a)

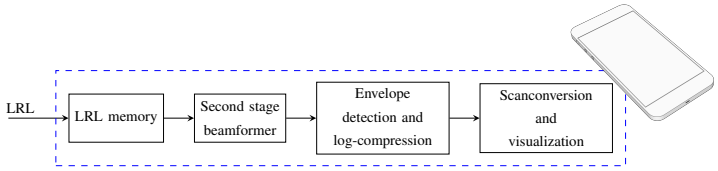

(b)

Figure 5.1: Schematic overview of the wireless ultrasound system: (a) receiving front-end and beamformation modules are integrated in the probe handle; (b) a post-processing unit is software-implemented in the mobile device.

Fig. 5.2 displays the model for the noise of the LNA. The received signals are attenuated by a factor α - equal to 0.5 dB cm^{-1} MHz^{-1} in the figure - to take into account the propagation losses, while a depth-independent noise is added to model the LNA's circuitry. Hence, the SNR of the noisy signal decreases as a function of the depth. A TGC amplification factor is applied thereafter. In the figure, the TGC amplification is limited to a range 0–42 dB, and the saturation of the amplifiers occurs at about 146 µs, corresponding to a depth of 11.2 cm. The amplitudes in the figure are normalized to the input voltage range of the ADC.

The noise model for the ADC is shown in Fig. 5.3. Quantization and thermal noise contributions are thought of as an additive, depth-independent, white Gaussian noise source. The TGC in Fig. 5.2 provides a way to use the entire input DR of the ADC at all the depths, and does not alter the SNR in this model. Nevertheless, when saturation of the TGC amplifiers occurs, the amplitude of the received signal is lower than the input DR of the ADC, and an additional SNR drop is introduced, which is also dependent on the depth.

5.1.2 Analog-to-Digital converter

A number of parameters can be used to characterize the performance of the ADC, including stated resolution, SNR, spurious-free dynamic range, two-tone intermodulation distortion, and power dissipation (Walden 1999). The performance discussions in this chapter are based on SNR considerations.

In an ideal ADC, the quantization is the only noisy operation. The quantization error can be considered to be a uniform, zero-mean, white noise, if the quantizer is not overloaded and under the assumption of uncorrelated successive quantization error samples (Oppenheim and Schafer 1989). The assumption is valid, if the quantization step is small compared with the signal amplitude, and the signal is sufficiently complex. For a conventional Nyquist-rate converter with sampling rate f_s and B bits of resolution, the theoretical signal-to-quantization noise ratio (SQNR) in dB is defined as:

$$SQNR = 10\log\left(\frac{\sigma_s^2}{\sigma_e^2}\right) = 6.02B + 10\log_{10} l + 1.76, \tag{5.1}$$

where σ_s^2 is the power of the signal, σ_e^2 the power of the in-band quantization noise, and $l = f_s/f_N$ the oversampling ratio.

The noise spectrum of a real ADC includes contributions from other sources such as thermal noise from the circuitry, aperture uncertainty, and comparator ambiguity, therefore the final SNR is lower than the SQNR. If the thermal noise generated by the ADC is taken into account, the total SNR in dB is

$$SNR = 10\log\left(\frac{\sigma_s^2}{\sigma_e^2 + \sigma_{th}^2}\right) = 10\log\left(\frac{\sigma_s^2}{\sigma_n^2}\right), \tag{5.2}$$

Figure 5.2: Noise model for the LNA: the received signals are attenuated due to the propagation in the tissue, and a depth-independent noise is added by the LNA. Therefore, a depth-dependent SNR is obtained. A variable gain is then applied as a function of the depth for the compensation of the attenuation. The amplitudes are normalized to the input voltage range of the ADC.

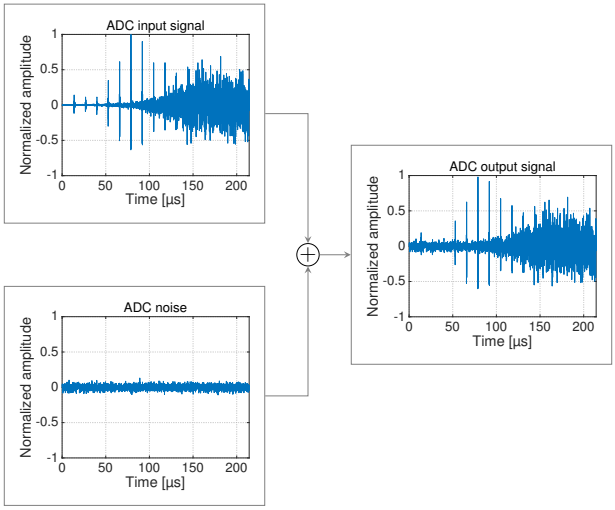

Figure 5.3: Noise model for the ADC: quantization and thermal noise are considered a depth-independent, white Gaussian noise source. An SNR drop is introduced as a function of the depth when the saturation of the TGC amplifier occurs.

where σ_{th}^2 is the power of the thermal noise and σ_n^2 the total noise power. It is common practice to design the ADC with an SQNR greater than the target SNR (Ortmanns and Gerfers 2006). For all the ADCs considered in this study, the SQNR was designed to be 6 dB greater than the target SNR.

5.1.2.1 Sigma-delta modulators

Conventional ADCs need precise analog circuits for their filters and comparators and can be very sensitive to noise and interference (Norsworthy, Shreier, and G. C. Temes 1996). Furthermore, a high-order analog filter is required at the input of the converter to avoid aliasing. Finely matched capacitors have to be used to achieve high precision conversion, which give large capacitive loads and, in turn, increased power dissipation and circuit area. These features make it difficult to implement conventional ADCs in VLSI technology.

SDMs simplify the architecture of the ADC by combining oversampling and noise shaping to push the quantization noise out of the signal bandwidth. In (5.1), it can be noticed that the SQNR increases by approximately 6 dB for every additional bit of resolution and by 3 dB for every doubling of the oversampling ratio. Hence, it is possible to trade sampling speed with resolution and use a very coarse quantization (Oppenheim and Schafer 1989). In the SDMs, the ADC is generally a simple 1-bit quantizer or comparator, and this simplifies the realization of fast processing systems. The quantization noise can be filtered in the digital domain before downsampling by using high-speed digital

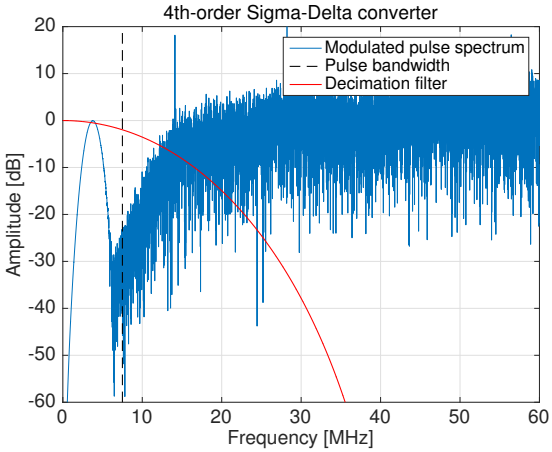

Figure 5.4: Spectrum of a 3.75 MHz pulse modulated with a single-bit 4th-order SDM converter with 360 MHz sampling frequency. Most of the quantization noise is out of signal bandwidth (black dashed line) and can be filtered in the digital domain. The transfer function of the decimation filter is plotted in red.

processing technologies (Aziz, Sorensen, and Spiegel 1996; Candy and G. Temes 1992; Norsworthy, Shreier, and G. C. Temes 1996).

The spectrum of a pulse with $f_0 = 3.75$ MHz modulated with a single-bit, 4^{th}-order SDM with a sampling frequency of 360 MHz is shown as an example in Fig. 5.4. The calculation of the SQNR in this case must also take into account the digital decimation filters to count for the residual noise after filtration. In this work, the SQNR was found by converting a full-scale sinusoid and by subtracting the decimated and the original signals to find the noise.

5.1.3 First-stage beamformer

In the digital beamformer, the actual delays are quantized to the sampling period $T_s = 1/f_s$, and the beamforming errors introduced by the delay quantization contribute to the amplitude of the sidelobes (Holm and Kristoffersen 1992). Different approaches can be used to achieve a suitable delay resolution.

A first method oversamples the signals with ratios $l > 1$ and typically in the range from five to ten (Mucci 1984). This introduces an additional overhead in the system complexity. However, the delay line can be easily realized by using simple shift registers.

Another approach uses digital interpolation to obtain the required delay resolution (Mucci 1984). The received signals are sampled at the Nyquist rate and $l - 1$ intra-sample values are calculated for each pair of successive samples to obtain an effective

Table 5.1: Power dissipation for the design of a 64-channel system based on commercial AFE ICs from Analog Devices, Inc., and Texas Instruments, Inc. The relevant features were read from the manufacturers' datasheets.

Model	# of bits ADC	Sampling frequency [MHz]	ADC SNR [dB]	VGA range [dB]	PD/ch. [mW]	PD 64 ch. [W]
AD9273-25	12	25	70	42	102	6.53
AD9278	12	40	70	45	88	5.63
AFE5816	12	40	70	39	55	3.53
AFE5807	12	40	72	40	97	6.21

oversampling ratio of l. A FIR filter with approximately $5l$ coefficients is required in each channel for this purpose (Mucci 1984).

The delay interpolation method typically represents a less expensive solution with multi-bit ADCs. Oversampling converters like SDM, on the other hand, have an inherently high sampling rate and can be better integrated with oversampling beamformers without any additional cost.

5.2 Design using commercial integrated circuits

The feasibility of the wireless digital probe was first investigated using the four least power consuming commercial AFEs from Analog Devices, Inc., and Texas Instruments, Inc. The ICs include an LNA, a VGA, and an ADC for each channel. The relevant features were read from the products datasheets. The total power dissipation (PD) of a 64-channel system is shown in Table 5.1 and is in all the cases greater than the target power budget of 3 W. Furthermore, additional power must be considered for the beamformation, in particular for the multi-bit interpolation needed to achieve the delay resolution and for inter-chip communication. Therefore, the power consumption of commercial AFE ICs exceeds the power budget of a hand-held scanner, and a dedicated IC is required to fit the power budget specifications. By integrating the beamformer and the AFE on the same chip, the pin count of the system can be minimized to decrease the power dissipated at the inter-chip interconnections.

5.3 System-level design

5.3.1 Methods

A simulation study was performed to investigate the effects of system-level choices on the quality of the B-mode image. The design requirements were a DR of 60 dB and a

Table 5.2: Simulation parameters

Parameter	Symbol	Value	Unit
Speed of sound	c	1490	$\mathrm{m\,s^{-1}}$
Attenuation	α	0.5	$\mathrm{dB\,cm^{-1}\,MHz^{-1}}$
Imaging setup			
Excitation	-	2 cycles	-
Center frequency	f_0	3.75	MHz
Signal bandwidth	-	7	MHz
Tx apodization	-	Rectangular	-
Rx apodization	-	Hamming	-
VS axial position	-	70	mm
Active elements	L	64	-
f-number	$F_\#$	3.3	-
Number of VSs	-	269	-
Distance between VSs	-	3.9	mrad
Processing			
LNA SNR	-	64	dB
TGC range	-	0–42	dB
Sampling frequency	f_s	60	MHz
SSB apodization	-	Hamming	-

penetration depth of 160 mm. Several AFE implementations using Nyquist-rate and SDM converters were simulated.

A model of the system was built in MATLAB (The MathWorks Inc., Natick, MA), and the analytic signals were obtained through a Hilbert transform. The SSB was implemented with the BFT3 toolbox (Hansen, Hemmsen, and Jensen 2011) and the HRIs were displayed with a DR of 60 dB.

A convex array transducer was simulated with the parameters in Table 4.1 and focused in Tx/Rx at a depth $z_f = 70\,\mathrm{mm}$. The PSF was simulated in Field II (Jensen 1996; Jensen and Svendsen 1992) from 10 to 160 mm in steps of 10 mm. Absorption and scattering losses were included by means of an attenuation factor $\alpha = 0.5\,\mathrm{dB\,cm^{-1}\,MHz^{-1}}$. The TGC was introduced as an amplification curve with a slope equal to αf_0 in the range 0–42 dB. For this setup, the saturation of the TGC amplifiers occurs at 11.2 cm. The parameters used in simulation are reported in Table 5.2.

The study focused on the analysis of the LNA and ADC while the TGC and apodization were considered ideal.

5.3.2 Preliminary SNR study

An ideal ADC was first considered with a sampling frequency of $f_N = 15\,\text{MHz}$ and infinite resolution. The beamformation was performed assuming non-quantized delay values. The same model of Fig. 5.2 was used for the LNA. The power of the additive noise was calculated in the signal bandwidth to provide the desired SNR relative to the power of a full-scale sinusoid. The SNR of the LNA was swept from 0 to 80 dB in steps of 5 dB, and 50 independent simulations were performed at each step to find the output SNR in the simulated B-mode image. A noiseless signal $\bar{y}$ was also simulated and, denoting with $y(n,i)$ the complex sample at the n-th axial point for the i-th simulation, the noise power was calculated as:

$$\sigma_n^2(n) = \left| \frac{1}{M} \sum_{i=1}^{M} (y(n,i) - \bar{y}(n))^2 \right|. \tag{5.3}$$

The SNR was found as:

$$SNR(n) = 10 \log \left(\frac{\sigma_s^2(n)}{\sigma_n^2(n)} \right), \tag{5.4}$$

with $\sigma_s^2 = |\bar{y}|^2$ the power of the noiseless signal.

The SNR of the LNA was then fixed to 48 dB and 64 dB to investigate the system performance in the two cases, and the same procedure was repeated to find the minimum SNR requirement for the ADC. The signals were sampled at $f_N = 15\,\text{MHz}$ and a white Gaussian noise was added to model the quantization and thermal noise of the ADC. The assumption of a uniformly distributed white quantization noise is valid, if the conditions stated in Section 5.1.2 are satisfied. The SNR of the ADC was swept from 0 to 80 dB in steps of 5 dB and 50 simulations were performed to find the SNR in the output image as indicated by (5.3) and (5.4).

5.3.2.1 Results

The result of the noise study for the LNA is shown in Fig. 5.5. The top curve shows in blue the DR and the bottom curve shows in red the SNR at the target penetration depth (PDSNR) as a function of the LNA SNR. A linear regression was fitted to the curves, and a minimum LNA SNR of 42 dB (green line) was found to be necessary to achieve the performance specifications. This corresponds to a noise voltage of $3\,\mu\text{V}/\sqrt{\text{Hz}}$ at the output of the LNA. The input noise voltage for the actual amplifier depends on the gain and is, therefore, a function of the amplitude of the received signals.

The result of the noise study for the ADC is plotted in Fig. 5.6(a) for LNA SNR = 48 dB. The curves saturate where DR and PDSNR equal the respective values for LNA SNR = 48 dB in Fig. 5.5, i.e. 66 dB and 19 dB. Beyond this point, improvements in the ADC SNR no longer translate in better image quality, and the noise is dominated by the LNA. The minimum ADC SNR requirement for this setup is equal to 45 dB. A similar

Table 5.3: Parameters for the ADCs used in the system-level simulation study

	Resolution [bit]	f_s [MHz]	Decimation -	SQNR [dB]	SNR [dB]
Nyquist	5	30	2	35	29
	8	30	2	53	47
	10	30	2	65	59
	Order -	f_s [MHz]	Decimation -	SQNR [dB]	SNR [dB]
$\Sigma\Delta$	2	120	2 and 4	35	29
	3	240	4 and 4	55	49
	4	300	5 and 4	65	59

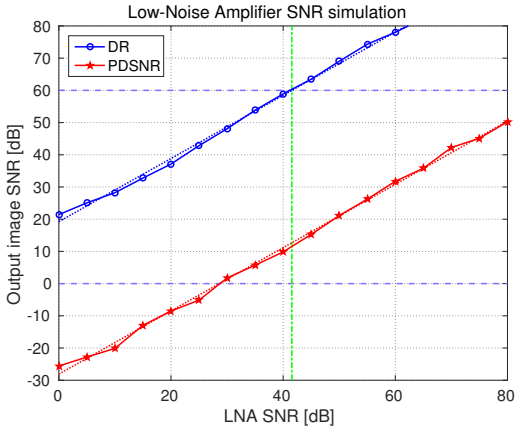

Figure 5.5: Result of the preliminary noise study for the LNA: the blue curve shows the DR and the red curve shows PDSNR as a function of the SNR of the LNA. The green dashed lines indicate the minimum LNA SNR to fulfil the design specifications, equal to 42 dB.

trend is shown in Fig. 5.6(b) for LNA SNR = 64 dB. The curves saturate at DR = 82 dB and PDSNR = 35 dB, and the minimum SNR requirement is 40 dB.

It is important to specify that the noise requirements for the two components are strictly related, and increasing the SNR of the LNA loosens the requirement on the ADC. However, how this factor translates in terms of actual circuitry depends on the design and implementation of both the components. The SNR at 160 mm is everywhere greater than 0 dB in Fig. 5.6(a) and 5.6(b), and this suggests the possibility of decreasing the range of the variable gain for the TGC amplifier.

5.3.3 System-level comparison

Six AFEs were simulated, three conventional Nyquist-rate ADCs and three single-bit SDMs. The parameters of the simulated ADCs are reported in Table 5.3. The SNR of the LNA was set equal to 64 dB in all the simulations.

A sampling frequency of $f_s = 30$ MHz ($l = 2$) and a resolution of 5, 8, and 10 bits were used for the Nyquist-rate converters. The three ADCs are referred to as Nyq5, Nyq8, and Nyq10. The SQNR was calculated using (5.1) and was equal to 35 dB, 53 dB, and 65 dB. White Gaussian noise was added to mimic the thermal noise, with a final SNR 6 dB lower than the SQNR. The actual delay values were quantized with a resolution of $T_0/24$. If $f_N = 4f_0$, the required oversampling ratio is $l = 6$, and a FIR interpolation filter with at least 15 coefficients is needed for each channel with a clock frequency of 30 MHz. A matched FIR decimation filter was used before downsampling the beamformed lines to the Nyquist rate.

Three single-bit SDMs were used: 2^{nd} order with $f_s = 120$ MHz ($l = 8$), 3^{rd} order with $f_s = 240$ MHz ($l = 16$), and 4^{th} order with $f_s = 300$ MHz ($l = 20$). The architectures are referred to as SDM2, SDM3, and SDM4. A MATLAB model was developed for the modulators following the method in (Adams et al. 1991). The noise transfer functions were designed as 2^{nd}, 3^{rd}, and 4^{th} order high-pass Butterworth filters. The downsampling of the beamformed lines was performed in two steps: a first *sinc* cascaded-integrator-comb filter (Hogenauer 1981) was used before downsampling with a decimation ratio of 2, 4, and 5 for the three architectures. Finally, the Nyquist rate was restored after matched filtering and decimation with a ratio of 4.

The SQNR for the oversampling converters was estimated from 50 simulations of a sinusoid $\bar{x}(k)$ with center frequency of 3.75 MHz. The sinusoid was modulated and A/D converted, and the resulting single-bit signal was then filtered and downsampled. The SQNR was calculated as:

$$SQNR = 10 \log \left(\frac{\sigma_{\bar{x}}^2}{\sigma_{qn}^2} \right), \tag{5.5}$$

where $\sigma_{\bar{x}}^2$ is the power of the sinusoid and:

$$\sigma_{qn}^2 = \frac{1}{50} \frac{1}{K} \sum_{i=1}^{50} \sum_{k=1}^{K} (x_i(k) - \bar{x}(k))^2 \tag{5.6}$$

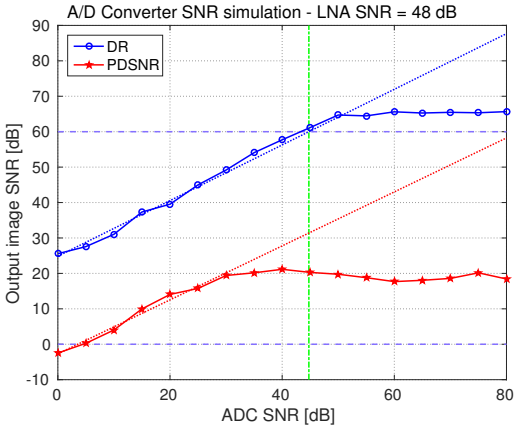

(a)

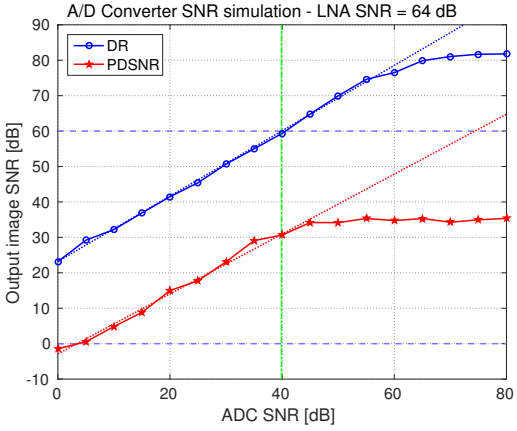

(b)

Figure 5.6: Result of the preliminary noise study for the ADC: (a) the blue curve shows DR and the red curve shows the PDSNR as a function of the SNR of the ADC for LNA SNR = 48 dB; (b) DR and PDSNR as a function of the SNR of the ADC for LNA SNR = 64 dB. The green dashed lines indicate the minimum SNR to fulfil the design specifications.

is the estimated quantization noise. In (5.6), x_i is the decimated signal from the $i-$th simulation and K the number of temporal samples. The resulting SQNR is equal to 35 dB, 55 dB, and 65 dB for the three converters. White Gaussian noise was added for a final SNR 6 dB lower than the SQNR. For the three oversampling architectures, the beamformation was performed by merely shifting the single-bit signals, and the delay resolution is equal to $T_0/32$, $T_0/64$, and $T_0/80$. Therefore, there is no need for temporal interpolation.

A 1-D gain compensation was applied after the second stage beamformer to the envelope detected signals to equalize the peak amplitudes of the point targets, and the PSF was evaluated in terms of lateral FWHM and −12 dB CR calculated as in (2.3).

5.3.3.1 Results

The B-mode images of the simulated PSFs are shown in Fig. 5.7 for the 5- and 10-bit Nyquist converters [(a) and (b)] and for the 2^{nd} and 4^{th} order SDMs [(c) and (d)]. The ellipses in Fig. 5.7(a) highlight the regions where the total PSF energy E_{tot} was found for the calculation of C in (2.3). In each region, the SNR was assumed constant. This was estimated from 50 independent simulations of the six architectures and is shown in Fig. 5.8 as a function of the depth. The maximum SNR is found in proximity of the focal position, and this is the value determining the output DR. As expected, equivalent architectures provide comparable results in the output image. Nyq8 and SDM3 are the ones that minimally fit the design specifications for the output DR and penetration depth. Nyq10 and SDM4 show a different slope beyond the VS position compared with the other architectures. This is caused by the noise of the LNA, which prevails on the overall performance.

The mean and standard deviation (SD) for the FWHM and CR were estimated from 50 simulations and are displayed in Fig. 9.2. On the left side, the mean FWHM is plotted on the top and the relative SD on the bottom figures. The mean FWHM increases with the depth, and small differences are visible between the simulated architectures. The calculation for Nyq5 and SDM2 failed in the points from 140 to 160 mm for several simulations due to the high noise, therefore these values were discarded. The relative SD also increases due to the decreasing SNR. High SDs were obtained for Nyq5 and SDM2.

On the right side in Fig. 9.2, the mean CR is plotted on the top and the relative SD on the bottom. The CR is affected by the delay resolution. The results were expected to show significant differences among the simulated systems due to the better resolution of SDMs compared with the Nyquist-rate ADCs. However, the results are comparable between equivalent architectures. This suggests that the contrast is dominated by the noise rather than the delay resolution.

For Nyq8, the mean lateral FWHM is between 1.02 and 4.45 mm, and between 0.94 and 4.45 mm for SDM3. The FWHM is in average 2.4% lower for SDM3 compared with Nyq8. The mean CR is between 0.93 and 9.97 mm for Nyq8, and between 0.81 and 10.05 mm for SDM3, and is in average 7.1% lower for the this architecture.

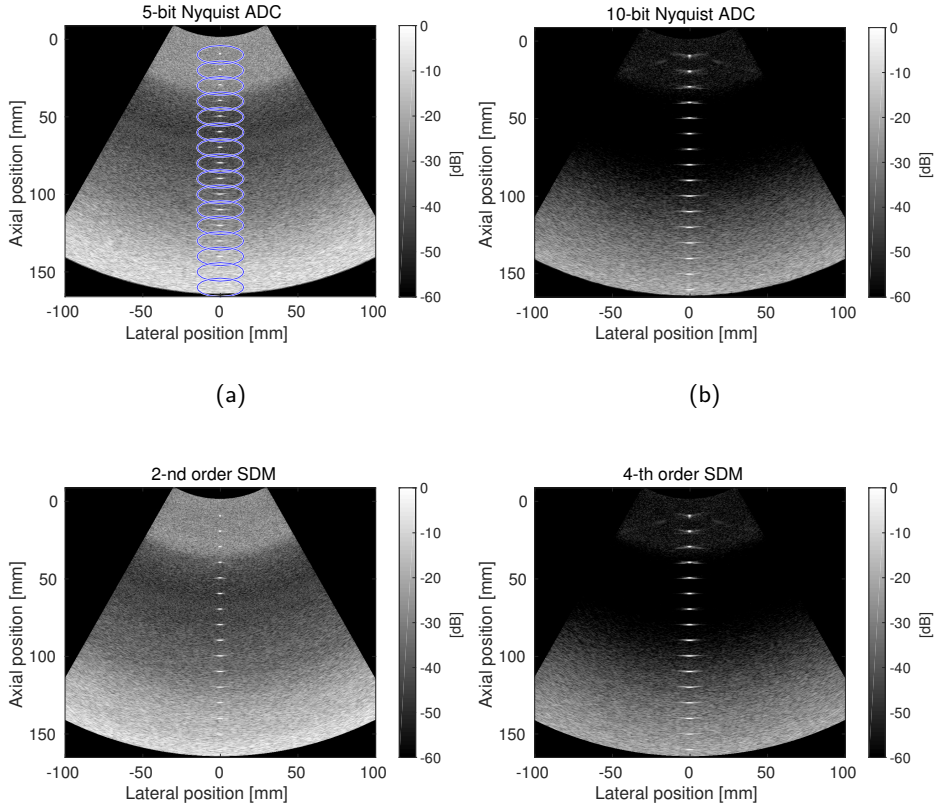

Figure 5.7: B-mode images of the simulated PSFs for the 5- and 10-bit Nyquist converters [(a) and (b)] and for the 2^{nd} and 4^{th} order SDMs [(c) and (d)]. The ellipses in (a) highlight the regions where the total PSF energy E_{tot} in (2.3) was calculated.

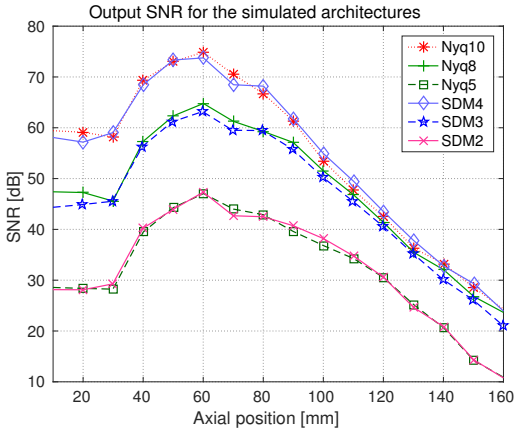

Figure 5.8: SNR of the output image as a function of the axial position for the six simulated architectures in Table 5.3.

5.4 Fabricated devices

The noise specifications derived in Ch. 4 and 5 were provided to the IC designers at the Department of Electrical Engineering at DTU and BK Ultrasound, where an integrated SDM ADC and a USB-linked convex probe were designed and fabricated.

5.4.1 Integrated SDM ADC

An ASIC ADC for a portable ultrasound scanner has been designed and fabricated at the Department of Electrical Engineering at DTU (Muntal, Jørgensen, and Bruun 2017; Muntal 2017). The ADC is a 4^{th} order SDM with 320 MHz sampling frequency implemented as a cascade-of-resonators feedback structure. The supply voltage of the chip is 1.2 V and it has a bandwidth of 10 MHz. The reported measured power consumption of the IC is 0.594 mW with a SNR of 41.6 dB. The die are is 0.0175 mm^2.

A microscopic picture of the fabricated ASIC is shown in Fig. 5.10(a). The structure reflects the layout from Cadence Virtuoso in Fig. 5.10(b). The fast Fourier transform (FFT) of the single-bit output signal for an input sinusoid with a frequency 5 MHz and input amplitude of 0.6 V is shown in Fig. 5.11. The blue plot is the schematic result, while the red one is the result with the extracted parasitic, which represents the expected behaviour.

5.4.2 ATLAS probe

The prototype of a digital ultrasound probe named ATLAS has been designed at BK Ultrasound (Fig. 5.12). The probe includes a 192-element convex array of transducers

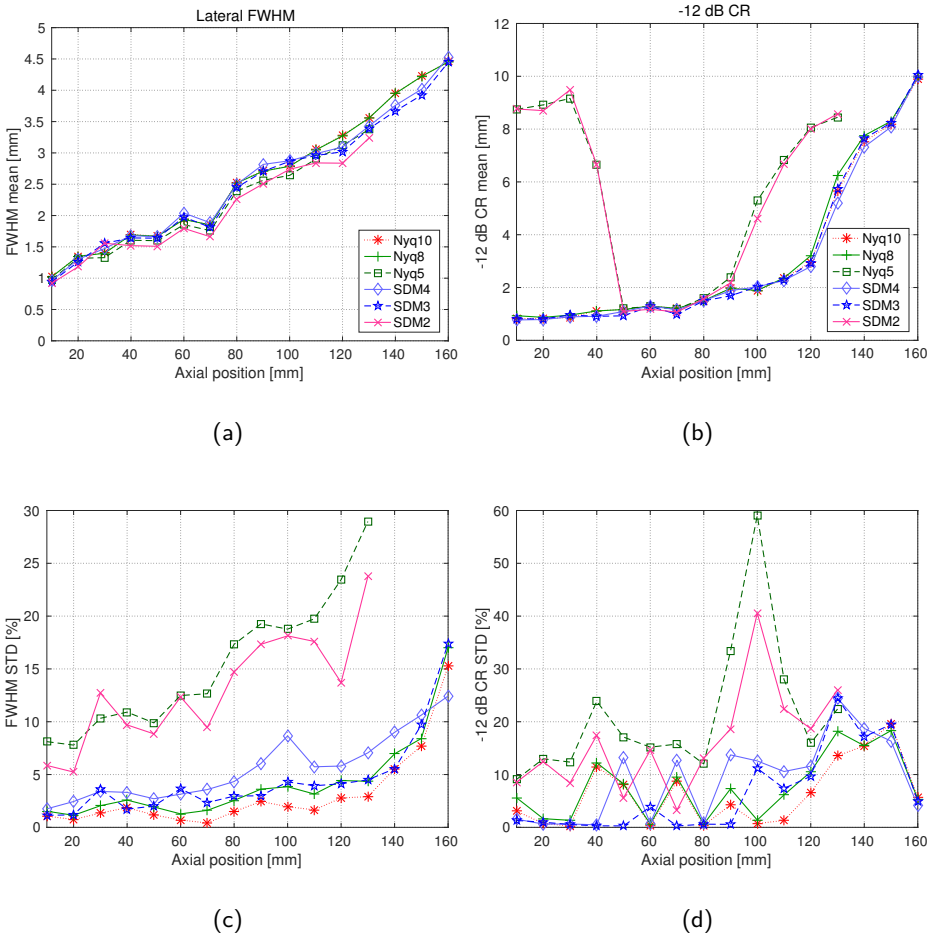

Figure 5.9: The figures on the left side show the mean (a) and relative standard deviation (c) of the FWHM from 50 PSF simulations at 16 axial positions using the six architectures in Table 5.3; on the right side, the mean (b) and relative standard deviation (d) are shown for the -12 dB cystic resolution.

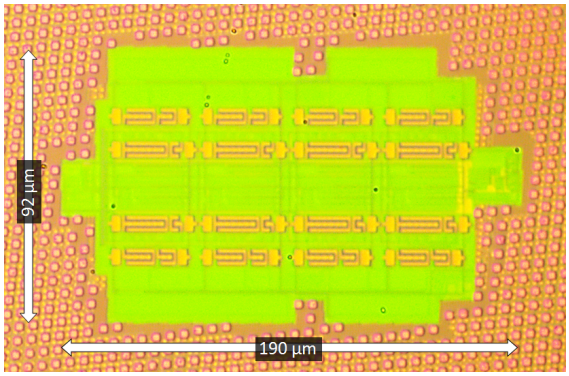

(a)

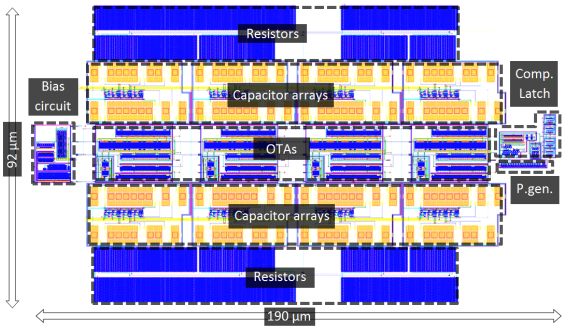

(b)

Figure 5.10: (a) Microscopic picture of the fabricated ASIC with a 4^{th} order SDM ADC; (b) layout of the chip from Cadence Virtuoso. Images from (Muntal 2017).

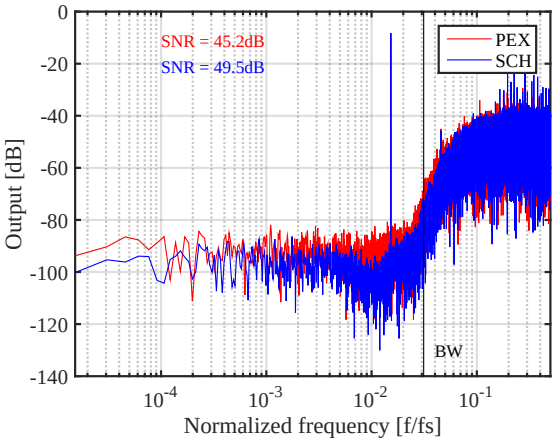

Figure 5.11: FFT of the single-bit output signal for an input sinusoid with a frequency 5 MHz and amplitude of 0.6 V. The blue plot (SCR) is the schematic result, while the red one (PEX) is the result with the extracted parasitic, and thus represents the expected behaviour. Image from (Muntal 2017).

with 64 active channels and AFEs and FSB integrated in-handle. The probe is linked to the host via a USB-C interface and has an output data bandwidth of 240 Mbps. The interface can connect to any Android, Windows, or iOS mobile device, where the SSB and visualization are performed. The power consumption is about 55 mW/ch with an input referred noise of 2.2 nV/$\sqrt{\text{Hz}}$. No further information was provided on the actual circuitry by the company, which owns the intellectual property rights for the device.

The B-mode image of a phantom including wires, hypoechoic and hyperechoic cysts is shown in Fig. 5.13 with an imaging depth of 14 cm. The image was reconstructed by the SSB implemented in the system host.

The probe does not currently include the possibility of transmission through Wi-Fi link, and additional challenges must be faced towards the development of a wireless system. More restrictive constraints apply, for example, to the circuit area if a battery must be integrated maintaining an acceptable form-factor, and the power consumption must be low enough to allow for a reasonable scanning time. In addition, it is important to guarantee a sufficient data throughput over time to and from the probe. The probe, however, represents a step forward toward the commercialization of a hand-held ultrasound device.

5.5 Discussion and conclusion

In this chapter, system-level design strategies were presented aimed at reducing the complexity and power dissipation of the AFE for a digital wireless ultrasound probe. The

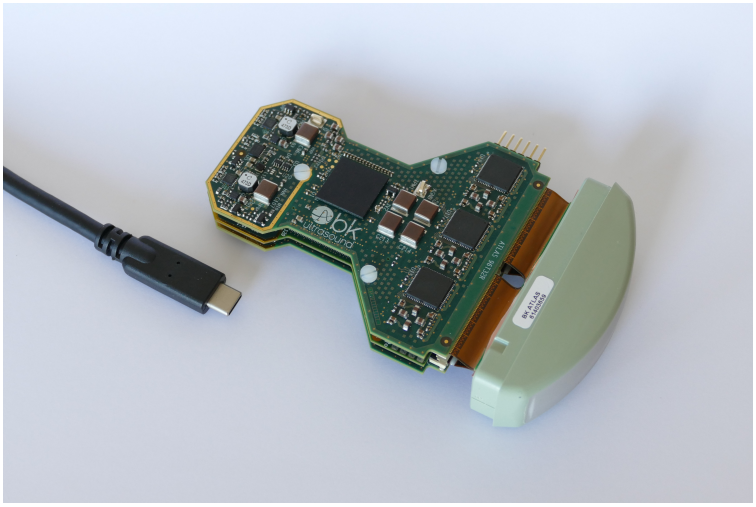

Figure 5.12: Prototype of the ATLAS probe engineered at BK Ultrasound. It is a 192-element convex array, with 64 active channels, AFE and FSB integrated in the probe handle. It is interfaced to the system host through a USB-C cable.

digital design has the advantage of improved flexibility and robustness compared with the analog one and represents an attractive choice towards the implementation of a versatile system. Commercially available off-the-shelf AFEs are overdesigned for the purposes of a portable scanner, and a dedicated chip is required to minimally fulfil the performance requirements and prevent undesired power dissipation. Integrating the beamformer in the same chip, furthermore, reduces the amount of off-chip interconnections eliminating high capacitive loads responsible for additional power usage.

The purpose of the study was to provide the IC designers with the minimum design specifications necessary to meet the image quality requirements. The investigations were carried out with simulations of the PSF for different system designs to evaluate the effect of architectural choices on the image quality. The LNA and ADC, in particular, were thought to have a significant influence on the power dissipation, circuit area, and cost of the system, and the investigations focused primarily on these modules. The minimum SNR levels were first derived for the two components to fulfil the the image quality requirements of a DR of 60 dB and a penetration depth of 160 mm. The resolution and contrast were then evaluated for six architectures based on Nyquist-rate as well as oversampling SDM ADCs.

The results showed good agreement in terms of contrast and lateral resolution between oversampling and Nyquist-rate implementations with equivalent SNR levels. Although it is difficult at this proof-of-concept stage to make solid assumptions on the power

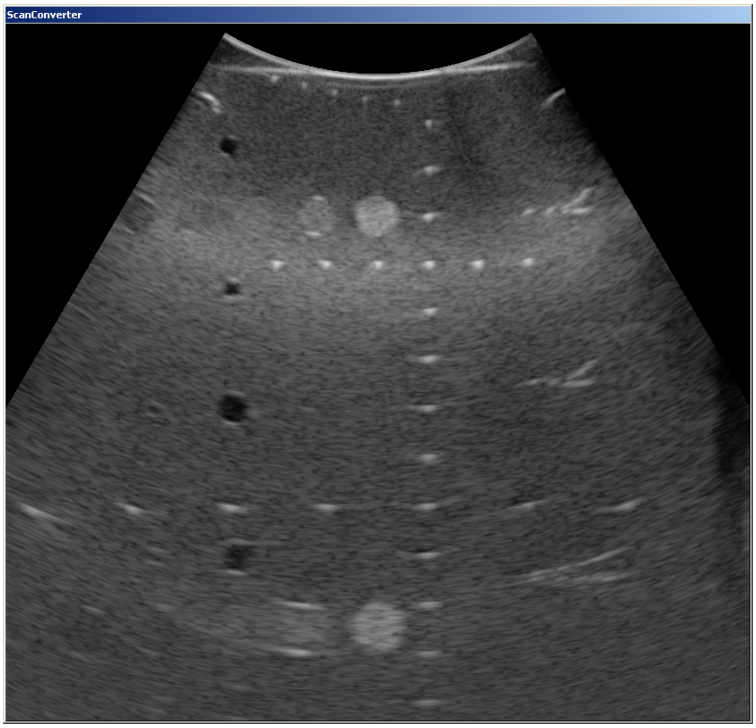

Figure 5.13: B-mode image of a phantom including wires and hypo- and hyperechoic cysts with an imaging depth of 14 cm. The image was acquired with the ATLAS probe and reconstructed by the second stage beamformer implemented in the system host.

consumption and circuit area of the different architectures (a worthwhile analysis would require the development and characterization of the chips), it was hypothesised that the SDM approach would provide a simplified design.

Conventional Nyquist-rate converters need precise electronics for their analog filters and comparators and can be very sensitive to noise and interference (Norsworthy, Shreier, and G. C. Temes 1996). Finely matched capacitors need to be used to achieve high precision conversion, with large capacitive loads and high power dissipation and circuit area. Furthermore, a high-order analog anti-aliasing filter is necessary at the input to remove the out-of-band components prior to the sampling process. Although extraordinary efforts have been put in optimizing the power efficiency of these ADCs (Murmann 2008), Nyquist converters are often difficult to integrate in VLSI technologies, focused on providing high-speed digital processing rather than accurate analog electronics (Norsworthy, Shreier, and G. C. Temes 1996),

Oversampling SDMs can be implemented using relatively high-tolerance electronics and moves the resource requirement towards the digital domain. The technology scaling continuously experienced by CMOS processes makes it convenient from a power dissipation and circuit area perspectives to concentrate the challenging hardware requirements in the digital section. In addition, the high-speed conversion removes the need for the sharp anti-aliasing filter, and noise and interference are filtered out in the digital domain. The interconnection complexity is also reduced due to the single-bit conversion. For these reasons, SDM converters can take advantage of VLSI technologies and are well suited for applications requiring high-integration, low-cost, and densely packed circuit designs (Norsworthy, Shreier, and G. C. Temes 1996). Finally, the use of oversampling converters also simplifies the beamformer architecture eliminating the need for any interpolation given the inherently high sampling frequency.

Based on these considerations and on the results of the image quality comparisons, the conclusion of this study is that single-bit SDM ADCs can be employed for the development of a dedicated IC for a hand-held ultrasound probe, and a prototype of the chip has been fabricated at the Department of Electrical Engineering at DTU.

Part II

Vector flow imaging

CHAPTER 6

Vector flow imaging

The noninvasive imaging of blood flow using ultrasound is extensively used in the clinic due to its high temporal resolution, portability, and low cost compared with other imaging technologies. Measurements of the blood velocity and flow rate, for example, are performed daily to help the clinician in the management of disease and trauma (Dodd et al. 1994; Grant et al. 2003), and a number of flow imaging features are found in ordinary ultrasound scanners (J. A. Jensen 1996). Firstly, imaging systems can be differentiated depending upon whether continuous waves (CWs) or pulsed waves are used. Only pulsed systems are considered in this work, as these are in line with the method presented in the following chapters.

In pulsed systems, an ultrasound pulse with center frequency f_0 is emitted repeatedly with a period T_{prf}. The Doppler frequency of the signal received from a sample volume over a number of pulses is (Baker 1970; J. A. Jensen 1996)

$$f_p = \frac{2|\vec{v}|\cos\theta}{c} f_0 = \frac{2v_z}{c} f_0, \tag{6.1}$$

where $\vec{v}$ is the velocity vector, θ the beam-to-flow angle in the (x, z) plane, $v_z = |\vec{v}|\cos\theta$ the velocity component parallel to the ultrasound beam, and c the speed of sound. The velocity can be, therefore, inferred from the measured Doppler frequency, and this concept is at the base of the spectral Doppler modality.

The main weakness of conventional flow imaging is revealed by (6.1) and is due to the fact that only v_z can be actually measured. The angle θ must be carefully determined before the velocity magnitude $|\vec{v}|$ is computed and should be less than 60° to avoid significant estimation errors (Gill 1985). Furthermore, it is not possible to invert the relation in (6.1) when $\theta = 90°$ and $\cos\theta = 0$.

The fact that the angle is usually determined manually by adjusting the incline of a cursor relative to the vessel wall makes the estimated velocity prone to error. In addition, complex flow patterns as vortices, helices, and recirculation are encountered in many clinical situations where it is not possible to determine the angle univocally. Examples of complex flow patterns are shown in Fig. 6.1. Fig. 6.1(a) displays the helical flow in the ascending aorta rotating in clock-wise direction, and Fig. 6.1(b) shows a vortex in the internal carotid artery.

Because of the angle limitation and given the impossibility of a local, dynamic compensation in an extended image region, quantitative velocity measurements are only possible in a limited number of points by using spectral Doppler. Moreover, the need

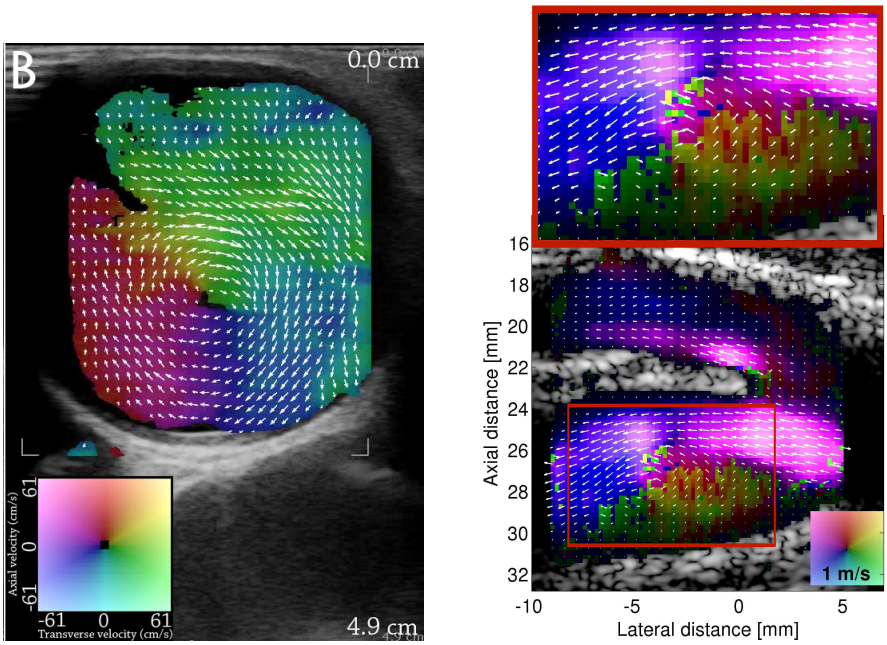

(a) (b)

Figure 6.1: (a) Example of helical flow in the ascending aorta rotating in clock-wise direction - image from (K. L. Hansen, Møller-Sørensen, Pedersen, et al. 2014); (b) Vortex in the internal carotid artery - image from (Villagomez-Hoyos, Stuart, et al. 2016).

for accurate manual adjustments compromises the operator workflow with increased cost in terms of affordability and quality of the healthcare. Two-dimensional modalities like CFM, in addition, provide only a qualitative indication of the blood stream into the vessels.

Vector flow imaging (VFI) techniques emerged to overcome the flow angle dependancy of conventional methods. Both velocity magnitude and direction are estimated directly from the measured ultrasound data. In the context of portable ultrasound, VFI has the potential to improve the clinical workflow by providing quantitative velocity data in 2- or 3-D with no need for manual adjustments. A VFI method was developed to suit the strict requirements of a portable scanner in terms of computational resources and data bandwidth. The method is presented in Ch. 8.

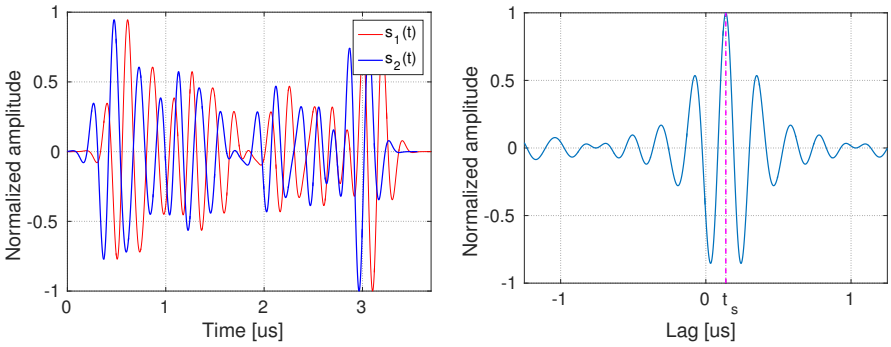

(a) (b)

Figure 6.2: (a) Example signals received from consecutively emitted pulses with a time shift t_s relative to each other; (b) cross-correlation function for the signals in (a). It can be noted that the peak is located at a lag corresponding to t_s.

6.1 Velocity estimation methods

Before digging into the existing literature on VFI, it is worth introducing two velocity estimation approaches which most of the CFM systems rely upon. To create full maps of the blood flow in 2- or 3-D and in real time, alternative strategies to (6.1) must be employed if a reasonable frame rate is to be maintained. Possible solutions are the time and phase shift estimators introduced in this section.

6.1.1 Time shift estimation

The time shift approach was first proposed by Dotti *et al.* (Dotti et al. 1976) and Bonnefous and Pesqué (Bonnefous and Pesqué 1986).

Two signals $s_1(t)$ and $s_2(t)$ are received from consecutively emitted pulses backscattered by a collection of scatterers moving with velocity v_z. The signals experience a time shift t_s relative to each other, which can be expressed as (J. A. Jensen 1996)

$$t_s = \frac{2v_z}{c} T_{prf}. \tag{6.2}$$

The signal s_2 can therefore be expressed as $s_2(t) = s_1(t - t_s)$. Two example signals are shown in Fig. 6.2(a).

The time shift is estimated from the peak of the cross-correlation function

$$R_{12}(\tau) = \frac{1}{2T}\int_T s_1(t)s_2(t+\tau)dt = \frac{1}{2T}\int_T s_1(t)s_1(t-t_s+\tau)dt = R_{11}(\tau - t_s), \tag{6.3}$$

with R_{11} the autocorrelation function of the signal s_1. $R_{11}(\tau - t_s)$ has a unique peak in $\tau = t_s$, hence t_s can be detected from the peak position, and v_z can be found by inverting (6.2). The cross-correlation function for the signals in Fig. 6.2(a) is displayed in 6.2(b). It can be noted that the peak is located at a lag corresponding to t_s.

In general, the time shift estimator provides good performance as the full frequency content of the signal is taken into account in the calculation of the cross-correlation function (Hoeks et al. 1993). Also, it does not suffer from aliasing and is more robust in presence of noise (Hoeks et al. 1993). In addition, no assumption is made on the bandwidth of the signals, and short pulses can be used. The disadvantage is the heavy computational demand, as the whole correlation function in Fig. 6.2 must be calculated with high time resolution.

6.1.2 Phase shift estimation

If narrowband signals are employed, the time shift in (6.2) can be approximated by a phase shift. The phase shift estimation approach was introduced in medical ultrasound by Kasai *et al.* (Kasai et al. 1985) and has the advantage of lower computational demands with respect to the time shift estimator. The velocity is found from the time derivative of the phase of the received signals, which is

$$\frac{d\phi}{dt} = -2\pi \frac{2v_z}{c} f_0. \tag{6.4}$$

The phase derivative can be described in terms of the complex autocorrelation function (J. A. Jensen 1996), and the velocity is

$$v_z = -\frac{c}{2\pi f_0 \, 2T_{prf}} \arctan\left(\frac{\Im\{R(1)\}}{\Re\{R(1)\}}\right), \tag{6.5}$$

with $\Re$ and $\Im$ the real and imaginary parts, and $R(1)$ the lag-1 autocorrelation function estimated from N_e emissions as

$$R(1) = \frac{1}{N_e - 1} \sum_{e=0}^{N_e-2} s(n,e)^* s(n,e+1). \tag{6.6}$$

The signal $s(n,e)$ in (6.6) is the analytic signal consisting of the I and Q components sampled after the emission e at the depth n. Note that also the autocorrelation function depends on the axial index n.

The major drawback of the phase shift estimator is that it is subject to aliasing, which is due to the ambiguity in the detected phases for multiples of 2π. Therefore, the velocity range for v_z is

$$|v_z| \leq v_z^{max} = \frac{1}{4} \frac{c}{f_0 T_{prf}}. \tag{6.7}$$

The velocity range can, however, be extended by using phase unwrapping methods (X. Lai, Torp, and Kristofferson 1997).

The phase shift approach has been extensively used in commercial systems due to its flexibility in terms of computational complexity, which makes it scalable to fit the available computational resources. In principle, the velocity can be found from as few as two complex samples, or the autocorrelations could be averaged over a higher number of lines and axial samples, if enough computational power is available. However, lower performance is achieved compared with the time shift estimator, mainly due to the assumption of narrowband signals that is not satisfied in pulsed systems (Hoeks et al. 1993).

6.2 Background literature on vector flow imaging

In this section, the VFI methods currently existing in the literature are reviewed, and a number of clinical applications are reported to provide a background introduction. A comprehensive review of VFI methods can be found in (J. A. Jensen et al. 2016a,b).

6.2.1 Cross-beam vector Doppler ultrasound

A first solution was proposed in the 1970s and relies on the measurement of multiple velocity components along different directions, which are combined using triangulation techniques to obtain the velocity vector. A review of vector Doppler methods can be found in (Dunmire et al. 2000). The first implementations used multiple transducers oriented at known angles to each other (Fahrbach 1970; P. L. Hansen, Cross, and Light 1974; Peronneau et al. 1974), but more flexible linear array implementations followed shortly after (Dunmire et al. 2000). The approach has also been extended to the estimation of velocities in 3-D (Daigle et al. 1975; Fox 1978). More recently, vector Doppler has been used combined with plane wave (PW) emissions by Ekroll *et al.* and Yiu *et al.* to take advantage of fast acquisition schemes for improved sensitivity and high frame rate (Ekroll et al. 2013; Yiu, S. S. Lai, and Yu 2014).

Additional directional information can be obtained from the spectral bandwidth of the received signal, which is proportional to the velocity component normal to the beam. This was demonstrated by Newhouse *et al.* (Newhouse et al. 1987). The same principle has been employed at the University of Florence to estimate velocity vectors over an investigation line in real-time (Ricci, Bassi, and Tortoli 2014; Tortoli, Bambi, and Ricci 2006).

The displacement of scatterers moving across the ultrasound beam can also be estimated by measuring the decorrelation rate of the RF signals measured in a range gate over successive emissions (Li, Lancée, et al. 1997). The approach was used by Li *et al.* to estimate blood velocities transverse to the direction of the ultrasound beam in an intravascular ultrasound system (Li, Steen, et al. 1998; Lupotti et al. 2003).

6.2.2 Speckle tracking

Speckle tracking refers to an angle-independent method for the estimation of tissue or blood motion introduced in 1987 by Trahey *et al.* (G. E. Trahey, Allison, and Ramm 1987; G. E. Trahey, Hubbard, and Ramm 1988). The motion is estimated by detecting the frame-to-frame displacement of the speckle patterns based on the hypothesis that local speckle distributions are maintained over successive frames. The detection is based on the cross-correlation between a kernel in a first image and a grid of neighbouring locations in a second one (Friemel, Bohs, and G. Trahey 1995).

Speckle tracking has been used by a number of research groups combined with PW emission to achieve high-frame-rate imaging (Bercoff et al. 2001; Fadnes, Ekroll, et al. 2015; Udesen et al. 2008). However, heavy computational demands are set by the need to compute a considerable amount of multi-dimensional correlations.

An alternative to speckle tracking uses contrast agents to enhance the backscattered signal and is referred to as echo particle image velocimetry (Kim, Hertzberg, and Shandas 2004; Poelma, Mari, Foin, M.-X. Tang, et al. 2009; Zhang et al. 2011). The contrast agents normally consist of gas microbubbles encapsulated in a lipid shell, and have been extensively used in medical ultrasound imaging as a mean to improve the contrast and SNR of the blood signal. The method has also been extended by using PW emission in (Leow et al. 2015).

6.2.3 Directional beamforming

The directional beamforming (DB) approach was proposed by Jensen (J. A. Jensen 2003; J. A. Jensen and Bjerngaard 2003) based on prior work by Bonnefous (Bonnefous 1988). The method uses a cross-correlation estimator to find the time shift from a number of lines beamformed along the direction of the flow. The decorrelation of the received signals is limited as the scatterers are followed in the direction of their movement.

Weakly focused or unfocused beams are needed to insonify a broad lateral region, and a uniform field across the beam is required. Therefore, the method fits well techniques as PW and SA, which make it possible to beamform lines in any direction (Nikolov and J. A. Jensen 2003). The implementation of CFM was demonstrated using DB combined with SA (J. A. Jensen and Nikolov 2004).

The DB approach requires the beam-to-flow angle to be known prior to beamforming, and several strategies have been proposed to estimate the angle and obtain a full VFI method (J. A. Jensen and Oddershede 2006; J. Jensen et al. 2017; Villagomez-Hoyos, Stuart, et al. 2016). A 3-D implementation has also been demonstrated in (Villagomez-Hoyos, Holbek, et al. 2016). These techniques provide highly accurate and precise flow estimates, but require massive computational efforts for the calculation of the cross-correlation functions in a number of directions.

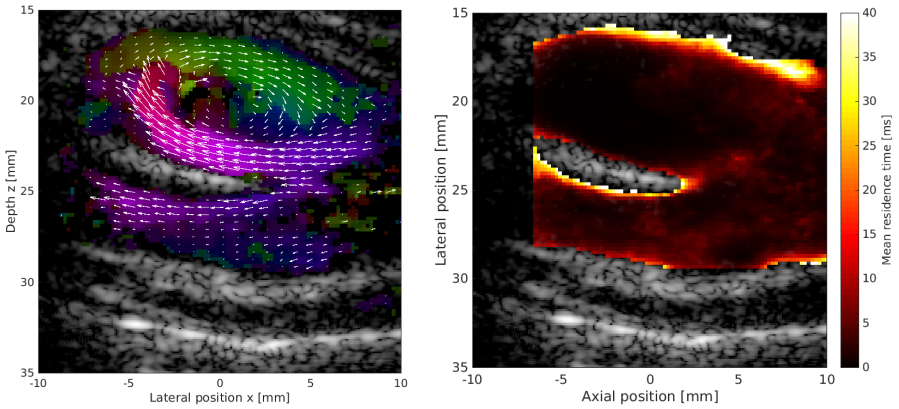

(a) (b)

Figure 6.3: (a) VFI image measured in the carotid bifurcation *in vivo*; (b) residence time derived from the VFI images averaged over a period of 250 ms. Images from (Villagomez-Hoyos 2016).

6.3 Validation and clinical applications

The pre-clinical validation of several VFI methods compared with MRI was documented in (K. L. Hansen, Udesen, et al. 2009). In (Pedersen et al. 2012), clinically relevant parameters like peak-systolic velocity (PSV), end-diastolic velocity (EDV), and resistive index obtained from VFI implemented on a commercial scanner were compared with those obtained from spectral Doppler. A similar comparison was performed by Tortoli *et al.* in (Tortoli, Lenge, et al. 2015), where several patients were included. These studies focused on the carotid arteries, and the choice is driven by the importance to estimate the velocity in these vessels for the identification and grading of atherosclerotic plaques responsible for the occurrence of ischemic strokes.

The cardiac imaging of neonates with atrial and ventricular septal defects for the quantification of the velocity in shunt flows was investigated by Fadnes *et al.* in (Fadnes, Nyrnes, et al. 2014). Sengupta *et al.* observed the effects of asynchronous electromechanical activation of the left ventricle on the shape of the vortices forming during isovolumic periods (Sengupta et al. 2007). In (K. L. Hansen, Møller-Sørensen, Kjaergaard, Lund, et al. 2016), twenty-five patients were scanned intra-operatively to evaluate the secondary helical flow and systolic backflow in the ascending aorta. The presence of atherosclerotic plaques in the ascending aorta was significantly associated with the occurrence of backflow. The influence of aortic valve stenosis on the flow in the ascending aorta was, in

addition, investigated by Hansen *et al.* before and after valve replacement, and a reduction of the systolic backflow was observed after surgery (K. L. Hansen, Møller-Sørensen, Kjaergaard, M. B. Jensen, et al. 2016). These studies aimed to find new biomarkers from the wealth of information of VFI images towards the earlier detection of cardiovascular pathological conditions.

The velocity fields provided by high-frame-rate VFI methods can be, in addition, used to calculate derived hemodynamic indices with the potential to improve the understanding of atherosclerotic lesion formation and vulnerability. Examples are the estimation of the wall shear stress (WSS), residence time (RT), and pressure gradients (PGs).

The WSS is the tangential force per unit area generated at the vessel wall by the blood flowing into the vessel. Low and oscillatory WSS appears to play a role in the inflammatory process promoting the formation and progression of atherosclerotic plaques (Slager, Wentzel, Gijsen, Schuurbiers, et al. 2005). Conversely, increased WSS has been associated with plaque destabilisation and rupture (Cheng, Tempel, et al. 2006; Slager, Wentzel, Gijsen, Thury, et al. 2005). The estimation of spatial variations in the WSS can lead to the early identification of atherosclerosis sites and allow for preventive interventions.

The WSS distribution is usually estimated through computational fluid dynamics simulations, where the vessel geometry is obtained by segmenting the lumen from measured anatomical images and fluid properties are assumed from known models (Cheng, Haperen, et al. 2005; Groen et al. 2007). However, the WSS can be directly derived from the velocity field (Poelma, Mari, Foin, M. Tang, et al. 2011; Poelma, Mijle, et al. 2012), although complications arise in case of inaccurate velocities in proximity of the vessel wall.

The RT is defined as the average amount of time that particles of a fluid spend in a certain volume. RT is recommended as a robust metric for the identification of low and oscillatory WSS regions (Lee, Antiga, and Steinman 2009). Villagòmez Hoyos investigated the RT distribution in carotid bifurcations *in vivo* (Villagomez-Hoyos 2016). An example of a RT map is shown in Fig. 6.3.

PGs provide an indication of the risk of embolism by estimating the pressure drop across stenotic regions (Baim and Grossman 2000). Currently, PGs are measured with invasive procedures that demand the insertion of pressure catheters in the diseased vessel. However, Olesen *et al.* demonstrated the possibility of deriving PGs non-invasively from the velocity field by solving the Navier-Stokes equations as shown in (Olesen et al. 2014; Olesen 2015). An example of PGs derived non-invasively using VFI is shown in Fig. 6.4.

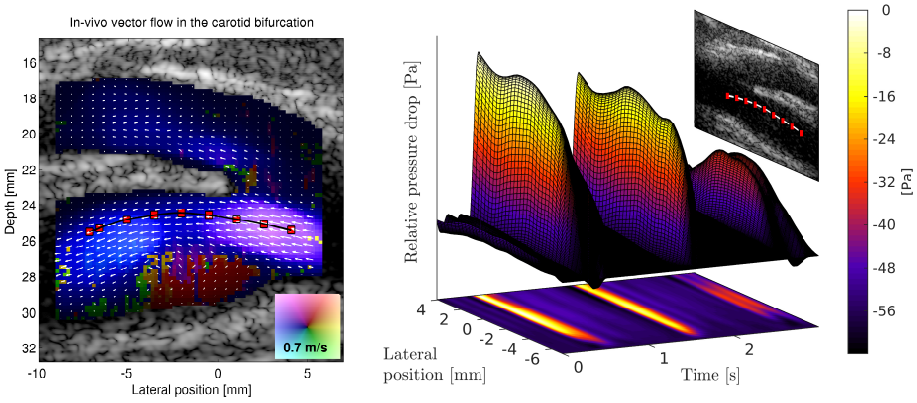

(a) (b)

Figure 6.4: (a) VFI image measured in the carotid bifurcation *in vivo*; (b) pressure drop derived non-invasively from the VFI images over a streamline indicated by the red dots in (a). Images from (Olesen 2015).

CHAPTER 7

Transverse oscillation

7.1 Introduction to transverse oscillation

The phase shift estimation is a relatively inexpensive approach for the measurement of blood velocities with advantages in terms of flexibility and computational requirements. The condition for the approach to work is the presence of narrowband oscillations in the direction parallel to the motion of the scatterers. Therefore, to extend the method for a 2-D velocity estimation, a double-oscillating field must be created. In other words, in order to detect transverse motion, i.e. in a direction perpendicular to the ultrasound beam ($\theta = 90°$), a narrowband oscillation must be generated in the transverse direction.

The transverse oscillation (TO) approach was introduced in 1998 by Jensen and Munk (J. A. Jensen and Munk 1998) and Anderson (Anderson 1998). A lateral modulation is created in the ultrasound field, which makes the received signals proportional to the lateral displacement of the scatterers allowing for the estimation of transverse velocities. Measurements of the I and Q components of the transverse signal are performed for each pulse emission, and the velocity can be estimated from the autocorrelation of the lateral analytic signal as in 6.6.

The TO modulation can be created in the pulse-echo field by introducing a double-peak apodization function in the Tx or Rx apertures. Creating the TO in Rx after a broad beam insonification normally provides a more flexible option. Two probing fields laterally shifted by $\lambda_x/4$ are needed to obtain the lateral I and Q components as shown in Fig. 7.1(a), with λ_x the wavelength of the lateral oscillation. Therefore, two beamformers must be employed, which must be dynamically adjusted during reception (Fig. 7.1(b)).

The TO approach was tested with linear, convex, and phased array transducers (Anderson 1998; J. A. Jensen, Brandt, and Nielsen 2015; J. A. Jensen and Munk 1998; Pihl, Marcher, and J. A. Jensen 2012), and a thorough evaluation of some significant parameters was carried out in (Udesen and J. A. Jensen 2006). Velocity estimators have been presented in (J. A. Jensen 2001) and (Anderson 2000), and *in vivo* studies have been performed to validate the method (Hansen et al. 2009; Pedersen et al. 2012; Udesen, Nielsen, et al. 2007). Its relatively low computational complexity, in addition, has pushed forward its implementation on several commercial platforms by BK Ultrasound, Herlev, Denmark.

The TO approach has been also exploited for tissue motion estimation (Heyde et al. 2017; Liebgott, Wilhjelm, et al. 2007). Liebgott *et al.* (Liebgott, Basarab, et al. 2008) and Sumi (Sumi 2008) synthesized a TO by using a synthetic transmit aperture for the

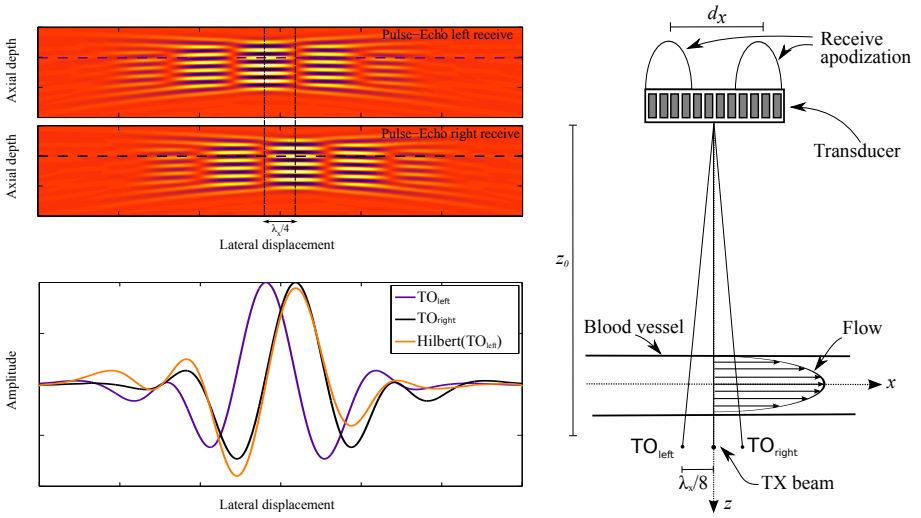

Figure 7.1: (a) top: probing pulse-echo fields laterally shifted by $\lambda_x/4$ to measure the I and Q lateral components; bottom: lateral signals sampled along the dashed horizontal line. The Hilbert transform of the I (left) component is shown for reference; (b) two Rx beamformers are needed to create the I/Q fields, and these are dynamically adjusted with the depth according to λ_x. Images from (Holbek, J. A. Jensen, and Stuart 2016).

optimization of the lateral oscillation frequency. A multi-resolution TO was proposed in (Varray and Liebgott 2013). The method has been extended to a 3-D VFI framework using conventional (Holbek, Ewertsen, et al. 2017; Pihl and J. A. Jensen 2014; Pihl, Stuart, et al. 2014) and row-column addressed arrays (Holbek, Christiansen, et al. 2016), and combined with PW emission to achieve high frame rate (J. Jensen et al. 2016; Lenge et al. 2015).

7.2 Double-oscillating field

The lateral PSF can be analytically derived if the Fraunhofer approximation is valid, i.e. under the assumption of CW emission, as previously described in (J. A. Jensen and Munk 1998) and (Liebgott, Basarab, et al. 2008). The far-field radiation pattern $P(x)$ in the lateral direction x can be expressed in terms of the Fourier transform of the aperture

function or apodization $p(\xi)$ (Goodman 1996):

$$P(x) = \mathcal{F}\{p(\xi)\} = \int_{-\infty}^{\infty} p(\xi) \exp\left(-j2\frac{\pi}{\lambda z}x\xi\right) d\xi, \tag{7.1}$$

with ξ the lateral position in the aperture domain, $\lambda = c/f_0$ the axial wavelength, and z the axial position. The pulse-echo pattern is, therefore, given by the multiplication of the Tx and Rx beam functions as

$$P_{tr}(x) = P_t(x)P_r(x) = \mathcal{F}\{p_t(\xi) * p_r(\xi)\}, \tag{7.2}$$

with p_t and p_r the Tx and Rx aperture functions.

Two probing fields are needed to sample the lateral I/Q components, therefore a double emission would be necessary if the lateral oscillation is created in Tx, i.e. by the aperture function p_t. In addition, this would prevent the possibility of dynamically adjusting the probing fields as a function of the depth. It is, hence, convenient to adjust the fields by calibrating the Rx beamformers. Non-diffracting Tx beams must be generated to ensure that $P_t(x)$ is independent of the depth, and the pulse-echo field can be approximated as being only dependent upon the function $P_r(x)$.

An aperture consisting of two Gaussian peaks of width σ separated by a distance D can be represented as

$$p(\xi) = \exp\left(-\frac{\xi}{2\sigma^2}\right) * \left[\delta\left(\xi + \frac{D}{2}\right) + \delta\left(\xi - \frac{D}{2}\right)\right], \tag{7.3}$$

and the beam becomes

$$P(x) = k \exp\left(-2\left(\frac{\pi}{\lambda z}\right)^2 \sigma^2 x^2\right) \cos\left(\frac{\pi}{\lambda z} Dx\right), \tag{7.4}$$

where all the multiplicative terms are included in the constant k.

The pulse-echo beam in (7.2) can then be expressed as

$$P_{tr}(x) \simeq P_r(x) = k \exp\left(-2\left(\frac{\pi}{\lambda z}\right)^2 \sigma^2 x^2\right) \cos\left(\frac{\pi}{\lambda z} Dx\right), \tag{7.5}$$

if a Rx aperture function $p_r(\xi)$ as (7.3) is used. Neglecting the constant k, the lateral beam is characterized by an oscillating cosine component modulated by a Gaussian function. The frequency of the lateral oscillation is equal to

$$f_x = \frac{1}{\lambda_x} = \frac{D}{2\lambda z}. \tag{7.6}$$

A more precise velocity estimation is obtained for increased lateral frequencies (J. A. Jensen 1996; Udesen and J. A. Jensen 2006). However, f_x in (7.6) decreases with the

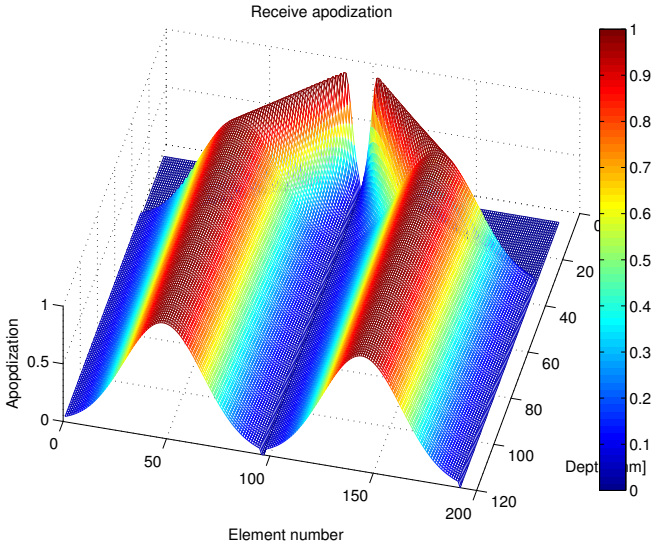

Figure 7.2: Apodization profiles dynamically adapted as a function of the depth to compensate for the depth-dependent nature of the lateral PSF. Image from (J. A. Jensen 2017)

depth in the form of a rectangular hyperbola and λ_x increases as a straight line. The frequency drop must be compensated for by dynamically adjusting the beamformers in reception expanding the distance between the apodization peaks D, which is nevertheless constrained by the width of the physical aperture. Increased f_x results in tighter aliasing limits for the phase-shift estimator (Sec. 6.1.2), and a trade-off exists between the precision and the range of detectable velocities.

The width of the Gaussian modulation in (7.5) is inversely proportional to σ, which is also limited by the width of the physical aperture. The width σ can be adjusted with the depth, and a possible depth-dependent Rx apodization is shown in Fig. 7.2. A narrower lateral PSF provides higher spatial resolution, and a compromise must be made with the accuracy of the autocorrelation estimator, which has better performance with wider PSFs (Udesen and J. A. Jensen 2006).

The equations (7.1)-(7.6) are strictly valid only in case of CW emission and at the transmit focus, hence represent an approximation for pulsed systems. However, the equations provide a simplified model for the prediction of the lateral modulation as a function of the emitted pulse, the depth, and the Tx and Rx apertures.

7.3 Velocity estimator

Owing to the presence of a TO in the probing pulse-echo fields, the received signals are affected by the axial as well as the lateral motions, and both velocity components can be measured. The equations of the velocity estimator are reviewed here from (J. A. Jensen 2001).

Two signals are received from the lateral I and Q beams (left and right pulse-echo fields in Fig. 7.1(a)), referred to as $r_{\mathrm{I}}(n,e)$ and $r_{\mathrm{Q}}(n,e)$, with n the index of the temporal sample or depth, and e the emission index. The two signals form a lateral quadrature pair, which can be rewritten as

$$r_{sq}(n,e) = r_{\mathrm{I}}(n,e) + jr_{\mathrm{Q}}(n,e), \tag{7.7}$$

with $j = \sqrt{-1}$ the imaginary unit. The signal in (7.7) is then Hilbert transformed in the axial direction

$$r_{sqh}(n,e) = r_{sq}(n,e) + j\mathcal{H}_n\{r_{sq}(n,e)\}, \tag{7.8}$$

where $\mathcal{H}_n$ is the Hilbert transform in the direction n.

Two signals are created,

$$\begin{aligned} r_1(n,e) = &\quad r_{sq}(n,e) + jr_{sqh}(n,e), \\ r_2(n,e) = &\quad r_{sq}(n,e) - jr_{sqh}(n,e), \end{aligned} \tag{7.9}$$

and the lag-1 autocorrelation functions

$$\begin{aligned} R_1(1) = &\quad \frac{1}{(N_e-1)} \sum_{e=0}^{N_e-2} r_1^*(n,e) r_1(n,e+1), \\ R_2(1) = &\quad \frac{1}{(N_e-1)} \sum_{e=0}^{N_e-2} r_2^*(n,e) r_2(n,e+1) \end{aligned} \tag{7.10}$$

are estimated using the signals from N_e emissions. Note that the autocorrelation functions in (7.10) are also dependent on the depth n and can be averaged in the axial direction over N_z samples corresponding to a pulse length. The lateral and axial velocities are finally estimated as

$$\begin{aligned} v_x = &\quad \frac{1}{2\pi f_x 2T} \times \\ &\arctan\left(\frac{\Im\{R_1(1)\}\Re\{R_2(1)\} - \Im\{R_1(1)\}\Re\{R_1(1)\}}{\Re\{R_1(1)\}\Re\{R_2(1)\} + \Im\{R_1(1)\}\Im\{R_2(1)\}}\right), \end{aligned} \tag{7.11}$$

$$\begin{aligned} v_z = &\quad \frac{c}{2\pi f_0 4T} \times \\ &\arctan\left(\frac{\Im\{R_1(1)\}\Re\{R_2(1)\} - \Im\{R_2(1)\}\Re\{R_1(1)\}}{\Re\{R_1(1)\}\Re\{R_2(1)\} + \Im\{R_1(1)\}\Im\{R_2(1)\}}\right), \end{aligned} \tag{7.12}$$

with T the period between successive emissions, and $\Re$ and $\Im$ the real and imaginary parts. The period T corresponds to the pulse repetition period T_{prf} for conventional TO implementations and is equal to the period between successive HRIs for SA or PW methods.

The range of detectable velocities in the lateral direction is limited to

$$|v_x| \leq v_x^{max} = \frac{1}{4}\frac{\lambda_x}{T} = \frac{1}{4}\frac{2\lambda z}{D}\frac{1}{T}, \tag{7.13}$$

where (7.6) is used for λ_x, and in the axial direction is

$$|v_z| \leq v_z^{max} = \frac{1}{8}\frac{\lambda}{T}. \tag{7.14}$$

The maximum v_x is lowered for increasing D due to the shorter lateral wavelength, and (7.13) and (7.14) are inversely proportional to T.

The accurate knowledge of f_x is necessary to calculate v_x in (7.11) and for the calibration of the I/Q beamformers. The lateral frequency can be, as a first-order approximation, calculated using the analytical model of Sec. 7.2. However, (7.6) overestimates f_x as can be observed in Fig. 7.3. The lateral frequency plotted in blue was estimated from a speckle phantom measurement using the method presented in Ch. 8 with the parameters in Tables 8.1 and 8.2, and the green hyperbole shows the theoretical frequency calculated using (7.6).

To obtain unbiased estimates, optimization procedures must be employed to accurately calibrate the beamformers, which complicate the system while failing to provide perfect quadrature pairs. In Fig. 7.4, examples of a lateral PSF (top) and the spectrum of the 2-D PSF (bottom) are shown from (J. A. Jensen, Brandt, and Nielsen 2015). In the top figure, it can be noticed that the right beam (green dashed) is not an exact replica of the Hilbert transform of the left beam (red dotted), and this causes leakage of the signal energy into the negative frequency spectrum. An alternative solution is provided by directional TO (DTO), which estimates f_x directly from the acquired ultrasound data to obtain unbiased velocities.

7.4 Directional transverse oscillation

The DTO approach solves the problems of the lateral frequency estimation by using the DB concept (J. A. Jensen 2016). A normal focused beam is emitted, and for each emission e, a signal $r(m, n, e)$ is beamformed in the lateral direction centered around the velocity point at each depth n. Here, m is the sample index along the lateral direction, i.e. $m = -M/2, ..., M/2 - 1$ with M the number of lateral samples. A quadrature pair is then obtained by means of a lateral Hilbert transform.

The lateral analytic signal is calculated as

$$r_{sq}(m, n, e) = r(m, n, e) + j\mathcal{H}_m\{r(m, n, e)\}, \tag{7.15}$$

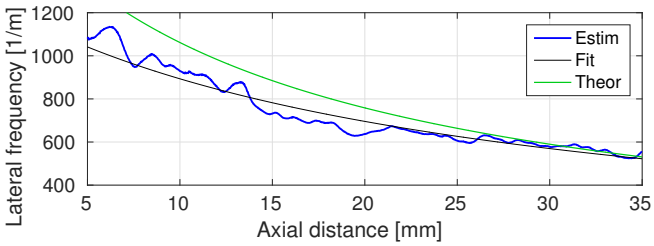

Figure 7.3: Lateral frequency estimated from a speckle phantom measurement using the method presented in Ch. 8 with the parameters in Tables 8.1 and 8.2. The hyperbole displayed in black was obtained from the linear fit to the estimated λ_x. The green curve shows the theoretical frequency calculated using (7.6), with $c = 1540\,\mathrm{m\,s^{-1}}$. The theoretical equation overestimates the lateral frequency introducing phase errors between the I and Q beams.

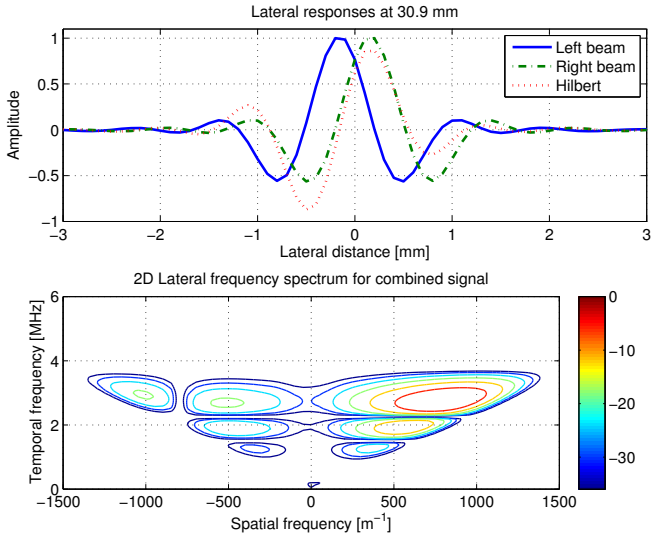

Figure 7.4: Example of a lateral PSF (top) and spectrum of the 2-D PSF (bottom). In the top figure, it can be noticed that right beam (green dashed) is not an exact replica of the Hilbert transform of the left beam (red dotted). This causes leakage of the signal energy into the negative frequency spectrum. Image from (J. A. Jensen, Brandt, and Nielsen 2015)

where $\mathcal{H}_m$ is the Hilbert transform in the lateral direction m. The lateral frequency can be estimated as

$$f_x(n) = \frac{1}{\lambda_x(n)} = \frac{\sum_{f=-F/2}^{F/2-1} \frac{f}{F\Delta x} |R_{sq}(f,n,e)|^2}{\sum_{f=-F/2}^{F/2-1} |R_{sq}(f,n,e)|^2}, \tag{7.16}$$

with $R_{sq}(f,n,e) = \mathcal{F}_m\{r_{sq}(m,n,e)\}$ the Fourier transform of r_{sq} along the lateral direction m, f the sample index in the discrete Fourier domain, F the number of Fourier coefficients, and Δx the lateral sampling period. The lateral frequencies from N_e emissions can be averaged to obtain smoother estimates. In addition, $f_x(n)$ can be averaged along the depth over a pulse length. The same estimator reported in Sec. 7.3 is then used by replacing the signal r_{sq} in (7.8) with the one in (7.15). It must be noted that the parameters M and N_e used for the velocity estimation are in general independent of those used for the estimation of f_x.

In Fig. 7.5, an example of a double-oscillating PSF simulated using the method presented in Ch. 8 with the parameters in Tables 8.1 and 8.2 is shown in the top plot. The middle plot displays the lateral beamformed signal obtained by sampling the PSF along the dashed horizontal line and its Hilbert transform, and the bottom plot is the spectrum of the analytic signal, where no spectral leakage is observed as the signals form a perfect quadrature pair. The lateral frequency estimated with (7.16) is 650 m^{-1} (dashed vertical line).

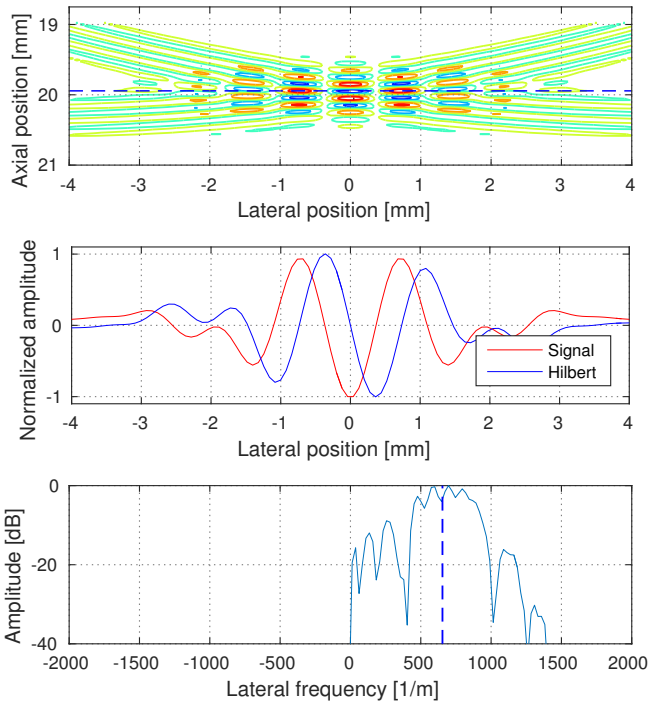

Figure 7.5: (top) Double-oscillating PSF simulated using the method presented in Ch. 8 with the parameters in Tables 8.1 and 8.2; (middle) lateral beamformed signal obtained by sampling the PSF along the dashed horizontal line and its Hilbert transform; (bottom) spectrum of the analytic signal. No spectral leakage is observed as the signals form a perfect quadrature pair. The lateral frequency estimated with (7.16) is $650\,\mathrm{m}^{-1}$ (dashed vertical line).

CHAPTER 8

A vector flow imaging method for wireless ultrasound: Theory and simulations

Summary *A VFI method has been developed to suit the computational requirements and data bandwidth of a portable scanner and is presented in this chapter. The method combines SASB and DTO to achieve the wireless transmission of the data and a low-complexity velocity estimation. The objective is the integration of quantitative flow measurements in a hand-held scanner with limited requirement for manual interaction. Simulations and measurements of a straight vessel have been performed for a preliminary investigation of the performance of the approach with linear and convex array transducers. The work is object of Paper I and V in appendix. A patent has been filed to the United States Patent and Trademark Office (Patent I) and is also included in appendix.*

8.1 Creation of a TO using SASB

A VFI method has been developed combining SASB and DTO to obtain the wireless transmission of the data and a low-complexity velocity estimation. A TO is created by using fixed Tx/Rx focused emissions. The data bandwidth necessary for the transmission of the ultrasound data from the probe to the processing unit can be minimized by integrating the FSB in the probe handle as described in Part I of this thesis. The velocity estimation can be performed using a 2-D autocorrelation estimator owing to the presence of a double-oscillating pattern in the beamformed HRIs. The method opens the way to the integration of quantitative blood flow measurements in portable devices. The use of SA focusing, in addition, makes it possible to obtain continuous data acquisition and high-frame-rate velocity estimation.

8.1.1 Acquisition and beamforming

The acquisition sequence is schematically displayed in Fig. 8.1 using a linear array of transducers. K emissions are sequentially transmitted at regular intervals of T_{PRF}, with $K = 4$ in the figure. At each emission, L transducer elements are excited and focused in a point located behind the array, therefore a diverging wave is emitted to insonify

the area inside the dashed line. The focal point can, however, be moved in front of the array for improved SNR in case of deeper regions of interest, as for the convex array implementation in Sec. 8.2.4. The focal positions can be considered VSs (Bae and Jeong 2000; Frazier and O'Brien 1998; Passmann and Ermert 1996), and two virtual apertures (VAs) are created, each including $K/2$ VSs. The VAs are laterally separated by a distance of D transducer elements. In Fig. 8.1, the left and right VAs are respectively depicted in blue and red.

The dual-stage beamforming involved in the creation of the HRIs is shown in Fig. 8.2. For the sake of simplicity, a case with one single VS per aperture ($K = 2$) is considered. The received data from each emission is focused by a FSB in a static point corresponding to the VS, and one single LRL is created and transmitted to the second stage after each emission. The data throughput between the probe and the processing unit is thus reduced by a factor L. In the second stage, the VS location is considered a VR, and the data in the LRLs are refocused based on the VS/VR assumption. The PSFs are shown in the second-stage boxes of Fig. 8.2 for the left (top) and right (bottom) VSs. A PSF oscillating in both directions is obtained when the responses of the emissions from the left and right VAs are coherently combined as displayed after the summation in Fig. 8.2.

Referring to the analytical derivation of the PSF in Sec. 7.2, it can be noticed that the Tx and Rx beam functions are in this case coincident, since the same VAs are used for the transmission and reception. In this case, $P_t = P_r$ and P_{tr} is the square of the beam in (7.4), equal to

$$P_{tr}(x) = P(x)^2 = k \exp\left(-4\left(\frac{\pi}{\lambda z}\right)^2 \sigma^2 x^2\right)\left(1 + \cos\left(\frac{2\pi}{\lambda z} D x\right)\right), \tag{8.1}$$

where the identity $\cos(2\theta) = 2\cos^2(\theta) - 1$ is used. Neglecting the constant k and the unity term, which introduces a low frequency modulation, the PSF in (8.1) has the same features of the one in (7.5). However, it can be noticed that the lateral frequency is doubled and is equal to

$$f_x = \frac{1}{\lambda_x} = \frac{D}{\lambda z}. \tag{8.2}$$

As discussed in Sec. 7.2, an increased frequency is beneficial to the precision of the estimator while it lowers the aliasing limit in (7.13). Furthermore, the impossibility of adjusting the beamformers in a dynamic manner during reception makes the estimation performance degrade with the depth. The lateral width of the PSF can be reduced to improve the resolution by increasing K, which is proportional to σ in (8.1), although this further decreases the velocity range.

8.1.2 Clutter filter

A schematic representation of the amplitude spectrum of the received signal $G(f)$ is displayed in Fig. 8.3 to show the principle of operation of the clutter filter used in this

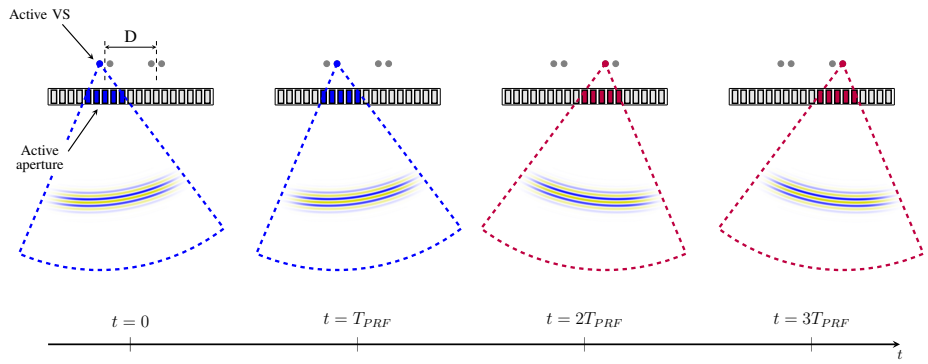

Figure 8.1: Acquisition sequence for the SASB DTO method. K emissions are sequentially transmitted at regular intervals of T_{PRF}, with $K = 4$ in this example. Each emission is focused behind the array, therefore a diverging wave is emitted to insonify the area inside the dashed line. The focal positions are considered as VSs, and are laterally divided in two VAs. The left VA is depicted in blue and the right one in red.

study. The tissue component $G_t(f)$ is low-frequency, and its bandwidth depends upon the velocity distribution in the tissue. $G_b(f)$ is the signal from the blood and $G_n(f)$ is electronic noise. The energy of the signals is represented by the colored areas. The goal of the clutter filter is to minimize the energy of G_t while preserving that of G_b.

A dual-stage filter was used. The first stage is a high-pass moving-average-subtraction filter $H_{hp}(f)$ with a –3 dB cutoff frequency of 120 Hz used on the LRLs. In ideal conditions of stationary tissue, $G_t(f)$ is narrowband and is effectively attenuated by $H_{hp}(f)$. However, significant components leak in the blood spectrum when tissue velocities cause a broadening of $G_t(f)$. These components have, in general, high amplitude and disrupt the velocity estimation.

The second stage consists of an amplitude threshold E, and sets $G(f) = E \; \forall f : G(f) > E$. This filter is used on the HRIs and attenuates any spectral components with amplitudes above the threshold E. As a result, the energy of G_t is further reduced respect to that of G_b. The threshold E was determined after inspecting the spectrum of the received signal at locations internal to the vessel. The spectrum was calculated by means of a windowed FFT. The time-domain signals were then restored after filtering by performing an inverse FFT. The approach has been previously used and described in (Villagomez-Hoyos et al. 2016) and (Villagomez-Hoyos 2016).

Only the high-pass filter has been used for the simulations and measurements of constant flow phantoms reported in these chapters. The energy-based filter has been employed for the pulsating and *in vivo* measurements, since the moving-average-subtraction filter alone failed to properly attenuate the signal from the tissue during the systolic phase. However, the choice of E is critical to the performance of the estimator. If E is higher

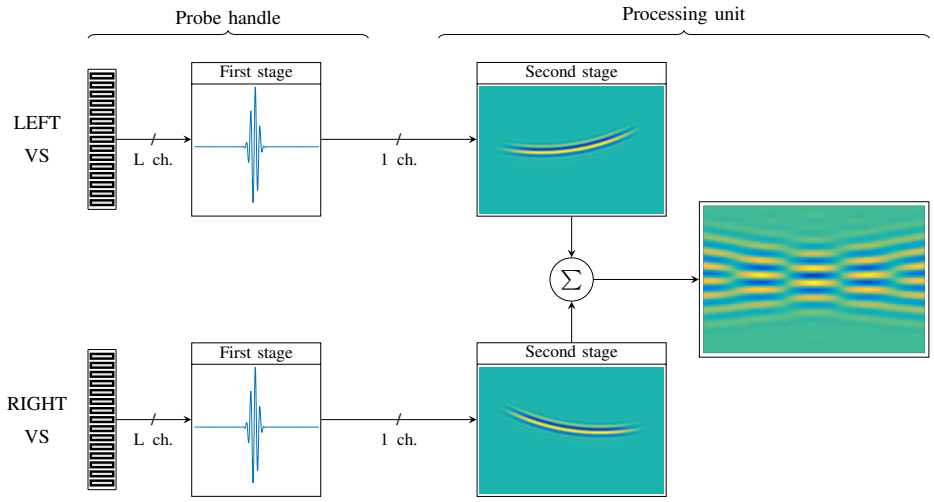

Figure 8.2: Beamforming involved in the creation of a TO using SASB in the case with one single VS per aperture ($K = 2$). The received data from each emission is focused by a first beamformer in a static point corresponding to the VS, and a LRL line is obtained. The VS is therefore also considered a virtual receiver (VR), the response of which is the LRL. In the second stage, the data in the LRLs are refocused based on the VS/VR assumption. The PSF is shown in the second-stage boxes for the left and right VSs. To obtain a double-oscillating PSF, the responses from the left and right VAs are coherently combined. The 2-D PSF is shown after summation in the top plot, and the lateral signal along the blue dashed line is shown in the bottom plot.

than the amplitude of the blood signal, a higher residual energy from the tissue signal will bias the estimation of the blood velocity. On the other hand, a low threshold will filter out energy from the blood spectrum.

8.1.3 Velocity estimation

After clutter filtration, a signal $r(m, n, e)$ is created in the lateral direction centered around the velocity point by selecting M lateral samples in the HRI. A quadrature pair is obtained by means of a lateral Hilbert transform as in (7.15). The lateral frequency is estimated from (7.16), and the velocity estimation proceeds as reported in Sec. 7.3 by replacing the signal r_{sq} in (7.15).

The velocities v_x and v_z can be estimated everywhere in the image after N_e HRIs are acquired. The period T in (7.11) and (7.12) becomes here the period between successive HRIs and is equal to KT_{PRF}. This is a limitation of the current implementation, as the aliasing limit of the autocorrelation estimator is lowered by the acquisition of a HRI over

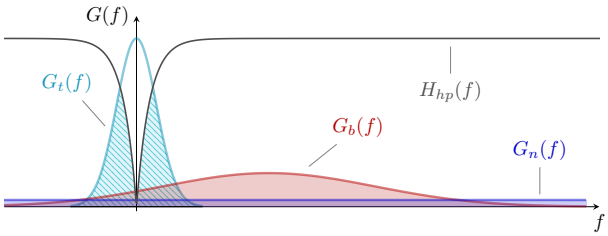

(a)

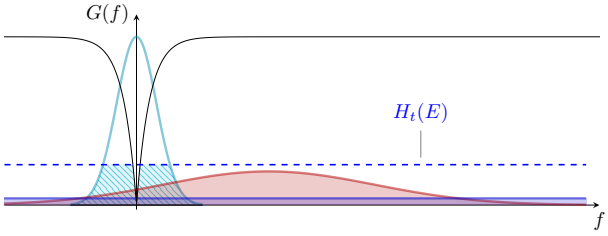

(b)

Figure 8.3: Schematic representation of the amplitude spectrum of the received signal $G(f)$. $G_t(f)$ is the spectrum of the signal scattered by the surrounding tissue; $G_b(f)$ is the spectrum of the signal from the blood; and $G_n(f)$ is white noise from the measuring system. The energy of the components is highlighted by the colored areas. (a): A high-pass filter $H_{hp}(f)$ is used to reduce the energy of G_t (area under the curve); (b): a second stage $H_t(E)$ is used to remove any spectral components with amplitude greater than a threshold E.

K emissions. In addition, the sequential acquisition causes distortions in the PSF due to the inter-emission motion of the scatterers, which affect the performance of the estimator, and the decorrelation is increased over successive HRIs.

8.2 Simulations

8.2.1 Setup

Simulations of a straight vessel were performed in Field II (Jensen 1996; Jensen and Svendsen 1992). A vessel with a radius of 6 mm and a beam-to-flow angle of 75° was modeled as a collection of randomly-distributed scatterers with a normal amplitude distribution. A parabolic flow was created with a peak velocity of $0.2\,\mathrm{m\,s^{-1}}$. At least

20 scatterers per resolution volume were considered to ensure fully developed speckle. Scatterers outside the vessel boundaries were used to model the surrounding tissue, with an amplitude approximately 40 dB higher than the blood scatterers. No tissue movement was considered in the simulation.

A duplex sequence was designed for the acquisition of B-mode and flow data. The pulse repetition frequency was set to $PRF = 9\,\text{kHz}$. B-mode and flow emissions were interleaved to achieve continuous data acquisition, i.e. one B-mode pulse was transmitted after every $K = 6$ flow emissions, with an effective repetition frequency $PRF_{eff} = PRF/(K+1)$. The period T is, therefore, $1/PRF_{eff} = (K+1)/PRF$. The estimator in (6.5) was used for the axial velocity component, as this has higher aliasing limit.

8.2.2 Processing

The processing scripts were developed in MATLAB (The MathWorks, Inc., Natick, MA, USA), and the beamformation was performed using the BFT3 toolbox (Hansen, Hemmsen, and Jensen 2011). The element data were beamformed in the FSB and then matched filtered. The HRIs were beamformed by the SSB in a Cartesian grid and Hilbert transformed in the lateral direction. The directional signals were then created by selecting M lateral samples. The frequency f_x was estimated using (7.16) as a function of the depth from signals of $M = 64$ samples and averaged over $N_e = 64$ HRIs and a pulse length in the axial direction. The curve $f_x(n)$ was then inverted, and a line was fitted to λ_x. The estimation of $f_x(n)$ was performed only once, and can be considered an initialization procedure.

The autocorrelation functions in (7.10) were calculated from $N_e = 32$ consecutive HRIs, and averaged over $M = 32$ lateral samples and a pulse length in the axial direction. The mean bias and the relative SD for the velocity profiles were calculated inside the vessel from 50 independent simulations.

8.2.3 Linear array

A 0.55λ-pitch linear array of transducers was used with the parameters in Table 8.1. The vessel was positioned at a depth of 20 mm. The parameters for the imaging setup and processing are reported in Table 8.2. Six emissions were used for each flow HRI ($K = 6$), regularly spaced with a distance of 2 transducer elements. The VAs were positioned behind the transducer and steered toward the center of the image with an angle of $\pm 2.5°$ (Fig. 8.4). The distance between the VAs was $D = 48$ transducer elements. The double-oscillating PSF created using the same simulation parameters is displayed in Fig. 7.5. Sixty-four emissions were used to create a B-mode image. The B-mode VSs were regularly distributed between ± 15 mm in the lateral direction.

Table 8.1: Linear array parameters

Parameter	Symbol	Value	Unit
Array type	-	Linear	-
Element pitch	p	0.2	mm
Element height	-	6	mm
Number of elements	-	192	-
Elevation focus	-	38	mm
Center frequency	-	4.1	MHz

Table 8.2: Imaging setup and processing parameters for the linear array investigations

Parameter	Symbol	Flow	B-mode	Unit
Speed of sound	c	1490		$\mathrm{m\,s^{-1}}$
Imaging setup				
Excitation	-	4 cycles	2 cycles	-
Pulse repetition freq.	PRF	9		kHz
Center frequency	f_0	4.1		MHz
Tx apodization	-	Tukey ($\alpha = 0.6$)		-
Rx apodization	-	Tukey ($\alpha = 0.6$)		-
VS axial position	-	−15	−30	mm
Active elements	L	64	96	-
f-number	$F_\#$	-1.17	-1.56	-
Number of VSs	-	$K = 6$	64	-
Distance between VSs	-	2	-	elements
Distance between VAs	D	48	-	elements
VA apodization	-	Rect	-	-
Processing				
Lateral sampling interval	Δx	0.1		mm
Axial sampling frequency	f_s	35		MHz
Lateral signal length:	M			
Frequency estimation		64	-	samples
Velocity estimation		32	-	samples
Number of HRIs :	N_e			
Frequency estimation		64	-	-
Velocity estimation		32	-	-

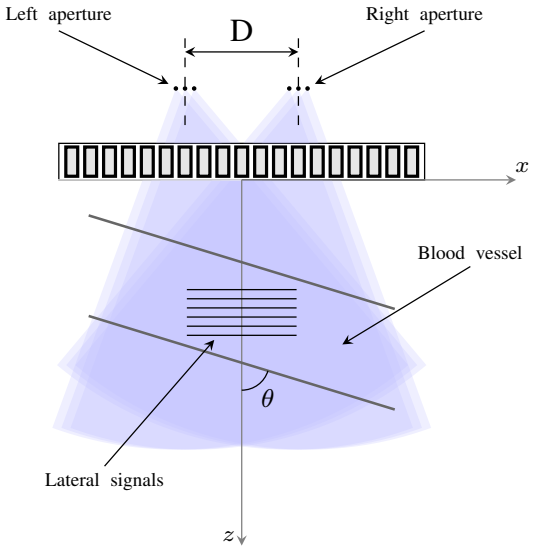

Figure 8.4: Imaging setup including the linear array transducer and the imaged vessel. The vessel was positioned below the transducer with a beam-to-flow angle θ. $K = 6$ VSs were used for each flow HRI and divided in two VAs separated by a distance D. The VAs were steered toward the center with an angle of $\pm 2.5^\circ$.

8.2.3.1 Results

In Fig. 8.5 the results are displayed for the simulation with the linear array. The mean velocity profiles (black) and SDs (shaded regions) are shown in Fig. 8.5(a) along with the reference profiles (red) in the lateral and axial directions (top and bottom plots, respectively). The mean bias is -2.78% and -1.82% for the lateral and axial profiles, and the average SD is 8.52% and 2.45%. Fig. 8.5(b) displays the estimated angle with a mean value of $74.95 \pm 4.39^\circ$ calculated from the points inside the vessel boundaries.

8.2.4 Convex array

A λ-pitch convex array was used with the parameters in Table 8.3. The transducer reflects the same geometry of the ATLAS probe presented in Sec. 5.4.2. The simulations have been performed to study the feasibility of a possible implementation with the portable probe prototype. The vessel was positioned at a depth of 50 mm. The parameters for the imaging setup and processing are reported in Table 8.4. Six emissions were used for each flow HRI ($K = 6$), regularly spaced with a distance of one transducer element. The VAs

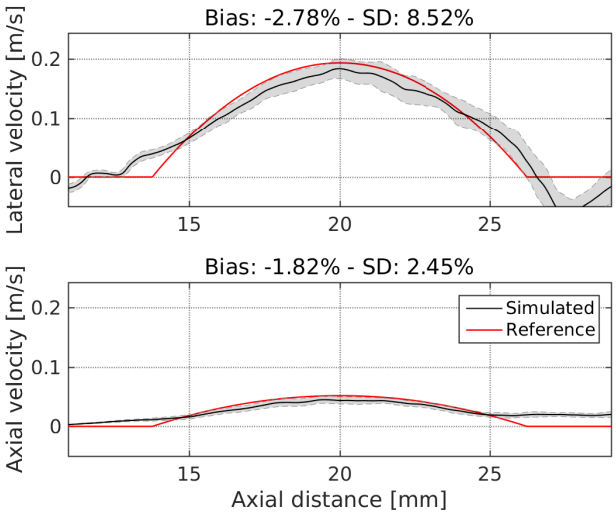

(a)

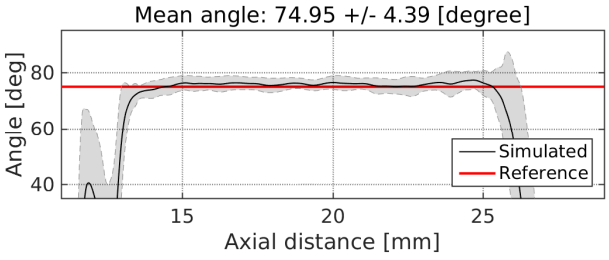

(b)

Figure 8.5: Simulation of a straight vessel with 75° flow angle and 20 mm depth with the linear array setup. (a) Mean velocity profiles (black), SD (shaded region), and reference profiles (red) for the lateral (top) and axial (bottom) velocities; (b) Estimated angle.

Table 8.3: Convex array parameters

Parameter	Symbol	Value	Unit
Array type	-	Convex	-
Element pitch	p	0.33	mm
Element height	-	13	mm
Number of elements	-	192	-
Elevation focus	-	70	mm
Radius of curvature	-	58.7	mm
Center frequency	-	3.3	MHz

were positioned at a depth of 20 mm and steered toward the center of the image with an angle of $\pm 7^\circ$ (Fig. 8.4). The distance between the VAs was $D = 32$ transducer elements. No B-mode emissions were included in these simulations.

8.2.4.1 Results

The results of the simulations with the convex array are reported in Fig. 8.6. The mean velocity profiles and SDs are shown in the lateral and axial directions in Fig. 8.6(a). The mean bias is -4.98% and -3.41% for the lateral and axial profiles, respectively, and the average SD is 12.85% and 2.30%. The estimated angle is displayed in Fig. 8.6(b), with a mean value of $73.12 \pm 9.50^\circ$ calculated from the points inside the vessel boundaries.

Table 8.4: Imaging setup and processing parameters for the convex array simulations

Parameter	Symbol	Flow	Unit
Speed of sound	c	1490	$\mathrm{m\,s^{-1}}$
Imaging setup			
Excitation	-	8 cycles	-
Pulse repetition freq.	PRF	9	kHz
Center frequency	f_0	3.1	MHz
Tx apodization	-	Tukey ($\alpha = 0.6$)	-
Rx apodization	-	Tukey ($\alpha = 0.6$)	-
VS axial position	-	20	mm
Active elements	L	64	-
f-number	$F_\#$	0.93	-
Number of VSs	-	$K = 6$	-
Distance between VSs	-	1	elements
Distance between VAs	D	32	elements
VA apodization	-	Rect	-
Processing			
Lateral sampling interval	Δx	0.1	mm
Axial sampling frequency	f_s	35	MHz
Lateral signal length:	M		
Frequency estimation		64	samples
Velocity estimation		32	samples
Number of HRIs :	N_e		
Frequency estimation		64	-
Velocity estimation		32	-

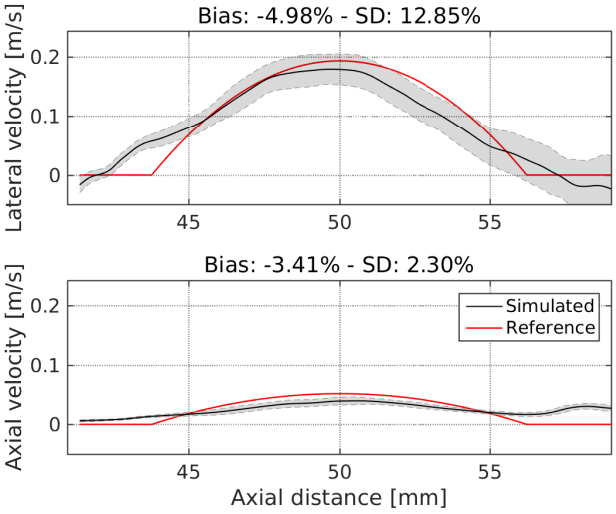

(a)

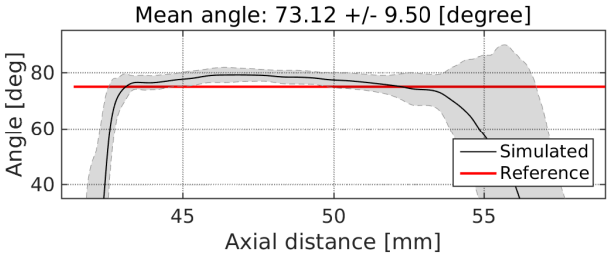

(b)

Figure 8.6: Simulation of a straight vessel with 75° flow angle and 50 mm depth with the convex array setup. (a) Mean velocity profiles (black), SD (shaded region), and reference profiles (red) for the lateral (top) and axial (bottom) velocities; (b) Estimated angle.

CHAPTER 9

A vector flow imaging method for wireless ultrasound: Measurements

Summary *A parametric study was carried out with constant flow measurements to evaluate the performance of the method as a function of relevant parameters.* In vivo *measurements of a common carotid artery and bifurcation were performed to study its capabilities in presence of realistic hemodynamic conditions. The method was implemented on a commercially available tablet for a proof-of-concept demonstration of the wireless transmission and real-time processing performance. The results reported in this chapter are the outcome of a collaboration with the Visual Computing Lab at the Alexandra Institute, Aarhus, Denmark, and with the Department of Radiology at Rigshospitalet, Copenhagen University Hospital, Copenhagen, Denmark. The Papers I, III, and IV in appendix are based on these results.*

9.1 Constant flow phantom

9.1.1 Setup

Measurements of a straight vessel were performed on a flow rig system consisting of a centrifugal pump (Cole-Parmer, Vernon-Hills, IL, USA) circulating a blood mimicking fluid and a vessel with a radius of 6 mm immersed in a water bath. The entrance length of the vessel ensured a fully developed parabolic, laminar flow profile. The volume flow was measured for reference by a magnetic flow meter (MAG3000, Danfoss, Nordborg, Denmark) and was set to obtain a peak velocity of approximately $0.2\,\mathrm{m\,s^{-1}}$. A linear array transducer with the same parameters of Table 8.1 was connected to the SARUS scanner (Jensen, Holten-Lund, et al. 2013) for the acquisition of the RF element data. The same duplex imaging sequence used in Sec. 8.2.1 for the linear array simulations was considered here, of which the parameters are reported in Table 8.2. The processing was performed off-line as explained in Sec. 8.2.2. The relative bias and SD were calculated inside the vessel from 50 independent velocity profiles.

A parametric study was first carried out to investigate the performance of the method as a function of the distance D and the parameters M and N_e used for the velocity estimation. The values for these parameters are reported in Table 9.1, where the default

Table 9.1: Varied imaging setup and processing parameters

Parameter	Symbol	Value	Unit
Distance between VAs	D	16 - 24 - 32 - 40 **48** - 56 - 64	element
Lateral signal length	M	4 - 8 - 16 24 - **32** - 48	samples
Number of HRIs	N_e	4 - 8 - 16 - **32** 64 - 96 - 128	-

values are displayed in bold ($D = 48; M = 32; N = 32$). The vessel was placed at a depth of approximately 20 mm with a beam-to-flow angle θ = 75°. This setup was chosen to optimize the imaging parameters for the measurement of a common carotid artery.

The constant parabolic flow profile with θ = 75° was measured, in addition, with the default setup at a depth of approximately 30 and 40 mm, and at 20 mm for flow angles of 90° and 65°.

The range in (7.13) was shifted to $\left[-\frac{1}{4}v_x^{max}, \frac{7}{4}v_x^{max}\right]$ to match the velocities expected *in vivo*. At the depth of 20 mm with $PRF = 9$ kHz, $v_x^{max} = 0.44\,\mathrm{m\,s^{-1}}$ and the velocity ranges are

$$\begin{aligned} -0.11\,\mathrm{m\,s^{-1}} \leq \quad v_x \leq \quad 0.77\,\mathrm{m\,s^{-1}}, \\ -0.12\,\mathrm{m\,s^{-1}} \leq \quad v_z \leq \quad 0.12\,\mathrm{m\,s^{-1}}. \end{aligned} \tag{9.1}$$

It must be noted here that the range is half that of (7.13) due to the doubled lateral frequency in (8.2). For the vessel at 65°, an axial velocity $v_z = v_z^{max} = 0.12\,\mathrm{m\,s^{-1}}$ gives a maximum peak velocity of $0.28\,\mathrm{m\,s^{-1}}$. Therefore, a peak velocity of $0.2\,\mathrm{m\,s^{-1}}$ was used to avoid aliasing.

To show the performance of the method with lateral velocities closer to those detected *in vivo*, the flow rig measurements were repeated with the default setup and a flow angle of 90°. The peak velocity was set to 0.32, 0.44, and $0.5\,\mathrm{m\,s^{-1}}$ with PRF = 9 kHz. The velocity was then kept equal to $0.5\,\mathrm{m\,s^{-1}}$ to maintain laminar flow and the PRF was lowered to 7.5 and 6.4 kHz to emulate velocities of 0.6 and $0.7\,\mathrm{m\,s^{-1}}$, respectively.

9.1.2 Results

The results for the vessel at 20 mm and 75° measured with the default setup are shown in Fig. 9.1. In Fig. 9.1(a), the mean profiles (black) and the SDs (shaded regions) are plotted along with the reference profiles (red) calculated from the measured volume flow. The lateral and axial velocities are displayed in the top and bottom graphs, respectively. The mean bias is -6.23% and 0.44% for the lateral and axial profiles, respectively. The mean SD is 8.16% and 2.84%. In Fig. 9.1(b), the estimated angle is shown as a function of the depth with a mean value of $72.65 \pm 2.48°$ calculated from the points inside the vessel boundaries.

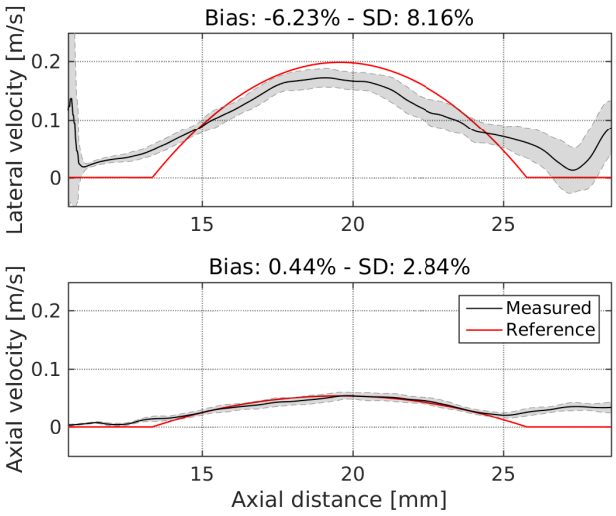

(a)

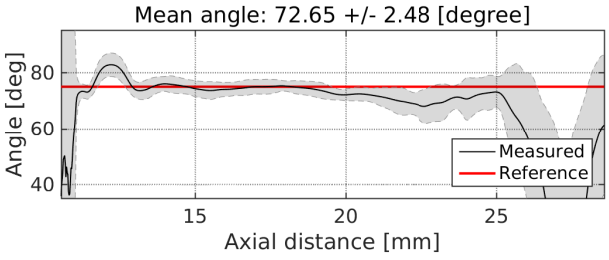

(b)

Figure 9.1: Measurement of a straight vessel with 75° flow angle and 20 mm depth. (a) Mean velocity profiles (black), SD (shaded region), and reference profiles (red) for the lateral (top) and axial (bottom) velocities; (b) Estimated angle.

Table 9.2: Constant flow measurements results

Flow angle	Lateral Bias	Lateral SD	Axial Bias	Axial SD	Estimated Angle
90°	-5.03%	6.06%	0.72%	2.59%	$89.13 \pm 0.79°$
75°	-6.23%	8.16%	0.44%	2.84%	$72.65 \pm 2.48°$
65°	5.62%	9.58%	0.32%	2.84%	$66.70 \pm 2.86°$

The results of the parameter study are displayed in Fig. 9.2(a), 9.2(b), and 9.3. The mean bias (top) and SD (bottom) are shown in Fig. 9.2(a) as a function of D for the lateral and axial profiles. By increasing D, shorter oscillation wavelengths are obtained in the lateral direction. For $D < 40$, λ_x is longer than the lateral signal ($M = 32$), and this gives an increased bias for the lateral velocity component. The mean lateral bias is between -5.6% and -11.7% for $D \geq 40$, and the SD is between 8.3% and 7.9%. The axial bias is lower than 1% in all the cases and the SD is between 1% and 3%.

In Fig. 9.2(b), a lower lateral SD is obtained by increasing M, while the other values are unaffected. In must be noted, however, that the lateral resolution decreases with increasing M. Signals of only four samples can be used to reduce the computational complexity with a limited loss in precision. $M = 32$ was used in the rest of the experiments.

The mean bias in Fig. 9.3 is only slightly affected by increasing N_e, while the SD decreases significantly, as expected. For $N_e = 128$, the SD is 4.4% and 1.6% in the lateral and axial directions. However, longer sequences provide a lower temporal resolution of the estimates.

In Fig. 9.4, the mean bias and SD are plotted as a function of the axial position of the vessel from 20 to 40 mm with $\theta = 75°$. The lateral bias is between -6.2% and -0.9%, while the SD is between 8.2% and 11.2%. Constant performance is obtained for the axial velocity.

The velocity profiles and estimated flow angles for the vessel at a depth of 20 mm with beam-to-flow angles of 90° and 65° are displayed in Fig. 9.5 and Fig. 9.6, respectively. The results are summarized in Table 9.2.

Finally, the mean bias and SD with increasing velocity are shown in Fig. 9.7. For velocities up to 0.6 m s^{-1}, the lateral bias is between -7.4% and 2.1% and the SD between 6.1% and 11.2%. Increased bias and SD (-15.4% and 24.3%) are reported for 0.7 m s^{-1} because of the occurrence of aliasing.

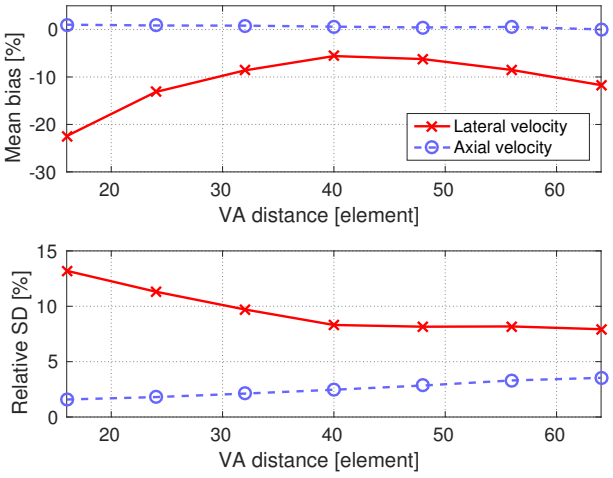

(a)

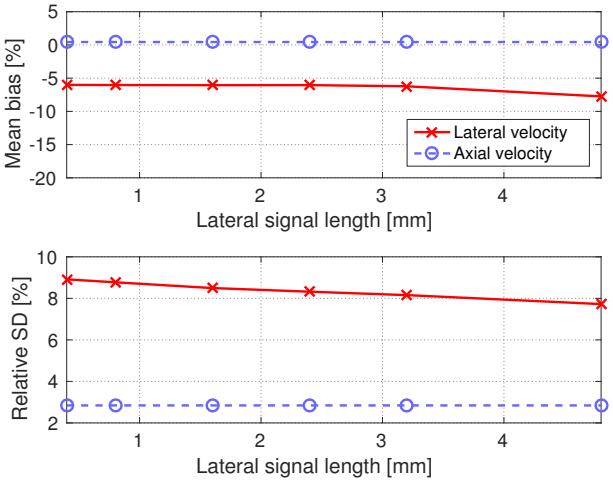

(b)

Figure 9.2: (a) Mean bias (top) and SD (bottom) for the lateral and axial velocity profiles as a function of the distance D between the VAs; (b) Mean bias (top) and SD (bottom) for the lateral and axial velocity profiles as a function of the length M of the lateral signal expressed in mm.

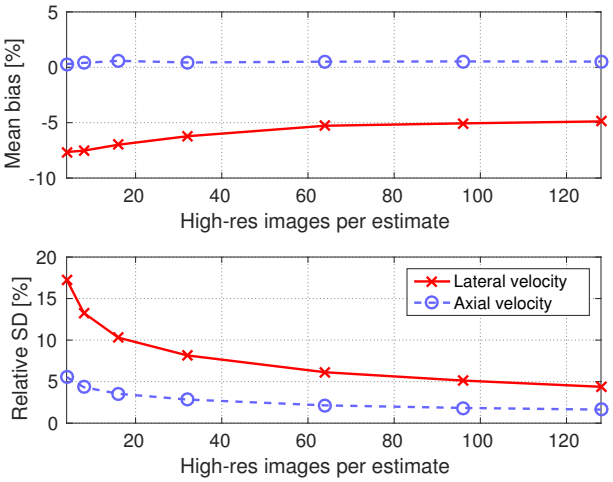

Figure 9.3: Mean bias (top) and SD (bottom) for the lateral and axial velocity profiles as a function of the number N_e of HRIs used for the velocity estimation.

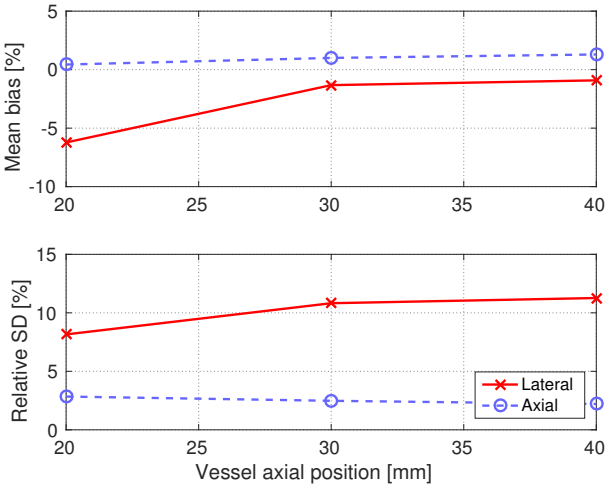

Figure 9.4: Mean bias (top) and SD (bottom) for the lateral and axial velocity profiles measured in the flow rig at depth from 20 to 40 mm.

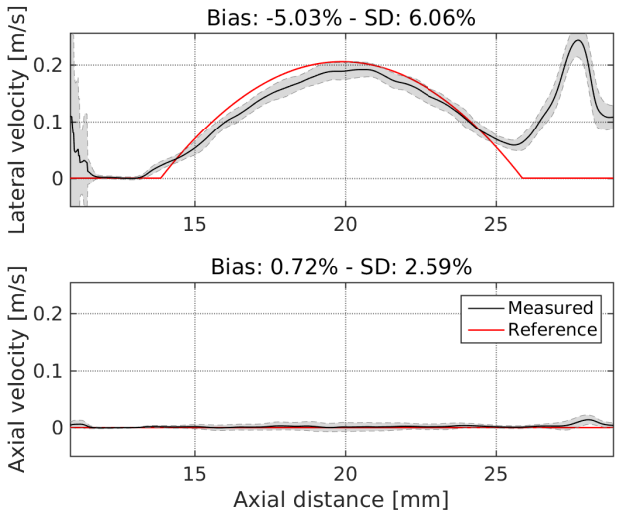

(a)

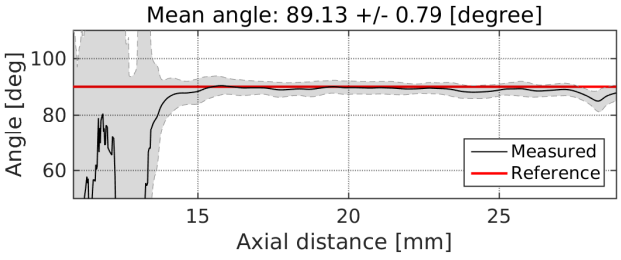

(b)

Figure 9.5: Measurement of a straight vessel with 90° flow angle and 20 mm depth. (a) Mean velocity profiles (black), SD (shaded region), and reference profiles (red) for the lateral (top) and axial (bottom) velocities; (b) Estimated angle.

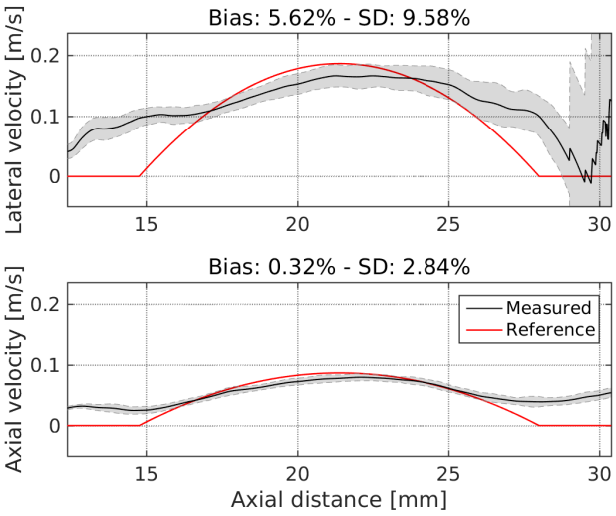

(a)

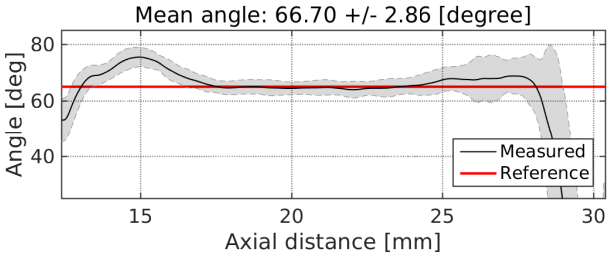

(b)

Figure 9.6: Measurement of a straight vessel with 65° flow angle and 20 mm depth. (a) Mean velocity profiles (black), SD (shaded region), and reference profiles (red) for the lateral (top) and axial (bottom) velocities; (b) Estimated angle.

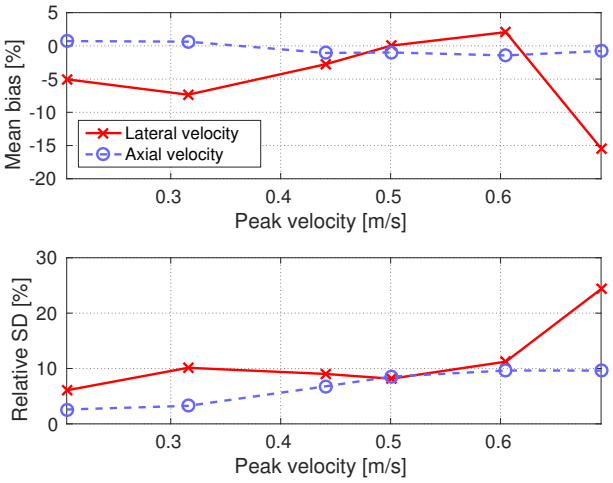

Figure 9.7: Mean bias (top) and SD (bottom) for the lateral and axial velocity profiles for peak velocities between 0.2 and 0.7 m s^{-1}. The velocities between 0.2 and 0.5 m s^{-1} were detected with PRF = 9 kHz, while for higher velocities the peak was kept equal to 0.5 m s^{-1} to avoid turbulent flow and the PRF was set to 7.5 and 6.4 kHz.

9.2 Pulsatile flow phantom

9.2.1 Setup

A pulsating flow was measured in an in-house fabricated phantom mimicking a common carotid artery. The vessel was immersed in tissue-mimicking material consisting of polyvinyl alcohol cryogel (S. S. M. Lai et al. 2013). The phantom was connected to a flow pump (CompuFlow 1000, Shelley Automation, Inc., Toronto, Ontario, Canada) circulating a blood-mimicking fluid. A carotid velocity profile was generated with a flow rate of 10 mL s^{-1}.

The same transducer and imaging sequence with the parameters in Table 8.1 and Table 8.2 were used for this measurement. The PRF was set to 15 kHz. The velocity ranges at the depth of 20 mm become

$$\begin{aligned} -0.18\,\mathrm{m\,s^{-1}} \leq \quad v_x \leq \quad 1.28\,\mathrm{m\,s^{-1}}, \\ -0.20\,\mathrm{m\,s^{-1}} \leq \quad v_z \leq \quad 0.20\,\mathrm{m\,s^{-1}}. \end{aligned} \tag{9.2}$$

The RF data were saved and the processing was performed off-line as explained in Sec. 8.2.2. Both stages of clutter filtering introduced in Sec. 8.1.2 were employed for this measurement, as the moving-average-subtraction filter alone failed to attenuate the tissue signal. To match the non-stationarity of the flow, $N_e = 16$ HRIs were used for the velocity estimation.

9.2.2 Results

In Fig. 9.8 the results of the pulsatile flow measurement are displayed during the late diastolic (9.8(a)) and peak systolic (9.8(b)) phases. The VFI and B-mode images are overlapped. The arrows in the VFI images show the local velocity vectors and the underlying colors encode the magnitudes and angles as shown in the color wheel in the bottom-right corner.

9.3 Intensities

The U.S. Food and Drug Administration (FDA) set regulatory limits for an imaging sequence in terms of intensity, mechanical index (MI), and transducer heating. These parameters must be measured before the sequence is used on humans (FDA 2008), and a procedure for conducting the measurements is reported in (Jensen, Rasmussen, et al. 2016).

The acoustic pressure in the 2-D imaging region can be sampled by using a hydrophone. The derated values are obtained by considering an attenuation of 0.3 dB/(MHz cm) at the center frequency f_0. The intensity is derived from the sampled acoustic pressure and averaged over time to obtain the temporal-average intensity I_{ta}. Its value at the position of maximum is referred to as spatial-peak-temporal-average intensity, which must satisfy

$I_{spta} \leq 720\,\mathrm{mW\,cm^{-2}}$ (FDA 2008). The MI must be below 1.9 and limits the maximum peak negative pressure. Finally, the probe surface temperature must be within the IEC limits (IEC 2015).

The safety parameters of the sequence were measured prior to the *in vivo* investigations. A calibrated hydrophone (Onda HGL-0400, Onda Corp., Sunnyvale, CA, USA) was connected to the AFE of the SARUS research scanner and moved in a water bath using an Acoustic Intensity Measurement System AIMS III (Onda Corp., Sunnyvale, CA, USA). The hydrophone signals where acquired while the imaging sequence was run. The PRF was set to 500 Hz to avoid reverberations in the water tank.

The measured I_{ta} is reported in Fig. 9.9(a). The derated I_{spta} at (2.5, 20) mm is $12.34\,\mathrm{mW\,cm^{-2}}$. For PRF = 15 kHz, the intensity is, therefore, $305.7\,\mathrm{mW\,cm^{-2}}$. The derated MI is displayed in Fig. 9.9(b) and is equal to 0.93 at (−5, 5) mm. Therefore, the FDA regulations are satisfied for this sequence. The temperature was also measured at the transducer surface and was verified to be within the regulatory limits.

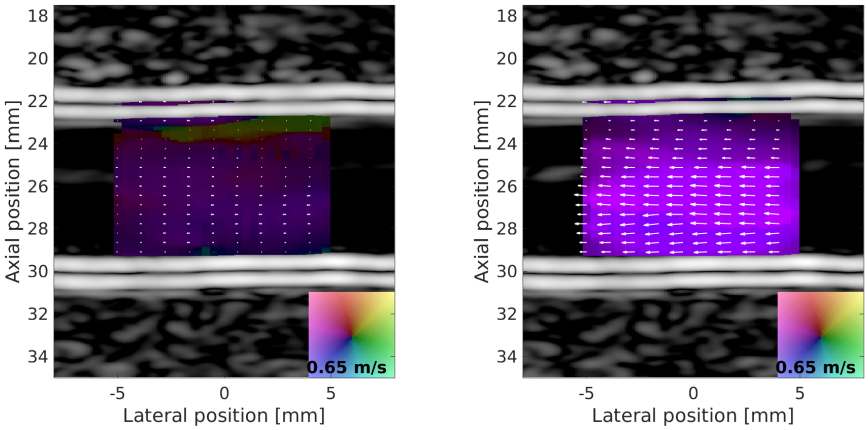

Figure 9.8: VFI plot of a pulsatile flow phantom mimiking a common artery during the late diastolic (a) and peak systolic (b) phases.

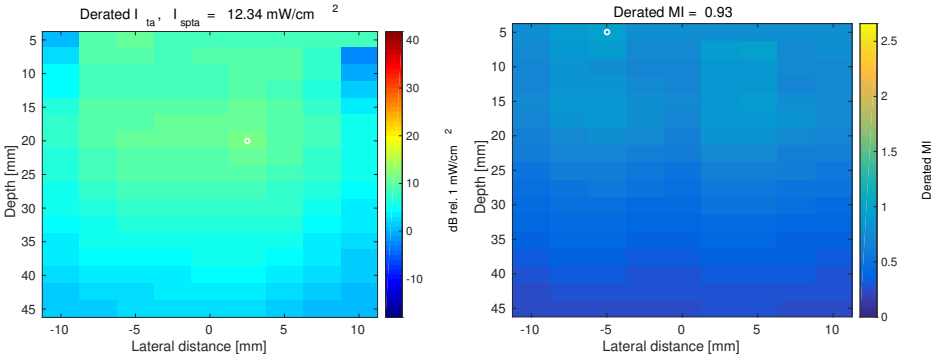

(a) (b)

Figure 9.9: (a) Measured I_{ta}. The derated I_{spta} at the point (2.5,20) mm is 12.34 mW cm^{-2}. For PRF $=$ 15 kHz, the intensity is 305.7 mW cm^{-2}. (b) Derated MI equal to 0.93 at the point ($-$5,5) mm. Both parameters are within the FDA limits.

9.4 *In vivo* investigations

In vivo measurements were carried out to investigate the performance of the method with realistic hemodynamic conditions. The same transducer and imaging sequence of Table 8.1 and Table 8.2 were used, with a repetition frequency $PRF = 15\,\text{kHz}$. Sequences of 9.5 s of RF data were saved, and the processing was carried out off-line as described in Sec. 8.2.2. Sixteen HRIs were used for each flow estimation. The velocity estimates were shown with a frame rate of 350 frames per second (FPS). However, according to the emission sequence only $PRF_{eff}/N_e = 134\,\text{FPS}$ were completely independent. The velocity estimates were filtered using a median filter in a temporal window of 25 ms and a spatial window of $1 \times 1\,\text{mm}^2$. The frame rate of the B-mode video was 33 FPS. A binary mask was generated from the B-mode images to discriminate the vessel area from the surrounding tissue. The VFI video was paced down by a factor 14.

9.4.1 Common carotid artery

A measurement was performed after approval by the Danish National Committee on Biomedical Research Ethics. The right common carotid artery of a healthy 28-year-old volunteer was scanned with a longitudinal view by an experienced radiologist. The volunteer was asked to rest in a supine position for approximately 10 min before the measurement to ensure steady flow conditions.

9.4.1.1 Results

The results of the *in vivo* measurement are shown in Fig. 9.10. In Fig. 9.10(a) and 9.10(b), the B-mode and VFI images are shown at late diastole and peak systole, respectively. The velocity magnitude at the position indicated by the yellow circle in Fig. 9.10(a) is displayed in Fig. 9.10(c) for nine cardiac cycles. The red and magenta dots show the times at which the velocities are plotted in the top figures. The mean PSV from the nine heart cycles is $0.62\,\text{m}\,\text{s}^{-1}$ with a SD of 2.9%.

The nine cycles in Fig. 9.10(c) were aligned by finding the peaks of the cross-correlation functions to calculate the mean profile and the relative SD plotted in Fig. 9.11. The relative SD averaged over a cardiac cycle is 4.33%.

9.4.2 Carotid bifurcation

The carotid bifurcation of a 54-year-old female volunteer with no history of cardiovascular disease was scanned by an experienced radiologist with the volunteer in supine position. The volunteer was asked to rest for approximately 10 min to ensure more stationary flow conditions. The objective of this study was to demonstrate the ability of the method to reveal complex and fast hemodynamic patterns like vortices and turbulence, when the host system allows for high-frame-rate processing of the velocity data. The formation of vortices and turbulence is associated with low or oscillatory WSS, and their visualization

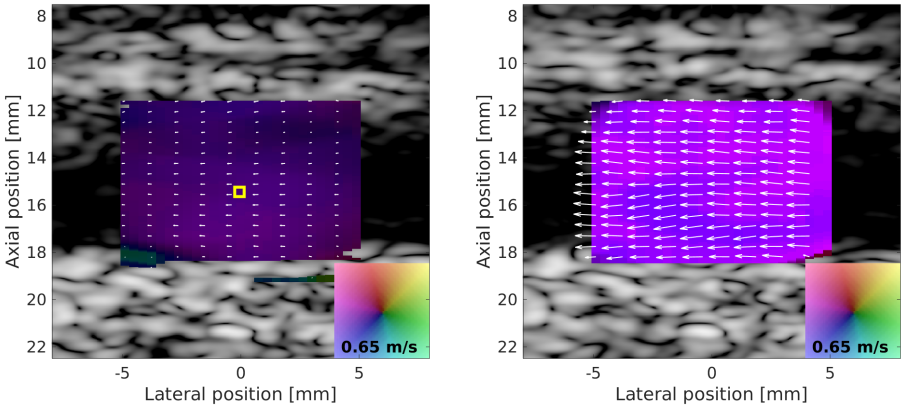

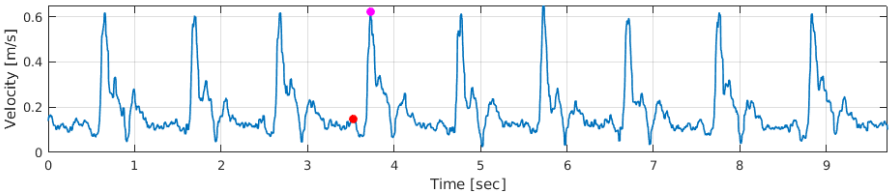

Figure 9.10: VFI plot of a common carotid artery at late diastole (a) and peak systole (b) measured *in vivo*. In (c), the velocity magnitude at the position indicated by the yellow circle in (a) is displayed as a function of the time for the nine measured cardiac cycles. The red and magenta circles show the times at which the VFI images are plotted. The mean PSV from the nine cycles is $0.62\,\mathrm{m\,s^{-1}}$ with a SD of 2.9%.

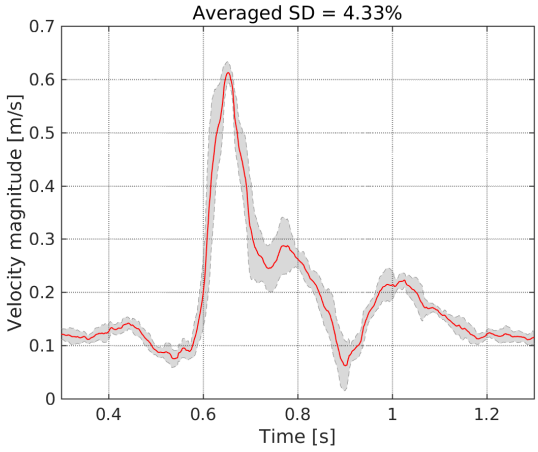

Figure 9.11: Mean profile and relative SD calculated from 9 cardiac cycles measured in the common carotid artery *in vivo*. The relative SD averaged over a cardiac cycle is 4.33%.

is relevant for the early identification and prediction of atherosclerosis, as discussed in Sec. 6.3. For further details on this study, readers are referred to Paper IV in appendix.

9.4.2.1 Results

A VFI frame is shown in Fig. 9.12(a) during the systolic phase. Figure 9.12(b) displays the velocity magnitude as a function of the time at the locations A and B in the left figure. The point A was selected in the common tract and B in the internal carotid artery (ICA). The mean PSV calculated in A from the 10 cardiac cycles is 0.76 m s^{-1} with a SD of 6.1%. The EDV was calculated by averaging the velocities in the period between 70% and 90% of the cardiac cycle, and the mean over the 10 cycles is 0.15 m s^{-1}. The SD was calculated relative to the mean EDV and is equal to 12.3%. The mean PSV in B is 0.77 m s^{-1} with a SD of 9%. A more turbulent flow and the occurrence of out-of-plane motion can be the reasons for the slightly higher SD registered at the ICA. The velocity field is available at any time everywhere in the image, and multiple profiles like the ones in Fig. 9.12(b) can be obtained in a multi-gated approach without the need for additional adjustments by the operator.

A low-velocity vortex can be identified in the bulb of the ICA and is displayed in Fig. 9.13 from the same VFI frame in Fig. 9.12(a). The vortex is consistent with the findings of previous studies (Hansen et al. 2008).

The mean velocity profile and SD were calculated by aligning the 10 cardiac cycles in the point A and are displayed in Fig. 9.14. The relative SD averaged over one cycle is 7.86%. The velocity profile can be compared with the spectral Doppler reported in

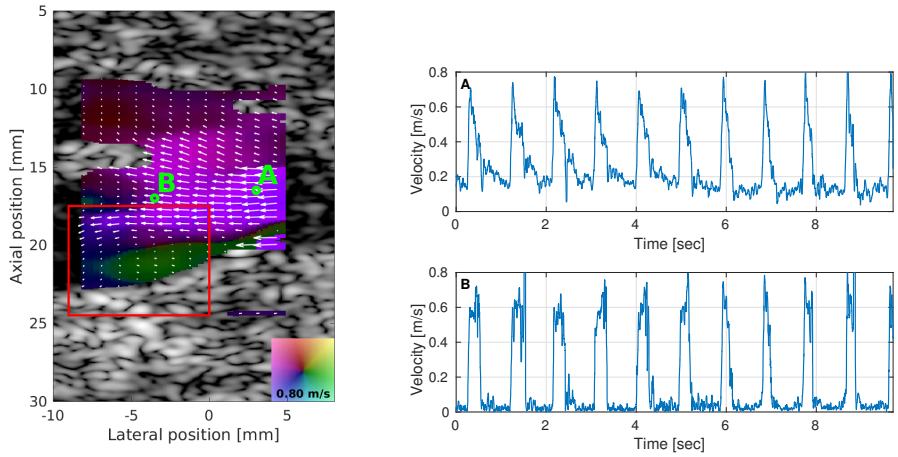

(a) (b)

Figure 9.12: (a) VFI frame measured *in vivo* during the systolic phase. A low-velocity vortex is observed in the bulb of the ICA; (b) velocity magnitude as a function of the time in the points A (top) and B (bottom) indicated in (a). The velocity is shown for 10 cardiac cycles.

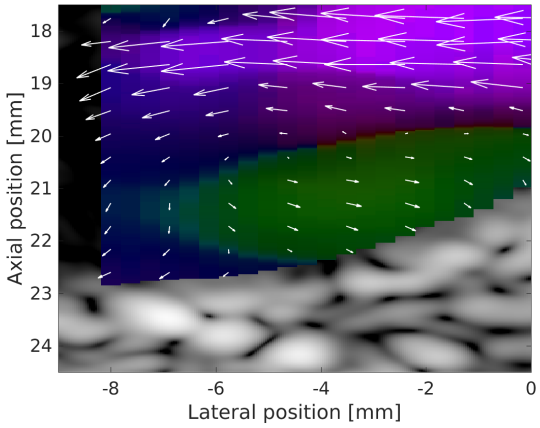

Figure 9.13: Vortex formed in the ICA in the red rectangle in Fig. 9.12(a).

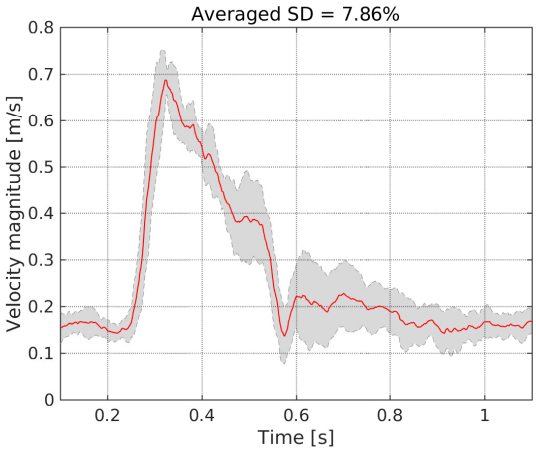

Figure 9.14: Mean profile and relative SD calculated from 10 cardiac cycles measured in the point A (ICA) in Fig. 9.12(b). The relative SD averaged over a cardiac cycle is 7.86%.

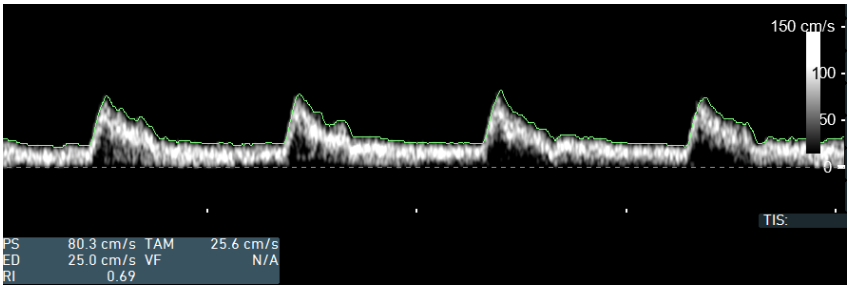

Figure 9.15: Spectral Doppler measured with a BK Ultrasound commercial platform as a baseline for the VFI velocity in the common carotid artery. The reported PSV and EDV are $0.803\,\mathrm{m\,s^{-1}}$ and $0.25\,\mathrm{m\,s^{-1}}$.

Fig. 9.15 measured with a BK Ultrasound commercial platform. It can be noted that the two waveforms are well correlated. The PSV and EDV reported by the commercial scanner at the common carotid artery are $0.80\,\mathrm{m\,s^{-1}}$ and $0.25\,\mathrm{m\,s^{-1}}$, respectively, and are slightly overestimated compared with the VFI velocities, as it expected because of spectral broadening.

9.5 Real time implementation on a commercial tablet

The VFI method presented in this thesis was implemented on a consumer level tablet to investigate the feasibility of the processing in the built-in GPU concurrent with the transmission of the data over Wi-Fi. The work was in collaboration with the Visual Computing Lab, Alexandra Institute. Further details on the implementation can be found in Paper III in appendix.

9.5.1 Methods

The emissions from the flow rig acquisition at 90° and 0.2 m s^{-1} displayed in Fig. 9.5 were beamformed in MATLAB to create the LRLs. These were re-sampled at 20 MHz and sent to a Nexus 9 tablet (HTC Corp., Taoyuan, Taiwan) through a Wi-Fi link to simulate a wireless probe. The connection was established through an ASUS RT-AC68U (ASUS, Taipei, Taiwan) router with a maximum theoretical link speed of 867 Mbit/s.

B-mode and VFI processing were performed on the tablet's built-in GPU, a Tegra K1 (NVIDIA Corp., Santa Clara, CA, USA) with 192 shader cores and 2 GB DDR3 RAM. The LRLs were buffered into the tablet's memory and then sent to the SSB. Sixteen HRIs of 32×512 samples were used for each velocity estimation.

The GPU was instructed to perform general purpose computations through the OpenGL ES 3.1 API. For further details on the GPU processing, readers are referred to Paper III in the appendix.

9.5.2 Results

The 2-D VFI images are shown in Fig. 9.16 relative to one frame processed in the tablet (9.16(a)) and in Matlab (9.16(b)) for comparison. The VFI and B-mode images are overlapped. The arrows show the velocity vectors, and the angle is shown encoded as in the color wheel in the bottom of the images. The 2-D velocities were calculated in a region of 0.8 cm $\times$ 1.9 cm.

The mean velocity profile and the SD are shown in Fig. 9.17(a) calculated from 50 profiles at the center of the VFI image processed in the tablet. The lateral velocity is displayed on the top ad the axial velocity on the bottom. The average bias is 2.91% in the lateral direction and 0.93% in the axial direction. The SD is 10.13% and 3.51% for the two velocity components. The estimated angle is shown in Fig. 9.17(b), with a mean value of $88.08 \pm 2.74°$. The velocity and angle profiles can be compared with the ones in Fig. 9.5.

The combined VFI and B-mode peak frame rate was 26 FPS, which is sufficient for real-time performance. The corresponding data rate of LRLs that are sent over the Wi-Fi link is 13 MB/s for 1648 16-bit samples per LRL. This was lower than the average throughput of 30 MB/s measured between the tablet and the Wi-Fi router. Hence, the operational rate of the entire system is limited by the GPU processing speed rather than the data bandwidth.

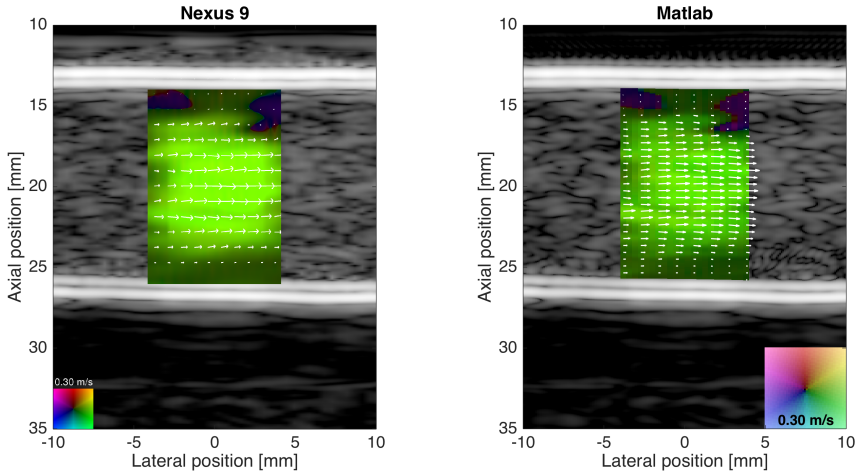

Figure 9.16: 2-D VFI frames processed in the tablet (a) and in Matlab (b). The VFI and B-mode images are overlapped. The arrows show the velocity vectors, and the angle is shown encoded as in the color wheel in the bottom of the images.

In a previous study with the same tablet model, heating issues were met when the GPU and network card operated concurrently at nearly the maximum load (Hemmsen et al. 2015). In order to test whether this is the case for the present implementation, continuous scanning simulations were carried out during several minutes. The benchmark covered data input from a) a pre-recorded dataset stored on the device and b) the Wi-Fi link. The resulting processing frame rate is shown in Fig. 9.18 as a function of the time. The frame rate was lowered significantly after a few minutes of combined GPU and network load and was below 15 fps after approximately 11 min of continuous scanning. To demonstrate that the drop in processing performance was due to thermal throttling, an external cooler was activated after approximately 12 min from the start of the simulation, and the peak frame rate was therefore restored after few minutes of cooling. Note that the thermal issues are less severe if the data are read from the memory and the network card is idle.

This study demonstrates that the presented 2-D VFI method can be implemented on a commercially available tablet, and real-time processing can be performed concurrent with the wireless transmission of the data. The frame rate is suitable for real-time imaging, also taking into account that the tablet and the built-in GPU were 2 years old. Therefore, it is likely that significantly better performance can be achieved by using a state-of-the-art

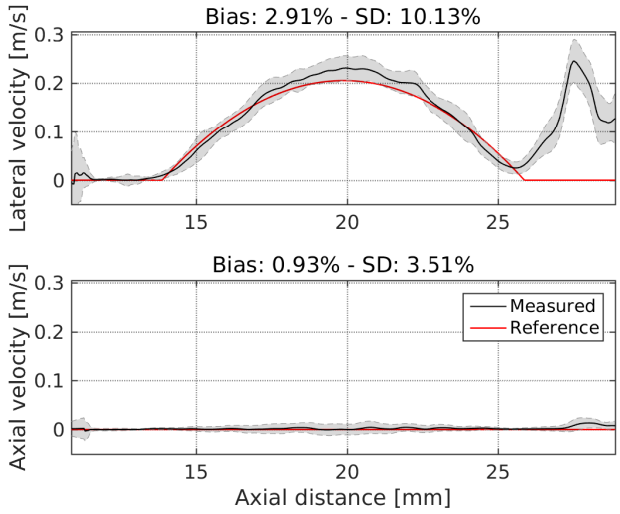

(a)

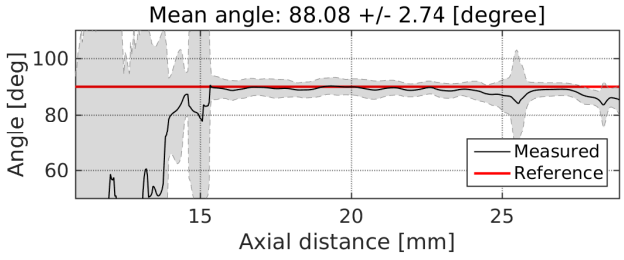

(b)

Figure 9.17: Tablet processing of the velocity data in Fig. 9.5. (a) Mean velocity profiles (black), SD (shaded region), and reference profiles (red) for the lateral (top) and axial (bottom) velocities; (b) Estimated angle.

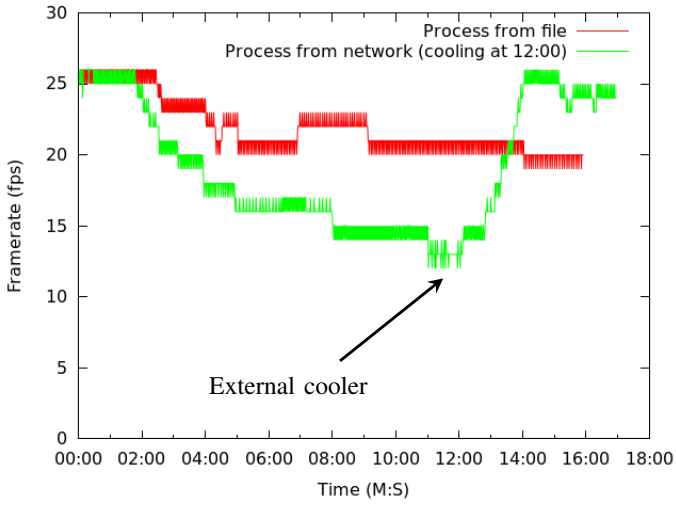

Figure 9.18: Processing framerates for continuous operation with data input from a local file (red) and from a Wi-Fi network (green). An external cooler was activated after 12 min for the Wi-Fi case.

device.

Under the same network conditions of this demonstration, 2.2 s are needed at an average data rate of 30 MB/s to transmit the LRLs necessary for the maximum frame of 134 FPS. Therefore, a memory buffer would be needed in-handle in case of operation at such frame rate.

9.6 Limitations and additional considerations

9.6.1 PSF distortions

The motion of the scatterers during the time of acquisition of an HRI is the reason for the occurrence of distortions in the PSF. In Fig. 9.19, the 2-D PSF is displayed in the top graph for a static scatterer at $(x = 0, z = 20)$ mm, and in the bottom graph for a scatterer moving around the same location with a velocity magnitude of –0.6 m s^{-1} in direction $\theta = 45°$. The PSFs were simulated in Field II with a pulse repetition frequency of 9 kHz.

It is evident that the movement introduces a lateral shift of the PSF and enhances the energy of the sidelobes due to the incoherent summation of the LRLs. The lateral signals for the static and in-motion cases are shown respectively in the top and bottom plots of Fig. 9.20, sampled along the red dashed line in Fig. 9.19. A lateral shift of approximately 1.3 mm in the positive direction can be identified by comparing the two signals. In Fig. 9.21, the lateral signals are displayed sampled along the blue dashed line in Fig. 9.19. The maximum amplitude of the right lobe is approximately three times higher in case of motion respect to the static case. These factors are disruptive for both the accuracy and precision of the velocity estimator and are more prominent for increasing velocities.

To restore the undistorted PSF, motion compensation approaches may be employed. However, the situation is complicated here by the dual-stage beamforming approach,

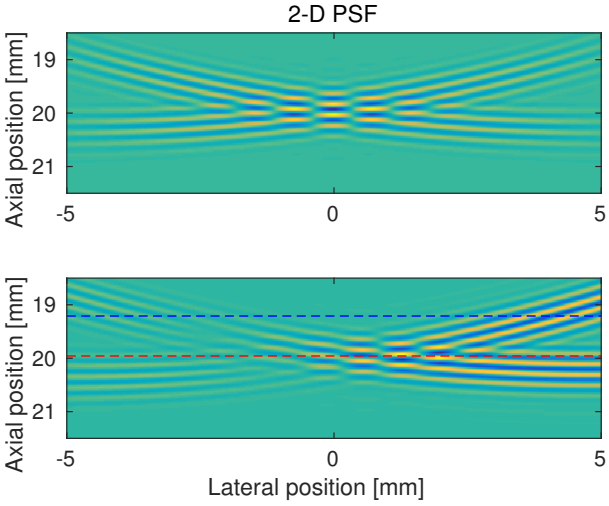

Figure 9.19: 2-D PSF for a static scatterer at $(x = 0, z = 20)$ mm (top) and for a scatterer moving around the same location with a velocity magnitude of -0.6 m s^{-1} in direction $\theta = 45°$ (bottom).

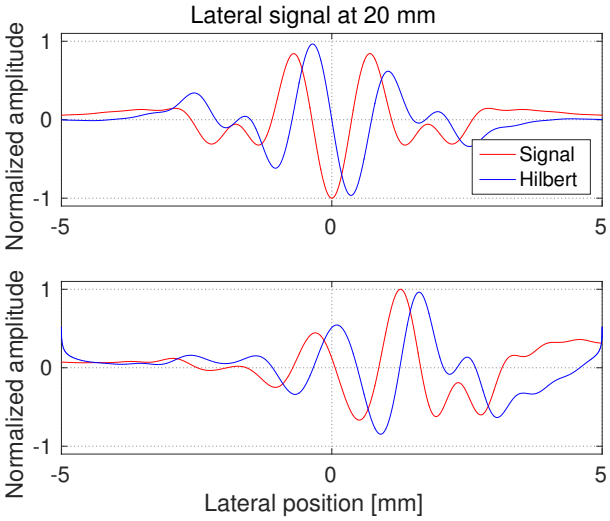

Figure 9.20: Lateral signals for the static (top) and in-motion (bottom) cases sampled along the red dashed line in Fig. 9.19. A lateral shift of approximately 1.3 mm in the positive direction can be identified.

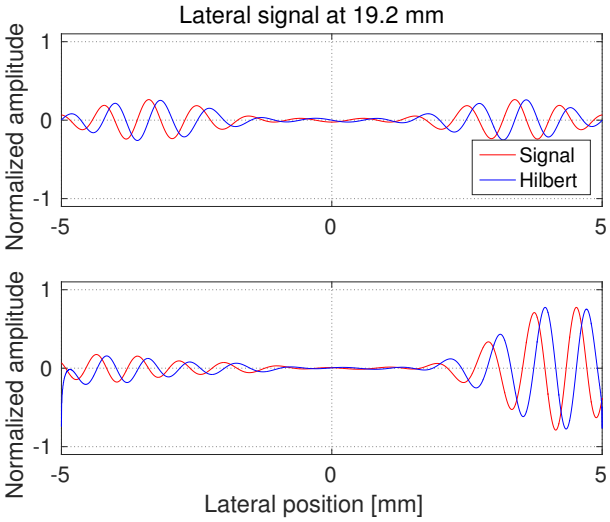

Figure 9.21: Lateral signals for the static (top) and in-motion (bottom) cases sampled along the blue dashed line in Fig. 9.19. The maximum amplitude of the right lobe is approximately three times higher in case of motion respect to the static case.

which does not give access to the RF element data. Due to the integration operated by the first stage beamformer, each sample in the LRL carries information from a collection of points along an arc. In general, these points experience motion in different directions and with different magnitudes, therefore the velocity estimated at a given sample is the average velocity over the full arc. For this reason, it is challenging to estimate the motion by using correlation techniques such as the ones proposed in (Denarie et al. 2013; Gammelmark and Jensen 2014) on the LRLs. Alternative Tx/Rx sequences may be considered to minimize the amount of emissions K and, in turn, the motion-induced distortions.

9.6.2 Aliasing correction

The conventional phase-shift estimator in (6.5) is affected by aliasing because of the periodicity of the phase over intervals of 2π radians. The periodicity causes an ambiguity on the estimated velocity, which can be solved by taking into account the magnitude of the autocorrelation as shown by Lai *et al.* (X. Lai, Torp, and Kristofferson 1997).

The lag-1 autocorrelation function can be written in a general form as

$$R(\tau,1)=\frac{1}{N_z}\frac{1}{N_e-1}\sum_{n=-N_z/2}^{N_z/2-1}\sum_{e=0}^{N_e-2}s(n,e)^*s(n+\tau,e+1), \tag{9.3}$$

where the dependence on the lag τ is expressed. The function in (9.3) is calculated from N_z axial samples and N_e emissions. It can be noted that (9.3) and 6.6 are equivalent if $N_z=1$ and $\tau=0$.

The relation between the phase of (9.3) and the time delay is

$$\angle R(0,1)+2k\pi=-2\pi f_0\tau_k, \qquad k=0,\pm1,\pm2,..., \tag{9.4}$$

where the values of τ_k are the possible time delay candidates. It is, therefore, not possible to determine the true time shift $\tau=t_s$ without uncertainty in case $|-2\pi f_0 t_s|>|\pi|$. However, it is known from Sec. 6.1.1 that a maximum is found in the envelope of the correlation function for $\tau=t_s$, and this information can be employed to solve the ambiguity.

In the extended autocorrelation method, the true time shift is determined by finding the value of τ_k that maximizes the magnitude of (9.3). The situation is depicted in Fig. 9.22 for the same signals of Fig. 6.2(a). The top and bottom plots show the magnitude and phase of the correlation function in a situation where aliasing occurs. The delay τ_0 is the one provided by the conventional autocorrelation estimator and does not correspond to the true time shift t_s. However, by examining the amplitude in the points τ_{-1}, τ_0, and τ_{+1}, a maximum is found for $k=+1$ and the correct time shift can be determined as

$$t_s=\tau_{+1}=-\frac{\arctan(R(0,1))}{2\pi f_0}-\frac{1}{f_0} \tag{9.5}$$

without the need to calculate the full correlation function.

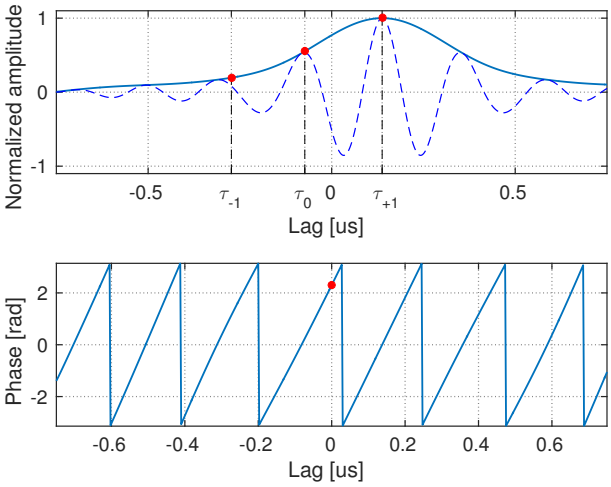

Figure 9.22: Magnitude (top) and phase (bottom) of the correlation function in a situation where aliasing occurs. The delay τ_0 is the one provided by the conventional autocorrelation estimator and does not correspond to the true time shift t_s. By examining the amplitude in the points τ_{-1}, τ_0, and τ_{+1}, a maximum is found for $k = +1$ and the correct time shift can be determined.

The extended autocorrelation approach has been adapted to the estimator in (7.11) and (7.11) to extend the range of detectable velocities. The results are shown in Fig. 9.23 for the flow rig measurement with peak velocity 0.5 m s^{-1} and $PRF = 6.4$ kHz. The bias is lowered from -15.43% to -0.28% and the SD from 24.35% to 10.45% by using the extended approach. The method has been tested only on flow rig data.

9.7 Discussion

A VFI method was presented combining SASB and DTO to suit the computational requirements and data rates of a portable scanner. The method creates HRIs from as few as six emissions, which are beamformed in fixed Tx/Rx foci based on the sequential beamforming approach. A single line per emission must be transferred from the probe to the host system if the first beamformer is integrated in the probe handle. A TO is created in the HRIs due to the spatial distribution of the VSs, which allows for a relatively inexpensive velocity estimation based on a 2-D phase-shift approach.

The performance of the method was investigated with simulations and measurements of a constant flow. A lateral mean bias between -5% and -6.2% was achieved, with a SD between 6% and 9.6% for beam-to-flow angles from 65° to 90°. The axial mean bias was

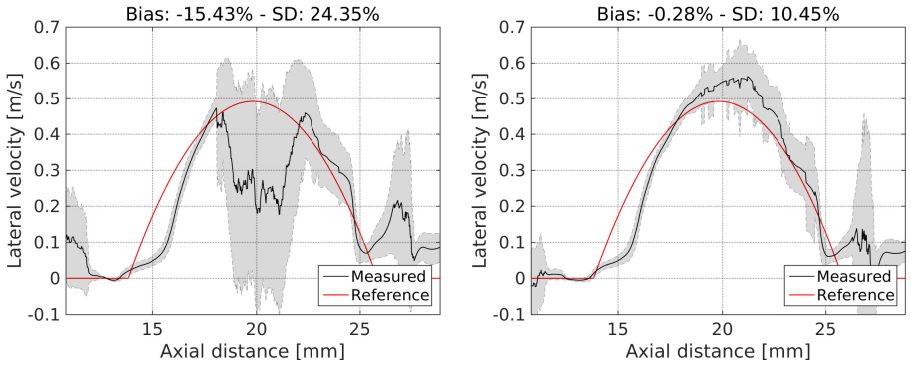

(a) (b)

Figure 9.23: Results obtained with the conventional (left) and extended (right) auto-correlation approaches for the flow rig measurement with peak velocity 0.5 m s^{-1} and $PRF = 6.4$ kHz.

lower than 1% with a SD around 2%. The method was then tested with pulsating flow in a phantom mimicking a carotid artery, and the intensities of the emission sequence were measured prior to the *in vivo* experiments to verify the compliance with FDA regulations.

The scan of the common carotid artery of a 28-year-old volunteer was performed to evaluate the potential of the method *in vivo*. The mean PSV from nine heart cycles was 0.62 m s^{-1} with a SD of 2.9%. An average relative SD of 4.33% was obtained averaged over one cycle. Measurements of a carotid bifurcation demonstrated the ability of the method to reveal complex flow patterns like vortices and turbulence with a frame rate of 134 FPS. In addition, the availability of the velocity data everywhere in the image at any time makes it possible to visualize multiple velocity profiles in a multi-gated approach with no need for manual angle adjustments, with potential benefit for the operator's workflow.

The method has been developed with the objective to integrate quantitative flow measurements in wireless systems. A proof-of-concept demonstration of the feasibility of concurrent wireless transmission and processing in a commercially available tablet was carried out, achieving a peak frame rate of 26 FPS, which is suitable for real-time flow imaging, and a data rate of 14 MB/s.

A number of drawbacks were identified for the proposed approach. The sequential acquisition of the HRI over six emissions causes distortions in the PSF due to the inter-emission motion of the scatterers. Also, the decorrelation is increased because of the longer time between successive HRIs. These factors negatively affect the accuracy and

precision of the velocity estimator. Nevertheless, the major limitation is the aliasing of both lateral and axial velocity components caused by the periodicity of the phase over intervals of 2π radians. A possible solution to extend the velocity range was tested with data from aliased flow measurements. The bias and SD were restored almost perfectly, and future research will address the implementation of this strategy for *in vivo* measurements.

CHAPTER 10

Project conclusion and perspectives

In this thesis, hardware strategies and imaging methods were investigated towards the development of a wireless ultrasound system. The overall infrastructure providing the foundation and motivation for this work is the so-called *app-based* ultrasound concept. The idea is to perform the sensing of the ultrasound data using a probe linked to general-purpose, mobile devices like smartphones or tablets, where the processing and visualization are performed. Advantages of this approach are the reduced upfront costs of the ultrasound system and the consequent potential to permeate any medical specialty out of the radiology department.

The data bandwidth between the probe and the outside world can be significantly reduced by using the SASB focusing approach, upon which all the demonstrations included in this thesis were based.

In the first part of the manuscript, the problem of the reduction of the hardware complexity required to suit the restricted power budget of an hand-held ultrasound system was addressed. Beamforming strategies were introduced, which provide significant architectural simplifications of the AFE and beamformer. Analog and digital solutions were considered, including a gradient beamformer and single-bit digital approaches. The quality of the B-mode image in terms of noise, resolution, and contrast was tested through simulations of several designs from a system-level point of view. The objective of this study was to provide the IC designers with first-order specifications necessary to start the development of a wireless probe with integrated electronics. The work led to the fabrication of an ASIC single-bit ADC with low power consumption and circuit area, and the design of a 192-element convex probe. The probe is linked to an external host device via a USB-C interface, which allows for data and power transfer to and from the host system. Currently, the possibility of transmission through Wi-Fi link is not included, and additional challenges must be faced towards the development of a wireless system. In particular, the use of a battery sets tighter conditions in terms of power consumption, weight, and circuit area.

The second part of the thesis investigated the feasibility of VFI in a hand-held system. A 2-D VFI method was developed by combining SASB and DTO to obtain the wireless transmission of the data along with a relatively inexpensive velocity estimation. Simulations and measurements in a controlled flow environment were firstly carried out to characterize the performance. The bias was lower than 6% for the lateral velocity and 1% for the axial velocity, and the SD was respectively lower that 10% and 2%. *In vivo* measurements were performed to show the ability of the method to reveal complex flow

dynamics. The frame rate of 134 FPS was sufficient for the visualization of a low-velocity vortex forming in the ICA during the systolic phase. Finally, the implementation on a commercially available tablet demonstrated the possibility of real-time wireless transmission and GPU processing, with a peak frame rate of 26 FPS and data rates compatible with current Wi-Fi technology.

The integration of the VFI feature in hand-held scanners has the potential to improve the clinical workflow. A highly flexible framework can be implemented based on the methods investigated in this thesis, where real-time processing is firstly performed on the host device (tablet), and more complex and advanced imaging modalities can be retrospectively attained by sending the data to a third processing system, e.g. exploiting the potential of cloud computing. Under the network conditions of the demonstrations in Sec. 9.5, 2.2 s are needed to transfer the data necessary for a frame rate of 134 FPS through Wi-Fi. Therefore, real-time transmission would not be possible and a memory buffer would be necessary in-handle. However, the data rates of Wi-Fi protocols are progressively increasing. More efficient, reliable, and modular algorithms must be also investigated to optimize the processing in distributed computing resources.

The velocity field is accessible everywhere in the image at any time, and it has been proposed in Ch. 9 to directly display velocity profiles in a multi-gated approach similar to that previously shown in (Ricci, Bassi, and Tortoli 2014). Clinically relevant measures like PSV and EDV can be directly derived from the velocity, being the frame rate sufficient to capture fast dynamics like systolic peaks. In addition, the method does not require manual angle adjustments and can potentially reduce the variability and the sources of error in the detection of velocity measures (Lui et al. 2005).

It is to be verified, however, whether the velocities provided by the proposed method are comparable with the state-of-the-art represented by spectral Doppler. This is an open research question that should be addressed in the future. Similar studies were performed in (Tortoli et al. 2015) and (Pedersen et al. 2012). A broader population should be taken into consideration in a pre-clinical validation study to evaluate the performance from a statistical perspective. The limited velocity range is expected here to be a significant complication, and a possible solution is represented by the extended autocorrelation approach. However, the implementation has not yet been tested with *in vivo* data.

Bibliography

References from Chapter 1

Edler, I. and C. H. Hertz (1954). "The use of ultrasonic reflectoscope for the continuous recording of the movement of heart walls". In: *Kungl. Fysiogr. Sällskap. i Lund Föhandl* 24, pp. 40–58 (cit. on p. 1).

Filly, R. A. (2003). "Is It Time for the Sonoscope? If So, Then Let's Do It Right". In: *J. Ultrasound Med.* 22, pp. 323–325 (cit. on p. 1).

Greenbaum, L. D. (2003). "It Is Time for the Sonoscope". In: *J. Ultrasound Med.* 22, pp. 321–322 (cit. on p. 1).

Harris, R. D. and W. M. Marks (2009). "Compact ultrasound for improving maternal and perinatal care in low-resource settings: review of the potential benefits, implementation challenges, and public health issues." In: *Journal of Ultrasound in Medicine* 28, pp. 1067–1076 (cit. on p. 2).

Jensen, J. A. (1996). *Estimation of Blood Velocities Using Ultrasound: A Signal Processing Approach*. New York: Cambridge University Press (cit. on p. 1).

Kirkpatrick, A. W., M. Sirois, K. B. Laupland, D. Liu, K. Rowan, C. G. Ball, S. M. Hameed, R. Brown, R. Simons, S. A. Dulchavsky, D. R. Hamiilton, and S. Nicolaou (2004). "Hand-held thoracic sonography for detecting post-traumatic pneumothoraces: the extended focused assessment with sonography for trauma (EFAST)". In: *J. Trauma* 57.2, pp. 288–295 (cit. on p. 2).

Lafitte, S., N. Alimazighi, P. Reant, M. Dijos, A. Zaroui, A. Mignot, M. Lafitte, X. Pillois, R. Roudaut, and A. D. Maria (2011). "Validation of the smallest pocket echoscopic device's diagnostic capabilities in the heart investigation". In: *Ultrasound Med. Biol.* 37.5, pp. 798–804 (cit. on p. 2).

Lapostolle, F., T. Petrovic, G. Lenoir, J. Catineau, M. Galinski, J. Metzger, E. Chanzy, and F. Adnet (2006). "Usefulness of hand-held ultrasound devices in out-of-hospital diagnosis performed by emergency physicians". In: *Am. J. Emerg. Med.* 24.2, pp. 237–242 (cit. on p. 2).

Liu, S., W. Chang, C. Huang, T. Weng, H. Matthew, and W. Chen (2005). "The value of portable ultrasound for evaluation of cardiomegaly patients presenting at the emergency department". In: *Resuscitation* 64.3, pp. 327–331 (cit. on p. 2).

Ludwig, G. D. and F. W. Struthers (1949). *Considerations underlying the use of ultrasound to detect gallstones and foreign bodies in tissue*. Project N. NM 004 001 - Report N. 4. United States Naval Medical Research Institute Reports (cit. on p. 1).

Mehta, M., T. Jacobson, D. Peters, E. Le, S. Chadderdon, A. J. Allen, A. B. Caughey, and S. Kaul (2014). "Handheld Ultrasound Versus Physical Examination in Patients Referred for Transthoracic Echocardiography for a Suspected Cardiac Condition". In: *J. Am. Coll. Cardiol. Img.* 7.10, pp. 983–990 (cit. on p. 2).

Prinz, C. and J. U. Voigt (2011). "Diagnostic Accuracy of a Hand-Held Ultrasound Scanner in Routine Patients Referred for Echocardiography". In: *J. Am. Soc. Echocardiog.* 24.2, pp. 111–116 (cit. on p. 2).

Razi, R., J. R. Estrada, J. Doll, and K. T. Spencer (2011). "Bedside Hand-Carried Ultrasound by Internal Medicine Residents Versus Traditional Clinical Assessment for the Identification of Systolic Dysfunction in Patients Admitted with Decompensated Hearth Failure". In: *J. Am. Soc. Echocardiog.* 24.2, pp. 1319–1324 (cit. on p. 2).

Roelandt, J. (2002). "A personal ultrasound imager (ultrasound stethoscope) - A revolution in physical cardiac diagnosis!" In: *Eur. Heart J.* 23.7, pp. 523–527 (cit. on p. 1).

Schleder, S., L. Dendl, A. Ernstberger, M. Nerlich, P. Hoffstetter, E. Jung, P. Heiss, C. Stroszczynski, and Schreyer (2013). "Diagnostic value of a hand-carried ultrasound device". In: *Emerg. Med. J.* 30.3, pp. 1–5 (cit. on p. 2).

Seward, J. B., P. S. Douglas, R. Erbel, R. E. Kerber, I. Kronzon, H. Rakowski, D. J. Sahn, E. J. Sisk, A. J. Tajik, and S. Wann (2002). "Hand-Carried Cardiac Ultrasound (HCU) Device: Recommendations Regarding New Technology. A Report from the Echocardiography Task Force on New Technology of the Nomenclature and Standard Committee of the American Society of Echocardiography". In: *J. Am. Soc. Echocardiog.* 15, pp. 369–373 (cit. on p. 2).

Sicari, R., M. Galderisi, J. U. Voigt, G. Habib, J. L. Zamorano, P. Lancellotti, and L. P. Badano (2011). "The use of pocket-size imaging devices: a position statement of the European Association of Echocardiography". In: *European Journal of Echocardiography* 12, pp. 85–87 (cit. on p. 2).

Sippel, S., K. Muruganandan, A. Levine, and S. Shah (2011). "Review article: Use of ultrasound in the developing world". In: *Int. J. Emerg. Med.* 72.4 (cit. on p. 2).

Szabo, T. L. (2014). *Diagnostic ultrasound imaging: Inside out*. 2nd ed. Elsevier (Oxford, UK) (cit. on p. 1).

Wild, J. J. (1950). "The use of ultrasonic pulses for the measurement of biologic tissues and the detection of tissue density changes". In: *Surgery* 27, pp. 183–188 (cit. on p. 1).

References from Chapter 2

Ahn, S., J. Kang, P. Kim, G. Lee, E. Jeong, W. Jung, M. Park, and T. Song (2015). "Smartphone-based portable ultrasound imaging system: Prototype implementation and evaluation". In: *Proc. IEEE Ultrason. Symp.* Pp. 1–4 (cit. on p. 10).

AIUM (1995). *Quality Assurance Manual for Gray-Scale Ultrasound Scanners, Stage 2*. Tech. rep. American Institute of Ultrasound in Medicine, Bethesda, Maryland (cit. on p. 11).

Austeng, A. and S. Holm (2002). “Sparse 2-D Arrays for 3-D Phased Array Imaging - Design Methods”. In: *IEEE Trans. Ultrason., Ferroelec., Freq. Contr.* 49.8, pp. 1073–1086 (cit. on p. 14).

Chebli, R. and M. Sawan (2007). “Fully Integrated High-Voltage Front-End Interface for Ultrasonic Sensing Applications”. In: *IEEE Trans. Circuits Syst. I, Reg. Papers* 54.1, pp. 179–190 (cit. on p. 14).

Fuller, M. I., K. Owen, T. N. Blalock, J. A. Hossack, and W. F. Walker (2009). “Real Time Imaging with the Sonic Window: A Pocket-Sized, C-Scan, Medical Ultrasound Device”. In: *Proc. IEEE Ultrason. Symp.* Pp. 196–199 (cit. on pp. 7, 8).

Fuller, M. I., K. Ranganathan, S. Zhou, T. N. Blalock, J. A. Hossack, and W. F. Walker (2008). “Experimental System Prototype of a Portable, Low-Cost, C-Scan Ultrasound Imaging Device”. In: *IEEE Trans. Biomed. Eng.* 55.2, pp. 519–530 (cit. on pp. 7, 8, 14).

Hemmsen, M. C., T. Kjeldsen, L. Lassen, C. Kjær, B. Tomov, J. Mosegaard, and J. A. Jensen (2014). “Implementation of synthetic aperture imaging on a hand-held device”. In: *Proc. IEEE Ultrason. Symp.* Pp. 2177–2180 (cit. on p. 10).

Hemmsen, M. C., L. Lassen, T. Kjeldsen, J. Mosegaard, and J. A. Jensen (2015). “Implementation of real-time duplex synthetic aperture ultrasonography”. In: *Proc. IEEE Ultrason. Symp.* Pp. 1–4 (cit. on p. 10).

Heuvel, T. van den, D. Graham, K. Smith, C. de Korte, and J. Neasham (2017). “Development of a low-cost medical ultrasound scanner using monostatic synthetic aperture”. In: *IEEE Trans. Biomed. Circuits Syst.* 11.4, pp. 849–857 (cit. on pp. 10, 18).

Holm, S. and K. Kristoffersen (1992). “Analysis of worst-case phase quantization sidelobes in focused beamforming”. In: *IEEE Trans. Ultrason., Ferroelec., Freq. Contr.* 39, pp. 593–599 (cit. on p. 15).

Jensen, J. A., S. Nikolov, K. L. Gammelmark, and M. H. Pedersen (2006). “Synthetic Aperture Ultrasound Imaging”. In: *Ultrasonics* 44, e5–e15 (cit. on p. 18).

Jeong, E., S. Bae, M. Park, W. Jung, J. Kang, and T. Song (2015). “Color Doppler imaging on a smartphone-based portable US system: Preliminary study”. In: *Proc. IEEE Ultrason. Symp.* Pp. 1–4 (cit. on p. 10).

Kang, J., C. Yoon, J. Lee, S. Kye, Y. Lee, J. Chang, G. Kim, Y. Yoo, and T. Song (2016). “A System-on-Chip Solution for Point-of-Care Ultrasound Imaging Systems: Architecture and ASIC Implementation”. In: *IEEE Trans. Ultrason., Ferroelec., Freq. Contr.* 10.2, pp. 412–423 (cit. on p. 10).

Karaman, M., A. Atalar, and H. Köymen (1993). “VLSI circuits for adaptive digital beamforming in ultrasound imaging”. In: *IEEE Trans. Med. Imag.* 12, pp. 711–720 (cit. on p. 16).

Karaman, M., P. C. Li, and M. O’Donnell (1995). “Synthetic aperture imaging for small scale systems”. In: *IEEE Trans. Ultrason., Ferroelec., Freq. Contr.* 42, pp. 429–442 (cit. on p. 18).

Kim, G. D., C. Yoon, S. B. Kye, Y. Lee, J. Kang, Y. Yoo, and T. K. Song (2012). “A Single FPGA-Based Portable Ultrasound Imaging System for Point-of-Care Applications”.

In: *IEEE Trans. Ultrason., Ferroelec., Freq. Contr.* 59.7, pp. 1386–1394 (cit. on pp. 10, 17).

Kortbek, J., J. A. Jensen, and K. L. Gammelmark (2013). "Sequential Beamforming for Synthetic Aperture Imaging". In: *Ultrasonics* 53.1, pp. 1–16. DOI: 10.1016/j.ultras.2012.06.006 (cit. on p. 10).

Larson III, J. D. (1993). *2-D Phased Array Ultrasound Imaging System With Distributed Phasing*. Patent US 5229933 (cit. on pp. 10, 18).

Ligtvoet, C., H. Rijsterborgh, L. Kappen, and N. Bom (1978). "Real time ultrasonic imaging with a hand-held scanner - Part I: Technical description". In: *Ultrasound Med. Biol.* 4, pp. 91–92 (cit. on pp. 7, 9).

Lockwood, G. R., P.-C. Li, M. O'Donnell, and F. S. Foster (1996). "Optimizing the Radiation Pattern of Sparse Periodic Linear Arrays". In: *IEEE Trans. Ultrason., Ferroelec., Freq. Contr.* 43, pp. 7–14 (cit. on p. 14).

Lockwood, G. R., J. R. Talman, and S. S. Brunke (1998). "Real-time 3-D ultrasound imaging using sparse synthetic aperture beamforming". In: *IEEE Trans. Ultrason., Ferroelec., Freq. Contr.* 45, pp. 980–988 (cit. on p. 18).

Lockwook, G. R. and F. S. Foster (1996). "Optimizing the Radiation Pattern of Sparse Periodic Two-Dimensional Arrays". In: *IEEE Trans. Ultrason., Ferroelec., Freq. Contr.* 43.1, pp. 15–19 (cit. on p. 14).

Mucci, R. A. (1984). "A Comparison of Efficient Beamforming Algorithms". In: *IEEE Trans. Acoustics, Speech and Signal Processing* ASSP-32.3, pp. 548–558 (cit. on pp. 15, 16).

Nikolov, S. I. (2001). "Synthetic Aperture Tissue and Flow Ultrasound Imaging". PhD thesis. 2800, Lyngby, Denmark: Ørsted•DTU, Technical University of Denmark (cit. on p. 15).

O'Donnel, M. (1988). "Applications of VLSI Circuits to Medical Imaging". In: *IEEE Proc.* 76.9, pp. 1106–1114 (cit. on p. 16).

Peterson, D. K. and G. S. Kino (1984). "Real-Time Digital Image Reconstruction: A Description of Imaging Hardware and an Analysis of Quantization Errors". In: *IEEE Trans. Son. Ultrason.* 31.4, pp. 337–351. DOI: 10.1109/T-SU.1984.31514 (cit. on pp. 15, 16).

Poland, M. and M. Wilson (2010). *Light Weight Wireless Ultrasound Probe*. Patent US 2010/0168576 A1 (cit. on pp. 9, 10).

Ramm, O. T. von, S. W. Smith, and H. G. Pavy (1991). "High speed ultrasound volumetric imaging system – Part II: Parallel Processing and Image Display". In: *IEEE Trans. Ultrason., Ferroelec., Freq. Contr.* 38.2, pp. 109–115 (cit. on p. 18).

Ranganathan, K., M. K. Santy, T. N. Blalock, J. A. Hossack, and W. F. Walker (2004). "Direct sampled I/Q beamforming for compact and very low-cost ultrasound imaging". In: *IEEE Trans. Ultrason., Ferroelec., Freq. Contr.* 51.9, pp. 1082–1094 (cit. on pp. 9, 17).

Ranganathan, K. and W. F. Walker (2007). “Cystic Resolution: A Performance Metric for Ultrasound Imaging Systems”. In: *IEEE Trans. Ultrason., Ferroelec., Freq. Contr.* 54.4, pp. 782–792. DOI: 10.1109/TUFFC.2007.311 (cit. on p. 12).

Rasmussen, M. F., T. L. Christiansen, E. V. Thomsen, and J. A. Jensen (2015). “3-D Imaging Using Row–Column-Addressed Arrays With Integrated Apodization — Part I: Apodization Design and Line Element Beamforming”. In: *IEEE Trans. Ultrason., Ferroelec., Freq. Contr.* 62.5, pp. 947–958 (cit. on p. 14).

Roelandt, J., J. W. Wladimiroff, and A. M. Baars (1978). “Ultrasonic real time imaging with a hand-held scanner - Part II: Initial clinical experience”. In: *Ultrasound Med. Biol.* 4, pp. 93–97 (cit. on p. 7).

Savord, B. J. (2000). *Beamforming method and apparatus for three-dimensional ultrasound imaging using two-dimensional transducer array*. Patent US 6013032 (cit. on p. 18).

Savord, B. and R. Solomon (2003). “Fully sampled matrix transducer for real time 3D ultrasonic imaging”. In: *Proc. IEEE Ultrason. Symp.* Vol. 1, pp. 945–953 (cit. on p. 18).

Sawan, M., R. Chebli, and A. Kassem (2003). “Integrated Front-End Receiver for a Portable Ultrasonic System”. In: *Analog Integrated Circuits Signal Process.* 36, pp. 57–67 (cit. on p. 14).

Schafer, M. E. and P. A. Lewin (1984). “The Influence of Front-End Hardware on Digital Ultrasonic Imaging”. In: *IEEE Trans. Son. Ultrason.* SU-31.4, pp. 295–306 (cit. on p. 14).

Shattuck, D. P., M. D. Weinshenker, S. W. Smith, and O. T. von Ramm (1984). “Explososcan: A parallel processing technique for high speed ultrasound imaging with linear phased arrays”. In: *J. Acoust. Soc. Am.* 75, pp. 1273–1282 (cit. on p. 17).

Thijssen, J. M., G. Weijers, and C. L. de Korte (2007). “Objective performance testing and quality assurance of medical ultrasound equipment”. In: *Ultrasound Med. Biol.* 33.3, pp. 460–471 (cit. on p. 11).

Tomov, B. and J. A. Jensen (2005). “Compact FPGA-based beamformer using oversampled 1-bit A/D converters”. In: *IEEE Trans. Ultrason., Ferroelec., Freq. Contr.* 52.5, pp. 870–880 (cit. on p. 17).

Vilkomerson, D., J. Greenleaf, and V. Dutt (1995). “Towards a Resolution Metric for Medical Ultrasound Imaging”. In: *Proc. IEEE Ultrason. Symp.* Pp. 1405–1410 (cit. on p. 12).

References from Chapter 3

Amaro, J., B. Y. S. Yiu, G. Falcão, M. A. Gomes, and A. C. H. Yu (2015). “Software-Based High-Level Synthesis Design of FPGA Beamformers for Synthetic Aperture Imaging”. In: *IEEE Trans. Ultrason., Ferroelec., Freq. Contr.* 62.5, pp. 862–869 (cit. on p. 22).

Bae, M. H. and M. K. Jeong (2000). “A study of synthetic-aperture imaging with virtual source elements in B-mode ultrasound imaging systems”. In: *IEEE Trans. Ultrason., Ferroelec., Freq. Contr.* Vol. 47, pp. 1510–1519 (cit. on p. 22).

Boni, E., L. Bassi, A. Dallai, F. Guidi, V. Meacci, A. Ramalli, S. Ricci, and P. Tortoli (2016). “ULA-OP 256: A 256-Channel Open Scanner for Development and Real-Time Implementation of New Ultrasound Methods”. In: *IEEE Trans. Ultrason., Ferroelec., Freq. Contr.* 63.10, pp. 1488–1495 (cit. on p. 22).

Brandt, A. B., M. Hemmsen, P. Hansen, K. Hansen, T. Lange, J. Jensen, and M. Nielsen (2014). “Clinical evaluation of Synthetic Aperture Sequential Beamforming and Tissue Harmonic Imaging.” In: *Proc. IEEE Ultrason. Symp.* IEEE_U_SYMP, pp. 1312–1315 (cit. on p. 26).

Burckhardt, C. B., P.-A. Grandchamp, and H. Hoffmann (1974). “An Experimental 2 MHz Synthetic Aperture Sonar System Intended for Medical Use”. In: *IEEE Trans. Son. Ultrason.* 21.1, pp. 1–6 (cit. on p. 21).

Corl, P. D., P. M. Grant, and G. S. Kino (1978). “A Digital Synthetic Focus Acoustic Imaging System for NDE”. In: *Proc. IEEE Ultrason. Symp.* Pp. 263–268 (cit. on p. 21).

Flaherty, J. J., K. R. Erikson, and V. M. Lund (1967). *Synthetic Aperture Ultrasound Imaging Systems*. United States Patent, US 3,548,642. United States Patent, US 3,548,642, 1967, Published 22 Dec 1970 (cit. on p. 21).

Frazier, C. H. and W. D. O’Brien (1998). “Synthetic aperture techniques with a virtual source element”. In: *IEEE Trans. Ultrason., Ferroelec., Freq. Contr.* 45.1, pp. 196–207. DOI: 10.1109/58.646925 (cit. on p. 22).

Hemmsen, M. C., P. M. Hansen, T. Lange, J. M. Hansen, K. L. Hansen, M. B. Nielsen, and J. A. Jensen (2012). “In Vivo Evaluation of Synthetic Aperture Sequential Beamforming”. In: *Ultrasound Med. Biol.* 38.4, pp. 708–716 (cit. on p. 26).

Hemmsen, M. C., T. Kjeldsen, L. Lassen, C. Kjær, B. Tomov, J. Mosegaard, and J. A. Jensen (2014). “Implementation of synthetic aperture imaging on a hand-held device”. In: *Proc. IEEE Ultrason. Symp.* Pp. 2177–2180 (cit. on p. 26).

Hemmsen, M. C., L. Lassen, T. Kjeldsen, J. Mosegaard, and J. A. Jensen (2015). “Implementation of real-time duplex synthetic aperture ultrasonography”. In: *Proc. IEEE Ultrason. Symp.* Pp. 1–4 (cit. on p. 26).

Hemmsen, M. C., J. Rasmussen, and J. A. Jensen (2014). “Tissue Harmonic Synthetic Aperture Ultrasound Imaging”. In: *J. Acoust. Soc. Am.* 136.4, pp. 2050–2056 (cit. on p. 26).

Hemmsen, M. C., M. F. Rasmussen, M. B. Stuart, and J. A. Jensen (2014). “Simulation study of real time 3D Synthetic Aperture Sequential Beamforming for Ultrasound imaging”. In: *Proc. SPIE Med. Imag.* Vol. 9040, pages (cit. on p. 26).

Jensen, J. A., O. Holm, L. J. Jensen, H. Bendsen, S. I. Nikolov, B. G. Tomov, P. Munk, M. Hansen, K. Salomonsen, J. Hansen, K. Gormsen, H. M. Pedersen, and K. L. Gammelmark (2005). “Ultrasound Research Scanner for Real-time Synthetic Aperture Image

Acquisition". In: *IEEE Trans. Ultrason., Ferroelec., Freq. Contr.* 52 (5), pp. 881–891 (cit. on p. 22).

Jensen, J. A., H. Holten-Lund, R. T. Nilsson, M. Hansen, U. D. Larsen, R. P. Domsten, B. G. Tomov, M. B. Stuart, S. I. Nikolov, M. J. Pihl, Y. Du, J. H. Rasmussen, and M. F. Rasmussen (2013). "SARUS: A Synthetic Aperture Real-time Ultrasound System". In: *IEEE Trans. Ultrason., Ferroelec., Freq. Contr.* 60.9, pp. 1838–1852 (cit. on p. 22).

Jensen, J. A., S. Nikolov, K. L. Gammelmark, and M. H. Pedersen (2006). "Synthetic Aperture Ultrasound Imaging". In: *Ultrasonics* 44, e5–e15 (cit. on p. 21).

Karaman, M., P. C. Li, and M. O'Donnell (1995). "Synthetic aperture imaging for small scale systems". In: *IEEE Trans. Ultrason., Ferroelec., Freq. Contr.* 42, pp. 429–442 (cit. on pp. 21, 22).

Karaman, M. and M. O'Donnell (1998). "Subaperture processing for ultrasonic imaging". In: *IEEE Trans. Ultrason., Ferroelec., Freq. Contr.* 45, pp. 126–135 (cit. on p. 21).

Kortbek, J., J. A. Jensen, and K. L. Gammelmark (2013). "Sequential Beamforming for Synthetic Aperture Imaging". In: *Ultrasonics* 53.1, pp. 1–16. DOI: 10.1016/j.ultras.2012.06.006 (cit. on pp. 22, 25).

Li, Y. and J. A. Jensen (2013). "Synthetic aperture flow imaging using dual stage beamforming: Simulations and experiments". In: *J. Acoust. Soc. Am.* 133.4, pp. 2014–2024 (cit. on p. 26).

Lockwood, G. R., J. R. Talman, and S. S. Brunke (1998). "Real-time 3-D ultrasound imaging using sparse synthetic aperture beamforming". In: *IEEE Trans. Ultrason., Ferroelec., Freq. Contr.* 45, pp. 980–988 (cit. on p. 21).

Lu, J., J. Cheng, and J. Wang (2006). "High Frame Rate Imaging System for Limited Diffraction Array Beam Imaging with Square-Wave Aperture Weightings". In: *IEEE Trans. Ultrason., Ferroelec., Freq. Contr.* 53.10, pp. 1796–1812 (cit. on p. 22).

Nikolov, S. I. (2001). "Synthetic Aperture Tissue and Flow Ultrasound Imaging". PhD thesis. 2800, Lyngby, Denmark: Ørsted•DTU, Technical University of Denmark (cit. on pp. 21, 23).

Nikolov, S. I. and J. A. Jensen (2002). "Virtual ultrasound sources in high-resolution ultrasound imaging". In: *Proc. SPIE - Progress in biomedical optics and imaging*. Vol. 3, pp. 395–405 (cit. on p. 22).

O'Donnell, M. and L. J. Thomas (1992). "Efficient synthetic aperture imaging from a circular aperture with possible application to catheter-based imaging". In: *IEEE Trans. Ultrason., Ferroelec., Freq. Contr.* 39, pp. 366–380 (cit. on p. 22).

Passmann, C. and H. Ermert (1996). "A 100-MHz ultrasound imaging system for dermatologic and ophthalmologic diagnostics". In: *IEEE Trans. Ultrason., Ferroelec., Freq. Contr.* 43, pp. 545–552 (cit. on p. 22).

Prine, D. W. (1972). "Synthetic Aperture Ultrasonic Imaging". In: *Proceedings of the Engineering Applications of Holography Symposium*, pp. 287–294 (cit. on p. 21).

Sandrin, L., S. Catheline, M. Tanter, X. Hennequin, and M. Fink (1999). "Time-resolved pulsed elastography with ultrafast ultrasonic imaging". In: *Ultrason. Imaging* 21.4, pp. 259–272 (cit. on p. 22).

Tortoli, P., L. Bassi, E. Boni, A. Dallai, F. Guidi, and S. Ricci (2009). "ULA-OP: An Advanced Open Platform for Ultrasound Research". In: *IEEE Trans. Ultrason., Ferroelec., Freq. Contr.* 56.10, pp. 2207–2216 (cit. on p. 22).

Vos, H., P. van Neer, M. M. Mota, M. Verweij, A. van der Steen, and A. Volker (2016). "F-k domain imaging for synthetic aperture sequential beamforming". In: *IEEE Trans. Ultrason., Ferroelec., Freq. Contr.* 63.1, pp. 60–71 (cit. on p. 25).

Ylitalo, J. T. and H. Ermert (1994). "Ultrasound synthetic aperture imaging: Monostatic approach". In: *IEEE Trans. Ultrason., Ferroelec., Freq. Contr.* 41, pp. 333–339 (cit. on p. 22).

References from Chapter 4

Carroll, A. and G. Heiser (2010). "An Analysis of Power Consumption in a Smartphone". In: *USENIX Annual Technical Conference* (cit. on p. 27).

FDA (2008). *Information for Manufacturers Seeking Marketing Clearance of Diagnostic Ultrasound Systems and Transducers*. Tech. rep. Center for Devices, Radiological Health, United States Food, and Drug Administration (cit. on p. 27).

Hansen, J. M., M. C. Hemmsen, and J. A. Jensen (2011). "An object-oriented multi-threaded software beamformation toolbox". In: *Proc. SPIE Med. Imag.* Vol. 7968, pages. DOI: 10.1117/12.878178 (cit. on p. 29).

IEC (2015). *Medical electrical equipment - Part 2-37: Particular requirements for the basic safety and essential performance of ultrasonic medical diagnostic and monitoring equipment*. Tech. rep. IEC 60601-2-37. Edition 2.1 2015-06. International Electrotechnical Commission (cit. on p. 27).

Jensen, J. A. (1996). "Field: A Program for Simulating Ultrasound Systems". In: *Med. Biol. Eng. Comp.* 10th Nordic-Baltic Conference on Biomedical Imaging, Vol. 4, Supplement 1, Part 1, pp. 351–353 (cit. on p. 29).

Jensen, J. A. and N. B. Svendsen (1992). "Calculation of Pressure Fields from Arbitrarily Shaped, Apodized, and Excited Ultrasound Transducers". In: *IEEE Trans. Ultrason., Ferroelec., Freq. Contr.* 39, pp. 262–267 (cit. on p. 29).

References from Chapter 5

Adams, R. W., P. F. Ferguson, A. Ganesan, S. Vincelette, A. Volpe, and R. Libert (1991). "Theory and Practical Implementation of a Fifth-Order Sigma-Delta A/D Converter". In: *J. Audio Eng. Soc.* 39.7/8, pp. 515–528 (cit. on p. 49).

Aziz, P. M., H. V. Sorensen, and J. V. der Spiegel (1996). "An Overview of Sigma-Delta Converters". In: *IEEE Signal Processing Magazine* 13, pp. 61–84 (cit. on p. 44).

Candy, J. and G. Temes (1992). "Oversampling methods for A/D and D/A conversion". In: *Oversampling Delta-Sigma Data Converters*. IEEE Press (cit. on p. 44).

Hansen, J. M., M. C. Hemmsen, and J. A. Jensen (2011). "An object-oriented multi-threaded software beamformation toolbox". In: *Proc. SPIE Med. Imag.* Vol. 7968, pages. DOI: 10.1117/12.878178 (cit. on p. 46).

Hogenauer, E. B. (1981). "An Economical Class of Digital Filters for Decimation and Interpolation". In: *IEEE Trans. Acoustics, Speech and Signal Processing* ASSP-29.2, pp. 155–162 (cit. on p. 49).

Holm, S. and K. Kristoffersen (1992). "Analysis of worst-case phase quantization side-lobes in focused beamforming". In: *IEEE Trans. Ultrason., Ferroelec., Freq. Contr.* 39, pp. 593–599 (cit. on p. 44).

Jensen, J. A. (1996). "Field: A Program for Simulating Ultrasound Systems". In: *Med. Biol. Eng. Comp.* 10th Nordic-Baltic Conference on Biomedical Imaging, Vol. 4, Supplement 1, Part 1, pp. 351–353 (cit. on p. 46).

Jensen, J. A. and N. B. Svendsen (1992). "Calculation of Pressure Fields from Arbitrarily Shaped, Apodized, and Excited Ultrasound Transducers". In: *IEEE Trans. Ultrason., Ferroelec., Freq. Contr.* 39, pp. 262–267 (cit. on p. 46).

Mucci, R. A. (1984). "A Comparison of Efficient Beamforming Algorithms". In: *IEEE Trans. Acoustics, Speech and Signal Processing* ASSP-32.3, pp. 548–558 (cit. on pp. 44, 45).

Muntal, P. L., I. H. Jørgensen, and E. Bruun (2017). "A continuous-time delta-sigma ADC for portable ultrasound". In: *Analog Integrated Circuits Signal Process.* Pp. 1–10. DOI: 10.1007/s10470-017-1004-5 (cit. on p. 53).

Muntal, P. L. (2017). "Custom Integrated Circuit Design for Portable Ultrasound Scanners". PhD thesis. Department of Electrical Engineering, Technical University of Denmark (cit. on pp. 53, 55, 56).

Murmann, B. (2008). "A/D Converter Trends: Power Dissipation, Scaling and Digitally Assisted Architectures". In: *IEEE Custom Integrated Circuits Conference*, pp. 105–112 (cit. on p. 58).

Norsworthy, S. R., R. Shreier, and G. C. Temes (1996). *Delta-Sigma Data Converters : Theory, design and simulation*. Wiley-IEEE Press (cit. on pp. 43, 44, 58, 59).

Oppenheim, A. V. and R. W. Schafer (1989). *Discrete-Time Signal Processing*. Englewood Cliffs, N.J.: Prentice-Hall (cit. on pp. 41, 43).

Ortmanns, M. and F. Gerfers (2006). *Continuous-time Sigma-Delta A/D Conversion*. Springer Berlin Heidelberg (cit. on p. 43).

Walden, R. H. (1999). "Analog-to-Digital Converter Survey and Analysis". In: *IEEE J. Sel. Areas Commun.* 17.4, pp. 539–550 (cit. on p. 41).

References from Chapter 6

Baim, D. S. and W. Grossman (2000). *Grossman's cardiac catheterization, angiography, and intervention*. Lippincott Williams & Wilkins (cit. on p. 70).

Baker, D. W. (1970). “Pulsed ultrasonic Doppler blood-flow sensing”. In: *IEEE Trans. Son. Ultrason.* SU-17.3, pp. 170–185 (cit. on p. 63).

Bercoff, J., M. Tanter, L. Sandrin, S. Catheline, and M. Fink (2001). “Ultrafast compound imaging for 2-D displacement vector measurements: application to transient elastography and color flow mapping”. In: *Proc. IEEE Ultrason. Symp.* Pp. 1619–1622 (cit. on p. 68).

Bonnefous, O. (1988). “Measurement of the complete (3D) velocity vector of blood flows”. In: *Proc. IEEE Ultrason. Symp.* Pp. 795–799 (cit. on p. 68).

Bonnefous, O. and P. Pesqué (1986). “Time Domain Formulation of Pulse-Doppler Ultrasound and Blood Velocity Estimation by Cross Correlation”. In: *Ultrason. Imaging* 8, pp. 73–85. DOI: 10.1016/0161-7346(86)90001-5 (cit. on p. 65).

Cheng, C., R. van Haperen, M. de Waard, L. van Damme, D. Tempel, L. H. nnd G.W.A. van Cappellen, J. Bos, C. Slager, D. Duncker, A. van der Steen, R. de Crom, and R. Krams (2005). “Shear stress affects the intracellular distribution of eNOS: direct demonstration by a novel in vivo technique”. In: *Blood* 106.12, pp. 3691–3698 (cit. on p. 70).

Cheng, C., D. Tempel, R. van Haperen, A. van der Baan, F. Grosveld, M. Daemen, R. Krams, and R. de Crom (2006). “Atherosclerotic Lesion Size and Vulnerability Are Determined by Patterns of Fluid Shear Stress”. In: *Circ. Res.* Pp. 2744–2753 (cit. on p. 70).

Daigle, R. E., C. W. Miller, M. B. Histand, F. D. McLeod, and D. E. Hokanson (1975). “Nontraumatic aortic blood flow sensing by use of an ultrasonic esophageal probe”. In: *J. Applied Phys.* 38, pp. 1153–1160 (cit. on p. 67).

Dodd, G. I., D. Memel, A. Zajko, R. Baron, and L. Santaguida (1994). “Hepatic artery stenosis and thrombosis in transplant recipients: Doppler diagnosis with resistive index and systolic acceleration time”. In: *Radiology* 192.3, pp. 657–661 (cit. on p. 63).

Dotti, D., E. Gatti, V. Svelto, A. Uggè, and P. Vidali (1976). “Blood flow measurements by ultrasound correlation techniques”. In: *Energia Nucleare* 23.11, pp. 571–575 (cit. on p. 65).

Dunmire, B., K. W. Beach, K.-H. Labs., M. Plett, and D. E. Strandness (2000). “Cross-beam vector Doppler ultrasound for angle independent velocity measurements”. In: *Ultrasound Med. Biol.* 26, pp. 1213–1235 (cit. on p. 67).

Ekroll, I. K., A. Swillens, P. Segers, T. Dahl, H. Torp, and L. Lovstakken (2013). “Simultaneous quantification of flow and tissue velocities based on multi-angle plane wave imaging”. In: *IEEE Trans. Ultrason., Ferroelec., Freq. Contr.* 60.4, pp. 727–738 (cit. on p. 67).

Fadnes, S., I. K. Ekroll, S. A. Nyrnes, H. Torp, and L. Løvstakken (2015). “Robust Angle-Independent Blood Velocity Estimation Based on Dual-Angle Plane Wave Imaging”. In: *IEEE Trans. Ultrason., Ferroelec., Freq. Contr.* 62.10, pp. 1757–1767. DOI: 10.1109/tuffc.2015.007108 (cit. on p. 68).

Fadnes, S., S. A. Nyrnes, H. Torp, and L. Lovstakken (2014). “Shunt Flow Evaluation in Congenital Heart Disease Based on Two-Dimensional Speckle Tracking”. In:

Ultrasound Med. Biol. 40.10, pp. 2379–2391. DOI: 10.1016/j.ultrasmedbio.2014.03.029 (cit. on p. 69).

Fahrbach, K. (1970). "Ein Beitrag Zur Blutgeschwindigkeitsmessung unter Anwendung des Dopplereffektes". In: *Elektromedizin* 15.1, pp. 26–36 (cit. on p. 67).

Fox, M. D. (1978). "Multiple crossed-beam ultrasound Doppler velocimetry". In: *IEEE Trans. Son. Ultrason.* SU-25, pp. 281–286 (cit. on p. 67).

Friemel, B., L. Bohs, and G. Trahey (1995). "Relative performance of two-dimensional speckle-tracking techniques: normalized correlation, non-normalized correlation and sum-absolute-difference". In: *Proc. IEEE Ultrason. Symp.* Pp. 1481–1484 (cit. on p. 68).

Gill, R. W. (1985). "Measurement of blood flow by ultrasound: Accuracy and sources of error". In: *Ultrasound Med. Biol.* 11, pp. 625–641 (cit. on p. 63).

Grant, E. G., C. B. Benson, G. L. Moneta, A. V. Alexandrov, J. D. Baker, E. I. Bluth, B. A. Carroll, and et al. (2003). "Carotid artery stenosis: gray-scale and Doppler US diagnosis - Society of radiologists in ultrasound consensus conference". In: *Radiology* 229.2. M. Eliasziw and J. Gocke and B. S. Hertzberg, pp. 340–346. DOI: 10.1148/radiol.2292030516 (cit. on p. 63).

Groen, H., F. Gijsen, A. van der Lugt, M. Ferguson, T. Hatsukami, A. van der Steen, C. Yuan, and J. Wentzel (2007). "Plaque rupture in the carotid artery is localized at the high shear stress region. A case report". In: *Stroke* 38, pp. 2379–2381 (cit. on p. 70).

Hansen, K. L., H. Møller-Sørensen, J. Kjaergaard, M. B. Jensen, J. T. Lund, M. M. Pedersen, T. Lange, J. A. Jensen, and M. B. Nielsen (2016). "Intraoperative vector flow imaging using ultrasound of the ascending aorta among 40 patients with normal, stenotic and replaced aortic valves". In: *Ultrasound Med. Biol.* 42.10, pp. 2414–2422 (cit. on p. 70).

Hansen, K. L., H. Møller-Sørensen, J. Kjaergaard, J. T. Lund, M. M. Pedersen, T. Lange, J. A. Jensen, and M. B. Nielsen (2016). "Analysis of Systolic Backflow and Secondary Helical Blood Flow in the Ascending Aorta Using Vector Flow Imaging". In: *Ultrasound Med. Biol.* 42.4, pp. 899–908. DOI: 10.1016/j.ultrasmedbio.2015.11.029 (cit. on p. 69).

Hansen, K. L., H. Møller-Sørensen, M. M. Pedersen, P. M. Hansen, J. Kjaergaard, J. T. Lund, J. C. Nilsson, J. A. Jensen, and M. B. Nielsen (2014). "First report on intraoperative vector flow imaging of the heart among patients with healthy and diseased aortic valves". In: *Ultrasonics* 56, pp. 243–250. DOI: 10.1016/j.ultras.2014.07.015 (cit. on p. 64).

Hansen, K. L., J. Udesen, N. Oddershede, L. Henze, C. Thomsen, J. A. Jensen, and M. B. Nielsen (2009). "In vivo comparison of three ultrasound vector velocity techniques to MR phase contrast angiography". In: *Ultrasonics* 49, pp. 659–667 (cit. on p. 69).

Hansen, P. L., G. Cross, and L. H. Light (1974). "Beam-angle independent Doppler velocity measurement in superficial vessels". In: *Clinical Blood Flow Measurement*. London: Sector Publishing (cit. on p. 67).

Hoeks, A. P. G., T. G. J. Arts, P. J. Brands, and R. S. Reneman (1993). "Comparison of the performance of the rf cross correlation and Doppler autocorrelation technique to estimate the mean velocity of simulated ultrasound signals". In: *Ultrasound Med. Biol.* 19, pp. 727–740 (cit. on pp. 66, 67).

Jensen, J. A. (1996). *Estimation of Blood Velocities Using Ultrasound: A Signal Processing Approach*. New York: Cambridge University Press (cit. on pp. 63, 65, 66).

— (2003). "Directional velocity estimation using focusing along the flow direction: I: Theory and simulation". In: *IEEE Trans. Ultrason., Ferroelec., Freq. Contr.* 50, pp. 857–872 (cit. on p. 68).

Jensen, J. A. and R. Bjerngaard (2003). "Directional velocity estimation using focusing along the flow direction: II: Experimental investigation". In: *IEEE Trans. Ultrason., Ferroelec., Freq. Contr.* 50, pp. 873–880 (cit. on p. 68).

Jensen, J. A. and S. I. Nikolov (2004). "Directional Synthetic Aperture Flow Imaging". In: *IEEE Trans. Ultrason., Ferroelec., Freq. Contr.* 51, pp. 1107–1118 (cit. on p. 68).

Jensen, J. A., S. I. Nikolov, A. Yu, and D. Garcia (2016a). "Ultrasound Vector Flow Imaging I: Sequential Systems". In: *IEEE Trans. Ultrason., Ferroelec., Freq. Contr.* 63.11, pp. 1704–1721. DOI: 10.1109/TUFFC.2016.2600763 (cit. on p. 67).

— (2016b). "Ultrasound Vector Flow Imaging II: Parallel Systems". In: *IEEE Trans. Ultrason., Ferroelec., Freq. Contr.* 63.11, pp. 1722–1732. DOI: 10.1109/TUFFC.2016.2598180 (cit. on p. 67).

Jensen, J. A. and N. Oddershede (2006). "Estimation of velocity vectors in synthetic aperture ultrasound imaging". In: *IEEE Trans. Med. Imag.* 25, pp. 1637–1644 (cit. on p. 68).

Jensen, J., C. A. Villagomez-Hoyos, M. B. Stuart, C. Ewertsen, M. B. Nielsen, and J. A. Jensen (2017). "Fast Plane Wave 2-D Vector Flow Imaging Using Transverse Oscillation and Directional Beamforming". In: *IEEE Trans. Ultrason., Ferroelec., Freq. Contr.* 64.7, pp. 1050–1062. DOI: 10.1109/TUFFC.2017.2693403 (cit. on p. 68).

Kasai, C., K. Namekawa, A. Koyano, and R. Omoto (1985). "Real-Time Two-Dimensional Blood Flow Imaging using an Autocorrelation Technique". In: *IEEE Trans. Son. Ultrason.* 32.3, pp. 458–463 (cit. on p. 66).

Kim, H. B., J. R. Hertzberg, and R. Shandas (2004). "Development and validation of echo PIV". In: *Exp. Fluids* 36, pp. 455–462 (cit. on p. 68).

Lai, X., H. Torp, and K. Kristofferson (1997). "An Extended Autocorrelation Method for Estimation of Blood Velocity". In: *IEEE Trans. Ultrason., Ferroelec., Freq. Contr.* 44.6, pp. 1332–1342 (cit. on p. 67).

Lee, S., L. Antiga, and D. A. Steinman (2009). "Correlations Among Indicators of Disturbed Flow at the Normal Carotid Bifurcation". In: *J. Biomech. Eng.* 131, pp. 1–7 (cit. on p. 70).

Leow, C. H., E. Bazigou, R. J. Eckersley, A. C. H. Yu, P. D. Weinberg, and M. X. Tang (2015). "Flow velocity mapping using contrast enhanced high-frame-rate plane wave

ultrasound and image tracking: Methods and initial in vitro and in vivo evaluation". In: *Ultrasound Med. Biol.* 41.11, pp. 2913–2925 (cit. on p. 68).

Li, W., C. Lancée, E. Ignacio Céspedes, A. Van Der Steen, and N. Bom (1997). "Decorrelation of intravascular echo signals: Potentials for blood velocity estimation". In: *J. Acoust. Soc. Am.* 102, pp. 3785–3794 (cit. on p. 67).

Li, W., A. F. W. van der Steen, C. T. Lancée, I. Céspedes, and N. Bom (1998). "Blood flow imaging and volume flow quantitation with intravascular ultrasound". In: *Ultrasound Med. Biol.* 24, pp. 203–214 (cit. on p. 67).

Lupotti, F., F. Mastik, S. Carlier, C. de Korte, W. van der Giessen, P. Serruys, and A. van der Steen (2003). "Quantitative IVUS blood flow: Validation in vitro, in animals and in patients". In: *Ultrasound Med. Biol.* 29.4, pp. 507–515 (cit. on p. 67).

Newhouse, V. L., D. Censor, T. Vontz, J. A. Cisneros, and B. B. Goldberg (1987). "Ultrasound Doppler probing of flows transverse with respect to beam axis". In: *IEEE Trans. Biomed. Eng.* BME-34, pp. 779–788 (cit. on p. 67).

Nikolov, S. I. and J. A. Jensen (2003). "In-vivo Synthetic Aperture Flow Imaging in Medical Ultrasound". In: *IEEE Trans. Ultrason., Ferroelec., Freq. Contr.* 50.7, pp. 848–856 (cit. on p. 68).

Olesen, J. B., M. S. Traberg, M. J. Pihl, and J. A. Jensen (2014). "Noninvasive esimation of 2-D pressure gradients in steady flow using ultrasound". In: *IEEE Trans. Ultrason., Ferroelec., Freq. Contr.* 61.8, pp. 1409–1418 (cit. on p. 70).

Olesen, J. B. (2015). "Imaging of In-Vivo Pressure using Ultrasound". PhD thesis. Technical University of Denmark (cit. on pp. 70, 71).

Pedersen, M. M., M. J. Pihl, P. Haugaard, J. M. Hansen, K. L. Hansen, M. B. Nielsen, and J. A. Jensen (2012). "Comparison of Real-Time In Vivo Spectral and Vector Velocity Estimation". In: *Ultrasound Med. Biol.* 38.1, pp. 145–151 (cit. on p. 69).

Peronneau, P., J.-P. Bournat, A. Bugnon, A. Barbet, and M. Xhaard (1974). "Theoretical and practical aspects of pulsed Doppler flowmetry real-time application to the measure of instantaneous velocity profiles in vitro and in vivo". In: *Cardiovascular applications of ultrasound*. Ed. by R. Reneman. North Holland Publishing, pp. 66–84 (cit. on p. 67).

Poelma, C., J. M. Mari, N. Foin, M.-X. Tang, R. Krams, C. G. Caro, P. D. Weinberg, and J. Westerweel (2009). "3D flow reconstruction using ultrasound PIV". In: *Experiments in Fluids* 50.4, pp. 777–785. DOI: 10.1007/s00348-009-0781-8 (cit. on p. 68).

— (2011). "3D Flow reconstruction using ultrasound PIV". In: *Exp. Fluids* 50.4, pp. 777–785 (cit. on p. 70).

Poelma, C., R. M. E. van der Mijle, J. M. Mari, M. .-.-X. Tang, P. D. Weinberg, and J. Westerweel (2012). "Ultrasound imaging velocimetry: toward reliable wall shear stress measurements". In: *European Journal of Mechanics - B/Fluids* 35, pp. 70–75. DOI: 10.1016/j.euromechflu.2012.03.003 (cit. on p. 70).

Ricci, S., L. Bassi, and P. Tortoli (2014). "Real-time vector velocity assessment through multigate Doppler and plane waves". In: *IEEE Trans. Ultrason., Ferroelec., Freq. Contr.* 61.2, pp. 314–324 (cit. on p. 67).

Sengupta, P. P., B. K. Khandheria, J. Korinek, A. Jahangir, S. Yoshifuku, I. Milosevic, and M. Belohlavek (2007). "Left ventricular isovolumic flow sequence during sinus and paced rhythms: new insights from use of high-resolution Doppler and ultrasonic digital particle imaging velocimetry". In: *J. Am. Coll. Cardiol.* 49.8, pp. 899–908. DOI: 10.1016/j.jacc.2006.07.075 (cit. on p. 69).

Slager, C. J., J. J. Wentzel, F. J. H. Gijsen, J. C. H. Schuurbiers, A. van der Wal, A. F. W. van der Steen, and P. W. Serruys (2005). "The role of shear stress in the generation of rupture-prone vulnerable plaques". In: *Nature Reviews Cardiology* 2.8, pp. 401–407. DOI: 10.1038/ncpcardio0274 (cit. on p. 70).

Slager, C. J., J. J. Wentzel, F. J. H. Gijsen, A. Thury, A. van der Wal, J. Schaar, and P. W. Serruys (2005). "The role of shear stress in the destabilization of vulnerable plaques and related therapeutic implications". In: *Nature Reviews Cardiology* 2.9, pp. 456–464 (cit. on p. 70).

Tortoli, P., G. Bambi, and S. Ricci (2006). "Accurate Doppler angle estimation for vector flow measurements". In: *IEEE Trans. Ultrason., Ferroelec., Freq. Contr.* 53.8, pp. 1425–1431 (cit. on p. 67).

Tortoli, P., M. Lenge, D. Righi, G. Ciuti, H. Liebgott, and S. Ricci (2015). "Comparison of carotid artery blood velocity measurements by vector and standard Doppler approaches". In: *Ultrasound Med. Biol.* 41.5, pp. 1354–1362. DOI: 10.1016/j.ultrasmedbio.2015.01.008 (cit. on p. 69).

Trahey, G. E., J. W. Allison, and O. T. von Ramm (1987). "Angle independent ultrasonic detection of blood flow". In: *IEEE Trans. Biomed. Eng.* BME-34.12, pp. 965–967 (cit. on p. 68).

Trahey, G. E., S. M. Hubbard, and O. T. von Ramm (1988). "Angle independent ultrasonic blood flow detection by frame-to-frame correlation of B-mode images". In: *Ultrasonics* 26, pp. 271–276 (cit. on p. 68).

Udesen, J., F. Gran, K. L. Hansen, J. A. Jensen, C. Thomsen, and M. B. Nielsen (2008). "High Frame-Rate Blood Vector Velocity Imaging Using Plane Waves: simulations and preliminary experiments". In: *IEEE Trans. Ultrason., Ferroelec., Freq. Contr.* 55.8, pp. 1729–1743 (cit. on p. 68).

Villagomez-Hoyos, C. A. (2016). "Synthetic Aperture Vector Flow Imaging". PhD thesis. Technical University of Denmark. URL: http://findit.dtu.dk/en/catalog/2347162876 (cit. on pp. 69, 70).

Villagomez-Hoyos, C. A., S. Holbek, M. B. Stuart, and J. A. Jensen (2016). "High Frame Rate Synthetic Aperture 3D Vector Flow Imaging". In: *Proc. IEEE Ultrason. Symp.* Pp. 1–4 (cit. on p. 68).

Villagomez-Hoyos, C. A., M. B. Stuart, K. L. Hansen, M. B. Nielsen, and J. A. Jensen (2016). "Accurate Angle Estimator for High Frame Rate 2-D Vector Flow Imaging". In: *IEEE Trans. Ultrason., Ferroelec., Freq. Contr.* 63.6, pp. 842–853 (cit. on pp. 64, 68).

Yiu, B. Y., S. S. Lai, and A. C. Yu (2014). "Vector projectile imaging: time-resolved dynamic visualization of complex flow patterns." In: *Ultrasound Med. Biol.* 40.9, pp. 2295–2309 (cit. on p. 67).

Zhang, F., C. Lanning, L. Mazzaro, A. J. Barker, P. E. Gates, W. D. Strain, J. Fulford, O. E. Gosling, A. C. Shore, N. G. Bellenger, and et al. (2011). "In vitro and preliminary in vivo validation of echo particle image velocimetry in carotid vascular imaging". In: *Ultrasound Med. Biol.* 37.3, pp. 450–464. DOI: 10.1016/j.ultrasmedbio.2010.11.017 (cit. on p. 68).

References from Chapter 7

Anderson, M. E. (1998). "Multi-dimensional velocity estimation with ultrasound using spatial quadrature". In: *IEEE Trans. Ultrason., Ferroelec., Freq. Contr.* 45, pp. 852–861 (cit. on p. 73).

— (2000). "A Heterodyning Demodulation Technique for Spatial Quadrature". In: *Proc. SPIE Med. Imag.* Pp. 1487–1490 (cit. on p. 73).

Goodman, J. W. (1996). *Introduction to Fourier optics*. Second. New York: McGraw Hill Inc. (cit. on p. 75).

Hansen, K. L., J. Udesen, N. Oddershede, L. Henze, C. Thomsen, J. A. Jensen, and M. B. Nielsen (2009). "In vivo comparison of three ultrasound vector velocity techniques to MR phase contrast angiography". In: *Ultrasonics* 49, pp. 659–667 (cit. on p. 73).

Heyde, B., N. Bottenus, J. D'Hooge, and G. E. Trahey (2017). "Evaluation of the transverse oscillation technique for cardiac phased array imaging: a theoretical study". In: *IEEE Trans. Ultrason., Ferroelec., Freq. Contr.* 64.2, pp. 320–334 (cit. on p. 73).

Holbek, S., T. L. Christiansen, M. B. Stuart, C. Beers, E. V. Thomsen, and J. A. Jensen (2016). "3-D Vector Flow Estimation with Row-Column Addressed Arrays". In: *IEEE Trans. Ultrason., Ferroelec., Freq. Contr.* 63.11, pp. 1799–1814 (cit. on p. 74).

Holbek, S., C. Ewertsen, H. Bouzari, M. J. Pihl, K. L. Hansen, M. B. Stuart, M. B. Nielsen, and J. A. Jensen (2017). "Ultrasonic 3-D vector flow method for quantitative in vivo peak velocity and flow rate estimation". In: *IEEE Trans. Ultrason., Ferroelec., Freq. Contr.* 64.3, pp. 544–554 (cit. on p. 74).

Holbek, S., J. A. Jensen, and M. B. Stuart (2016). "3-D Vector Flow Imaging". PhD thesis. Technical University of Denmark, Department of Electrical Engineering (cit. on p. 74).

Jensen, J. A. (1996). *Estimation of Blood Velocities Using Ultrasound: A Signal Processing Approach*. New York: Cambridge University Press (cit. on p. 75).

— (2001). "A New Estimator for Vector Velocity Estimation". In: *IEEE Trans. Ultrason., Ferroelec., Freq. Contr.* 48.4, pp. 886–894 (cit. on pp. 73, 77).

— (2016). "Directional Transverse Oscillation Vector Flow Estimation". In: *IEEE Trans. Ultrason., Ferroelec., Freq. Contr.* 63, Submitted (cit. on p. 78).

Jensen, J. A. (2017). "Directional Transverse Oscillation Vector Flow Estimation". In: *IEEE Trans. Ultrason., Ferroelec., Freq. Contr.* DOI: 10.1109/TUFFC.2017.2710361 (cit. on p. 76).

Jensen, J. A., A. H. Brandt, and M. B. Nielsen (2015). "Convex Array Vector Velocity Imaging Using Transverse Oscillation and Its Optimization". In: *IEEE Trans. Ultrason., Ferroelec., Freq. Contr.* 62.12, pp. 2043–2053. DOI: 10.1109/TUFFC.2015.006970 (cit. on pp. 73, 78, 79).

Jensen, J. A. and P. Munk (1998). "A New Method for Estimation of Velocity Vectors". In: *IEEE Trans. Ultrason., Ferroelec., Freq. Contr.* 45.3, pp. 837–851 (cit. on pp. 73, 74).

Jensen, J., C. A. Villagomez-Hoyos, M. B. Stuart, C. Ewertsen, M. B. Nielsen, and J. A. Jensen (2016). "In Vivo High Frame Rate Vector Flow Imaging Using Plane Waves and Directional Beamforming". In: *Proc. IEEE Ultrason. Symp.* Pp. 1–4 (cit. on p. 74).

Lenge, M., A. Ramalli, P. Tortoli, C. Cachard, and H. Liebgott (2015). "Plane-Wave Transverse Oscillation for High-Frame-Rate 2-D Vector Flow Imaging". In: *IEEE Trans. Ultrason., Ferroelec., Freq. Contr.* 62.12, pp. 2126–2137 (cit. on p. 74).

Liebgott, H., A. Basarab, P. Gueth, C. Cachard, and P. Delachartre (2008). "Lateral RF image synthesis using a synthetic aperture imaging technique." In: *IEEE Trans. Ultrason., Ferroelec., Freq. Contr.* 55.9, pp. 2097–2103 (cit. on pp. 73, 74).

Liebgott, H., J. Wilhjelm, J. A. Jensen, D. Vray, and P. Delachartre (2007). "PSF dedicated to estimation of displacement vectors for tissue elasticity imaging with ultrasound". In: *IEEE Trans. Ultrason., Ferroelec., Freq. Contr.* 54.4, pp. 746–756 (cit. on p. 73).

Pedersen, M. M., M. J. Pihl, P. Haugaard, J. M. Hansen, K. L. Hansen, M. B. Nielsen, and J. A. Jensen (2012). "Comparison of Real-Time In Vivo Spectral and Vector Velocity Estimation". In: *Ultrasound Med. Biol.* 38.1, pp. 145–151 (cit. on p. 73).

Pihl, M. J. and J. A. Jensen (2014). "A Transverse Oscillation Approach for Estimation of Three-Dimensional Velocity Vectors. Part I: Concept and Simulation Study". In: *IEEE Trans. Ultrason., Ferroelec., Freq. Contr.* 61, pp. 1599–1607 (cit. on p. 74).

Pihl, M. J., J. Marcher, and J. A. Jensen (2012). "Phased-Array Vector Velocity Estimation Using Transverse Oscillations". In: *IEEE Trans. Ultrason., Ferroelec., Freq. Contr.* 59.12, pp. 2662–2675 (cit. on p. 73).

Pihl, M. J., M. B. Stuart, B. G. Tomov, M. F. Rasmussen, and J. A. Jensen (2014). "A Transverse Oscillation Approach for Estimation of Three-Dimensional Velocity Vectors. Part II: Experimental Validation". In: *IEEE Trans. Ultrason., Ferroelec., Freq. Contr.* 51.10, pp. 1608–1618 (cit. on p. 74).

Sumi, C. (2008). "Displacement vector measurement using instantaneous ultrasound signal phase - Multidimensional autocorrelation and Doppler methods". In: *IEEE Trans. Ultrason., Ferroelec., Freq. Contr.* 55.1, pp. 24–43 (cit. on p. 73).

Udesen, J. and J. A. Jensen (2006). "Investigation of Transverse Oscillation Method". In: *IEEE Trans. Ultrason., Ferroelec., Freq. Contr.* 53, pp. 959–971 (cit. on pp. 73, 75, 76).

Udesen, J., M. B. Nielsen, K. R. Nielsen, and J. A. Jensen (2007). "Examples of in-vivo blood vector velocity estimation". In: *Ultrasound Med. Biol.* 33, pp. 541–548 (cit. on p. 73).

Varray, F. and H. Liebgott (2013). "Multi-resolution transverse oscillation in ultrasound imaging for motion estimation". In: *IEEE Trans. Ultrason., Ferroelec., Freq. Contr.* 60.7, pp. 1333–1342 (cit. on p. 74).

References from Chapter 8

Bae, M. H. and M. K. Jeong (2000). "A study of synthetic-aperture imaging with virtual source elements in B-mode ultrasound imaging systems". In: *IEEE Trans. Ultrason., Ferroelec., Freq. Contr.* Vol. 47, pp. 1510–1519 (cit. on p. 84).

Frazier, C. H. and W. D. O'Brien (1998). "Synthetic aperture techniques with a virtual source element". In: *IEEE Trans. Ultrason., Ferroelec., Freq. Contr.* 45.1, pp. 196–207. DOI: 10.1109/58.646925 (cit. on p. 84).

Hansen, J. M., M. C. Hemmsen, and J. A. Jensen (2011). "An object-oriented multi-threaded software beamformation toolbox". In: *Proc. SPIE Med. Imag.* Vol. 7968, pages. DOI: 10.1117/12.878178 (cit. on p. 88).

Jensen, J. A. (1996). "Field: A Program for Simulating Ultrasound Systems". In: *Med. Biol. Eng. Comp.* 10th Nordic-Baltic Conference on Biomedical Imaging, Vol. 4, Supplement 1, Part 1, pp. 351–353 (cit. on p. 87).

Jensen, J. A. and N. B. Svendsen (1992). "Calculation of Pressure Fields from Arbitrarily Shaped, Apodized, and Excited Ultrasound Transducers". In: *IEEE Trans. Ultrason., Ferroelec., Freq. Contr.* 39, pp. 262–267 (cit. on p. 87).

Passmann, C. and H. Ermert (1996). "A 100-MHz ultrasound imaging system for dermatologic and ophthalmologic diagnostics". In: *IEEE Trans. Ultrason., Ferroelec., Freq. Contr.* 43, pp. 545–552 (cit. on p. 84).

Villagomez-Hoyos, C. A. (2016). "Synthetic Aperture Vector Flow Imaging". PhD thesis. Technical University of Denmark. URL: http://findit.dtu.dk/en/catalog/2347162876 (cit. on p. 85).

Villagomez-Hoyos, C. A., M. B. Stuart, T. Bechsgaard, M. B. Nielsen, and J. A. Jensen (2016). "High frame rate synthetic aperture vector flow imaging for transthoracic echocardiography". In: *Proc. SPIE Med. Imag.* (Cit. on p. 85).

References from Chapter 9

Denarie, B., T. A. Tangen, I. K. Ekroll, N. Rolim, H. H. Torp, T. Bjastad, and L. Løvstakken (2013). "Coherent Plane Wave Compounding for Very High Frame Rate Ultrasonography of Rapidly Moving Targets". In: *IEEE Trans. Ultrason., Ferroelec., Freq. Contr.* 32.7, pp. 1265–1276 (cit. on p. 118).

FDA (2008). *Information for Manufacturers Seeking Marketing Clearance of Diagnostic Ultrasound Systems and Transducers*. Tech. rep. Center for Devices, Radiological Health, United States Food, and Drug Administration (cit. on pp. 104, 105).

Gammelmark, K. L. and J. A. Jensen (2014). "2-D Tissue Motion Compensation of Synthetic Transmit Aperture Images". In: *IEEE Trans. Ultrason., Ferroelec., Freq. Contr.* Pp. 594–610. DOI: http://dx.doi.org/10.1109/TUFFC.2014.2948 (cit. on p. 118).

Hansen, K. L., J. Udesen, F. Gran, J. A. Jensen, and M. B. Nielsen (2008). "Fast Blood Vector Velocity Imaging using ultrasound, In-vivo examples of complex blood flow in the vascular system". In: *Proc. IEEE Ultrason. Symp.* Pp. 1068–1071 (cit. on p. 109).

Hemmsen, M. C., L. Lassen, T. Kjeldsen, J. Mosegaard, and J. A. Jensen (2015). "Implementation of real-time duplex synthetic aperture ultrasonography". In: *Proc. IEEE Ultrason. Symp.* Pp. 1–4 (cit. on p. 113).

IEC (2015). *Medical electrical equipment - Part 2-37: Particular requirements for the basic safety and essential performance of ultrasonic medical diagnostic and monitoring equipment*. Tech. rep. IEC 60601-2-37. Edition 2.1 2015-06. International Electrotechnical Commission (cit. on p. 105).

Jensen, J. A., H. Holten-Lund, R. T. Nilsson, M. Hansen, U. D. Larsen, R. P. Domsten, B. G. Tomov, M. B. Stuart, S. I. Nikolov, M. J. Pihl, Y. Du, J. H. Rasmussen, and M. F. Rasmussen (2013). "SARUS: A Synthetic Aperture Real-Time Ultrasound System". In: *IEEE Trans. Ultrason., Ferroelec., Freq. Contr.* 60.9, pp. 1838–1852 (cit. on p. 95).

Jensen, J. A., M. F. Rasmussen, M. J. Pihl, S. Holbek, C. A. Villagomez-Hoyos, D. P. Bradway, M. B. Stuart, and B. G. Tomov (2016). "Safety Assessment of Advanced Imaging Sequences, I: Measurements". In: *IEEE Trans. Ultrason., Ferroelec., Freq. Contr.* 63.1, pp. 110–119 (cit. on p. 104).

Lai, S. S. M., B. Y. S. Yiu, A. K. K. Poon, and A. C. H. Yu (2013). "Design of Anthropomorphic Flow Phantoms Based on Rapid Prototyping of Compliant Vessel Geometries". In: *Ultrasound Med. Biol.* 39.9, pp. 1654–1664 (cit. on p. 104).

Lai, X., H. Torp, and K. Kristofferson (1997). "An Extended Autocorrelation Method for Estimation of Blood Velocity". In: *IEEE Trans. Ultrason., Ferroelec., Freq. Contr.* 44.6, pp. 1332–1342 (cit. on p. 118).

References from Chapter 10

Lui, E., A. Steinman, R. Cobbold, and K. Johnston (2005). "Human factors as a source of error in peak Doppler velocity measurement". In: *J. Vasc. Surg.* 42.5, pp. 972–979. DOI: 10.1016/j.jvs.2005.07.014 (cit. on p. 124).

Pedersen, M. M., M. J. Pihl, P. Haugaard, J. M. Hansen, K. L. Hansen, M. B. Nielsen, and J. A. Jensen (2012). "Comparison of Real-Time In Vivo Spectral and Vector Velocity Estimation". In: *Ultrasound Med. Biol.* 38.1, pp. 145–151 (cit. on p. 124).

Ricci, S., L. Bassi, and P. Tortoli (2014). “Real-time vector velocity assessment through multigate Doppler and plane waves”. In: *IEEE Trans. Ultrason., Ferroelec., Freq. Contr.* 61.2, pp. 314–324 (cit. on p. 124).

Tortoli, P., M. Lenge, D. Righi, G. Ciuti, H. Liebgott, and S. Ricci (2015). “Comparison of carotid artery blood velocity measurements by vector and standard Doppler approaches”. In: *Ultrasound Med. Biol.* 41.5, pp. 1354–1362. DOI: 10.1016/j.ultrasmedbio.2015.01.008 (cit. on p. 124).

Paper I

A Vector Flow Imaging Method for Portable Ultrasound using Synthetic Aperture Sequential Beamforming

Tommaso Di Ianni, Carlos Armando Villagómez-Hoyos, Caroline Ewertsen, Thomas Kim Kjeldsen, Jesper Mosegaard, Michael Bachmann Nielsen, and Jørgen Arendt Jensen

Accepted for publication after minor revisions in *IEEE Trans. Ultrasons., Ferroelec., Freq. Contr.*

A Vector Flow Imaging Method for Portable Ultrasound using Synthetic Aperture Sequential Beamforming

Tommaso Di Ianni[1], Carlos Armando Villagómez Hoyos[1], Caroline Ewertsen[2], Thomas Kim Kjeldsen[3], Jesper Mosegaard[3], Michael Bachmann Nielsen[2], and Jørgen Arendt Jensen[1]

[1]Center for Fast Ultrasound Imaging, Department of Electrical Engineering, Technical University of Denmark, Kongens Lyngby 2800, Denmark
[2]Department of Radiology, Rigshospitalet, Copenhagen University Hospital, Copenhagen 2100, Denmark
[3]Visual Computing Lab, Alexandra Institute, Aarhus 8200, Denmark

***Abstract*—This paper presents a vector flow imaging (VFI) method for the integration of quantitative blood flow imaging in portable ultrasound systems. The method combines directional transverse oscillation (TO) and synthetic aperture sequential beamforming (SASB) to yield continuous velocity estimation in the whole imaging region. Six focused emissions are used to create a high-resolution image (HRI), and a dual-stage beamforming approach is used to lower the data throughput between the probe and the processing unit. The transmit/receive focal points are laterally separated to obtain a TO in the HRI that allows for the velocity estimation along the lateral and axial directions using a phase-shift estimator. The performance of the method was investigated with constant flow measurements in a flow rig system using the SARUS scanner and a 4.1 MHz linear array. A sequence was designed with interleaved B-mode and flow emissions to obtain continuous data acquisition. A parametric study was carried out to evaluate the effect of critical parameters. The vessel was placed at depths from 20 to 40 mm, with beam-to-flow angles of 65°, 75°, and 90°. For the lateral velocities at 20 mm, a bias between -5% and -6.2% was obtained, and the standard deviation (SD) was between 6% and 9.6%. The axial bias was lower than 1% with a SD around 2%. The mean estimated angles were $66.70 \pm 2.86°$, $72.65 \pm 2.48°$, and $89.13 \pm 0.79°$ for the three cases. A proof-of-concept demonstration of the real-time processing and wireless transmission was tested in a commercial tablet obtaining a frame rate of 27 fps and a data rate of 14 MB/s. An *in-vivo* measurement of a common carotid artery of a healthy volunteer was finally performed to show the potential of the method in a realistic setting. The relative SD averaged over a cardiac cycle was 4.33%.**

***Index Terms*—Vector flow imaging, synthetic aperture, transverse oscillation, portable ultrasound.**

I. Introduction

Noninvasive imaging of blood flow using ultrasound is extensively used in the clinic due to the high temporal resolution, the portability, and the low cost compared with other imaging modalities. Pocket-size devices have the potential to bring ultrasound out of the radiology department, increasing its use in other medical fields with improved diagnostic accuracy and cost-effectiveness [1]–[3]. As highlighted by Prinz and Voigt [1], however, limited flow imaging capabilities and the absence of the spectral Doppler prevent the possibility of quantitative flow measurements, and further improvements are needed.

Vector flow imaging (VFI) methods estimate the velocity vectors directly from the measured ultrasound data with no need for manual angle adjustments and allow for the quantitative analysis of the blood flow even in presence of fast and complex flow dynamics [4]–[6]. The estimated angle can be used to reduce the inter-observer variability in the detection of the peak systolic velocity (PSV) [7]–[9]. Integrating the VFI feature in a portable scanner would improve the operator's workflow and reduce the inter-observer variability due to the angle-independent velocity estimation [10].

A first VFI approach relies on the combination of velocity components measured along several directions to obtain the estimated vector [11]. The 2-D tracking of blood speckle patterns was proposed by Trahey *et al.* [12], and was combined with plane wave (PW) excitation [13]. PWs have also been used in a number of other VFI approaches [14], [15]. Jensen and Munk [16] and Anderson [17] proposed the introduction in the ultrasound field of a transverse oscillation (TO), i.e. an oscillation lateral to the direction of the beam, which creates a modulation in the received signals proportional to the lateral displacement. Therefore, the velocity can be estimated along the lateral and axial directions using a phase-shift estimator [18]. Liebgott *et al.* [19] and Sumi [20] synthesized a TO by using a synthetic aperture (SA) for the optimization of the lateral oscillation frequency. A directional TO (DTO) approach was also proposed by Jensen [21] using directional beamforming in the lateral direction.

Parallel techniques as PW and SA acquire an entire image after every emission and provide continuous data [13], [22]. As a result, the time of observation is solely limited by the non-stationarity of the flow, and long sequences can be used for the estimation to obtain low standard deviation (SD) and high frame rate. In addition, the clutter filter has reduced complexity. Nevertheless, these techniques require considerable computational resources and conventional implementations are not suitable for a portable scanner.

An alternative solution is provided by SA sequential beam-

forming (SASB) [23]. In SASB, the data received by an aperture of L transducers are first beamformed in a static point, and one single line is obtained per emission, referred to as low-resolution line (LRL). The first beamformer can be integrated into the transducer front-end to reduce the data throughput of the probe by a factor L [24], [25]. The fixed focal position is considered as a virtual source (VS) [26]–[28], and a second beamformer is used to re-focus the LRLs and obtain a high-resolution image (HRI) dynamically focused in transmit and receive. Due to the dual-stage beamforming, SASB alleviates the system requirements compared with conventional SA and enables the wireless transmission of the data with current Wi-Fi technologies. The 1-D flow estimation using SASB has been previously demonstrated by Li and Jensen [29], and the sequence has been implemented in a consumer level tablet by Hemmsen *et al.* [30].

In this paper, a 2-D VFI method is proposed for a portable ultrasound system combining SASB and DTO. The paper is an extension of [31]. B-mode and flow emissions are interleaved to obtain continuous data acquisition, and six emissions are used for each flow HRI. The TO is created in the HRIs due to the spatial distribution of the VSs, which are divided in two virtual apertures (VAs) separated by a lateral distance. The velocity estimation is, therefore, performed by correlating a number of HRIs in the two directions.

The remainder of the paper is organized as follows: the creation of the TO using SASB and the velocity estimator are introduced in Section II. The imaging setup and the processing are described in Section III. The experimental investigations are introduced in Section IV and the results for the constant flow measurements and *in-vivo* images from a common carotid artery are presented in Section V. The results are finally discussed in Section VI.

II. Theory

To estimate the 2-D velocity components, a point spread function (PSF) oscillating in both the axial and lateral directions is needed. For the analytical derivation of the PSF, readers are referred to [16] and [19]. The frequency of the lateral oscillation is $f_x = Dp/2\lambda z$ in the case of a broad transmit beam. Here, D is the lateral distance between the apertures in number of transducer elements, p the pitch of the array, λ the axial wavelength equal to c/f_0, and z the distance from the apertures. If separated apertures are used in both transmit and receive, as for the method proposed here, the lateral frequency is doubled, and it is

$$f_x = \frac{1}{\lambda_x} = \frac{Dp}{\lambda z}, \tag{1}$$

where λ_x is the lateral wavelength.

The expression in (1) is strictly valid only for continuous wave excitation and at the transmit focus, hence it represents an approximation for pulsed wave emissions. Inaccurate frequencies yield biased velocities, and for this reason, f_x has to be directly estimated from the acquired ultrasound data using DTO, as previously shown in [21]. Also, DTO does not require the calibration of the beamformers at each depth as in conventional TO.

A. TO creation using SASB

The novelty of the method proposed in this paper is the creation of the TO based on SASB using fixed-focused emissions in transmit and receive. This allows for a reduction of the data throughput that makes the method suitable for implementation on a wireless system. In this section, the acquisition and beamforming are described to provide an understanding of the method.

1) Acquisition: The acquisition sequence is schematically displayed in Fig. 1. K emissions are sequentially transmitted at regular intervals of T_{PRF}, with $K = 4$ in the figure. At each emission, L transducer elements are excited and focused in a point located behind the array, therefore a diverging wave is emitted to insonify the area inside the dashed line. The focal positions can be considered as VSs [26]–[28], and are laterally divided in two VAs to create a TO as described in the beamforming section. The VAs are laterally separated by a distance of D transducer elements. In Fig. 1, the left VA is depicted in blue and the right VA in red.

2) Beamforming: The dual-stage beamforming involved in the method presented in this paper is shown in Fig. 2. For the sake of simplicity, a case is considered with one single VS per aperture ($K = 2$). The received data from L transducers at each emission is focused by a first beamformer in a static point corresponding to the VS, and a LRL is obtained. The VS is therefore also considered a virtual receiver (VR), the response of which is the LRL. This is optimally focused only at the focal position. The first beamformer can be integrated in the probe handle [24], [25] and one single LRL has to be transmitted to the second stage after each emission. The data throughput between the probe and the processing unit is thus reduced by a factor L compared to a full SA system. In the second stage, the data in the LRLs are refocused based on the VS/VR assumption. In Fig. 2, the PSF is shown in the second-stage boxes for the left VS on the top and for the right VS on the bottom. The computational complexity of the second stage equals that of a monostatic SA beamformer, where the LRLs are used in place of the transducer signals. For a thorough understanding of the second beamformer, readers are referred to [23].

A PSF oscillating in both directions is obtained in the HRI by coherently combining the responses from the VSs in the left and right VAs. The example of a double-oscillating PSF at a depth of 20 mm with a distance $D = 48$ between the VAs is displayed in Fig. 2 after the summation. The top plot shows the 2-D PSF and the bottom plot the lateral sampling along the blue dashed line.

The shape of the PSF is affected by the distance D as given by (1) and by the number K of VSs. In particular, the lateral width of the PSF can be reduced by increasing K to yield better resolution. On the other hand, a narrower PSF gives a broader lateral bandwidth, which in turn increases the lateral bias as discussed in [32]. Furthermore, the velocity range decreases with increasing K due to aliasing as discussed in Sec. II-B

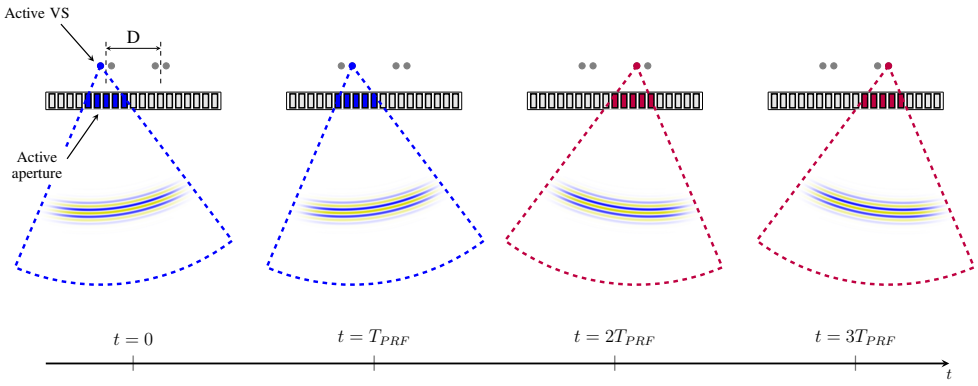

Fig. 1. Acquisition sequence for the SASB TO method. K emissions are sequentially transmitted at regular intervals of T_{PRF}, with $K = 4$ in this example. Each emission is focused behind the array, therefore a diverging wave is emitted to insonify the area inside the dashed line. The focal positions are considered as VSs, and are laterally divided in two VAs. The left VA is depicted in blue and the right one in red.

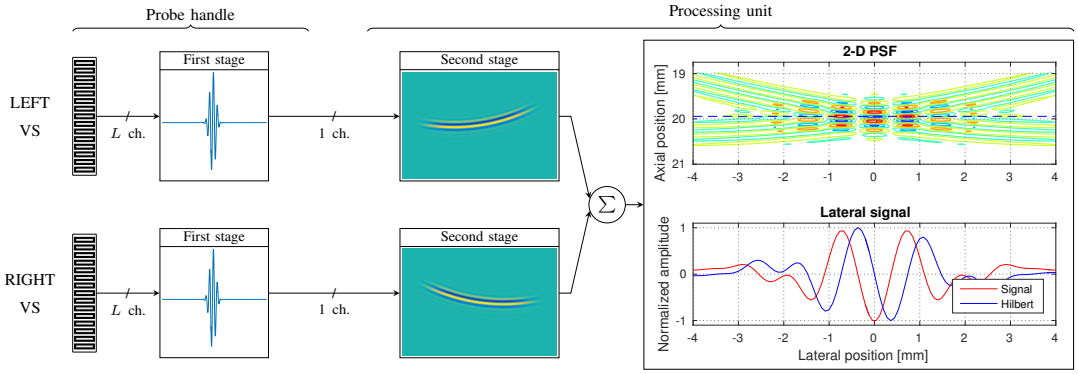

Fig. 2. Beamforming involved in the creation of a TO using SASB in the case with one single VS per aperture ($K = 2$). For each emission, the data received from L transducers is focused by a first beamformer in a static point corresponding to the VS, and a LRL line is obtained. The VS is therefore also considered a virtual receiver (VR), the response of which is the LRL. In the second stage, the data in the LRLs are refocused based on the VS/VR assumption. The PSF is shown in the second-stage boxes for the left and right VSs. To obtain a double-oscillating PSF, the responses from the left and right VAs are coherently combined. The 2-D PSF is shown after summation in the top plot, and the lateral signal along the blue dashed line is shown in the bottom plot.

B. Velocity estimation

The velocity vectors can be estimated from the HRIs produced by the second-stage beamformer based on DTO [21]. The estimator's equations are reviewed here. To estimate the velocity at a given point, M samples are selected in the HRI centred around the velocity point to create a lateral signal $s(m, n, e)$. Here, m is the sample index along the lateral direction, i.e. $m = -M/2, ..., M/2 - 1$, n is the axial sample index, and e the index of the HRI. The analytic signal is calculated as

$$r_{sq}(m, n, e) = s(m, n, e) + j\mathcal{H}_m\{s\}(m, n, e), \qquad (2)$$

where $\mathcal{H}_m$ is the Hilbert transform in the lateral direction m. The lateral frequency can be estimated at each depth as

$$f_x(n) = \frac{1}{\lambda_x(n)} = \frac{\sum_{f=-F/2}^{F/2-1} \frac{f}{F\Delta x} |R_{sq}(f, n, e)|^2}{\sum_{f=-F/2}^{F/2-1} |R_{sq}(f, n, e)|^2}, \qquad (3)$$

with $R_{sq}(f, n, e) = \mathcal{F}_m\{r_{sq}(m, n, e)\}$ the Fourier transform of r_{sq} along the lateral direction m, f the sample index in the discrete Fourier domain, F the number of Fourier coefficients, and Δx the lateral sampling period. The lateral frequencies from a number of HRIs can be averaged to obtain smoother estimates. In addition, f_x can be averaged along the depth over a pulse length.

In the PSF in Fig. 2, a lateral beamformed signal and its Hilbert transform are displayed in the bottom graph from a point scatterer at a depth of 20 mm for $K = 6$ and $D = 48$. The analytic signal is used to calculate the lateral frequency using (3).

Two signals are created from r_{sq},

$$\begin{aligned} r_1(m, n, e) &= r_{sq}(m, n, e) + j\mathcal{H}_n\{r_{sq}\}(m, n, e), \\ r_2(m, n, e) &= r_{sq}(m, n, e) - j\mathcal{H}_n\{r_{sq}\}(m, n, e), \end{aligned} \qquad (4)$$

where $\mathcal{H}_n$ is the Hilbert transform in the axial direction n,

and the lag-1 autocorrelation functions are calculated as

$$R_1(1) = \frac{1}{M(N-1)} \sum_{m=-M/2}^{M/2-1} \sum_{e=0}^{N-2} r_1^*(m,n,e) r_1(m,n,e+1),$$
$$R_2(1) = \frac{1}{M(N-1)} \sum_{m=-M/2}^{M/2-1} \sum_{e=0}^{N-2} r_2^*(m,n,e) r_2(m,n,e+1). \quad (5)$$

The autocorrelation estimates in (5) are averaged over M lateral samples and N HRIs. The lateral and axial velocities are finally estimated as [18], [21]

$$v_x = \frac{\lambda_x}{2\pi 2T} \times \arctan\left(\frac{\Im\{R_1(1)\}\Re\{R_2(1)\} + \Im\{R_2(1)\}\Re\{R_1(1)\}}{\Re\{R_1(1)\}\Re\{R_2(1)\} - \Im\{R_1(1)\}\Im\{R_2(1)\}}\right), \quad (6)$$

$$v_z = \frac{\lambda}{2\pi 4T} \times \arctan\left(\frac{\Im\{R_1(1)\}\Re\{R_2(1)\} - \Im\{R_2(1)\}\Re\{R_1(1)\}}{\Re\{R_1(1)\}\Re\{R_2(1)\} + \Im\{R_1(1)\}\Im\{R_2(1)\}}\right), \quad (7)$$

with T the period between successive HRIs, and $\Re$ and $\Im$ the real and imaginary parts. The velocities v_x and v_z can be estimated for every point in the image after N HRIs are acquired.

The value of v_x in (6) is directly proportional to λ_x, therefore it is important to use the estimated value and avoid biasing of the lateral velocities. The length M used in (3) can, in general, be different than that used in (5). Longer signals in (3) provide better estimates due to the reduced spectral broadening, while lower SD can be achieved by averaging (5) over a greater M. Nevertheless, this reduces the spatial resolution of the estimates. The distance D can be chosen to optimize the lateral wavelength as pointed out in (1).

The range of detectable velocities is limited by aliasing, which is more severe here due to the acquisition of the HRIs over a number of K emissions. The limit for v_x is

$$|v_x| \leq v_x^{max} = \frac{1}{4}\frac{\lambda_x}{T} = \frac{1}{4}\frac{\lambda z}{Dp}\frac{1}{T}, \quad (8)$$

where (1) is used for λ_x, and for v_z it is

$$|v_z| \leq v_z^{max} = \frac{1}{4}\frac{\lambda}{T}. \quad (9)$$

The maximum v_x is lower for increased D due to the shorter lateral wavelength. Both (8) and (9) are inversely proportional to T, and this is in turn given by the T_{PRF} and the number K of VSs. Therefore, a tradeoff exists between the resolution of the PSF and the maximum detectable velocity.

III. Methods

The method was first investigated through constant flow measurements in a flow rig system, and then the measurement of a common carotid artery was performed to test the performance *in vivo*. A parametric study was carried out to optimize the imaging parameters prior to the *in vivo* measurement. In this section, the details are provided about the imaging setup and the processing parameters used in the experiments.

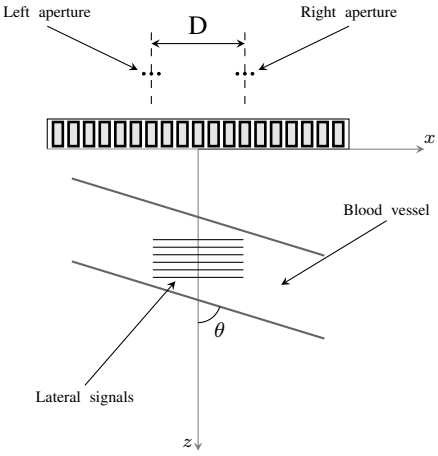

Fig. 3. Imaging setup including the transducer array and the imaged vessel. The vessel was positioned below with a beam-to-flow angle θ. $K = 6$ VSs were used for each flow HRI, spatially divided in two VAs separated by a distance D.

TABLE I
Transducer parameters

Parameter	Value	Unit
Array type	Linear	-
Element pitch - p	0.2	mm
Element height	6	mm
Number of elements	192	-
Elevation focus	38	mm
Center frequency	4.1	MHz

A. Imaging setup

In Fig. 3, the setup is shown including the transducer array and the imaged vessel. The position of the VAs relative to the array is also displayed. A 0.55λ-pitch linear array was used, with the parameters shown in Table I. The array was connected to the SARUS scanner [33] for the acquisition of the element data. The vessel was positioned below the transducer with a beam-to-flow angle θ (Fig. 3). A duplex sequence was designed with the parameters in Table II. The VAs were positioned behind the transducer and steered toward the center of the image with an angle of $\pm 2.5°$. The distance D was optimized in the parametric study described in Section IV, and its values are reported in Table III, where the default is displayed in bold. The B-mode VSs were regularly distributed between ± 15 mm in the lateral direction.

The pulse repetition frequency was set to $PRF = 9$ kHz for the constant flow and 15 kHz for the *in vivo* measurements. B-mode and flow emissions were interleaved to achieve continuous data acquisition, i.e. one B-mode pulse was transmitted after every $K = 6$ flow emissions, with an effective repetition frequency $PRF_{eff} = PRF/(K+1)$. The period T in (6), (7), (8), and (9) is, thus, equal to $1/PRF_{eff} = (K+1)/PRF$.

TABLE II
FIXED IMAGING SETUP AND PROCESSING PARAMETERS

Parameter	Flow	B-mode	Value
Imaging setup			
Excitation	4 cycles	2 cycles	-
Center frequency - f_0	4.1		MHz
Transmit apodization	Tukey ($\alpha = 0.6$)		-
Receive apodization	Tukey ($\alpha = 0.6$)		-
VS axial position	−15	−30	mm
Active elements	64	96	-
f-number - f#	-1.17	-1.56	-
Number of VSs	$K = 6$	64	-
VA apodization	Rect	-	-
Pulse repetition freq. - PRF:			
Constant flow	9		kHz
In-vivo	15		kHz
Processing			
Lateral sampling interval	0.1		mm
Axial sampling frequency	35		MHz

TABLE III
VARIED IMAGING SETUP AND PROCESSING PARAMETERS

Parameter	Value	Unit
Distance between VAs - D	16 - 24 - 32 - 40 **48** - 56 - 64	transducer elements
Lateral signal length - M	4 - 8 - 16 24 - **32** - 48	samples
Number of HRIs - N	4 - 8 - 16 - **32** 64 - 96 - 128	-

B. Processing

The processing scripts were developed in MATLAB (The MathWorks, Inc., Natick, MA, USA), and the beamformation was performed using the BFT3 toolbox [34]. The measured element data were beamformed in the first-stage beamformer and then matched filtered. For the flow data, a stationary echo cancelling filter was used as described in Section III-C. The HRIs were beamformed by the second stage in a Cartesian grid and were Hilbert transformed in the lateral direction. The directional signals were created by selecting the lateral samples. The frequency f_x was estimated as in (3) for all the depths using signals of $M = 64$ samples, and averaged over $N = 64$ HRIs and a pulse length in the axial direction. The curve $f_x(n)$ was then inverted, and a line was fitted to the λ_x. The estimation of $f_x(n)$ was performed only once, and can be considered as an initialization procedure. The lateral frequency displayed in Fig. 4 was estimated from a speckle phantom measurement with $D = 48$. The hyperbole displayed in black was obtained from the linear fit to the estimated λ_x. The green curve shows the theoretical f_x calculated using (1), with $c = 1540\,\mathrm{m\,s^{-1}}$ and z the axial distance from the VAs. The theoretical equation overestimates f_x and would provide biased velocities.

The length M used for the velocity estimation was changed as in Table III, where the default value is displayed in bold. The autocorrelation functions in (5) were calculated from N consecutive HRIs, and averaged over M lateral samples and a pulse length in the axial direction. The performance with varying N was also investigated in the parametric study, and the values are reported in Table III with the default value displayed in bold. The velocity estimates were averaged over a pulse length.

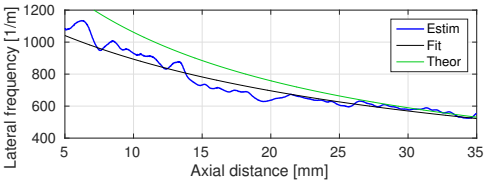

Fig. 4. Lateral frequency estimated from a speckle phantom measurement with $D = 48$ using lateral signals of $M = 64$ samples. The estimated frequencies were averaged over $N = 64$ HRIs and a pulse length in the axial direction. The hyperbole displayed in black was obtained from the linear fit to the estimated λ_x. The green curve shows the theoretical frequency calculated using (1), with $c = 1540\,\mathrm{m\,s^{-1}}$.

The B-mode HRIs were beamformed by the second stage beamformer and the analytic signals were calculated using a Hilbert transform in the axial direction. The envelope-detected and log-compressed images were shown with a dynamic range of 40 dB. The processing parameters for the flow and B-mode data are reported in Table II.

C. Clutter filter

A schematic representation of the amplitude spectrum of the received signal $G(f)$ is displayed in Fig. 5 to show the principle of operation of the clutter filter used in this study. The tissue component $G_t(f)$ is low-frequency, and its bandwidth depends upon the velocity distribution in the tissue. $G_b(f)$ is the signal from the blood and $G_n(f)$ is electronic noise. The energy of the signals is represented by the coloured areas. The goal of the clutter filter is to minimize the energy of G_t while preserving that of G_b.

A dual-stage filter was used. The first stage is a high-pass moving-average-subtraction filter $H_{hp}(f)$ with a −3 dB cutoff frequency of 120 Hz used on the LRLs. In ideal conditions of stationary tissue, $G_t(f)$ is narrowband and is effectively attenuated by $H_{hp}(f)$. However, significant components leak in the blood spectrum when tissue velocities cause a broadening of $G_t(f)$. These components have, in general, high amplitude and disrupt the velocity estimation.

The second stage consists of an amplitude threshold E, and sets $G(f) = E\ \forall f : G(f) > E$. This filter is used on the HRIs and removes any spectral components with amplitudes above the threshold E. As a result, the energy of G_t is further attenuated compared with that of G_b. The threshold E was determined after inspecting the spectrum of the signal received from inside the vessel calculated by means of a windowed fast Fourier transform (FFT). The time-domain signals were then restored after filtering by performing an inverse FFT. The approach has been previously used and described in [35] and [36].

The energy-based filter was used in addition to the moving average as the latter alone failed to properly attenuate the signal from the tissue during the systolic phase. However, the choice of E is critical to the performance of the estimator. If

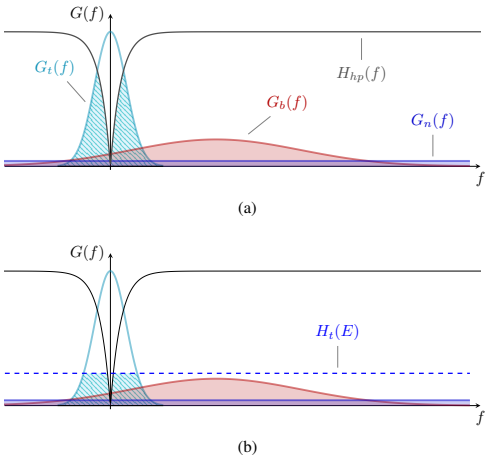

Fig. 5. Schematic representation of the amplitude spectrum of the received signal $G(f)$. $G_t(f)$ is the spectrum of the signal scattered by the surrounding tissue; $G_b(f)$ is the spectrum of the signal from the blood; and $G_n(f)$ is white noise from the measuring system. The energy of the components is highlighted by the coloured areas. (a): A high-pass filter $H_{hp}(f)$ is used to reduce the energy of G_t (area under the curve); (b): a second stage $H_t(E)$ is used to remove any spectral components with amplitude greater than a threshold E.

E is higher than the amplitude of the blood signal, a higher residual energy from the tissue signal will bias the estimation of the blood velocity. On the other hand, a low threshold will filter out energy from the blood spectrum.

IV. Experimental investigations

A. Constant flow measurements

Measurements were performed on a flow rig system consisting of a centrifugal pump (Cole-Parmer, Vernon-Hills, IL, USA) circulating a blood mimicking fluid, and a vessel with a radius of 6 mm immersed in a water bath. The entrance length of the vessel ensured a fully developed parabolic, laminar flow profile. The volume flow was measured for reference by a magnetic flow meter (MAG3000, Danfoss, Nordborg, Denmark) and was set to obtain a peak velocity of approximately $0.2\,\mathrm{m\,s^{-1}}$. The relative bias and SD were calculated inside the vessel from 50 independent velocity profiles.

A parametric study was first carried out to investigate the performance of the method as a function of the distance D, the length M, and the number N of HRIs used for the velocity estimation. The vessel was placed at a depth of approximately 20 mm with a beam-to-flow angle $\theta = 75°$. This setup was chosen to optimize the imaging parameters for the measurement of a common carotid artery.

The constant parabolic flow profile with $\theta = 75°$ was in addition measured with the default setup ($D = 48; M = 32; N = 32$) at a depth of approximately 30 and 40 mm, and at 20 mm for flow angles of 90° and 65°.

The range in (8) was shifted to $\left[-\frac{1}{4}v_x^{max}, \frac{7}{4}v_x^{max}\right]$ to match the velocities expected in the *in vivo* measurement. At the depth of 20 mm with $PRF = 9\,\mathrm{kHz}$, $v_x^{max} = 0.44\,\mathrm{m\,s^{-1}}$ and the velocity ranges are

$$\begin{aligned} -0.11\,\mathrm{m\,s^{-1}} \leq\ & v_x \leq\ 0.77\,\mathrm{m\,s^{-1}}, \\ -0.12\,\mathrm{m\,s^{-1}} \leq\ & v_z \leq\ 0.12\,\mathrm{m\,s^{-1}}. \end{aligned} \tag{10}$$

For the vessel at 65°, an axial velocity $v_z = v_z^{max} = 0.12\,\mathrm{m\,s^{-1}}$ gives a maximum peak velocity equal to $0.28\,\mathrm{m\,s^{-1}}$. A peak velocity of $0.2\,\mathrm{m\,s^{-1}}$ was used to avoid aliasing.

To show the performance of the method with lateral velocities closer to those detected *in vivo*, the flow rig measurements were repeated with the default setup and a vessel positioned at 90°. The peak velocity was set to 0.32, 0.44, and $0.5\,\mathrm{m\,s^{-1}}$ with $PRF = 9\,\mathrm{kHz}$. The velocity was then kept equal to $0.5\,\mathrm{m\,s^{-1}}$ to maintain laminar flow, and the PRF was lowered to 7.5 and 6.4 kHz to emulate velocities of 0.6 and $0.7\,\mathrm{m\,s^{-1}}$, respectively.

B. Real-time tablet implementation

The proposed method was implemented on a consumer level tablet for a proof-of-concept investigation of the feasibility of the wireless data transmission and real-time processing. The LRLs beamformed by the first-stage from the flow rig acquisition at 90° and $0.2\,\mathrm{m\,s^{-1}}$ were sampled at 20 MHz and sent to a Nexus 9 (HTC Corp., Taoyuan, Taiwan) through an RT-AC68U (ASUS, Taipei, Taiwan) Wi-Fi router to emulate a wireless probe. The tablet integrates a dual-core 64-bit CPU at 2.3 GHz and a Tegra K1 GPU, NVIDIA Corp., Santa Clara, CA, USA, with 192 shader cores and 2 GB DDR3 RAM. The LRLs were buffered into the tablet's memory and then beamformed by the second-stage. Sixteen HRIs of 32×512 samples were used for each velocity estimation. B-mode and VFI processing, including beamforming, stationary echo cancelling, velocity estimation and displaying, were implemented on the tablet's GPU through the OpenGL ES 3.1 API. The 2-D velocities were estimated from 16 HRIs in a region of $0.8\,\mathrm{cm} \times 1.9\,\mathrm{cm}$. The processing and wireless transmission were performed simultaneously to take into account the contribution of the Wi-Fi chipset to the heating of the system.

C. In vivo measurement

An *in vivo* measurement was performed after approval by the Danish National Committee on Biomedical Research Ethics. The right common carotid artery of a healthy 28-year-old volunteer was scanned with a longitudinal view by an experienced radiologist using the setup in Section III-A. The volunteer was asked to rest in a supine position for approximately 10 min before the measurement to ensure steady flow conditions.

The spatial-peak temporal-average intensity and mechanical index (MI) of the sequence were measured prior to the *in vivo* experiment to verify the fulfilment of the FDA safety guidelines. These require MI ≤ 1.9 and $I_{spta} \leq 720\,\mathrm{mW\,cm^{-2}}$ [37]. An Acoustic Intensity Measurement System AIMS III (Onda Corp., Sunnyvale, CA, USA) was used with a hydrophone Onda HGL-0400 following the procedure in [38]. The PRF was set to 500 Hz during the measurement to

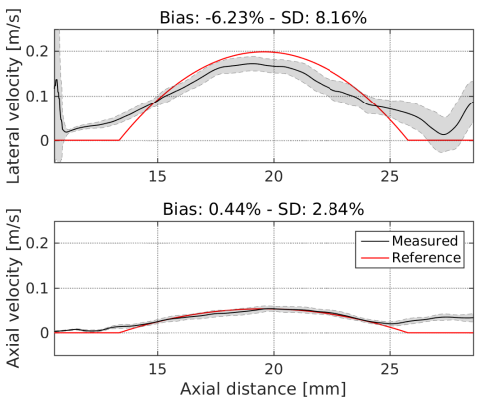

Fig. 6. Measured and reference profiles for the lateral (top) and axial (bottom) velocities measured in the flow rig for the default setup: $D = 48$; $M = 32$; $N = 32$. The vessel was placed at a depth of 20 mm with a flow angle of 75°.

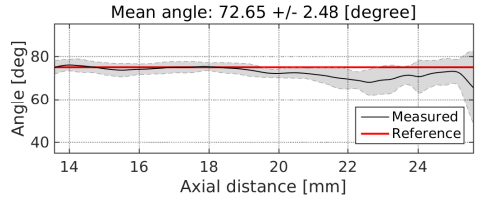

Fig. 7. Estimated angle inside the boundaries of a vessel measured for the default setup: $D = 48$; $M = 32$; $N = 32$. The vessel was placed at a depth of 20 mm with a flow angle of 75°.

avoid reverberations in the water tank. The derated MI was equal to 0.91 and the derated I_{spta} = 10.19 mW cm^{-2}. For PRF = 15 kHz, the intensity is therefore 305.74 mW cm^{-2}, which satisfies the FDA regulations. The temperature was also measured at the transducer surface and was within the FDA limits.

A sequence of 9.5 s of data was saved, and the processing was carried out off-line as described in Section III-B. To match the non-stationary characteristic of the flow, 16 HRIs were used for each flow estimation. The velocity estimates were shown with a frame rate of 350 frames per second (FPS), while the frame rate of the B-mode sequence was 33 FPS. The VFI video was paced down by a factor 14. A binary mask was generated from the B-mode images to discriminate the vessel area from the surrounding tissue. The velocity estimates were filtered using a median filter in a temporal window of 25 ms and a spatial window of 1 × 1 mm^2.

V. Results

A. Constant flow measurement

The estimated velocities for the default setup - $D = 48$; $M = 32$; $N = 32$ - are shown in Fig. 6 for the vessel at 20 mm and 75°. The mean profiles (black) and the SDs

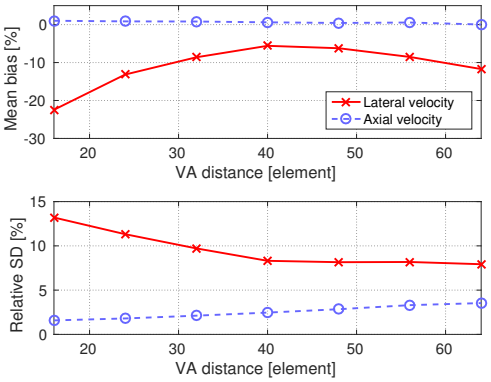

Fig. 8. Mean bias (top) and SD (bottom) as a function of the distance D between the VAs for the lateral and axial velocities. These were measured in the flow rig at a depth of 20 mm with a flow angle of 75°.

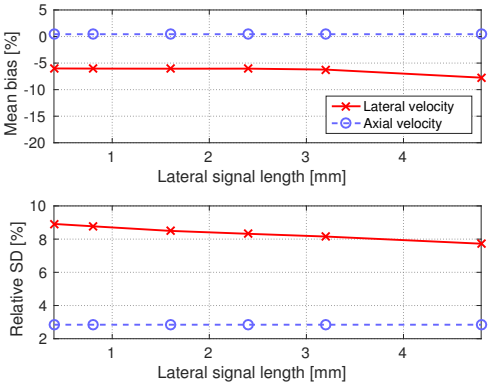

Fig. 9. Mean bias (top) and SD (bottom) as a function of the length M of the lateral signal expressed in mm. Lateral and axial flow profiles were measured in the flow rig at a depth of 20 mm with a flow angle of 75°.

(shaded regions) are plotted along with the reference profiles (red) calculated from the measured volume flow. The lateral and axial velocities are displayed in the top and bottom graphs, respectively. The mean bias is -6.23% and 0.44% in the lateral and axial directions, respectively. The mean SD is 8.16% and 2.84%. In Fig. 7, the estimated angle is shown as a function of the depth for the points inside the vessel boundaries, with a mean value of 72.65 ± 2.48°.

The results of the parametric study are displayed in Fig. 8, 9, and 10. The mean bias (top graph) and SD (bottom graph) are shown in Fig. 8 as a function of D for the lateral and axial profiles. By increasing D, shorter oscillation wavelengths are obtained in the lateral direction. For $D < 40$, λ_x is longer than the lateral signal ($M = 32$), and this results in increased bias of the lateral velocity. The mean lateral bias is between -5.6% and -11.7% for $D \geq 40$, and the SD is between 8.3% and 7.9%. The axial bias is lower than 1% in all the cases and the SD is between 1% and 3%.

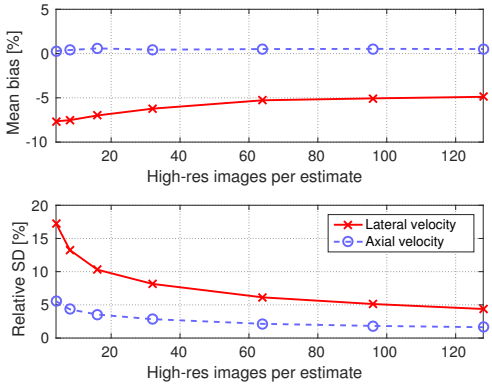

Fig. 10. Mean bias (top) and SD (bottom) as a function of the number N of HRIs used per velocity estimate. Lateral and axial flow profiles were measured in the flow rig at a depth of 20 mm with a flow angle of 75°.

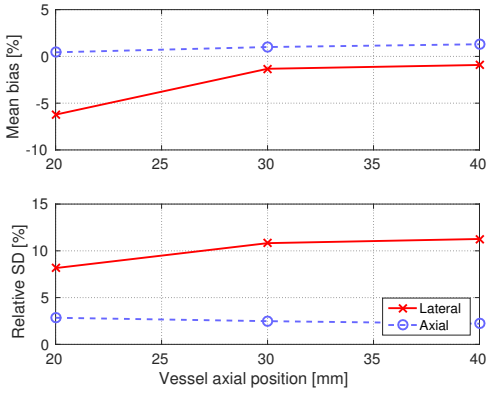

Fig. 11. Mean bias (top) and SD (bottom) for the lateral and axial flow profiles measured in the flow rig with a flow angle of 75° at depth from 20 to 40 mm.

In Fig. 9, a lower lateral SD is obtained by increasing M, while the other values are unaffected. Signals of only 4 samples can be used to reduce the computational complexity of the calculations. $M = 32$ was used in the rest of the experiments.

The mean bias in Fig. 10 is only slightly affected by increasing N, while the SDs decrease significantly. For $N = 128$, the SD is 4.4% and 1.6% in the lateral and axial directions.

In Fig. 11, the mean bias and SD are plotted as a function of the axial position of the vessel from 20 to 40 mm with θ = 75°. The lateral bias is between -6.2% and -0.9%, while the SD is between 8.2% and 11.2%. Constant performance is obtained for the axial velocity.

In Table IV, the results are show for the vessel at a depth of 20 mm with beam-to-flow angles of 90°, 75°, and 65°.

Finally, the mean bias and SD with increasing velocity are shown in Fig. 12. For velocities up to 0.6 m s^{-1}, the lateral bias is between -7.4% and 2.1% and the SD between 6.1% and 11.2%. An increased bias and SD (-15.4% and 24.3%) are found for 0.7 m s^{-1} because of the aliasing.

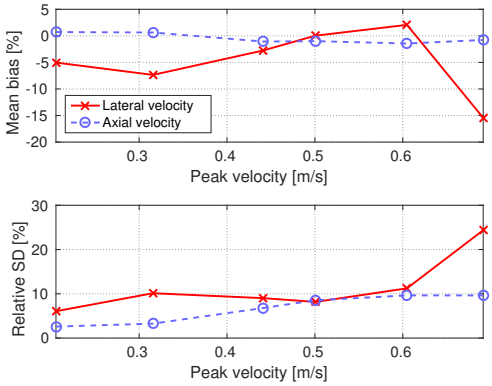

Fig. 12. Mean bias (top) and SD (bottom) for the lateral and axial flow profiles measured in the flow rig with a flow angle of 90° at 20 mm for peak velocities between 0.2 and 0.7 m s^{-1}. The velocities between 0.2 and 0.5 m s^{-1} were detected with PRF = 9 kHz, while for higher velocities the peak was kept equal to 0.5 m s^{-1} to avoid turbulent flow and the PRF was set to 7.5 and 6.4 kHz.

TABLE IV
CONSTANT FLOW MEASUREMENTS RESULTS

Flow angle	Lateral Bias	Lateral SD	Axial Bias	Axial SD	Estimated Angle
90°	-5.03%	6.06%	0.72%	2.59%	$89.13 \pm 0.79°$
75°	-6.23%	8.16%	0.44%	2.84%	$72.65 \pm 2.48°$
65°	5.62%	9.58%	0.32%	2.84%	$66.70 \pm 2.86°$

B. Real-time tablet implementation

The maximum data throughput between the tablet and the Wi-Fi router was first measured, and was higher than 30 MB/s. The peak frame rate of the tablet VFI processing was 27 FPS (37 ms/frame), which corresponds to a data rate of 14 MB/s. The processing frame rate was gradually lowered due to the heating of the chipset, and was 15 FPS after 12 min of continuous processing. It is, however, suitable for performing real-time imaging into the tablet. The data rate is lower than the maximum throughput between the tablet and the router, therefore the wireless transmission of the data can be achieved. The real time wireless transmission could not be tested concurrently with the acquisition of the data, since a wireless probe was not available.

C. In vivo measurement

The result of the *in vivo* measurement is shown in Fig. 13 and a video sequence is available in the digital version of the paper. In Fig. 13a and 13b, the B-mode and VFI images are shown at late diastole and peak systole, respectively. The arrows show the local velocity vectors and the underlying color map encodes the magnitude and angle as in the color wheel in the bottom-right corner. The velocity magnitude at the position indicated by the yellow circle in Fig. 13a is displayed in Fig. 13c for nine cardiac cycles. The red and magenta dots show

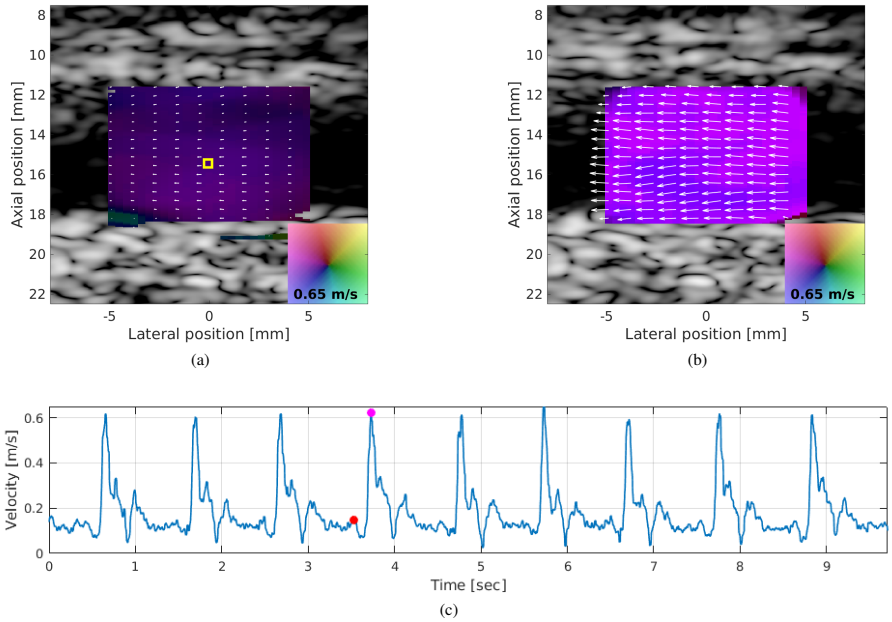

Fig. 13. VFI plot of a common carotid artery at late diastole (a) and peak systole (b) measured *in-vivo*. In (c), the velocity magnitude at the position indicated by the yellow circle in (a) is displayed as a function of the time for the nine measured cardiac cycles. The red and magenta circles shows the times at which the VFI images are plotted. The mean PSV for the nine measured heart cycles is $0.62\,\mathrm{m\,s^{-1}}$ with a SD of 2.9%.

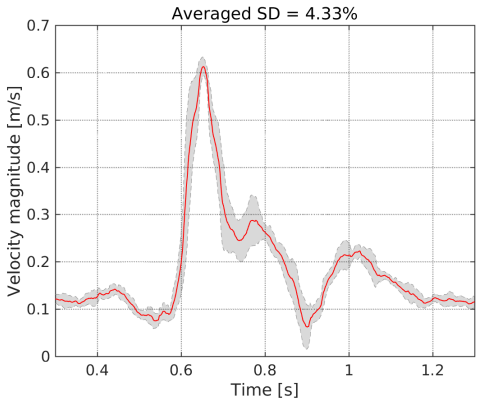

Fig. 14. Mean profile and relative SD calculated from 9 cardiac cycles measured in the common carotid artery. The relative SD averaged over a cardiac cycle is 4.33%.

the times at which the velocities are plotted in the top figures. The mean PSV from the nine heart cycles is $0.62\,\mathrm{m\,s^{-1}}$ with a SD of 2.9%.

The nine cycles in Fig. 13c were finally aligned by finding the peaks of the cross-correlation functions to calculate the mean profile and the relative SD plotted in Fig. 14. The relative SD averaged over a cardiac cycle is 4.33%. It should be noted that such measurements can be obtained anywhere in the VFI region at any time.

VI. Discussion

A VFI method was presented for a wireless ultrasound system combining SASB and DTO. The performance of the method was investigated with constant flow measurements in a flow rig system. A lateral mean bias between -5% and -6.2% was achieved, with a SD between 6% and 9.6% for beam-to-flow angles from 65° to 90°. The axial mean bias was lower than 1% with a SD around 2%. The scan of a common carotid artery of a 28-year-old healthy volunteer was performed to evaluate the potential of the method *in vivo* obtaining an average SD of 4.33% over nine cardiac cycle.

The method is developed for the integration of VFI in wireless systems. The proof-of-concept feasibility of the wireless transmission and the processing in a consumer level tablet were tested, achieving a peak frame rate of 27 FPS and a data rate of 14 MB/s, which is suitable for real-time flow imaging.

The limited data bandwidth required for the transmission of the first-stage LRLs makes it possible to implement a highly flexible framework, where real-time processing is firstly performed in the host system (e.g. tablet), and advanced and complex techniques can be retrospectively employed by sending the data to the cloud or to an external processing system. The velocities are simultaneously estimated everywhere

in the VFI image, and it is possible to obtain quantitative measurements in multiple points in a multi-gated approach without any manual angle correction.

A number of limitations are given by the sequential acquisition of the flow images over K emissions. First, distortions are introduced in the PSF because of the non stationarity of the medium throughout the acquisition time. Second, the long acquisition makes the method more affected by decorrelation of the scatterers. Finally, the range of detectable velocities is limited by aliasing, which depends upon the number of emissions used to create a HRI. Therefore, a tradeoff exists between the resolution of the method and the maximum detectable velocity. The velocity range can be, however, extended by using phase unwrapping methods [39].

ACKNOWLEDGEMENT

This work was supported by grant 82-2012-4 from the Danish National Advanced Technology Foundation and by BK Ultrasound.

REFERENCES

[1] C. Prinz and J. U. Voigt, "Diagnostic accuracy of a hand-held ultrasound scanner in routine patients referred for echocardiography," *J. Am. Soc. Echocardiog.*, vol. 24, no. 2, pp. 111–116, 2011.

[2] S. Lafitte, N. Alimazighi, P. Reant, M. Dijos, A. Zaroui, A. Mignot, M. Lafitte, X. Pillois, R. Roudaut, and A. D. Maria, "Validation of the smallest pocket echoscopic device's diagnostic capabilities in the heart investigation," *Ultrasound Med. Biol.*, vol. 37, no. 5, pp. 798–804, 2011.

[3] A. W. Kirkpatrick, M. Sirois, K. B. Laupland, D. Liu, K. Rowan, C. G. Ball, S. M. Hameed, R. Brown, R. Simons, S. A. Dulchavsky, D. R. Hamiilton, and S. Nicolaou, "Hand-held thoracic sonography for detecting post-traumatic pneumothoraces: the extended focused assessment with sonography for trauma (EFAST)," *J. Trauma*, vol. 57, no. 2, pp. 288–295, 2004.

[4] P. P. Sengupta, B. K. Khandheria, J. Korinek, A. Jahangir, S. Yoshifuku, I. Milosevic, and M. Belohlavek, "Left ventricular isovolumic flow sequence during sinus and paced rhythms: new insights from use of high-resolution Doppler and ultrasonic digital particle imaging velocimetry," *J. Am. Coll. Cardiol.*, vol. 49, no. 8, pp. 899–908, 2007.

[5] G.-R. Hong, G. Pedrizzetti, G. Tonti, P. Li, Z. Wei, J. K. Kim, A. Baweja, S. Liu, N. Chung, H. Houle, and et al., "Characterization and quantification of vortex flow in the human left ventricle by contrast echocardiography using vector particle image velocimetry," *JACC: Cardiovascular Imaging*, vol. 1, no. 6, pp. 705–717, 2008.

[6] K. L. Hansen, H. Møller-Sørensen, J. Kjaergaard, J. T. Lund, M. M. Pedersen, T. Lange, J. A. Jensen, and M. B. Nielsen, "Analysis of systolic backflow and secondary helical blood flow in the ascending aorta using vector flow imaging," *Ultrasound Med. Biol.*, vol. 42, no. 4, pp. 899–908, 2016.

[7] M. M. Pedersen, M. J. Pihl, P. Haugaard, J. M. Hansen, K. L. Hansen, M. B. Nielsen, and J. A. Jensen, "Comparison of real-time in vivo spectral and vector velocity estimation," *Ultrasound Med. Biol.*, vol. 38, no. 1, pp. 145–151, 2012.

[8] I. K. Ekroll, T. Dahl, H. Torp, and L. Løvstakken, "Combined vector velocity and spectral Doppler imaging for improved imaging of complex blood flow in the carotid arteries," *Ultrasound Med. Biol.*, vol. 40, no. 7, pp. 1629–1640, 2014.

[9] S. Ricci, D. Vilkomerson, R. Matera, and P. Tortoli, "Accurate blood peak velocity estimation using spectral models and vector Doppler," *IEEE Trans. Ultrason., Ferroelec., Freq. Contr.*, vol. 62, no. 4, pp. 686–696, 2015.

[10] R. W. Gill, "Measurement of blood flow by ultrasound: Accuracy and sources of error," *Ultrasound Med. Biol.*, vol. 11, pp. 625–641, 1985.

[11] P. Peronneau, J.-P. Bournat, A. Bugnon, A. Barbet, and M. Xhaard, "Theoretical and practical aspects of pulsed doppler flowmetry real-time application to the measure of instantaneous velocity profiles in vitro and in vivo," in *Cardiovascular applications of ultrasound*, R. Reneman, Ed. North Holland Publishing,, 1974, pp. 66–84.

[12] G. E. Trahey, J. W. Allison, and O. T. von Ramm, "Angle independent ultrasonic detection of blood flow," *IEEE Trans. Biomed. Eng.*, vol. BME-34, no. 12, pp. 965–967, 1987.

[13] J. Bercoff, M. Tanter, L. Sandrin, S. Catheline, and M. Fink, "Ultrafast compound imaging for 2-D displacement vector measurements: application to transient elastography and color flow mapping," in *Proc. IEEE Ultrason. Symp.*, 2001, pp. 1619–1622.

[14] B. Y. Yiu, S. S. Lai, and A. C. Yu, "Vector projectile imaging: time-resolved dynamic visualization of complex flow patterns." *Ultrasound Med. Biol.*, vol. 40, no. 9, pp. 2295–2309, sept 2014.

[15] M. Lenge, A. Ramalli, P. Tortoli, C. Cachard, and H. Liebgott, "Plane-wave transverse oscillation for high-frame-rate 2-D vector flow imaging," *IEEE Trans. Ultrason., Ferroelec., Freq. Contr.*, vol. 62, no. 12, pp. 2126–2137, December 2015.

[16] J. A. Jensen and P. Munk, "A new method for estimation of velocity vectors," *IEEE Trans. Ultrason., Ferroelec., Freq. Contr.*, vol. 45, no. 3, pp. 837–851, 1998.

[17] M. E. Anderson, "Multi-dimensional velocity estimation with ultrasound using spatial quadrature," *IEEE Trans. Ultrason., Ferroelec., Freq. Contr.*, vol. 45, pp. 852–861, 1998.

[18] J. A. Jensen, "A new estimator for vector velocity estimation," *IEEE Trans. Ultrason., Ferroelec., Freq. Contr.*, vol. 48, no. 4, pp. 886–894, 2001.

[19] H. Liebgott, A. Basarab, P. Gueth, C. Cachard, and P. Delachartre, "Lateral RF image synthesis using a synthetic aperture imaging technique." *IEEE Trans. Ultrason., Ferroelec., Freq. Contr.*, vol. 55, no. 9, pp. 2097–2103, 2008.

[20] C. Sumi, "Displacement vector measurement using instantaneous ultrasound signal phase - multidimensional autocorrelation and Doppler methods," *IEEE Trans. Ultrason., Ferroelec., Freq. Contr.*, vol. 55, no. 1, pp. 24–43, 2008.

[21] J. A. Jensen, "Directional transverse oscillation vector flow estimation," *IEEE Trans. Ultrason., Ferroelec., Freq. Contr.*, vol. 63, p. Submitted, 2016.

[22] S. I. Nikolov and J. A. Jensen, "In-vivo synthetic aperture flow imaging in medical ultrasound," *IEEE Trans. Ultrason., Ferroelec., Freq. Contr.*, vol. 50, no. 7, pp. 848–856, 2003.

[23] J. Kortbek, J. A. Jensen, and K. L. Gammelmark, "Sequential beamforming for synthetic aperture imaging," *Ultrasonics*, vol. 53, no. 1, pp. 1–16, 2013.

[24] T. Di Ianni, M. C. Hemmsen, J. P. Bagge, H. Jensen, N. Vardi, and J. A. Jensen, "Analog gradient beamformer for a wireless ultrasound scanner," in *Proc. SPIE Med. Imag.*, vol. 9790, 2016, pp. 979 010–1 – 8.

[25] T. Di Ianni, M. C. Hemmsen, P. L. Muntal, I. H. Jørgensen, and J. A. Jensen, "System-level design of an integrated receiver front end for a wireless ultrasound probe," *IEEE Trans. Ultrason., Ferroelec., Freq. Contr.*, vol. 63, no. 11, pp. 1935–1946, 2016.

[26] C. Passmann and H. Ermert, "A 100-MHz ultrasound imaging system for dermatologic and ophthalmologic diagnostics," *IEEE Trans. Ultrason., Ferroelec., Freq. Contr.*, vol. 43, pp. 545–552, 1996.

[27] C. H. Frazier and W. D. O'Brien, "Synthetic aperture techniques with a virtual source element," *IEEE Trans. Ultrason., Ferroelec., Freq. Contr.*, vol. 45, no. 1, pp. 196–207, 1998.

[28] M. H. Bae and M. K. Jeong, "A study of synthetic-aperture imaging with virtual source elements in B-mode ultrasound imaging systems," in *IEEE Trans. Ultrason., Ferroelec., Freq. Contr.*, vol. 47, 2000, pp. 1510–1519.

[29] Y. Li and J. A. Jensen, "Synthetic aperture flow imaging using dual stage beamforming: Simulations and experiments," *J. Acoust. Soc. Am.*, vol. 133, no. 4, pp. 2014–2024, 2013.

[30] M. C. Hemmsen, L. Lassen, T. Kjeldsen, J. Mosegaard, and J. A. Jensen, "Implementation of real-time duplex synthetic aperture ultrasonography," in *Proc. IEEE Ultrason. Symp.*, 2015, pp. 1–4.

[31] T. Di Ianni, M. C. Hemmsen, and J. A. Jensen, "Vector velocity estimation for portable ultrasound using directional transverse oscillation and synthetic aperture sequential beamforming," in *Proc. IEEE Ultrason. Symp.*, 2016, pp. 1–4.

[32] J. Udesen and J. A. Jensen, "Investigation of Transverse Oscillation Method," *IEEE Trans. Ultrason., Ferroelec., Freq. Contr.*, vol. 53, pp. 959–971, 2006.

[33] J. A. Jensen, H. Holten-Lund, R. T. Nilsson, M. Hansen, U. D. Larsen, R. P. Domsten, B. G. Tomov, M. B. Stuart, S. I. Nikolov, M. J. Pihl, Y. Du, J. H. Rasmussen, and M. F. Rasmussen, "Sarus: A synthetic aperture real-time ultrasound system," *IEEE Trans. Ultrason., Ferroelec., Freq. Contr.*, vol. 60, no. 9, pp. 1838–1852, September 2013.

Paper II

System-level Design of an Integrated Receiver Front-end for a Wireless Ultrasound Probe

Tommaso Di Ianni, Martin Christian Hemmsen, Pere Llimós Muntal, Ivan Harald Holger Jørgensen, and Jørgen Arendt Jensen

IEEE Trans. Ultrasons., Ferroelec., Freq. Contr., vol. 63, no. 11, pp. 1935-1946, Nov. 2016.

System-Level Design of an Integrated Receiver Front End for a Wireless Ultrasound Probe

Tommaso Di Ianni, Martin Christian Hemmsen, Pere Llimós Muntal, Ivan Harald Holger Jørgensen, and Jørgen Arendt Jensen, *Fellow, IEEE*

***Abstract*— In this paper, a system-level design is presented for an integrated receive circuit for a wireless ultrasound probe, which includes analog front ends and beamformation modules. This paper focuses on the investigation of the effects of architectural design choices on the image quality. The point spread function is simulated in Field II from 10 to 160 mm using a convex array transducer. A noise analysis is performed, and the minimum signal-to-noise ratio (SNR) requirements are derived for the low-noise amplifiers (LNAs) and A/D converters (ADCs) to fulfill the design specifications of a dynamic range of 60 dB and a penetration depth of 160 mm in the B-mode image. Six front-end implementations are compared using Nyquist-rate and ΣΔ modulator ADCs. The image quality is evaluated as a function of the depth in terms of lateral full-width at half-maximum (FWHM) and −12-dB cystic resolution (CR). The designs that minimally satisfy the specifications are based on an 8-b 30-MSPS Nyquist converter and a single-bit third-order 240-MSPS ΣΔ modulator, with an SNR for the LNA in both cases equal to 64 dB. The mean lateral FWHM and CR are 2.4% and 7.1% lower for the ΣΔ architecture compared with the Nyquist-rate one. However, the results generally show minimal differences between equivalent architectures. Advantages and drawbacks are finally discussed for the two families of converters.**

***Index Terms*— Portable ultrasound, receiver front end, synthetic aperture sequential beamforming (SASB), wireless probe.**

I. Introduction

In RECENT years, the benefits of point-of-care ultrasound imaging performed using handheld scanners were identified as a game changer in a large variety of clinical situations. These include austere medical departments, such as ambulances and emergency rooms, and remote areas of developing countries [1], [2]. Several studies demonstrated that portable ultrasound devices are able to provide good image quality compared with high-end scanners, and allow a more accurate diagnosis than the stethoscope-based physical examination for patients suspected of cardiovascular abnormalities and referred for echocardiography [3], [4].

For such devices to undergo a widespread distribution, severe restrictions must be considered in terms of cost, size, and power consumption, while the image quality must be preserved. Fuller *et al.* [5], [6] developed a low-cost, pocket-sized device for medical ultrasound imaging that integrates a fully sampled 2-D array transducer, transmit/receive circuitry, an LCD display, and a battery in a very compact enclosure. However, the device is a C-scan imaging system conceived for needle-tracking and catheter insertion purposes, while the system object of this paper is a general-purpose probe, and is, therefore, a more complex architecture. Comparable devices are present on the market, but very limited technical information is publicly available.

Poland and Wilson [7] proposed a battery-powered wireless probe integrating an array of transducer elements, a microbeamformer [8], and transmit/receive circuits and antennas in a compact enclosure. The sampled partially beamformed signals are sent to an external host system for further beamforming, image processing, and displaying. The cable-free solution has the twofold advantage of effectively improving the maneuverability while reducing the cost of the probe, as the bulky cable has a significant impact on the market price of the system.

Recently, Siemens Medical Solutions USA, Inc., developed and commercialized a wireless scanner (ACUSON Freestyle) using proprietary ultrawideband radio communication protocols and high-speed antennas [9]. However, taking advantage of general-purpose mobile devices would significantly benefit the cost effectiveness and help supply ultrasound imaging to nonconventional markets.

Hemmsen *et al.* [10], [11] demonstrated the feasibility of a wireless ultrasound system using consumer-level mobile devices, such as smartphones and tablets. The overall objective is to use the mobile devices as system hosts for the data processing and visualization, interfaced to an external probe for the acquisition of the ultrasound field. The system is based on synthetic aperture sequential beamforming (SASB) [12], [13]. The received field is beamformed within the probe handle using a fixed-focus, and further processing is performed in the mobile device after the wireless transmission of the ultrasound data. The idea enables the possibility to critically lower the price of the imaging system, taking ultrasound devices closer to the mobile health concept emerged in the past decade.

Having demonstrated that the wireless transmission of the ultrasound data is possible, a suitable hardware implementation must be found that suits the power consumption limitations while satisfying the image quality requirements. The low-noise amplifier (LNA) and A/D

Manuscript received June 9, 2016; accepted July 24, 2016. Date of publication July 28, 2016; date of current version November 1, 2016. This work was supported in part by the Danish National Advanced Technology Foundation under Grant 82-2012-4 and in part by BK Ultrasound.

T. Di Ianni, M. C. Hemmsen, and J. A. Jensen are with the Center for Fast Ultrasound Imaging, Department of Electrical Engineering, Technical University of Denmark, Kongens Lyngby DK-2800, Denmark (e-mail: todiian@elektro.dtu.dk; mah@elektro.dtu.dk; jaj@elektro.dtu.dk).

P. Llimós Muntal and I. H. H. Jørgensen are with the Department of Electrical Engineering, Technical University of Denmark, Kongens Lyngby DK-2800, Denmark (e-mail: plmu@elektro.dtu.dk; ihhj@elektro.dtu.dk).

Digital Object Identifier 10.1109/TUFFC.2016.2594769

converter (ADC) have, in particular, a significant influence on the power dissipation, circuit area, and cost of the system. The state-of-the-art commercial integrated circuits (ICs) are overdesigned for the imaging performance of a portable system, at the expenses of the power dissipation, which makes it difficult to integrate the circuitry in a compact form factor. This is discussed in Section III-A, where it is shown that the power consumption of current, commercial chipsets exceeds the power budget for a handheld scanner. A dedicated chip is, therefore, required to minimally fulfill the performance requirements and prevent avoidable power usage.

A system-level investigation is presented in this paper for the design of a dedicated IC that includes analog front-end (AFE) and beamforming modules. The minimum noise requirements for the LNA and the ADC are derived to fulfill the specifications of a 60-dB dynamic range (DR) and a penetration depth of 160 mm in the B-mode image. The resolution and the contrast are evaluated considering Nyquist-rate and oversampling $\Sigma\Delta$ converters to investigate the effects of architectural design choices on the image quality.

The remainder of the paper is organized as follows. The SASB focusing technique is introduced in Section II. In Section III, the architecture is presented and the design using commercial integrated devices is considered. The details on the critical components are introduced and discussed in Section IV. Section V describes the simulation setup for the preliminary noise study and the system-level comparison. The results are presented in Section VI, and system-level considerations are finally discussed in Section VII.

II. Synthetic Aperture Sequential Beamforming

In conventional ultrasound imaging, a sector is scanned by sweeping a set of narrow beams in a number of directions. For a given depth of field, tradeoffs between image quality and frame rate are imposed by the speed of sound and the number of acquired lines. In addition, the image is optimally focused only at one depth, if a single focused transmission is used per direction. Synthetic aperture (SA) [14]–[17] techniques overcome these limitations by collecting the information from the entire imaged sector at once using defocused spherical waves, dynamically focused in receive to obtain low-resolution frames. A fully focused image with spatially independent resolution is, therefore, synthesized by coherently combining a number of low-resolution frames.

The heavy data handling demand imposed by the need to compute and store several frames for creating a high-resolution image makes the implementation of a full SA beamformer challenging in a real system. The sequential beamforming idea was introduced to loosen the system requirements combining the monostatic SA focusing technique [14] with the concept of virtual source (VS) created by means of a focused emission [18]–[20]. A dual-stage beamformer is used in receive to reduce the data throughput and storage demand, taking advantage of the SA approach in a downscaled setup. The first stage is a fixed-focus beamformer with the focal point coincident with the VS position. A number of beamformed RF-lines—referred to as low-resolution lines (LRLs) in the remainder of this paper—from a number of emissions are then stored and sent to the second-stage beamformer for refocusing. For a thorough understanding of the sequential beamforming implementation, readers are referred to the cited articles.

The performance of the SASB approach was first investigated by Kortbek *et al.* [12], [13] with a linear array transducer, demonstrating that the lateral resolution is globally improved compared with the conventional dynamic receive focusing and less depth-dependent. Hemmsen *et al.* [21] showed the feasibility with a convex array through wires and tissue mimicking phantoms. Finally, the clinical evaluation of the method was performed by Hemmsen *et al.* [22], and SASB was proved to provide an image quality comparable with that of conventional imaging. In [22], the VSs were positioned at a depth of 70 mm using 64 active elements in transmit and receive. The same setup is maintained here and used as a starting point for the design of the probe with the intention of keeping consistency with the imaging setup evaluated in the clinic.

III. Architecture Overview

A block diagram of the wireless ultrasound system is schematically outlined in Fig. 1. In particular, Fig. 1(a) shows the receiver front end addressed in this paper. The $N = 64$ channels consisting of analog preamplifiers, ADCs, and delay-and-sum modules process the signals received by a subarray of transducer elements. The beamformation is performed in the digital domain although the first fixed-focus beamformer can be realized using simple analog circuitry [23]. Flexibility and robustness considerations make the digital implementation a more attractive option, and the possibility for the focal point to be moved along the depth and the beam steered across different directions opens the way for the integration of a wide spectrum of imaging modalities in a very versatile system.

The beamformed LRLs are first downsampled to the Nyquist rate f_N and Hilbert transformed to obtain the in-phase and quadrature components. These are sent via wireless link to the external processing unit [Fig. 1(b)], where a set of lines are stored. In [10], a setup similar to the one investigated here was implemented, and a data throughput of 25.3 MB/s was demonstrated to be sufficient for achieving real-time performance. A high-resolution image is finally created by the second-stage beamformer, and envelope detection, log compression, and scan conversion are performed before the image is displayed.

A. Design Using Commercial Integrated Circuits

Particular conditions are imposed on the power consumption of a portable system compared with that of a cart-based scanner due to the integration of the front end into the handle. The heating of the transducer surface in contact with the patient's skin must be kept below the limits of the Food and Drug Administration (FDA) [24] and the International Electrotechnical Commission (IEC) [25]. Furthermore, the IEC limits to 75 °C the temperature for continuously held plastic components. In addition, the battery capacity is limited by size and weight constraints. Referring for comparison with a consumer-level smartphone, it is frequent during a phone

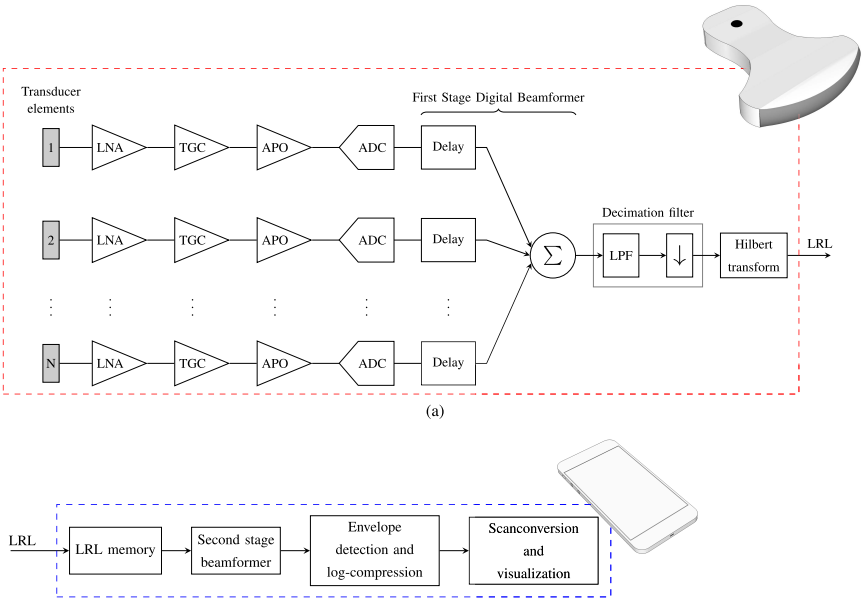

Fig. 1. Schematic overview of the wireless ultrasound system. (a) Receiving front-end and beamformation modules are integrated in the probe handle. (b) Postprocessing unit is software-implemented in the mobile device.

TABLE I
POWER DISSIPATION FOR THE DESIGN BASED ON COMMERCIAL ICS

Model	# of bits ADC	Sampling frequency [MSPS]	ADC SNR [dB]	Variable gain range [dB]	Power dissipation/ch. [mW/ch]	Total power dissipation (64 ch.) [W]
AD9273-25	12	25	70	42	102	6.53
AD9278	12	40	70	45	88	5.63
AFE5816	12	40	70	39	55	3.53
AFE5807	12	40	72	40	97	6.21

call to experience the heating of the device, which causes discomfort for the user. For such use-case, the average power is reported in [26] to be between 747 and 1135 mW.

A wireless probe encounters the same thermal design challenges of mobile devices. Due to maneuverability requirements, active cooling strategies cannot be used; therefore, the heat is conveyed by conduction to the casing, and then partially transferred to the user's hand. Taking into account an external surface of the wireless probe approximately doubled compared with the one of a conventional smartphone, the ideal power consumption is about 2.2 W, and should not exceed 3 W for comfortable use.

As a first step, the feasibility of the wireless probe was investigated using the four least power consuming commercial AFEs from Analog Devices, Inc., and Texas Instruments, Inc. The ICs include an LNA, a variable gain amplifier (VGA), and an ADC for each channel. The total power dissipation for a 64-channel system is shown in Table I, and results for all the cases greater than 3 W. Furthermore, additional power usage must be considered for the beamformation, in particular for the multibit interpolation needed to achieve the suitable delay resolution (see Section IV-C), and for chip-to-chip communication. Therefore, the power consumption of current, commercial circuits exceeds the power budget of a handheld scanner.

Owing to the considerations discussed earlier, a dedicated IC is required to minimally fit the design specifications while fulfilling the power demands. Integrating beamformer and front end on the same chip offers the advantage of minimized connector pin count, resulting in a lower power consumption. A system-level design for such device is presented in the remainder of this paper.

IV. PROBE DESIGN

In this section, the models considered for the design of the AFE are introduced. Time and depth are used here interchangeably, being the quantities related by a

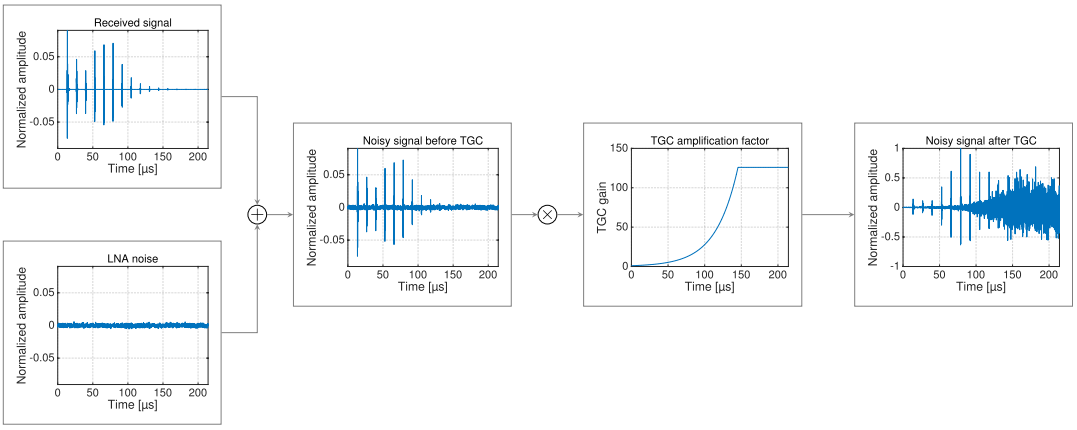

Fig. 2. Noise model for the LNA: the received signals are attenuated due to the propagation in the tissue, and a depth-independent noise is added in the LNA stage giving a depth-dependent SNR. A variable gain is then applied as a function of the depth for the TGC. The amplitudes are normalized to the input voltage range of the ADC.

direct proportionality in the case of constant speed of sound.

A. Analog Front End

In the AFE in Fig. 1(a), the received echoes are first amplified by LNAs located close to the transducer elements, and a depth-dependent gain factor is introduced by VGAs for the time-gain compensation (TGC) of the attenuation caused by the propagation in the tissue. Finally, an apodization function is used to suppress the side lobes in the LRLs.

In Fig. 2, the model for the noise of the LNA is displayed. The received signals are attenuated by a factor α—equal to 0.5 dB cm^{-1}MHz^{-1} in Fig. 2—to take into account the propagation losses, and a depth-independent noise is added in the LNA stage. As a consequence, the signal-to-noise ratio (SNR) of the noisy signal is decreasing as a function of the depth. A TGC amplification factor is applied to compensate for the attenuation. In Fig. 2, the TGC amplification is limited to a range of 0–42 dB, and the saturation occurs at about 146 μs, corresponding to a depth of 11.2 cm. The amplitudes in Fig. 2 are normalized to the input voltage range of the ADC. The model is used for the simulations described in Section V.

The noise model for the ADC is shown in Fig. 3. Quantization and thermal noise contributions are thought of as an additive depth-independent white Gaussian noise source. The TGC in Fig. 2 provides a way of using the entire input DR of the ADC at all the depths, and does not alter the SNR in this model. However, the amplitude of the received signal is lower than the input range of the ADC at the depths, where the saturation of the TGC amplifier occurs. This introduces a further depth-dependent SNR degradation, being the noise of the ADC at a constant level throughout the depth.

The performance of the LNA is critical to achieving the design specifications, in particular for what concerns the depth of penetration. Nonlinearities and distortions introduced at this stage are unlikely to be removed in subsequent steps, and a high SNR is required to limit the amount of noise introduced

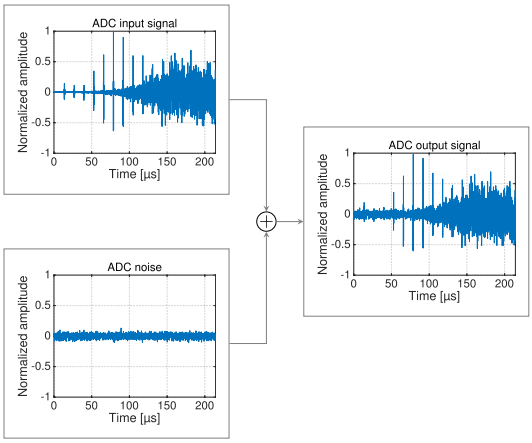

Fig. 3. Noise model for the ADC: quantization and thermal noise are considered as a depth-independent, white Gaussian noise source, and a depth-dependent SNR degradation is introduced where the saturation of the TGC amplifier occurs.

in the signal processing chain. High-performance, however, is directly translated into increased power consumption, and has an important impact on the power budget.

B. Analog-to-Digital Converter

A number of parameters can be used for the characterization of A/D conversion performance, including stated resolution, SNR, spurious-free DR, two-tone intermodulation distortion, and power dissipation [27]. The following discussion is based on SNR considerations, due to the fact that the design specifications are highly influenced by the noise level. In an ideal ADC, the quantization is the only process introducing noise in the digital signal. The quantization error can be considered to be a uniformly distributed, zero-mean, white

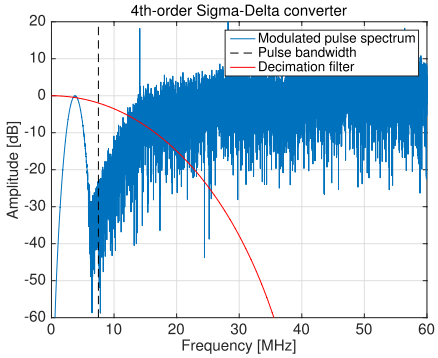

Fig. 4. Spectrum of a 3.75-MHz pulse modulated with a single-bit fourth-order $\Sigma\Delta$ converter with 360-MSPS sampling frequency. Most of the quantization noise is out of signal bandwidth (black dashed line) and can be filtered in the digital domain. The transfer function of the decimation filter is plotted in red.

noise, if the quantizer is not overloaded and under the assumption of uncorrelated successive quantization error samples [28]. The assumption is valid, if the quantization step is small compared with the signal amplitude, and the signal is sufficiently complex. For a conventional Nyquist-rate converter with sampling rate f_s and L bits of resolution, the theoretical signal-to-quantization noise ratio (SQNR) in dB is defined as

$$\mathrm{SQNR} = 10\log\left(\frac{\sigma_s^2}{\sigma_e^2}\right) = 6.02L + 10\log_{10} m + 1.76 \quad (1)$$

where σ_s^2 and σ_e^2 identify the power for the signal and the in-band quantization noise, and $m = f_s/f_N$ is the oversampling ratio. In a real ADC, however, the noise spectrum contains contributions from other sources, such as thermal noise from the circuitry, aperture uncertainty, and comparator ambiguity. These result in a lower SNR compared with the SQNR, and the effective number of bits (ENOBs), defined as

$$\mathrm{ENOB} = \frac{\mathrm{SNR} - 1.76}{6.02} \quad (2)$$

is used, which takes into account all the noise contributions. In [27], the average difference between stated resolution and ENOB for the state-of-the-art ADCs was reported to be approximately 1.5 b. Only quantization and thermal noise are considered in this paper.

It can be noted in (1) that the SQNR is increased by approximately 6 dB for every additional bit of resolution and 3 dB for every doubling of the oversampling ratio. Hence, it is possible to trade speed with resolution [28], and this opens the way to the realization of low-complexity, high-speed processing systems. The $\Sigma\Delta$ ADCs [29]–[31] combine oversampling with noise shaping to modify the power spectral density of the quantization noise such that most of the noise is out of the signal bandwidth and can be filtered in the digital domain before the signal is downsampled.

The spectrum of a 3.75-MHz pulse modulated with a single-bit fourth-order $\Sigma\Delta$ converter with a sampling frequency of 360 MSPS is shown as an example in Fig. 4. For such converters, the calculation of the SQNR must take into account the noise-shaping transfer function as well as the digital decimation filters to account for the residual out-of-band noise that partially aliases in the signal bandwidth when decimation occurs. For the $\Sigma\Delta$ modulators used in Section V-B, the SQNR was found by simulating a full-scale sinusoid.

If the thermal noise generated by the ADC's circuitry is taken into account, the total SNR in dB can be defined as

$$\mathrm{SNR} = 10\log\left(\frac{\sigma_s^2}{\sigma_e^2 + \sigma_{\mathrm{th}}^2}\right) = 10\log\left(\frac{\sigma_s^2}{\sigma_n^2}\right) \quad (3)$$

where σ_{th}^2 is the thermal noise power, and σ_n^2 is the total noise power. It is common practice to design the ADC with an SQNR greater than the target SNR [32]. The overall performance is, therefore, limited by the thermal noise rather than the quantization noise. For all the ADCs considered in the following Section V-B, the SQNR was designed to be 6 dB greater than the target SNR.

C. First-Stage Beamformer

In the digital fixed-focus beamformer, actual delay values are quantized to the sampling period, and a phase error is introduced in the beamformed line, which contributes to the side lobe amplitude [33]. Different approaches can be used to achieve the adequate delay resolution needed for the side lobe level to drop below the system's DR.

The first method oversamples with a ratio $m > 1$. Typical ratios are in the range from five to ten [34], and this introduces an additional overhead. However, the delay line can be easily realized by means of a simple first-in-first-out shift register.

As an alternative, digital delay interpolation can be used to obtain the required delay resolution saving ADC and memory resources [34]. The received signals are in this case sampled at the Nyquist rate, and $K-1$ intrasample values are calculated for each pair of successive samples giving an effective oversampling ratio of K. A finite-impulse response (FIR) filter with approximately $5K$ coefficients is required in each channel for this purpose [34], with increased computational cost.

The delay interpolation is typically preferred with multibit ADCs, as this provides in this case a less expensive solution. Conversely, oversampling converters, such as $\Sigma\Delta$ modulators, yield an inherently high sampling frequency, and better suit the oversampling beamforming approach without any additional cost.

V. Methods

A simulation study was performed to investigate the effects of design choices on the image quality. The minimum noise requirements were derived for the LNA and ADC to satisfy the specifications of a 60-dB DR and 160-mm penetration depth in the B-mode image. Several front end implementations using equivalent Nyquist-rate and $\Sigma\Delta$ converters were examined to evaluate the influence of system-level considerations on the imaging resolution and contrast.

A model of the system was built in MATLAB (The MathWorks Inc., Natick, MA, USA), and the analytic signals were obtained through a Hilbert transform. The

TABLE II
SIMULATION PARAMETERS

Speed of sound	1540 m s^{-1}
Attenuation factor - α	0.5 dB cm^{-1} MHz^{-1}
Transducer parameters	
Transducer	Convex array
Center frequency	3.75 MHz
Number of elements	192
Transducer element pitch	0.33 mm
Transducer element height	13 mm
Convex curvature radius	61 mm
Elevation focus	65 mm
Transmit parameters	
Center frequency - f_0	3.75 MHz
Signal bandwidth	7 MHz
Excitation	2-cycle weighted sinusoid
Apodization function	Rect function
Active aperture size	64 elements
Focus axial position	70 mm
$f\#$	3.3
Number of emissions	269
Receive parameters	
Apodization function	Hamming
Active aperture size	64 elements
Focus axial position	70 mm
$f\#$	3.3
TGC range	0–42 dB
Second stage parameters	
Apodization function	Hamming

second-stage beamformer was implemented with the BFT3 toolbox [35], and the high-resolution images showed with a DR of 60 dB.

The simulation parameters are shown in Table II. A 192-element convex array transducer with center frequency $f_0 = 3.75$ MHz was used and focused in transmit/receive at a depth $z_f = 70$ mm. The active aperture was limited to $N = 64$ elements and gives a transmit f-number $f\# = 3.3$, where $f\# = z_f/L_A$ and L_A is the aperture length. A Hamming function was used for weighting the received echoes in the first stage as well as the beamformed LRLs in the second stage, while no apodization was applied on the emitting aperture. The point spread function (PSF) was simulated in Field II [36], [37] from 10 to 160 mm in steps of 10 mm. Absorption and scattering losses were included by means of an attenuation factor $\alpha = 0.5$ dB cm^{-1}MHz^{-1}. The TGC was introduced as an amplification curve with a slope equal to αf_0 in the range of 0–42 dB. For this setup, the maximum gain of the amplifier is attained at a depth of 11.2 cm.

The study focused on the analysis of the LNA and ADC modules, as these components are expected to significantly contribute to the final power consumption, owing to the considerations discussed in Section III-A. The TGC and apodization amplifiers were, therefore, considered ideal throughout all the simulations.

A. SNR Study

The noise introduced by the analog circuitry and by the ADC has a direct influence on the DR and depth of penetration, as illustrated in Section IV-A. An ideal ADC was first considered with a sampling frequency of $f_N = 15$ MSPS and infinite resolution. The beamformation was performed assuming nonquantized delay values. The same model, as shown in Fig. 2, was used for the LNA, consisting of a depth-independent white Gaussian noise source $e(t)$. The power of $e(t)$ in the 7-MHz signal bandwidth was calculated to obtain the desired SNR relative to the power of a full-scale sinusoid. The SNR of the LNA was swept from 0 to 80 dB in steps of 5 dB, and $M = 50$ independent simulations were performed at each step to find the output SNR at the 16 points where the PSF was simulated. A noiseless signal $\bar{y}$ was also simulated, and denoting by $y(n, i)$ the complex sample at the nth point for the ith noisy simulation, with $n = 1, \ldots, 16$, the noise power was calculated as

$$\sigma_n^2(n) = \left| \frac{1}{M} \sum_{i=1}^{M} (y(n,i) - \bar{y}(n))^2 \right|. \tag{4}$$

The SNR was found as

$$\mathrm{SNR}(n) = 10 \log \left(\frac{\sigma_s^2(n)}{\sigma_n^2(n)} \right) \tag{5}$$

with $\sigma_s^2 = |\bar{y}|^2$ the power of the noiseless signal.

A minimum requirement of 42 dB for the LNA results from the preceding simulations. This corresponds to a noise voltage of 3 μV/$\sqrt{\text{Hz}}$ at the output of the LNA. The input noise voltage for an actual amplifier depends on the gain, and is, therefore, a function of the amplitude of the received signals. The SNR of the LNA was then fixed to 48 and 64 dB to analyze the system behavior in two different cases, and the same procedure was repeated to find the minimum requirement for the ADC to fulfill the design specifications. The signals were sampled at $f_N = 15$ MSPS, and a second white Gaussian noise source was added to model the ADC quantization and thermal noise contributions. The assumption of a uniformly distributed white quantization noise is valid, if the conditions stated in Section IV-B are satisfied. The SNR of the ADC was swept from 0 to 80 dB in steps of 5 dB, and $M = 50$ simulations were performed to find the SNR in the output image as indicated by (4) and (5).

TABLE III
PARAMETERS OF THE ADCS USED IN THE SYSTEM-LEVEL SIMULATION STUDY

	Resolution [bit]	f_s [MSPS]	Decimation -	SQNR [dB]	SNR [dB]
Nyquist	5	30	2	35	29
	8	30	2	53	47
	10	30	2	65	59
	Order -	f_s [MSPS]	Decimation -	SQNR [dB]	SNR [dB]
$\Sigma\Delta$	2	120	2 and 4	35	29
	3	240	4 and 4	55	49
	4	300	5 and 4	65	59

B. System-Level Comparison

Six AFE implementations were simulated to investigate the effect of architectural design choices on the image quality.

Three conventional Nyquist-rate converters were compared along with three single-bit $\Sigma\Delta$ ADCs. The parameters of the simulated ADCs are reported in Table III. The SNR of the LNA was set equal to 64 dB in all the simulations.

For the Nyquist-rate converters, a sampling frequency of $f_s = 30$ MSPS ($m = 2$) was used, with a resolution of 5, 8, and 10 b. The three architectures are referred to as Nyq5, Nyq8, and Nyq10 in the remainder of this paper. The SQNR calculated according to (1) is equal to 35, 53, and 65 dB, respectively. White Gaussian noise was added to mimic the thermal noise, with a final SNR of 6 dB lower than the SQNR. The actual delay values were quantized with a resolution of $T_0/24$, with $T_0 = 1/f_0$ the pulse period. If $f_N = 4f_0$, the required oversampling ratio is 6, and an FIR interpolation filter with at least 15 coefficients and 30-MHz clock frequency is needed for each channel, as discussed in Section IV-C. A matched FIR decimation filter was used before downsampling the beamformed lines to the Nyquist rate.

Three single-bit $\Sigma\Delta$ ADCs were used: second order with $f_s = 120$ MSPS ($m = 8$), third order with $f_s = 240$ MSPS ($m = 16$), and fourth order with $f_s = 300$ MSPS ($m = 20$). The architectures are referred to as SDM2, SDM3, and SDM4. The MATLAB model was developed for the modulators following the procedure in [38]. The noise transfer functions were determined by designing second-, third-, and fourth order high-pass Butterworth filters. The downsampling of the beamformed lines was performed in two steps: a first *sinc* cascaded-integrator-comb stage [39] was used before downsampling with a decimation ratio of 2, 4, and 5 for the three architectures. Finally, the Nyquist rate was restored after matched filtering and decimation with a ratio of 4.

The SQNR for the oversampling converters was estimated from $M = 50$ simulations of each modulator cascaded with the relative decimation filters to take into account the out-of-band quantization noise aliased in the signal bandwidth when decimation occurs. A sinusoid $\bar{x}(k)$ with the center frequency of 3.75 MHz was modulated, and the resulting single-bit signal filtered and downsampled. The SQNR was calculated as

$$\mathrm{SQNR} = 10\log\left(\frac{\sigma_{\bar{x}}^2}{\sigma_{qn}^2}\right) \tag{6}$$

where $\sigma_{\bar{x}}^2$ is the power of the sinusoid and

$$\sigma_{qn}^2 = \frac{1}{M}\frac{1}{K}\sum_{i=1}^{M}\sum_{k=1}^{K}(x_i(k) - \bar{x}(k))^2 \tag{7}$$

is the estimated quantization noise. In (7), x_i is the decimated signal from the ith simulation and K is the number of temporal samples. The resulting SQNR is equal to 35, 55, and 65 dB for the three architectures. White Gaussian noise was added for a final SNR of 6 dB lower than the estimated SQNR. For the three oversampling architectures, the beamformation was performed by merely shifting the single-bit signals, and the delay resolution is equal to $T_0/32$, $T_0/64$, and $T_0/80$, respectively, with no need for temporal interpolation.

A 1-D gain compensation was applied after the second-stage beamformer to the envelope detected signals for equalizing the peak amplitudes of the point targets. The PSF was evaluated in terms of lateral full-width at half-maximum (FWHM) and -12-dB cystic resolution (CR) to investigate the effects on the image quality of architectural choices in presence of noise, in particular concerning the delay quantization. The latter metric is defined as the radius ρ of a void centered on the maximum of the PSF providing a contrast $C(\rho)$ equal to -12 dB [40], calculated by

$$C(\rho) = 10\log\left(\frac{1 + \mathrm{SNR}^2\left(1 - \frac{E_{\mathrm{in}}(\rho)}{E_{\mathrm{tot}}}\right)}{1 + \mathrm{SNR}^2}\right) \tag{8}$$

where $E_{\mathrm{in}}(\rho)$ is the PSF energy inside the void and E_{tot} is the total PSF energy.

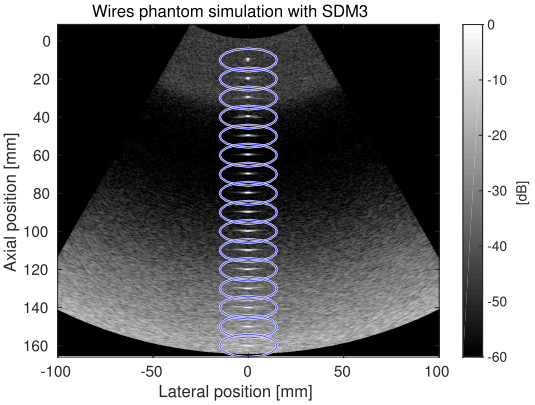

Fig. 5. B-mode image of the wire phantom simulated with the SDM3 architecture. The highlighted regions surrounding each point target were used for the calculation of the CR, as stated in (8). The SNR was estimated from 50 simulations (see Fig. 7), and it is assumed constant in each region.

A B-mode image of the wire phantom simulated with the architecture SDM3 is shown in Fig. 5. The ellipses highlight the regions, in which the total PSF energy E_{tot} was calculated. In each region, the SNR was assumed constant. This was estimated from $M = 50$ independent simulations as stated in (4) and (5) for each of the six architectures considered. The mean and the standard deviation of the FWHM and CR showed in Section VI were also estimated from the 50 simulations.

VI. Results

In this section, the results of the simulation studies introduced earlier are shown, and the effects of design choices on the image quality are discussed.

A. SNR Study

The result of the noise study for the LNA is shown in Fig. 6(a). The top curve in blue shows the DR and the bottom curve in red shows the SNR at a depth of 160 mm [penetration depth SNR (PDSNR)] in the B-mode image as a function of the LNA SNR. A linear regression is fitted to both the curves, and the minimum SNR requirement is highlighted by the green dashed line. The output SNR shows, as expected, a linear trend, and the minimum SNR requirement is equal to 42 dB. For this value, PDSNR is equal to 12.7 dB, and

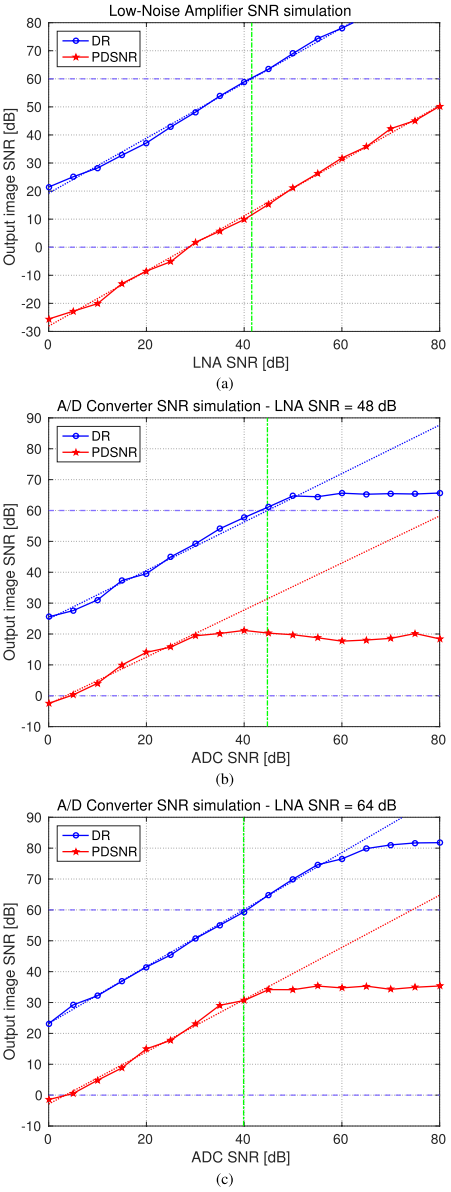

Fig. 6. Result of the preliminary noise study for the LNA and ADC. (a) Blue curve shows the DR and the red curve shows the SNR at a depth of 160 mm (PDSNR) in the B-mode image as a function of the SNR of the LNA. (b) DR and PDSNR as a function of the SNR of the ADC for LNA SNR = 48 dB. (c) DR and PDSNR as a function of the SNR of the ADC for LNA SNR = 64 dB. The green dashed lines indicate the minimum SNR requirements to fulfill the design specifications.

therefore, the tightest constraint for this setup is set by the DR specification.

The results of the noise study for the ADC are plotted in Fig. 6(b) for LNA SNR = 48 dB. The curves initially follow a linear trend, up to the point where DR and PDSNR equal the respective values for LNA SNR = 48 dB in Fig. 6(a), i.e., 66 and 19 dB. Beyond this point, improvements in the ADC SNR no longer translate in better image quality, and the noise is dominated by the noise level of the LNA. The minimum ADC SNR requirement for this configuration is equal to 45 dB. A similar trend is shown in Fig. 6(c) for LNA SNR = 64 dB. The curves saturate at DR = 82 dB and PDSNR = 35 dB, and the minimum SNR requirement is 40 dB.

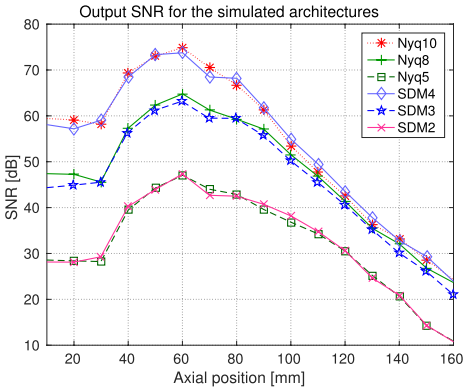

Fig. 7. SNR of the output image as a function of the axial position for the six simulated architectures in Table III.

It is important to notice here that the noise requirements for the two components are strictly related, and increasing the SNR of the LNA loosens the requirement on the ADC. However, how this factor translates in terms of circuitry depends on the actual design and implementation of both the components. The SNR at 160 mm is everywhere greater than 0 dB in Fig. 6(b) and (c); this suggests the possibility of decreasing the range of the variable gain for the TGC amplifier.

Different factors contribute to the DR and to the SNR at the penetration depth. The noise introduced by the LNA and ADC propagates to the output image through a cascade of two beamformers. In the first stage, a fixed focus is used with a static apodization. The SNR of the LRL is, therefore, improved compared with the received signals, and the improvement depends on the apodization window. In the second stage, the focus and the apodization are dynamic, and the SNR of the high-resolution line increases as a function of the apodization window and the number of LRLs coherently added. The SNR is improved at all the depths except at the VS position, where one single LRL is considered. As shown in Fig. 7, the maximum SNR (DR) occurs in proximity of the VS position, and is for this reason only partially influenced by the second-stage beamformer. On the other hand, the SNR at 160 mm is largely determined by the dynamic apodization of the second stage.

B. System-Level Comparison

According to the results of the preliminary SNR study, the architectures Nyq10, Nyq8, SDM4, and SDM3 satisfy the

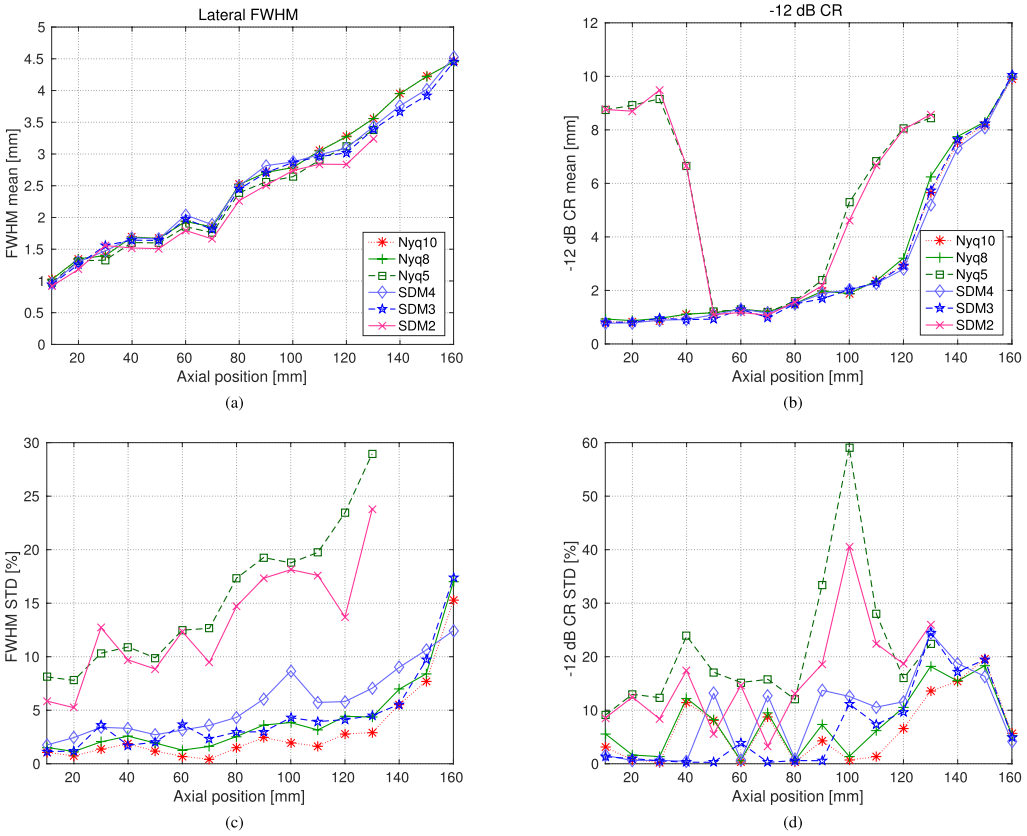

Fig. 8. Lateral FWHM (left column) and −12-dB CR (right column) as a function of the axial position for the architectures simulated in Section V-B. Mean (top) and relative standard deviation (bottom) were obtained from 50 PSF simulations.

minimum SNR requirement to fulfill the design specifications, while Nyq5 and SDM2 provide an SNR of 11 dB below the minimum requirement. The latter were chosen to investigate the image quality in the case of underdesigned configurations.

In Fig. 7, the SNR in the output image is shown as a function of the depth for the six architectures in Table III. As previously mentioned, the SNR shows a peak in proximity of the focal position, and this is the value determining the output DR. As expected, architectures similar in terms of SNR provide comparable results in the output image. Nyq8 and SDM3 are the ones which minimally fit the design specifications of a DR equal to 60 dB and a penetration depth of 160 mm. Nyq10 and SDM4 show a different slope beyond the VS position compared with the other architectures; this is caused by the noise of the LNA dominating the overall performance in the case of high SNR ADCs. The values in Fig. 7 were used for the calculation of the CR in (8), assuming a constant SNR throughout each elliptical region in Fig. 5.

The results for the lateral FWHM and CR are displayed in Fig. 8 for the six architectures. The mean FWHM calculated from 50 independent simulations is plotted in Fig. 8(a), and the relative standard deviation is shown in Fig. 8(c). The mean FWHM shows as expected an increasing trend, and small differences are noticeable between the simulated architectures. The calculation for Nyq5 and SDM2 failed in the points from 140 to 160 mm for several simulations, and the values for these points were, therefore, discarded. This was due to the high noise in the output image that made it difficult to identify the PSF. The relative standard deviation also shows an increasing trend due to the decreasing SNR as a function of the depth. In particular, high values were obtained for Nyq5 and SDM2 due to the lower SNR of these architectures.

The mean CR is plotted in Fig. 8(b) and the relative standard deviation in Fig. 8(d). The CR gives a measure of the contrast, and is influenced by the delay resolution. The results were expected to show significant differences among the simulated systems due to the better delay resolution of all the oversampling architectures compared with the Nyquist-rate ones. However, the results from pairs of similar architectures are comparable. This suggests that the contrast is actually

dominated here by the noise rather than the delay resolution, i.e., errors in the beamformation introduced by the delay quantization yield a degradation in the output image, which is negligible compared with the noise where this is at a relatively high level. This is an important consideration that should be taken into account in further steps of the design process. The relative standard deviation is also comparable between the simulated architectures.

For Nyq8, the mean lateral FWHM is between 1.02 and 4.45 mm, and between 0.94 and 4.45 mm for SDM3. The FWHM is in average 2.4% lower for SDM3 compared with Nyq8. The mean CR is between 0.93 and 9.97 mm for Nyq8, and between 0.81 and 10.05 mm for SDM3, and results in average 7.1% lower for the latter architecture.

VII. Conclusion and Discussion

In this paper, a system-level design was performed for the receiver front end circuit for a wireless ultrasound probe. This paper focused on the investigation of the effects of architectural design choices on the image quality, with the purpose of determining the systems that minimally fulfill the image quality specifications. As a consequence of the compact form factor required for a portable system, strict limitations are posed in terms of power consumption if enough scanning time is to be ensured and the FDA and IEC limits satisfied. In Section III-A, a power dissipation of 3 W was identified as a target for such system.

The minimum SNR requirements for critical components were derived by simulating the PSF using a convex array transducer, and the details of the noise propagation from the circuitry to the output image were introduced and discussed. Architectural design choices were argued and evaluated through the simulation of six different implementations based on Nyquist-rate converters and oversampling single-bit $\Sigma\Delta$ modulators. The results showed no considerable differences in terms of lateral resolution and contrast between equivalent Nyquist-rate and oversampling ADCs.

In [41], trends are shown for the performance and power efficiency of ADC designs as a function of time. The average power dissipation is reduced by a factor 2 approximately every two years, and this demonstrates that the ADCs are constantly object of optimization. The gain is due to technology scaling and simplified architectures. However, it is difficult to characterize this trend as a function of the ADC architecture; the performance and power efficiency also depend upon the target application and the semiconductor technology. The same conclusion can be deduced from [27], where the most power-efficient converters are pointed out from different families, such as flash, folded-flash, pipelined, and $\Sigma\Delta$ modulators. For these reasons, it is a great challenge at this proof-of-concept phase to make any assumptions on the power consumption and circuit area of the systems, and a worthwhile analysis would require their full development and characterization. Some considerations are summarized here from [29]–[31].

Conventional Nyquist-rate converters need precise analog circuits for their filters and comparators, and can be very sensitive to noise and interference [29]. Furthermore, a high-order analog antialiasing filter is required at the input of the converter to smooth the out-of-band components before they alias in the signal band as a consequence of the sampling process. Finely matched capacitors need to be used to achieve high precision conversion, which leads to large capacitive loads and, in turn, increased power dissipation, circuit area, and cost.

Extraordinary efforts have been put in optimizing the power efficiency of these converters, using simplified analog circuits and digitally assisted A/D architectures [41]. However, they are often difficult to integrate in fine-line very-large-scale integration (VLSI) technologies [29], focused on providing high-speed digital processing rather than accurate analog circuits. Oversampling conversion, on the other hand, can be implemented using relatively high-tolerance analog components, and moves the resource requirement toward the digital domain. The technology scaling continuously experienced by CMOS processes makes it convenient from a power dissipation and circuit area perspectives to concentrate the challenging hardware requirements in the digital section. Furthermore, the high-speed conversion removes the need for the sharp antialiasing analog filter, and noise and interference are attenuated in the digital domain before the signal is downsampled to the Nyquist rate. The interconnection complexity between the ADC and the following processing modules is also reduced, as the signals are converted in single-bit strings. For these reasons, $\Sigma\Delta$ converters well suit applications that require high-integration, low-cost, and densely packed circuit designs by taking advantage of fine-line VLSI technologies [29]. Finally, the use of oversampling converters also simplifies the beamformer architecture due to the inherently high sampling frequency that avoids temporal interpolation on the RF data.

This paper demonstrated that single-bit $\Sigma\Delta$ converters can be employed in a handheld setup maintaining the image quality. Further studies will investigate whether a power dissipation below 3 W can be attained for this system.

References

[1] S. Sippel, K. Muruganandan, A. Levine, and S. Shah, "Review article: Use of ultrasound in the developing world," *Int. J. Emerg. Med.*, vol. 4, p. 1, Dec. 2011.

[2] D. Adler, K. Mgalula, D. Price, and O. Taylor, "Introduction of a portable ultrasound unit into the health services of the Lugufu refugee camp, Kigoma District, Tanzania," *Int. J. Emergency Med.*, vol. 1, no. 4, pp. 261–266, Dec. 2008.

[3] C. Prinz and J.-U. Voigt, "Diagnostic accuracy of a hand-held ultrasound scanner in routine patients referred for echocardiography," *J. Amer. Soc. Echocardiograp.*, vol. 24, no. 2, pp. 111–116, 2011.

[4] M. Mehta *et al.*, "Handheld ultrasound versus physical examination in patients referred for transthoracic echocardiography for a suspected cardiac condition," *JACC, Cardiovascular Imag.*, vol. 7, no. 10, pp. 983–990, 2014.

[5] M. I. Fuller, K. Ranganathan, S. Zhou, T. N. Blalock, J. A. Hossack, and W. F. Walker, "Experimental system prototype of a portable, low-cost, C-scan ultrasound imaging device," *IEEE Trans. Biomed. Eng.*, vol. 55, no. 2, pp. 519–530, Feb. 2008.

[6] M. I. Fuller, K. Owen, T. N. Blalock, J. A. Hossack, and W. F. Walker, "Real time imaging with the sonic window: A pocket-sized, C-scan, medical ultrasound device," in *Proc. IEEE Ultrason. Symp.*, Sep. 2009, pp. 196–199.

[7] M. Poland and M. Wilson, "Light weight wireless ultrasound probe," U.S. Patent 2010 0 168 576 A1, Jul. 1, 2010.

[8] J. D. Larson, "2-D phased array ultrasound imaging system with distributed phasing," U.S. Patent 5 229 933, Jul. 1993.

[9] *Datasheet—ACUSON Freestyle Ultrasound System—Release 3.5*, Siemens Medical Solutions USA, Inc., Mountain View, CA, USA, 2014.

[10] M. C. Hemmsen *et al.*, "Implementation of synthetic aperture imaging on a hand-held device," in *Proc. IEEE Ultrason. Symp.*, Sep. 2014, pp. 2177–2180.
[11] M. C. Hemmsen, L. Lassen, T. Kjeldsen, J. Mosegaard, and J. A. Jensen, "Implementation of real-time duplex synthetic aperture ultrasonography," in *Proc. IEEE Ultrason. Symp.*, Oct. 2015, pp. 1–4.
[12] J. Kortbek, J. A. Jensen, and K. L. Gammelmark, "Synthetic aperture sequential beamforming," in *Proc. IEEE Ultrason. Symp.*, Nov. 2008, pp. 966–969.
[13] J. Kortbek, J. A. Jensen, and K. L. Gammelmark, "Sequential beamforming for synthetic aperture imaging," *Ultrasonics*, vol. 53, no. 1, pp. 1–16, 2013.
[14] J. T. Ylitalo and H. Ermert, "Ultrasound synthetic aperture imaging: Monostatic approach," *IEEE Trans. Ultrason., Ferroelectr., Freq. Control*, vol. 41, no. 3, pp. 333–339, May 1994.
[15] M. Karaman, P.-C. Li, and M. O'Donnell, "Synthetic aperture imaging for small scale systems," *IEEE Trans. Ultrason., Ferroelectr., Freq. Control*, vol. 42, no. 3, pp. 429–442, May 1995.
[16] S. I. Nikolov, "Synthetic aperture tissue and flow ultrasound imaging," Ph.D. dissertation, Dept. Ørsted DTU, Tech. Univ. Denmark, Kongens Lyngby, Denmark, 2001.
[17] J. A. Jensen, S. I. Nikolov, K. L. Gammelmark, and M. H. Pedersen, "Synthetic aperture ultrasound imaging," *Ultrasonics*, vol. 44, pp. e5–e15, Dec. 2006.
[18] C. H. Frazier and W. D. O'Brien, "Synthetic aperture techniques with a virtual source element," *IEEE Trans. Ultrason., Ferroelectr., Freq. Control*, vol. 45, no. 1, pp. 196–207, Jan. 1998.
[19] S. Nikolov and J. A. Jensen, "Virtual ultrasound sources in high-resolution ultrasound imaging," *Proc. SPIE*, vol. 4687, pp. 395–405, Apr. 2002.
[20] M.-H. Bae and M.-K. Jeong, "A study of synthetic-aperture imaging with virtual source elements in B-mode ultrasound imaging systems," *IEEE Trans. Ultrason., Ferroelectr., Freq. Control*, vol. 47, no. 6, pp. 1510–1519, Nov. 2000.
[21] M. C. Hemmsen, J. M. Hansen, and J. A. Jensen, "Synthetic aperture sequential beamformation applied to medical imaging," in *Proc. 9th EUSAR*, Apr. 2012, pp. 34–37.
[22] M. C. Hemmsen *et al.*, "*In vivo* evaluation of synthetic aperture sequential beamforming," *Ultrasound Med. Biol.*, vol. 38, no. 4, pp. 708–716, 2012.
[23] T. Di Ianni, M. C. Hemmsen, J. Bagge, H. Jensen, N. Vardi, and J. A. Jensen, "Analog gradient beamformer for a wireless ultrasound scanner," *Proc. SPIE*, vol. 9790, pp. 979010-1–979010-8, Apr. 2016.
[24] *Information for Manufacturers Seeking Marketing Clearance of Diagnostic Ultrasound Systems and Transducers*, Center for Devices and Radiological Health, United States Food and Drug Administration, Rockville, MD, USA, 2008.
[25] "Medical electrical equipment—Part 2–37: Particular requirements for the basic safety and essential performance of ultrasonic medical diagnostic and monitoring equipment," International Electrotechnical Commision, Tech. Rep. 60601-2-37, 2015.
[26] A. Carroll and G. Heiser, "An analysis of power consumption in a smartphone," in *Proc. USENIX Annu. Tech. Conf.*, 2010, p. 21.
[27] R. H. Walden, "Analog-to-digital converter survey and analysis," *IEEE J. Sel. Areas Commun.*, vol. 17, no. 4, pp. 539–550, Apr. 1999.
[28] A. V. Oppenheim and R. W. Schafer, *Discrete-Time Signal Processing*. Englewood Cliffs, NJ, USA: Prentice-Hall, 1989.
[29] S. R. Norsworthy, R. Schreier, and G. C. Temes, *Delta-Sigma Data Converters: Theory, Design, and Simulation*. New York, NY, USA: Wiley, 1996.
[30] J. Candy and G. Temes, "Oversampling methods for A/D and D/A conversion," in *Oversampling Delta-Sigma Data Converters*. Piscataway, NJ, USA: IEEE Press, 1992.
[31] P. M. Aziz, H. V. Sorensen, and J. van der Spiegel, "An overview of sigma-delta converters," *IEEE Signal Process. Mag.*, vol. 13, no. 1, pp. 61–84, Jan. 1996.
[32] F. Gerfers and M. Ortmanns, *Continuous-Time Sigma-Delta A/D Conversion*. Heidelberg, Germany: Springer, 2006.
[33] S. Holm and K. Kristoffersen, "Analysis of worst-case phase quantization sidelobes in focused beamforming," *IEEE Trans. Ultrason., Ferroelectr., Freq. Control*, vol. 39, no. 5, pp. 593–599, Sep. 1992.
[34] R. Mucci, "A comparison of efficient beamforming algorithms," *IEEE Trans. Acoust., Speech, Signal Process.*, vol. ASSP-32, no. 3, pp. 548–558, Jun. 1984.
[35] J. M. Hansen, M. C. Hemmsen, and J. A. Jensen, "An object-oriented multi-threaded software beamformation toolbox," *Proc. SPIE*, vol. 7968, pp. 79680Y-1–79680Y-9, Mar. 2011.
[36] J. A. Jensen and N. B. Svendsen, "Calculation of pressure fields from arbitrarily shaped, apodized, and excited ultrasound transducers," *IEEE Trans. Ultrason., Ferroelectr., Freq. Control*, vol. 39, no. 2, pp. 262–267, Mar. 1992.
[37] J. A. Jensen, "Field: A program for simulating ultrasound systems," in *Proc. 10th Nordicbaltic Conf. Biomed. Imag.*, vol. 4. 1996, pp. 351–353.
[38] R. W. Adams, P. F. Ferguson, A. Ganesan, S. Vincelette, A. Volpe, and R. Libert, "Theory and practical implementation of a fifth-order sigma-delta A/D converter," *J. Audio Eng. Soc.*, vol. 39, nos. 7–8, pp. 515–528, 1991.
[39] E. Hogenauer, "An economical class of digital filters for decimation and interpolation," *IEEE Trans. Acoust., Speech, Signal Process.*, vol. ASSP-29, no. 2, pp. 155–162, Apr. 1981.
[40] K. Ranganathan and W. F. Walker, "Cystic resolution: A performance metric for ultrasound imaging systems," *IEEE Trans. Ultrason., Ferroelectr., Freq. Control*, vol. 54, no. 4, pp. 782–792, Apr. 2007.
[41] B. Murmann, "A/D converter trends: Power dissipation, scaling and digitally assisted architectures," in *Proc. IEEE Custom Integr. Circuits Conf.*, Sep. 2008, pp. 105–112.

Tommaso Di Ianni received the M.Sc. degree in electronic engineering from the University of Bologna, Bologna, Italy, in 2014. He is currently pursuing the Ph.D. degree in biomedical engineering with the Center for Fast Ultrasound Imaging, Technical University of Denmark, Kongens Lyngby, Denmark, where he works on the development of new technologies for portable ultrasound imaging.

His current research interests include signal processing for medical imaging, estimation of blood flow velocities, synthetic aperture imaging, and compressed sampling.

Martin Christian Hemmsen received the M.Sc. degree in electrical engineering and the Ph.D. degree from the Technical University of Denmark (DTU), Kongens Lyngby, Denmark, in 2008 and 2011, respectively.

He is currently an Associate Professor of Biomedical Engineering with the Department of Electrical Engineering, DTU. His current research interests include simulation of ultrasound imaging, synthetic aperture imaging, innovation of handheld ultrasound imaging systems, and image perception and quality assessment.

Pere Llimós Muntal received the B.Sc. and M.Sc. combined degree in industrial engineering with a minor in electronics from the School of Industrial Engineering of Barcelona, which is part of the Polytechnic University of Catalonia, Barcelona, Spain, in 2012. He coursed his last year of his M.Sc., including his master's thesis in digital integrated circuit design, with the Technical University of Denmark, Kongens Lyngby, Denmark, as part of an international exchange program. He is currently pursuing the Ph.D. degree in analog integrated circuit design with the Technical University of Denmark, working with transmitting and receiving circuitry for portable ultrasound scanners.

His current research interests include high-voltage transmitting circuitry and low-voltage receiving circuitry for ultrasonic transducer interfaces and continuous-time sigma delta A/D converters.

Ivan Harald Holger Jørgensen received the M.Sc. degree in digital signal processing and the Ph.D. degree in integrated analog electronics for sensor systems from the Technical University of Denmark, Kongens Lyngby, Denmark, in 1993 and 1997, respectively.

After receiving the Ph.D. degree, he was with Oticon AS, an employment that lasted for 15 years. For the first five years of the employment, he worked with all aspects of low-voltage and low-power integrated electronics for hearing aids with special focus on analog-to-digital converters, digital-to-analog converters, and system design. For the last ten years of his employment with Oticon AS, he held various management roles ranging from Competence Manager and Systems Manager to Director with the responsibility of a group of more than 20 people and several IC projects. In 2012, he was an Associate Professor with the Technical University of Denmark. He has authored 14 publications mainly related to low-voltage and low-power integrated data converters, and holds seven patents either pending or granted. His current research interests include the field of integrated sound systems, i.e., preamplifiers, analog-to-digital converters, digital-to-analog converters for audio and ultrasound applications, and integrated high-frequency power converters.

Jørgen Arendt Jensen (M'93–SM'02–F'12) received the Master of Science degree in electrical engineering in 1985 and the Ph.D. degree in 1989, both from the Technical University of Denmark. He received the Dr.Techn. degree from the university in 1996.

Since 1993, he has been Full Professor of Biomedical Signal Processing with the Department of Electrical Engineering, Technical University of Denmark and head of the Center for Fast Ultrasound Imaging since its inauguration in 1998. He has published more than 450 journal and conference papers on signal processing and medical ultrasound and the book *Estimation of Blood Velocities Using Ultrasound* (Cambridge Univ. Press), 1996. He is also the developer and maintainer of the Field II simulation program. He has been a visiting scientist at Duke University, Stanford University, and the University of Illinois at Urbana-Champaign. He was head of the Biomedical Engineering group from 2007 to 2010. In 2003, he was one of the founders of the biomedical engineering program in Medicine and Technology, which is a joint degree program between the Technical University of Denmark and the Faculty of Health and Medical Sciences at the University of Copenhagen. The degree is one of the most sought-after engineering degrees in Denmark. He was chairman of the study board from 2003 to 2010 and Adjunct Professor with the University of Copenhagen from 2005 to 2010. He has given a number of short courses on simulation, synthetic aperture imaging, and flow estimation at international scientific conferences and teaches biomedical signal processing and medical imaging at the Technical University of Denmark. His research is centered around simulation of ultrasound imaging, synthetic aperture imaging, vector blood flow estimation, and construction of ultrasound research systems.

Dr. Jensen has given more than 60 invited talks at international meetings and received several awards for his research.

Paper III

Real-time implementation of synthetic aperture vector flow imaging on a consumer-level tablet

Tommaso Di Ianni, Thomas Kim Kjeldsen, Carlos Armando Villagómez-Hoyos, Jesper Mosegaard, and Jørgen Arendt Jensen

To be published in *Proceedings of 2017 IEEE International Ultrasonics Symposium.*
Accepted for oral presentation in Washington, D.C., USA, 2017.

Real-time Implementation of Synthetic Aperture Vector Flow Imaging on a Consumer-level Tablet

Tommaso Di Ianni[1], Thomas Kim Kjeldsen[2], Carlos Armando Villagómez Hoyos[1], Jesper Mosegaard[2], Jørgen Arendt Jensen[1]

[1]Center for Fast Ultrasound Imaging, Department of Electrical Engineering, Technical University of Denmark, DK-2800 Lyngby, Denmark
[2]Visual Computing Lab, Alexandra Institute, DK-8200 Aarhus N, Denmark

***Abstract*—In this work, a 2-D vector flow imaging (VFI) method based on synthetic aperture sequential beamforming (SASB) and directional transverse oscillation is implemented on a commercially available tablet. The SASB technique divides the beamforming process in two parts, whereby the required bandwidth between the probe and back-end can be reduced by a factor of 64 compared to conventional delay-and-sum focusing. The lowered datarate enables real-time wireless transfer for both B-mode and VFI data. In the present setup, element data were acquired from a straight vessel with the SARUS research scanner and focused in a static point. The data were subsequently transferred to an HTC Nexus 9 tablet through an ASUS RT-AC68U Wi-Fi router to simulate a wireless probe. The second stage beamforming of the B-mode and flow data and the velocity estimation were implemented on the tablet's built-in GPU (Nvidia Tegra K1) through the OpenGL ES 3.1 API. Real-time performance was achieved with rates up to 26 frames per second (38 ms/frame) for concurrent processing and Wi-Fi transmission.**

I. Introduction

This paper presents an implementation of 2-D synthetic aperture (SA) vector flow imaging (VFI) on a commercially available tablet. The objective is the integration of quantitative blood flow imaging in portable ultrasound systems.

Pocket-size devices have the potential to open new possibilities for the healthcare system bringing ultrasound out of the radiology department and closer to the point of care [1]. An attempt of integrating a flow imaging modality in a general-purpose mobile device has been previously made by Hemmsen *et al.* [2] based on the method presented in [3]. However, the implementation has two major limitations. First, the velocity estimation is limited to the axial component and a prior knowledge of the flow angle is required. Second, it relies on a cross-correlation estimator that necessitates significant computational resources for the calculation of the correlation functions, which makes the method not optimal for the strict requirements of a mobile device. Other portable ultrasound systems with flow capabilities have been previously presented in literature [4], [5] or are available on the market. However, these systems only perform 1-D flow estimation and are affected by flow angle limitations.

VFI methods estimate the velocity in 2-D and do not require any manual angle adjustments providing quantitative velocity measurements [6]–[8]. For these reasons, the integration of VFI in hand-held devices has the potential to improve the clinical workflow. A 2-D SA VFI method for portable ultrasound has been recently proposed in [9] combining SA sequential beamforming (SASB) [10] and directional transverse oscillation (TO) [11]. The method enables the wireless transmission of the ultrasound data and uses a relatively inexpensive 2-D phase-shift approach for the velocity estimation. The present paper demonstrates a real-time implementation on a consumer-level mobile device in order to address the feasibility of the processing in the built-in GPU concurrent to the transmission of the data over Wi-Fi.

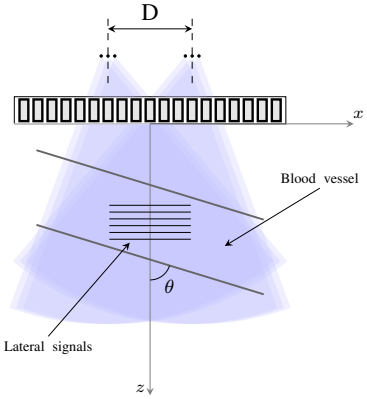

Fig. 1. Imaging setup with a linear array transducer and relative position of the VSs.

II. Background and Theory

The ultrasound data received by L transducer elements are first beamformed in a fixed point corresponding to the transmit focal position or virtual source (VS). The VS is located behind the array, therefore a diverging wave is emitted to insonify the whole image area at each emission. The fixed-focus beamformer can be integrated in the front-end of the ultrasound probe [12], therefore one single beamformed line, referred to as low-resolution line (LRL), is obtained for each

TABLE I
MEASUREMENT SETUP AND PROCESSING PARAMETERS

Parameter	Flow	B-mode	Value
Transducer			
Array type	Linear		-
Element pitch	0.2		mm
Element height	6		mm
Number of elements	192		-
Elevation focus	38		mm
Center frequency	4.1		MHz
Imaging setup			
Excitation	4 cycles	2 cycles	-
Center frequency - f_0	4.1		MHz
Tx/Rx apodization	Tukey ($\alpha = 0.6$)		-
VS axial position	−15	−30	mm
Active elements - L	64	96	-
f-number - f#	-1.17	-1.56	-
Number of VSs	$K = 6$	64	-
Distance between VAs - D	48	-	elements
Pulse repetition freq. - PRF:	9		kHz
Processing			
Lateral sampling interval	0.1		mm
Axial sampling frequency	35		MHz
Lateral signal length - M	32	-	-
Number of HRIs - N	16	-	-

emission, with a reduction of the data throughput by a factor L. The LRLs are then sent to the mobile device where a second beamforming stage takes place.

A high-resolution image (HRI) is created in the second stage after K emissions. The second beamformer is based on the VS assumption [13], [14] and its computational complexity equals that of a monostatic SA beamformer. The K VSs are divided in two virtual apertures (VAs) that are laterally separated by a distance D as shown in Fig. 1. This separation gives rise to a TO in the HRIs, which allows to estimate the velocity in both lateral and axial directions.

A moving-average-subtraction filter is used on the LRLs to remove the signal from the tissue. The beamformed HRIs are Hilbert transformed in the lateral direction, and the lateral frequency is estimated through a Fourier transform [9]. For each velocity point, M lateral samples are selected, and the velocity is estimated from N HRIs using an autocorrelation approach [11]. The method provides velocity estimates everywhere in the image, therefore continuous data acquisition can be obtained.

III. METHODS

A. Measurement setup

An experimental setup was constructed to assess the data transmission and processing performance on a consumer-level tablet. A linear array was connected to the SARUS scanner [15] for the acquisition of the element data, and a duplex sequence was designed with the parameters in Table I. The VAs were steered toward the center of the image with an angle of $\pm 2.5°$. No apodization was used on the VAs. The B-mode VSs were regularly distributed between ± 15 mm in the lateral direction. B-mode and flow emissions were interleaved

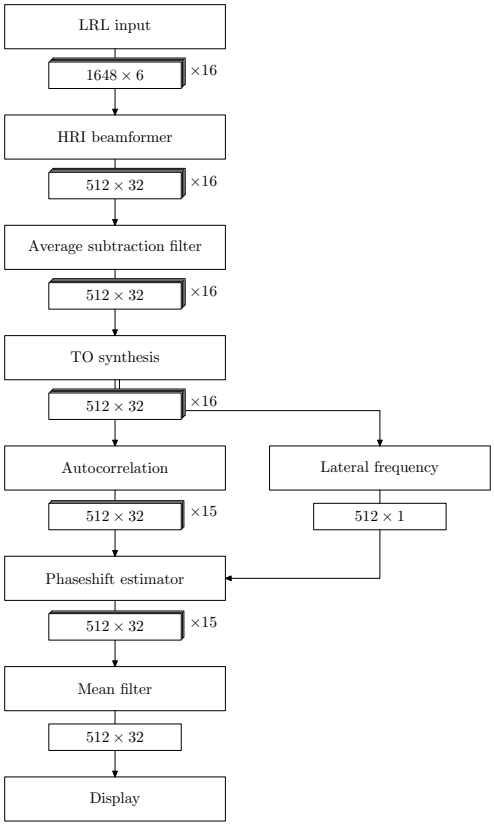

Fig. 2. Schematic overview of the VFI processing sequence on the GPU.

to achieve continuous data acquisition, i.e. one B-mode pulse was transmitted after every $K = 6$ flow emissions, with an effective pulse repetition frequency $PRF_{eff} = PRF/(K+1)$.

Measurements were performed on a flow rig system consisting of a centrifugal pump (Cole-Parmer, Vernon-Hills, IL, USA) circulating a blood mimicking fluid. A laminar flow profile was created in a vessel with a radius of 6 mm placed at a depth of approximately 20 mm with a beam-to-flow angle of 90°. The volume flow was measured for reference by a magnetic flow meter (MAG3000, Danfoss, Nordborg, Denmark) and was set to obtain a peak velocity of approximately 0.2 m s^{-1}.

For each emission, the received channel data were beamformed in Matlab (The MathWorks, Inc., Natick, MA, USA) in a fixed point to create the LRLs. These were sent to a Nexus 9 tablet (HTC Corp., Taoyuan, Taiwan) through a Wi-Fi link to simulate a wireless probe. The connection was established through an ASUS RT-AC68U (ASUS, Taipei, Taiwan) router with a maximum theoretical link speed of 867 Mbit/s. B-mode and VFI processing were performed on the tablet's built-in

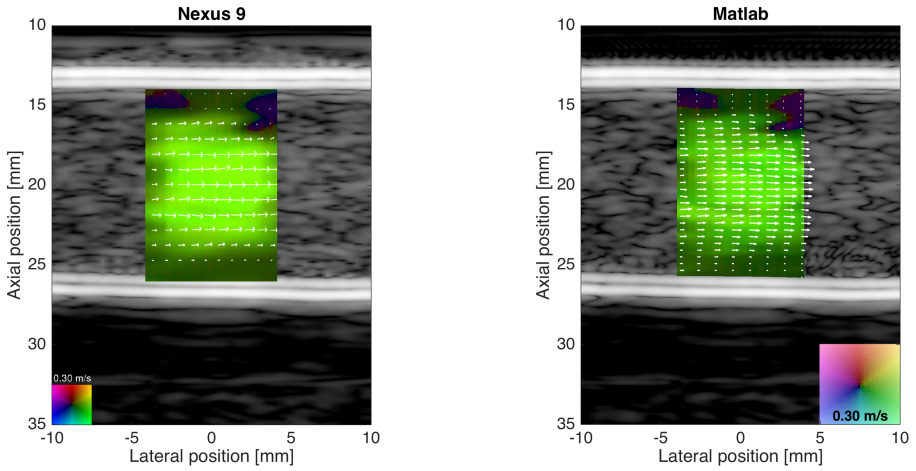

(a) (b)

Fig. 3. Comparison of the 2-D VFI frames processed in the tablet (a) and in Matlab (b). The VFI and B-mode images are overlapped. The arrows show the velocity vectors, and the angle is shown encoded as in the color wheel in the bottom of the images.

GPU.

B. GPU implementation

In order to achieve real-time performance, all the VFI computations outlined in Sec. II and described in [9] must be implemented on the tablet's GPU (Nvidia Tegra K1). Fig. 2 shows the GPU processing graph for each VFI frame in addition to the data flow arranged in 2-D texture arrays. The LRLs are buffered into the tablet's memory and copied to the GPU texture memory for further processing. The GPU was instructed to perform general purpose computations through the OpenGL ES 3.1 API and each of the tasks in Fig. 2 were implemented as compute or fragment shaders.

The GPU is perfectly suited for most of the steps, such as individual per-pixel operations, which are straightforwardly executed in parallel. However, some of the tasks require more effort to run efficiently, in particular the TO synthesis where spatial quadrature signals are created by discrete Hilbert transformations. These are generated by making the frequency spectrum one-sided using forward and inverse fast Fourier transforms (FFT) [16]. In the present work, radix-2 FFTs are implemented in OpenGL ES 3.1 compute shaders with use of fast inter-thread shared memory for efficient parallel computation.

Finally, each VFI frame is interleaved with a B-mode frame, which is computed on the GPU by refocusing, envelope detection, and scanconversion as described in detail in [17], [18].

The software implementation was written in C++ and GLSL and compiled either to a desktop application or cross-compiled to Android with the Android Native Development Kit. The performance can thus be evaluated easily on a range of discrete and mobile GPUs and operating systems.

IV. Results

The results of the 2-D VFI implementation are shown in Fig. 3, where frames processed in the tablet (3a) and in Matlab (3b) are shown for comparison. The VFI and B-mode images are overlapped. The arrows show the velocity vectors, and the angle is shown encoded as in the color wheel in the bottom of the images. The 2-D velocities were calculated in a region of $0.8 \times 1.9\,\mathrm{cm}^2$ with a resolution of 32×512 pixels.

The mean velocity profile +/- one standard deviation (SD) is shown in Fig. 4 calculated from 50 velocity profiles at the center of the VFI image processed in the tablet. The average bias is 2.91% in the lateral direction and 0.93% in the axial direction. The SD is 10.13% and 3.51% for the two velocity components.

The combined VFI and B-mode peak frame rate was 26 fps, which is sufficient for real-time performance. The corresponding data rate of LRLs that are sent over the Wi-Fi link is 13 MB/s for 1648 16-bit samples per LRL. This was lower than the average throughput of 30 MB/s measured between the tablet and the Wi-Fi router. Hence, the operational rate of the entire system is limited by the GPU processing speed rather than the data bandwidth.

Previously, it was identified that the particular tablet model suffers from heating issues when the GPU and network card operate concurrently close to the maximum load [2]. To test whether this is the case for the present implementation, continuous scanning simulations were carried out for a duration of several minutes. The benchmark covered data input from a)

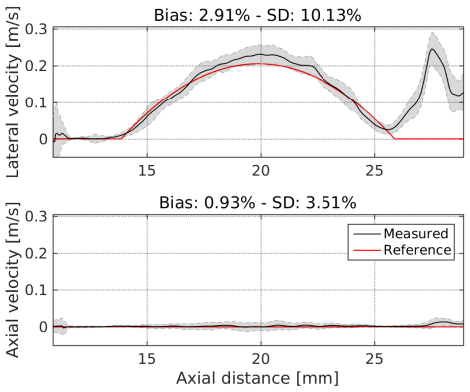

Fig. 4. Mean lateral (top) and axial (bottom) velocity profiles +/- one standard deviation calculated from 50 velocity profiles at the center of the VFI image.

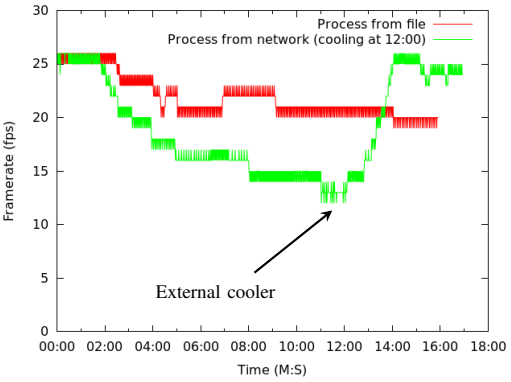

Fig. 5. Processing framerates for continuous operation with data input from a local file (red) and from a Wi-Fi network (green). An external cooler is activated after 12 minutes for the Wi-Fi case.

a pre-recorded dataset stored on the device and b) the Wi-Fi link. In Fig. 5, the processing frame rate is shown as a function of the time since the session was started. The figure clearly shows that the frame rate was lowered significantly after a few minutes of combined GPU and network load. This issue is indeed related to thermal throttling because the initial peak frame rate is restored when an external cooler is activated. Note that the thermal issues are much less severe if the data are read from the memory and the network card is idle.

V. Conclusion

In conclusion, SA VFI is feasible in a commercial tablet with real-time performance. The computational tasks were efficiently implemented on the GPU, and the data reduction of the sequential beamforming enables real-time wireless transmission. For continuous scanning sessions of several minutes duration, however, performance degraded due to heating of the chipset of the Nexus 9 tablet used in the experiment.

Acknowledgement

This work was supported by grant 82-2012-4 from the Danish National Advanced Technology Foundation and by BK Ultrasound.

References

[1] C. Prinz and J. U. Voigt, "Diagnostic accuracy of a hand-held ultrasound scanner in routine patients referred for echocardiography," *J. Am. Soc. Echocardiog.*, vol. 24, no. 2, pp. 111–116, 2011.

[2] M. C. Hemmsen, L. Lassen, T. Kjeldsen, J. Mosegaard, and J. A. Jensen, "Implementation of real-time duplex synthetic aperture ultrasonography," in *Proc. IEEE Ultrason. Symp.*, 2015, pp. 1–4.

[3] Y. Li and J. A. Jensen, "Synthetic aperture flow imaging using dual stage beamforming: Simulations and experiments," *J. Acoust. Soc. Am.*, vol. 133, no. 4, pp. 2014–2024, 2013.

[4] C. Huang, P. Lee, P. Chen, and T. Liu, "Design and implementation of a smartphone-based portable ultrasound pulsed-wave Doppler device for blood flow measurement," *IEEE Trans. Ultrason., Ferroelec., Freq. Contr.*, vol. 59, no. 1, pp. 182–188, 2012.

[5] E. Jeong, S. Bae, M. Park, W. Jung, J. Kang, and T. Song, "Color Doppler imaging on a smartphone-based portable US system: Preliminary study," *Proc. IEEE Ultrason. Symp.*, pp. 1–4, 2015.

[6] B. Dunmire, K. W. Beach, K.-H. Labs., M. Plett, and D. E. Strandness, "Cross-beam vector Doppler ultrasound for angle independent velocity measurements," *Ultrasound Med. Biol.*, vol. 26, pp. 1213–1235, 2000.

[7] G. E. Trahey, J. W. Allison, and O. T. von Ramm, "Angle independent ultrasonic detection of blood flow," *IEEE Trans. Biomed. Eng.*, vol. BME-34, no. 12, pp. 965–967, 1987.

[8] J. A. Jensen and P. Munk, "A new method for estimation of velocity vectors," *IEEE Trans. Ultrason., Ferroelec., Freq. Contr.*, vol. 45, no. 3, pp. 837–851, 1998.

[9] T. Di Ianni, C. Villagomez-Hoyos, C. Ewertsen, T. Kjeldsen, J. Mosegaard, and J. A. Jensen, "A vector flow imaging method for portable ultrasound using synthetic aperture sequential beamforming," *IEEE Trans. Ultrason., Ferroelec., Freq. Contr.*, p. Submitted, 2017.

[10] J. Kortbek, J. A. Jensen, and K. L. Gammelmark, "Sequential beamforming for synthetic aperture imaging," *Ultrasonics*, vol. 53, no. 1, pp. 1–16, 2013.

[11] J. A. Jensen, "Directional transverse oscillation vector flow estimation," *IEEE Trans. Ultrason., Ferroelec., Freq. Contr.*, vol. 63, p. Submitted, 2016.

[12] T. Di Ianni, M. C. Hemmsen, P. L. Muntal, I. H. Jørgensen, and J. A. Jensen, "System-level design of an integrated receiver front end for a wireless ultrasound probe," *IEEE Trans. Ultrason., Ferroelec., Freq. Contr.*, vol. 63, no. 11, pp. 1935–1946, 2016.

[13] C. Passmann and H. Ermert, "A 100-MHz ultrasound imaging system for dermatologic and ophthalmologic diagnostics," *IEEE Trans. Ultrason., Ferroelec., Freq. Contr.*, vol. 43, pp. 545–552, 1996.

[14] M. H. Bae and M. K. Jeong, "A study of synthetic-aperture imaging with virtual source elements in B-mode ultrasound imaging systems," in *IEEE Trans. Ultrason., Ferroelec., Freq. Contr.*, vol. 47, 2000, pp. 1510–1519.

[15] J. A. Jensen, H. Holten-Lund, R. T. Nilsson, M. Hansen, U. D. Larsen, R. P. Domsten, B. G. Tomov, M. B. Stuart, S. I. Nikolov, M. J. Pihl, Y. Du, J. H. Rasmussen, and M. F. Rasmussen, "Sarus: A synthetic aperture real-time ultrasound system," *IEEE Trans. Ultrason., Ferroelec., Freq. Contr.*, vol. 60, no. 9, pp. 1838–1852, September 2013.

[16] S. Marple, "Computing the discrete-time "analytic" signal via FFT," *IEEE Trans. Sig. Proc.*, vol. 47, no. 9, pp. 2600–2603, 1999.

[17] M. C. Hemmsen, T. Kjeldsen, L. Lassen, C. Kjær, B. Tomov, J. Mosegaard, and J. A. Jensen, "Implementation of synthetic aperture imaging on a hand-held device," in *Proc. IEEE Ultrason. Symp.*, 2014, pp. 2177–2180.

[18] T. Kjeldsen, L. Lassen, M. Hemmsen, C. Kjær, B. Tomov, J. Mosegaard, and J. Jensen, "Synthetic aperture sequential beamforming implemented on multi-core platforms," *Proc. IEEE Ultrason. Symp.*, pp. 1–4, 2014.

Paper IV

High-frame-rate imaging of a carotid bifurcation using a low-complexity velocity estimation approach

Tommaso Di Ianni, Carlos Armando Villagómez-Hoyos, Caroline Ewertsen, Michael Bachmann Nielsen, and Jørgen Arendt Jensen

To be published in *Proceedings of 2017 IEEE International Ultrasonics Symposium.*
Accepted for poster presentation in Washington, D.C., USA, 2017.

High-frame-rate Imaging of a Carotid Bifurcation using a Low-complexity Velocity Estimation Approach

Tommaso Di Ianni[1], Carlos Armando Villagómez Hoyos[1], Caroline Ewertsen[2], Michael Bachmann Nielsen[2], Jørgen Arendt Jensen[1]

[1]Center for Fast Ultrasound Imaging, Department of Electrical Engineering, Technical University of Denmark, DK-2800 Lyngby, Denmark
[2]Department of Radiology, Rigshospitalet, Copenhagen University Hospital, Copenhagen 2100, Denmark

***Abstract*—In this paper, a 2-D vector flow imaging (VFI) method developed by combining synthetic aperture sequential beamforming and directional transverse oscillation is used to image a carotid bifurcation. Ninety-six beamformed lines are sent from the probe to the host system for each VFI frame, enabling the possibility of wireless transmission. The velocity is estimated using a relatively inexpensive 2-D phase-shift approach, and real-time performance can be achieved in mobile devices. However, high-frame-rate velocities can be obtained by sending the data to a cluster of computers. The objective of this study is to demonstrate the scalability of the method's performance according to the needs of the user and the processing capabilities of the host system. *In vivo* measurements of a carotid bifurcation of a 54-year-old volunteer were conducted using a linear array transducer connected to the SARUS scanner. The velocities were estimated at a rate of 134 independent frames per second to reveal complex flow patterns. VFI images are shown during the systolic phase revealing the formation of a vortex in the internal carotid artery. The peak systolic velocity from a range gate in the common tract was 0.76 m s^{-1} with a standard deviation (SD) of 6.1%. The mean velocity profile was calculated from the same range gate with an average SD of 7.86%.**

I. Introduction

A number of pocket-size ultrasound devices are today available on the market with anatomical and functional imaging features and a form factor such as to fit in a lab coat pocket. These systems have enabled the possibility of diagnostic ultrasound imaging at the point of care, allowing a more prompt assessment of the patient's condition. Several studies have demonstrated the value of hand-held ultrasound equipment in a number of medical specialties such as emergency medicine, intensive care and echocardiography [1], [2], as well as in rural districts of low and middle-income countries [3].

App-based systems allow to significantly reduce the cost of the scanner by exploiting general-purpose mobile devices as smartphones or tablets for the processing and visualization. Several attempts have been previously made to integrate flow imaging capabilities in such systems [4], [5], and color flow mapping is currently accessible in most of the commercial scanners. However, these implementations are unable to estimate the velocity in multiple directions and thus require a prior knowledge of the flow angle.

Vector flow imaging (VFI) overcomes the flow angle limitations by estimating the velocity components along the lateral and axial directions. Several VFI approaches have been comprehensively investigated, including vector Doppler [6], speckle tracking [7], and transverse oscillation (TO) [8]. The integration of VFI in a portable scanner has the potential to improve the clinical workflow, as quantitative flow measurements are made available with limited operator interaction. Furthermore, by using synthetic aperture (SA) techniques, the velocity field can be accessed everywhere at any time with high temporal resolution, and velocity profiles can be visualized in a multi-gated approach similar to that previously shown in [9].

A 2-D VFI method has been recently proposed [10], which combines SA sequential beamforming (SASB) [11] and directional TO (DTO) [12]. The method enables the wireless transmission of the ultrasound data along with a relatively inexpensive 2-D velocity estimation. In the accompanying paper [13], the method is implemented on a commercially available tablet attaining processing performance suitable for real-time imaging. Nevertheless, the maximum frame rate of 26 frames per second (FPS) is limited by the processing capabilities of the device rather than the acquisition sequence.

In this work, the same VFI approach is used to image a carotid bifurcation *in vivo* with high frame rate revealing complex flow patterns in the lumen. The objective is to demonstrate the possibility to implement a flexible imaging framework with scalable performance according to the needs of the operator and the computing capabilities of the host system.

II. Background and theory

The SASB approach uses a dual-stage beamforming process to lower the datarate between the probe and the processing unit. The received data are first beamformed in a fixed point considered a virtual source (VS), and the beamformer can be integrated in the probe handle [14]. One single beamformed line, referred to as low-resolution line (LRL), is obtained

TABLE I
MEASUREMENT SETUP AND PROCESSING PARAMETERS

Parameter	Flow	B-mode	Value
Transducer			
Array type	Linear		-
Element pitch	0.2		mm
Element height	6		mm
Number of elements	192		-
Elevation focus	38		mm
Center frequency	4.1		MHz
Imaging setup			
Excitation	4 cycles	2 cycles	-
Center frequency - f_0	4.1		MHz
Tx/Rx apodization	Tukey ($\alpha = 0.6$)		-
VS axial position	−15	−30	mm
Active elements - L	64	96	-
f-number - f#	-1.17	-1.56	-
Number of VSs	$K = 6$	64	-
Distance between VAs - D	48	-	elements
Pulse repetition freq. - PRF:	15		kHz
Processing			
Lateral sampling interval	0.1		mm
Axial sampling frequency	35		MHz
Lateral signal length - M	32	-	-
Number of HRIs - N	16	-	-

for each emission. The LRLs are used by a second-stage beamformer to create a high-resolution image (HRI) after K emissions. Therefore, only K lines per HRI must be sent to the host system.

A TO is obtained in the HRIs due to the spatial distribution of the VSs. These are divided in two virtual apertures (VAs) laterally separated by a distance D. The TO is exploited to estimate the velocity in both lateral and axial directions from N HRIs using a relatively inexpensive 2-D phase-shift estimator [12]. For further details on the method and implementation, readers are referred to [10].

III. METHODS

A duplex sequence was designed with the parameters in Table I. A linear array of transducers was connected to the SARUS scanner [15] for the acquisition of B-mode and flow data. A sequence of 9.5 s of data was saved from the left carotid bifurcation of a 54-year-old female volunteer with no history of cardiovascular disease. The acquisition was performed by an experienced radiologist with the volunteer in supine position. The volunteer was asked to rest for approximately 10 min to ensure more stationary flow conditions.

The VAs were positioned behind the transducer and steered toward the center of the image with an angle of $\pm 2.5°$. Continuous data acquisition was achieved by transmitting one B-mode pulse after every $K = 6$ flow emissions, with an effective pulse repetition frequency $PRF_{eff} = PRF/(K+1)$.

All the processing was carried out off-line in Matlab (The MathWorks, Inc., Natick, MA, USA) using in-house developed code. The received channel data were first beamformed in fixed points to create the LRLs, which were sent to the second beamformer to obtain the HRIs. The beamformation was performed using the BFT3 toolbox [16]. After clutter filtration, $N = 16$ HRIs were used for the velocity estimation, therefore only $16 \times 6 = 96$ LRLs are sent from the probe to the host per VFI frame. The velocity estimation was performed in a high-performance computing cluster with a frame rate of 350 FPS. However, according to the emission sequence, only $PRF_{eff}/N = 134$ FPS were completely independent. The velocities were filtered using a median filter in a temporal window of 25 ms and a spatial window of $1 \times 1\,\text{mm}^2$.

The frame rate of the B-mode sequence was 33 FPS. A binary mask was generated from the B-mode images to discriminate the vessel area from the surrounding tissue. The video was paced down by a factor 14.

IV. RESULTS

A VFI frame is shown in Fig. 1a during the systolic phase. B-mode and VFI images are overlapped. The arrows show the local velocity vectors while the underlying colors encode the velocity magnitude and direction as specified by the color wheel in the bottom of the image. Figure 1b displays the velocity magnitude as a function of the time at the locations A and B in the left figure. The point A was selected in the common tract and B in the internal carotid artery (ICA). The mean peak-systolic velocity (PSV) calculated in A from the 10 cardiac cycles is $0.76\,\text{m}\,\text{s}^{-1}$ with a SD of 6.1%. The end-diastolic velocity was calculated by averaging the velocities in the period between 70% and 90% of the cardiac cycle, and the mean over the 10 cycles is $0.15\,\text{m}\,\text{s}^{-1}$. The SD was calculated relative to the mean EDV and is equal to 12.3%. The mean PSV in B is $0.77\,\text{m}\,\text{s}^{-1}$ with a SD of 9%. A more turbulent flow and the occurrence of out-of-plane motion can be the reasons for the slightly higher SD registered at the ICA. The velocity field is available at any time everywhere in the image, and multiple profiles like the ones in Fig. 1b can be obtained in a multi-gated approach without the need for any additional manual adjustments by the operator.

A low-velocity vortex can be identified in the bulb of the ICA and is displayed magnified in Fig. 2 from the same VFI frame in Fig. 1a. The vortex is consistent with the findings of previous studies [17].

In Fig. 3, the mean velocity profile is shown in read along with the SD displayed as the shadowed area calculated by aligning the 10 cardiac cycles in the point A in Fig. 1b. The SD averaged over one cycle is 7.86%.

A VFI frame during late systole is displayed in Fig. 4. No vortex is identified in the carotid bulb and a more parabolic profile is observed in the common tract.

V. DISCUSSION AND CONCLUSIONS

In this paper, a 2-D VFI method previously developed for wireless ultrasound combining SASB and DTO was used to image a carotid bifurcation *in vivo*. A frame rate of 134 independent frames per second was achieved, which was sufficient to reveal the presence of complex and fast flow dynamics in the carotid bifurcation. The velocity profiles were shown in the common and ICA with SDs between 6 and 9%.

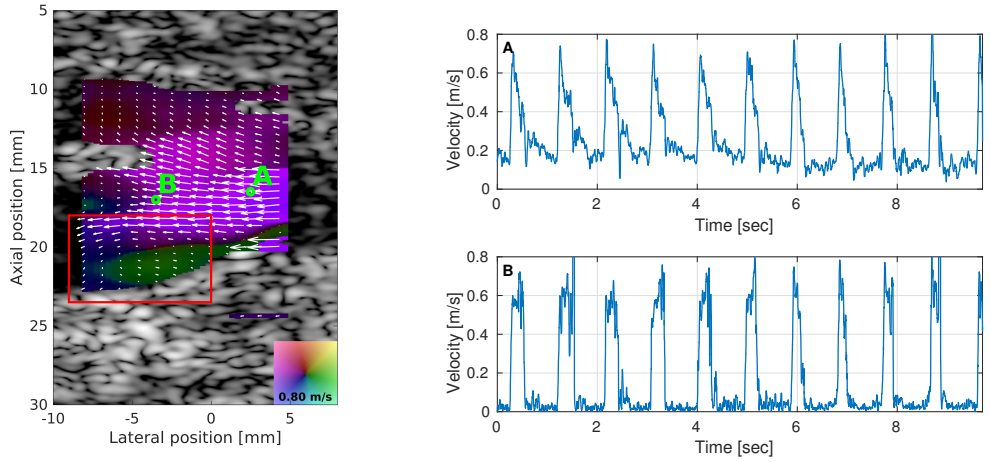

(a) (b)

Fig. 1. (a) VFI frame during the peak systolic phase. A low-velocity vortex is observed in the bulb of the internal carotid artery; (b) velocity magnitude as a function of the time in the points A (top) and B (bottom) specified in (a). The velocity is shown for 10 cardiac cycles.

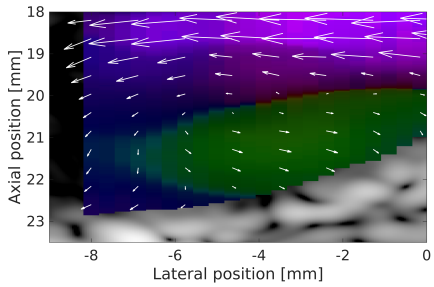

Fig. 2. Vortex formed in the internal carotid artery in the red rectangle in Fig. 1a.

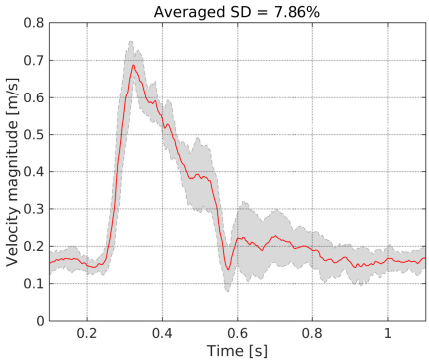

Fig. 3. Mean velocity profile (read) and SD (shadowed area) calculated by aligning the 10 cardiac cycles relative to the point A in Fig. 1b. The SD averaged over one cycle is 7.86%.

The formation of vortices and turbulence is associated with the occurrence of atherosclerotic lesions, therefore the visualization of these phenomena has the potential to lead to an early identification of atherosclerotic sites and allow for preventive intervention. The availability of the velocity field, in addition, opens new possibilities for derived hemodynamic measures like the wall shear stress [18].

The method makes it possible to integrate the advantages of VFI features in hand-held systems. Under the same conditions of the demonstration in [13], 2.2 s are needed to transmit the LRLs relative to 134 frames at an average data rate of 30 MB/s. Therefore, real-time transfer would not be possible at this frame rate, and a memory buffer would be necessary in-handle.

However, the paper demonstrates, in conclusion, that a highly flexible framework can be implemented, where real-time processing is firstly performed in the host device (tablet), and more complex and advanced imaging modalities can be attained on-demand by sending the same data to a third processing system.

Acknowledgement

This work was supported by grant 82-2012-4 from the Danish National Advanced Technology Foundation and by BK Ultrasound.

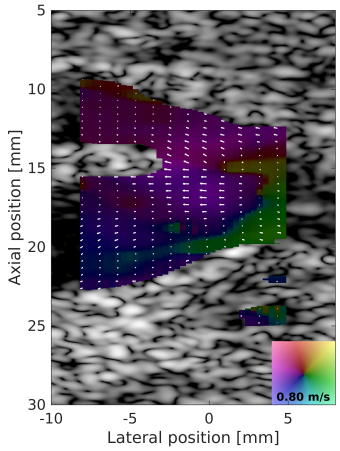

Fig. 4. VFI frame during late systole. No vortex is identified in the carotid bulb and a more parabolic profile is observed in the common tract.

REFERENCES

[1] A. W. Kirkpatrick, M. Sirois, K. B. Laupland, D. Liu, K. Rowan, C. G. Ball, S. M. Hameed, R. Brown, R. Simons, S. A. Dulchavsky, D. R. Hamiilton, and S. Nicolaou, "Hand-held thoracic sonography for detecting post-traumatic pneumothoraces: the extended focused assessment with sonography for trauma (EFAST)," *J. Trauma*, vol. 57, no. 2, pp. 288–295, 2004.

[2] C. Prinz and J. U. Voigt, "Diagnostic accuracy of a hand-held ultrasound scanner in routine patients referred for echocardiography," *J. Am. Soc. Echocardiog.*, vol. 24, no. 2, pp. 111–116, 2011.

[3] S. Sippel, K. Muruganandan, A. Levine, and S. Shah, "Review article: Use of ultrasound in the developing world," *Int. J. Emerg. Med.*, vol. 72, no. 4, December 2011.

[4] M. C. Hemmsen, L. Lassen, T. Kjeldsen, J. Mosegaard, and J. A. Jensen, "Implementation of real-time duplex synthetic aperture ultrasonography," in *Proc. IEEE Ultrason. Symp.*, 2015, pp. 1–4.

[5] E. Jeong, S. Bae, M. Park, W. Jung, J. Kang, and T. Song, "Color Doppler imaging on a smartphone-based portable US system: Preliminary study," *Proc. IEEE Ultrason. Symp.*, pp. 1–4, 2015.

[6] B. Dunmire, K. W. Beach, K.-H. Labs., M. Plett, and D. E. Strandness, "Cross-beam vector Doppler ultrasound for angle independent velocity measurements," *Ultrasound Med. Biol.*, vol. 26, pp. 1213–1235, 2000.

[7] G. E. Trahey, J. W. Allison, and O. T. von Ramm, "Angle independent ultrasonic detection of blood flow," *IEEE Trans. Biomed. Eng.*, vol. BME-34, no. 12, pp. 965–967, 1987.

[8] J. A. Jensen and P. Munk, "A new method for estimation of velocity vectors," *IEEE Trans. Ultrason., Ferroelec., Freq. Contr.*, vol. 45, no. 3, pp. 837–851, 1998.

[9] S. Ricci, L. Bassi, and P. Tortoli, "Real-time vector velocity assessment through multigate Doppler and plane waves," *IEEE Trans. Ultrason., Ferroelec., Freq. Contr.*, vol. 61, no. 2, pp. 314–324, 2014.

[10] T. Di Ianni, C. Villagomez-Hoyos, C. Ewertsen, T. Kjeldsen, J. Mosegaard, and J. A. Jensen, "A vector flow imaging method for portable ultrasound using synthetic aperture sequential beamforming," *IEEE Trans. Ultrason., Ferroelec., Freq. Contr.*, p. Submitted, 2017.

[11] J. Kortbek, J. A. Jensen, and K. L. Gammelmark, "Sequential beamforming for synthetic aperture imaging," *Ultrasonics*, vol. 53, no. 1, pp. 1–16, 2013.

[12] J. A. Jensen, "Directional transverse oscillation vector flow estimation," *IEEE Trans. Ultrason., Ferroelec., Freq. Contr.*, vol. 63, p. Submitted, 2016.

[13] T. Di Ianni, T. Kjeldsen, C. Villagomez-Hoyos, J. Mosegaard, and J. A. Jensen, "Real-time implementation of synthetic aperture vector flow imaging in a consumer-level tablet," *Proc. IEEE Ultrason. Symp.*, pp. 1–4, 2017.

[14] T. Di Ianni, M. C. Hemmsen, P. L. Muntal, I. H. Jørgensen, and J. A. Jensen, "System-level design of an integrated receiver front end for a wireless ultrasound probe," *IEEE Trans. Ultrason., Ferroelec., Freq. Contr.*, vol. 63, no. 11, pp. 1935–1946, 2016.

[15] J. A. Jensen, H. Holten-Lund, R. T. Nilsson, M. Hansen, U. D. Larsen, R. P. Domsten, B. G. Tomov, M. B. Stuart, S. I. Nikolov, M. J. Pihl, Y. Du, J. H. Rasmussen, and M. F. Rasmussen, "Sarus: A synthetic aperture real-time ultrasound system," *IEEE Trans. Ultrason., Ferroelec., Freq. Contr.*, vol. 60, no. 9, pp. 1838–1852, September 2013.

[16] J. M. Hansen, M. C. Hemmsen, and J. A. Jensen, "An object-oriented multi-threaded software beamformation toolbox," in *Proc. SPIE Med. Imag.*, vol. 7968, March 2011, pp. 79 680Y–1–79 680Y–9.

[17] K. L. Hansen, J. Udesen, F. Gran, J. A. Jensen, and M. B. Nielsen, "Fast blood vector velocity imaging using ultrasound, in-vivo examples of complex blood flow in the vascular system," in *Proc. IEEE Ultrason. Symp.*, 2008, pp. 1068–1071.

[18] C. Poelma, R. M. E. van der Mijle, J. M. Mari, M. X. Tang, P. D. Weinberg, and J. Westerweel, "Ultrasound imaging velocimetry: toward reliable wall shear stress measurements," *European Journal of Mechanics - B/Fluids*, vol. 35, pp. 70–75, 2012.

Paper V

Vector Velocity Estimation for Portable Ultrasound using Directional Transverse Oscillation and Synhtetic Aperture Sequential Beamforming

Tommaso Di Ianni, Martin Christian Hemmsen, and Jørgen Arendt Jensen

Proceedings of 2016 IEEE International Ultrasonics Symposium, pp. 1-4. Accepted for poster presentation in Tours, France, 2016.

Vector Velocity Estimation for Portable Ultrasound using Directional Transverse Oscillation and Synthetic Aperture Sequential Beamforming

Tommaso Di Ianni, Martin Christian Hemmsen, Jørgen Arendt Jensen

Center for Fast Ultrasound Imaging, Department of Electrical Engineering,
Technical University of Denmark, DK-2800 Lyngby, Denmark

***Abstract*—In this paper, a vector flow imaging method is presented, which combines the directional transverse oscillation approach with synthetic aperture sequential beamforming to achieve an efficient estimation of the velocities. A double-oscillating field is synthesized using two sets of focused emissions separated by a distance in the lateral direction. A low-resolution line (LRL) is created for each emission in the first stage beamformer, and a second beamformer provides the high-resolution data used for the velocity estimation. The method makes it possible to have continuously available data in the whole image. Therefore, high and low velocities can be estimated with a high frame rate and a low standard deviation. The first stage is a fixed-focus beamformer that can be integrated in the transducer handle, enabling the wireless transmission of the LRLs. The approach does not require any angle compensation or prior knowledge on the beam-to-flow angle. The feasibility of the method is demonstrated through simulations and flow rig measurements of a parabolic flow in a vessel at 90-degree beam-to-flow angle. The mean bias obtained from 50 independent measurements is equal to -0.67% for the lateral profile and -0.43% for the axial profile. The relative standard deviation is 3.19% and 0.47% for the lateral and axial profiles. It is, therefore, demonstrated that vector velocity estimation can be efficiently integrated in a portable ultrasound scanner with state-of-the-art performance.**

I. Introduction

The visualization of blood flow dynamics in a vectorial form is an effective tool for the assessment of a number of cardiovascular diseases. The estimation of 2-D velocity vectors allows the clinicians to extract useful information from complex flow patterns and perform quantitative measurements. A number of vector flow imaging (VFI) methods have been proposed in the literature [1]–[4]. Recently, Jensen [5] presented a directional transverse oscillation (DTO) approach, which improves the previous transverse oscillation (TO) implementation.

The integration of VFI in a handheld scanner opens a wide range of new potential applications. The feasibility of a color flow mapping sequence implemented in a consumer-level tablet was demonstrated by Hemmsen *et al.* [6] based on synthetic aperture sequential beamforming (SASB) [7], [8]. The fixed-focused ultrasound lines were wirelessly transmitted to the tablet, where re-focusing and velocity estimation were performed. The approach was based on directional beamforming [9]. Due to the high computational requirements of the method, given, in particular, by the necessity of cross-correlating the directional lines for the velocity estimation, thermal issues compromised the real-time performance of the imaging sequence. Furthermore, the method requires the knowledge of the flow angle, which needs to be estimated with increased computational demand.

In this paper, a VFI method is presented, which combines SASB with DTO to achieve a more efficient estimation of the velocities. The method is based on an autocorrelation approach, and does not require any prior estimation of the flow angle. Simulations of a parabolic flow profile in a vessel at 90° beam-to-flow angle were performed in Field II [10], [11] using a linear array transducer to demonstrate the feasibility of the approach. Measurements in a flow rig, finally, demonstrate its performance in a realistic situation.

II. Background and Theory

A. Directional Transverse Oscillation

In DTO, a weakly focused beam is emitted and the ultrasound field received by all the transducer elements is beamformed using two apodized apertures separated by a distance in the lateral direction. This creates a double-oscillating pulse-echo field, which allows to estimate the blood velocity in the axial and lateral dimensions.

At a given depth l, the signal $x(k,l,m)$ is beamformed in the direction transverse to the direction of propagation of the ultrasound beam, with k the sample index along the lateral direction, and m the emission index. The quadrature signal required for the velocity estimation [12] is then obtained by performing a Hilbert transform of the lateral signal

$$y(k,l,m) = \mathcal{H}_k\{x(k,l,m)\}, \tag{1}$$

where $\mathcal{H}_k$ is the Hilbert transform in the direction of k.

A complex signal

$$r_{sq}(k,l,m) = x(k,l,m) + jy(k,l,m) \tag{2}$$

is created by combining the in-phase and quadrature lateral signals, and the lateral wavelength is calculated as:

$$\frac{1}{\lambda_x(l,m)} = f_x(l,m) = \frac{\sum_{f=-N/2}^{N/2} \frac{f}{N\Delta k} |R_{sq}(f,l,m)|^2}{\sum_{f=-N/2}^{N/2} |R_{sq}(f,l,m)|^2} \tag{3}$$

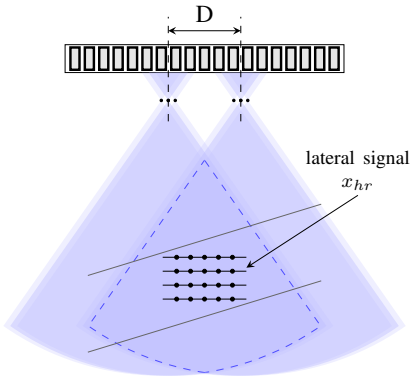

Fig. 1. Imaging setup for SASB DTO with a linear array transducer.

with R_{sq} the Fourier transform of the directional signal r_{sq} along the lateral direction, N the number of Fourier coefficients, f the sample index in the Fourier domain, and Δk the lateral spatial sampling period. For the equations involved in the velocity estimation, readers are referred to [5].

Contrary to conventional TO, the lateral oscillation wavelength λ_x is directly estimated as a function of the depth from the beamformed data, relieving the method of the need to precisely calibrate the beamformers. λ_x can also be averaged over the axial dimension to improve the variance of the estimate. Furthermore, DTO decouples the lateral wavelength from the apodization function, maintaining a low bias for the velocity estimation along the depth.

B. Laterally oscillating field using SASB

In the proposed method, the laterally oscillating field is synthesized using two sets of virtual sources (VSs) separated by a distance D, as shown in Fig. 1. Each set is referred to as virtual aperture (VA). The VSs are obtained by using a static focus in transmit and receive. For each emission, a low-resolution line (LRL) is beamformed in the first stage. A double-oscillating field is then created by the second stage beamformer from a set of K weighted LRLs - $K = 6$ in Fig. 1 - in the whole high-resolution image (HRI) at once (dashed line in Fig. 1). The extent of this image is a function of the f-number of the VSs and the distance D.

The high-resolution lateral signal $x_{hr}(k, l, m)$ is found at the depth l in the m-th HRI. The velocity estimation is performed as explained in Sec. II-A, where x_{hr} is used in place of x in (1) and (2). A new lateral signal is calculated after every K emissions. Therefore, the effective pulse repetition period for the flow estimation, referred to as T_{prf}^{eff}, is equal to KT_{prf}, with T_{prf} the repetition period of the flow sequence.

It must be noticed that, unlike DTO, which estimates the velocities on a line base, the proposed approach provides velocity estimates everywhere in the HRI. Therefore, continuous data is available, and high and low velocities can be estimated at once with a high frame rate and a low standard deviation. Furthermore, only one beamformed LRL for each emission needs to be transmitted from the probe to the processing unit, if the fixed-focus beamformer is implemented in the probe handle. As a result, the transmission can be achieved through a wireless link.

TABLE I
FIXED SIMULATION AND MEASUREMENT PARAMETERS

Speed of sound	1490	$\mathrm{m\,s^{-1}}$
Transducer parameters		
Transducer	Linear array	-
Element pitch	0.55	λ
Virtual sources parameters		
Excitation	4-cycle weighted	-
Center frequency	4.1	MHz
Transmit apodization	Rectangular	-
Receive apodization	Hamming	-
f-number - f#	1.19	-
Axial position	10	mm
Number of VSs - K	6	-
Effective repetition frequency - f_{prf}^{eff}	1.5	kHz
VA apodization	Rectangular	-
Beamforming parameters		-
Lateral sampling frequency	10 000	1/m
Lateral signal length	32	sample

TABLE II
PARAMETERS VARIED IN SIMULATION

VA distance - D	16 - 24 - 32 - 40 **48** - 56 - 64 - 72	element
HRI per estimate - M	8 - 16 - **32** 64 - 96 - 128	-

III. METHODS

A. Simulation setup

Simulations were performed in Field II to investigate the potential of the method. A simulation model was developed in MATLAB (The MathWorks Inc., Natick, MA, USA), and the second stage beamformer was implemented using the BFT3 toolbox [13]. The parameters fixed for all the simulations are reported in Table I. A 0.55λ-pitch linear array transducer was used with a center frequency of 4.1 MHz. The effective pulse repetition frequency for the flow sequence was set to $f_{prf}^{eff} = 1.5\,\mathrm{kHz}$ ($T_{prf}^{eff} = 1/f_{prf}^{eff}$). The f-number was $f\# = 1.19$.

A parabolic flow in a vessel with a 6−mm radius located at a depth of 50 mm with 90° beam-to-flow angle was simulated. At least 20 scatterers per resolution volume were considered to ensure fully developed speckle. The peak velocity was $v_{max} = 0.2\,\mathrm{m\,s^{-1}}$. The distance D between the VAs and the number M of HRIs used per velocity estimate were varied to investigate their effect on the performance of the approach (Table II). The mean bias and the relative standard deviation for the velocity estimation were calculated inside the vessel from 50 independent simulations.

B. Measurement setup

A parabolic flow in a 6−mm radius tube was scanned in a flow rig system. The SARUS scanner [14] was connected to a

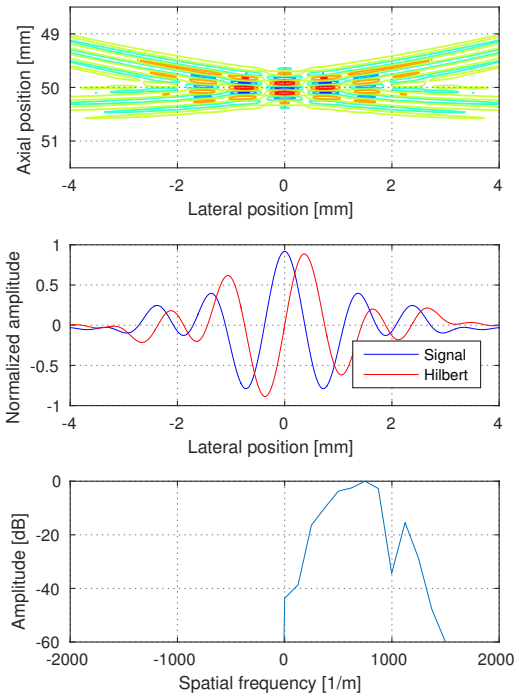

Fig. 2. The simulated double-oscillating PSF at 50 mm for $D = 48$ is shown in the top figure; the signal obtained by sampling the PSF at the peak point in the lateral direction and its Hilbert transform are shown in the middle image; the bottom image shows the one-sided spectrum used for the estimation of the lateral wavelength.

BK Ultrasound (Herlev, Denmark) 2L8 linear array transducer, which has a center frequency of 4.1 MHz and a 0.55λ pitch. The volume flow was measured for reference using a magnetic flow meter (MAG3000, Danfoss, Nordborg, Denmark). The vessel was located at a depth of 50 mm with a beam-to-flow angle of 90° and a peak velocity of 0.21 m s^{-1}. The same parameters as in Table I were used for the measurements. The distance between the VAs was varied as in Table II, while M was fixed to 32. The pulse repetition frequency of the system was set to $f_{prf} = 9$ kHz. Stationary-echo cancelling was achieved by averaging 16 high-resolution images. The mean bias and the relative standard deviation were calculated for the points inside the vessel from 50 estimations with independent data.

IV. Results

The simulated double-oscillating point spread function (PSF) at a depth of 50 mm is displayed in Fig. 2 (top) for $D = 48$, along with the signal obtained by sampling the PSF at the peak point in the lateral direction and its Hilbert transform (middle). The bottom figure shows the one-sided spectrum

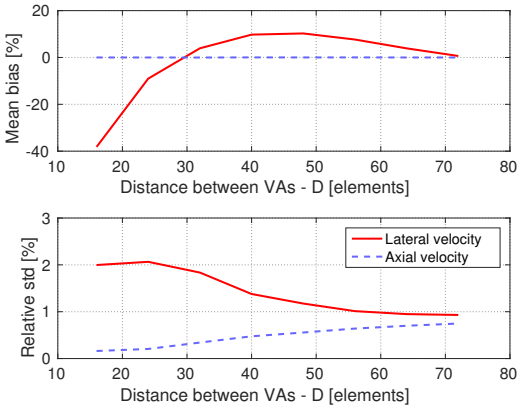

Fig. 3. Mean bias (top) and relative standard deviation (bottom) for the simulated lateral (red-solid) and axial (blue-dotted) velocity profiles as a function of the distance D between VAs.

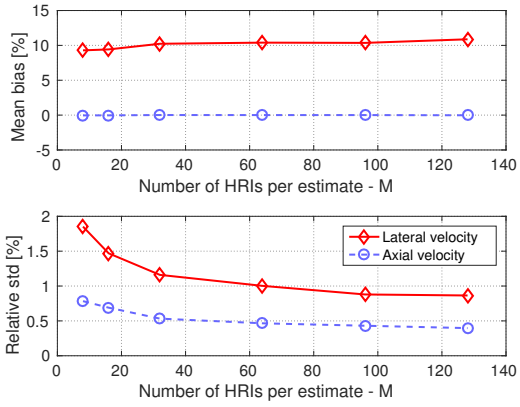

Fig. 4. Mean bias (top) and relative standard deviation (bottom) for the simulated lateral and axial profiles as a function of the number M of HRIs used per estimate.

obtained by Fourier transforming the complex lateral signal. This is used to estimate the lateral wavelength as in (3).

Fig. 3 shows the mean bias (top) and the relative standard deviation (bottom) for the simulated velocity profiles as a function of the distance D. The mean bias for the lateral profile decreases with increasing D, and the minimum value for this setup is found for $D = 72$, and is equal to -0.64%. The distance D can be thought of as the aperture width of the DTO system, and has a significant impact on the lateral oscillation wavelength. Larger distances provide shorter wavelengths, hence a higher lateral resolution, at the expenses of a slightly reduced image.

The mean bias and the relative standard deviation as a function of the number M of HRIs used per estimate are

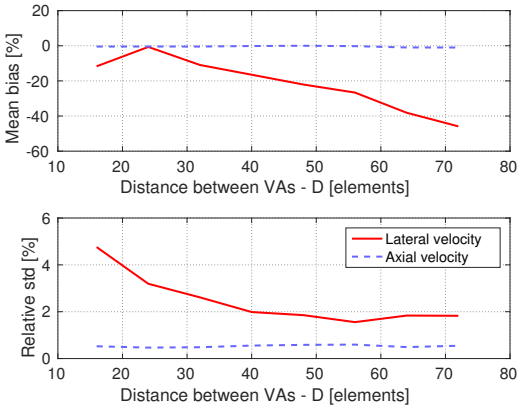

Fig. 5. Mean bias (top) and relative standard deviation (bottom) for the measured lateral (red-solid) and axial (blue-dotted) velocity profiles as a function of the distance D between VAs.

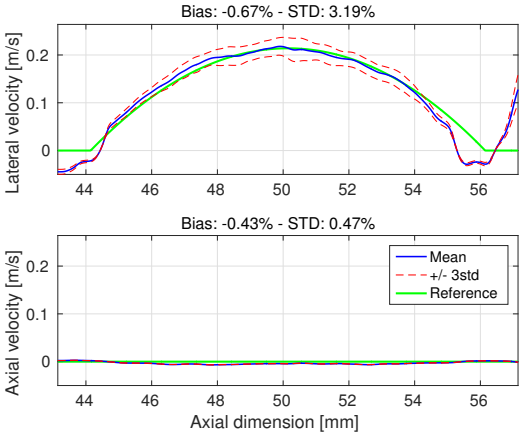

Fig. 6. Lateral (top) and axial (bottom) velocity profiles measured in the flow rig at 90° beam-to-flow angle.

shown in Fig. 4 for simulated data. The standard deviation is, in particular, decreased by increasing M, and is equal to 0.86% and 0.4% for the lateral and axial profiles with $M = 128$.

Fig. 5 shows the mean bias (top) and the relative standard deviation (bottom) for the measured velocity profiles as a function of the distance D. A significant mismatch is noticed in the mean bias for the measured lateral profile compared with the simulated one. In particular, a minimum is found for $D = 24$, which is equal to -0.67%, and the curve diverges for increasing values of D. Further research is needed to investigate the reasons of this inconsistency.

The measured lateral (top) and axial (bottom) velocity profiles for $D = 24$ are displayed in Fig. 6. The green curves show the reference profiles calculated from the measured volume flow, the blue curves are the mean profiles from 50 independent estimations, and the red curves show +/-3 standard deviations. The mean bias is equal to -0.67% for the lateral profile and -0.43% for the axial profile. The mean relative standard deviation is 3.19% for the lateral profile and 0.47% for the axial profile.

V. Conclusion

This paper presented a VFI method, which combines DTO and SASB to achieve an efficient velocity estimation. The method makes it possible to have continuous data acquisition, i.e. data used for the estimation is continuously available everywhere in the HRI. This allows for a high frame rate and a low standard deviation, and simplifies the implementation of the stationary-echo filter. Furthermore, if the first stage beamformer is integrated in the probe handle, wireless transmission of the ultrasound data to the processing unit can be achieved. The approach also enables the possibility of implementing synthetic aperture VFI in cart-based commercial scanners, owing to the lower computational complexity compared with previous implementations.

References

[1] M. D. Fox, "Multiple crossed-beam ultrasound Doppler velocimetry," *IEEE Trans. Son. Ultrason.*, vol. SU-25, pp. 281–286, 1978.

[2] G. E. Trahey, J. W. Allison, and O. T. von Ramm, "Angle independent ultrasonic detection of blood flow," *IEEE Trans. Biomed. Eng.*, vol. BME-34, pp. 965–967, 1987.

[3] J. A. Jensen and P. Munk, "A new method for estimation of velocity vectors," *IEEE Trans. Ultrason., Ferroelec., Freq. Contr.*, vol. 45, pp. 837–851, 1998.

[4] M. E. Anderson, "Multi-dimensional velocity estimation with ultrasound using spatial quadrature," *IEEE Trans. Ultrason., Ferroelec., Freq. Contr.*, vol. 45, pp. 852–861, 1998.

[5] J. A. Jensen, "Improved vector velocity estimation using directional transverse oscillation," in *Proc. IEEE Ultrason. Symp.* IEEE, 2015, pp. 1–4.

[6] M. C. Hemmsen, L. Lassen, T. Kjeldsen, J. Mosegaard, and J. A. Jensen, "Implementation of real-time duplex synthetic aperture ultrasonography," in *Proc. IEEE Ultrason. Symp.*, 2015, pp. 1–4.

[7] J. Kortbek, J. A. Jensen, and K. L. Gammelmark, "Sequential beamforming for synthetic aperture imaging," *Ultrasonics*, vol. 53, no. 1, pp. 1–16, 2013.

[8] M. C. Hemmsen, P. M. Hansen, T. Lange, J. M. Hansen, K. L. Hansen, M. B. Nielsen, and J. A. Jensen, "In vivo evaluation of synthetic aperture sequential beamforming," *Ultrasound Med. Biol.*, vol. 38, no. 4, pp. 708–716, 2012.

[9] J. A. Jensen and S. I. Nikolov, "Directional synthetic aperture flow imaging," *IEEE Trans. Ultrason., Ferroelec., Freq. Contr.*, vol. 51, pp. 1107–1118, 2004.

[10] J. A. Jensen and N. B. Svendsen, "Calculation of pressure fields from arbitrarily shaped, apodized, and excited ultrasound transducers," *IEEE Trans. Ultrason., Ferroelec., Freq. Contr.*, vol. 39, pp. 262–267, 1992.

[11] J. A. Jensen, "Field: A program for simulating ultrasound systems," *Med. Biol. Eng. Comp.*, vol. 10th Nordic-Baltic Conference on Biomedical Imaging, Vol. 4, Supplement 1, Part 1, pp. 351–353, 1996.

[12] J. A. Jensen, "A new estimator for vector velocity estimation," *IEEE Trans. Ultrason., Ferroelec., Freq. Contr.*, vol. 48, no. 4, pp. 886–894, 2001.

[13] J. M. Hansen, M. C. Hemmsen, and J. A. Jensen, "An object-oriented multi-threaded software beamformation toolbox," in *Proc. SPIE Med. Imag.*, vol. 7968, March 2011, pp. 79 680Y–1–79 680Y–9.

[14] J. A. Jensen, H. Holten-Lund, R. T. Nilsson, M. Hansen, U. D. Larsen, R. P. Domsten, B. G. Tomov, M. B. Stuart, S. I. Nikolov, M. J. Pihl, Y. Du, J. H. Rasmussen, and M. F. Rasmussen, "Sarus: A synthetic aperture real-time ultrasound system," *IEEE Trans. Ultrason., Ferroelec., Freq. Contr.*, vol. 60, no. 9, pp. 1838–1852, September 2013.

Paper VI

Analog Gradient Beamformer for a Wireless Ultrasound Scanner

Tommaso Di Ianni, Martin Christian Hemmsen, Jan P. Bagge, Henrik Jensen, Nitsan Vardi, and Jørgen Arendt Jensen

Proceedings of SPIE Medical Imaging 2016: Ultrasonic Imaging and Tomography, vol. 9790.
Accepted for oral presentation in San Diego, CA, USA, 2016.

Analog Gradient Beamformer for a Wireless Ultrasound Scanner

Tommaso Di Ianni[a], Martin Christian Hemmsen[a], Jan Bagge[b], Henrik Jensen[b], Nitsan Vardi[b], Jørgen Arendt Jensen[a]

[a]Center for Fast Ultrasound Imaging, Department of Electrical Engineering, Technical University of Denmark, DK-2800 Lyngby, Denmark
[b]BK Ultrasound, DK-2730 Herlev, Denmark

ABSTRACT

This paper presents a novel beamformer architecture for a low-cost receiver front-end, and investigates if the image quality can be maintained. The system is oriented to the development of a hand-held wireless ultrasound probe based on Synthetic Aperture Sequential Beamforming, and has the advantage of effectively reducing circuit complexity and power dissipation. The array of transducers is divided into sub-apertures, in which the signals from the single channels are aligned through a network of cascaded gradient delays, and summed in the analog domain before A/D conversion. The delay values are quantized to simplify the shifting unit, and a single A/D converter is needed for each sub-aperture yielding a compact, low-power architecture that can be integrated in a single chip. A simulation study was performed using a 3.75 MHz convex array, and the point spread function (PSF) for different configurations was evaluated in terms of lateral full-width-at-half-maximum (FWHM) and −20 dB cystic resolution (CR). Several setups were simulated varying the sub-aperture size N and the quantization step, and design constraints were obtained comparing the PSF to that of an ideal non-quantized system. The PSF is shown for $N = 32$ with a quantization step of 12 ns. For this configuration, the FWHM is degraded by 0.25% and the CR is 8.70% lower compared to the ideal situation. The results demonstrate that the gradient beamformer provides an adequate image quality, and open the way to a fully-integrated chip for a compact, low-cost, wireless ultrasound probe.

Keywords: analog beamformer, portable scanner, Synthetic Aperture Sequential Beamforming, point-of-care ultrasound

1. INTRODUCTION

The use of portable ultrasound for point-of-care examinations in non-conventional setups has attracted increasing interest among the medical community. Hand-held devices have the potential to bring ultrasound imaging out of the hospital setting and improve the access to healthcare in developing countries.[1,2] The development of a battery-powered low-weight scanner brings about new requirements in terms of power consumption, cost and flexibility. On the other hand, a proper image quality needs to be maintained to preserve the clinical functionality of the device.

The first challenge in the design of a wireless system is represented by the minimization of the data transfer rate between the probe and the processing unit. In a conventional digital dynamic receive beamformer, 208 µs need to be transferred per emission for each of the active receiving elements, if a depth of 16 cm is to be visualized. For a $M = 64$ channels aperture, for instance, with a sampling frequency $f_s = 30$ MHz, the data throughput is $208\,\mu\text{s} \times f_s M \sim 400$k samples per emission.

A number of different approaches in the last decades have addressed the relaxation of the data throughput requirement. Poland *et al.*[3] presented a low-weight wireless solution based on micro-beamforming.[4–6] The method lightens the burden of interconnection between the probe and the central unit moving part of the

Send correspondence to: Tommaso Di Ianni, E-mail: todiian@elektro.dtu.dk

beamformation in the transducer handle. K elements are grouped together in a sub-aperture that is pre-beamformed before transmission, thus the transfer rate is reduced by a factor of K. For a sub-aperture size $K = 8$, for example, $208\,\mu s \times f_s M/K \sim 50$k samples are transferred per emission.

A wireless ultrasound scanner was also commercialized by Siemens Medical Solutions USA, Inc.[7] However, the system uses proprietary protocols for the radio communication, and therefore dedicated circuitry needs to be used. The cost of the system may be drastically lowered by using commercial general-purpose components.

Hemmsen *et al.*[8,9] demonstrated the feasibility of B-mode and blood flow imaging using commercial mobile devices such as tablets and smartphones. These are wirelessly connected to an external probe for the acquisition of the ultrasound data, that is pre-beamformed in the transducer handle to minimize the data throughput. The system is based on Synthetic Aperture Sequential Beamforming (SASB).[10] The approach has been demonstrated in the clinic to provide images equally good compared to conventional dynamic receive focusing,[11] while reducing the system requirements due to the implementation of a static-focus beamformer in the transducer handle. Only a single beamformed line per emission needs to be transmitted to the central unit, and the transfer rate is reduced by a factor M. Referring to the previous example, the transfer rate is equal to $208\,\mu s \times f_s \sim 6$k samples per emission.

In this paper, a novel delay-and-sum beamformer oriented to the development of a SASB wireless probe is described. The array of transducers is divided into sub-apertures, and for each receive channel the delay value is integrated in successive steps through a series of cascaded all-pass filters. The signals from the sub-apertures are summed together before A/D conversion, and therefore a single A/D converter (ADC) is needed for each sub-aperture. In addition, the actual delay gradients are quantized to further reduce the circuit complexity, yielding a low-power architecture that can be integrated in a single chip. A simulation study was carried out with a 3.75 MHz convex array to evaluate the image quality and obtain operative design specifications based on a compromise between system complexity and image degradation.

The beamformer architecture and the simulation setup are described in Section 2, and the results presented in Section 3. Finally, Section 4 discusses the conclusions to the study.

2. METHODS

2.1 Synthetic Aperture Sequential Beamforming

SASB takes advantage of the improved image quality of Synthetic Aperture (SA) imaging without the need for computing and transferring a complete set of low-resolution frames.[10] The method has been clinically demonstrated to be equally good compared to conventional dynamic receive focusing,[11] with the advantages of reduced system requirements and effective reduction of the data transfer rate between the probe and the processing unit. A virtual source (VS) is emulated in front of the transducer by means of a focused emission. For each k-th emission, a single RF line $\ell_k(t)$ is beamformed in receive using a static focus located in the VS position. The beamformed RF lines are referred to as low-resolution lines in the remaining of the article.

The round trip time-of-flight for the first stage beamformer is calculated based on the propagation path shown in Fig. 1a, and is equal to

$$t_{fs}(\vec{r}_{ip}, k, j) = \frac{1}{c}(z_{pf_k} \pm |\vec{r}_{ip} - \vec{r}_{fp_k}| \pm |\vec{r}_{fp_k} - \vec{r}_{ip}| + |\vec{r}_{r_j} - \vec{r}_{fp_k}|). \tag{1}$$

In Eq. (1), $z_{pf_k} = |\vec{r}_{fp_k} - \vec{r}_{e_k}|$ is the distance from the focus point $\vec{r}_{fp_k}$ to the center of the aperture $\vec{r}_{e_k}$, $\vec{r}_{ip}$ is the image point, and $\vec{r}_{r_j}$ is the position of the $j-$th receiving transducer in the active aperture of M elements, with $j = 1, ..., M$. The $\pm$ in (1) refers to whether the image point is above or below the VS. The time-of-flight t_{fs} is therefore dependent on the image point, the emission index, and the receiving element.

In the second stage, a high-resolution image is obtained by re-focusing a number of low-resolution lines. The beamformed signals ℓ_k are considered as the responses of the virtual elements emitting/receiving spherical waves that propagate in a region spatially confined by the angle $\alpha = 2\arctan(1/2F\#)$. $F\#$ is the F-number equal to z_{fp}/L_A, where L_A is the aperture width. The sample for the image point $\vec{r}_{ip}$ is found in the k-th low-resolution line at the time

$$t_{ss}(\vec{r}_{ip}, k) = \frac{2}{c}(z_{pf} \pm |\vec{r}_{ip} - \vec{r}_{fp_k}|). \tag{2}$$

Again, the $\pm$ in (2) refers to the position of the image point relative to that of the VS. The time of flight t_{ss} is used in the second stage for the re-focusing of the low-resolution lines. For further details on the second stage beamformer, readers are referred to the cited articles on SASB.

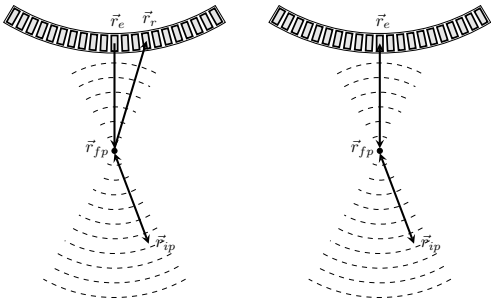

(a) (b)

Figure 1. Wave propagation path for the first stage (a) and second stage (b) beamformers. $\vec{r}_e$ and $\vec{r}_r$ are the emission reference point and the receiving element position, respectively; $\vec{r}_{fp}$ is the static focal position (virtual source); and $\vec{r}_{ip}$ is the image point.

2.2 Analog gradient beamformer

The core idea of gradient beamforming is illustrated in Fig. 2a. The array of transducer elements is divided into sub-apertures Σ_N of N receiving channels. The received signals are fed to a cascade of analog amplifiers for time-gain compensation and apodization, and pre-beamformed in the analog domain before A/D conversion. A coarse group delay T_g is then applied to the sub-aperture signal in the digital domain, and the digital sub-aperture signals are finally summed together before the transmission to the central processing unit, where the high-resolution images are attained by the second stage beamformer.

For each $k-$th emission, the delay value for the i-th channel is equal to $t_{fs}(k,i) = T_g + t_i$, with t_i the channel-dependent fine delay. Here $i = 1, ..., N$ is the channel index internal to the sub-aperture. The fine delays t_i are integrated in N-i+1 successive steps, as illustrated in Fig. 3, and are calculated as:

$$t_i = t_{fs}(k,i) - T_g = \nabla t_i + \nabla t_{i+1} + \cdots + \nabla t_N, \tag{3}$$

where ∇t_i is the difference between the delay values of the i-th and $(i+1)$-th channels. These values will be referred to as delay gradients in the remaining of the article. The fine delays are realized in the analog domain through a network of phase shifting all-pass filters, and the sum is calculated by the analog summer before the next delay is applied. To further simplify the architecture, only a discrete set of fine delay values can be considered, and these are assumed to be multiples of a the quantization step δt, as shown in Fig. 2b. This translates to the actual implementation by using a variable-length bank of elemental delay networks, cascaded to round the gradient ∇t_i to the nearest possible value. The coarse delay T_g is applied in the digital domain, and can be implemented by merely shifting the samples, if a sampling frequency adequately high is used, or by interpolating inter-sample values.

As a consequence of the grouping and quantization, the receiving channels experience dissimilar delay errors, and artefacts appear in the high-resolution images. For instance, the delay t_1 relative to the signal to be delayed the most (left edge in Fig. 3) is integrated through N gradients, each of which is quantized. The design of the proper sub-aperture size N and the quantization step size δt is of great importance to minimize the number of ADC's and the complexity of the delaying network while maintaining an adequate image quality.

The advantage of the gradient beamformer is the use of a single ADC for each sub-aperture Σ_N, and this effectively reduces the system complexity, power consumption and cost. Furthermore, the analog delaying function can be implemented with a compact RC network, and enables the possibility for the whole system to be

integrated in a single chip. This architecture differs from a micro-beamformer in the way that only a static focus is considered in receive, and a dynamic focus is obtained in the second stage beamformer.[4,5] The fine delay profile is therefore updated for every emission, and maintained for the whole duration of the receive event. Conversely, in a micro-beamformer the fine delays must be continuously updated during reception, and this complicates the sub-aperture processing, even if strong approximations such as linearization are considered.[6]

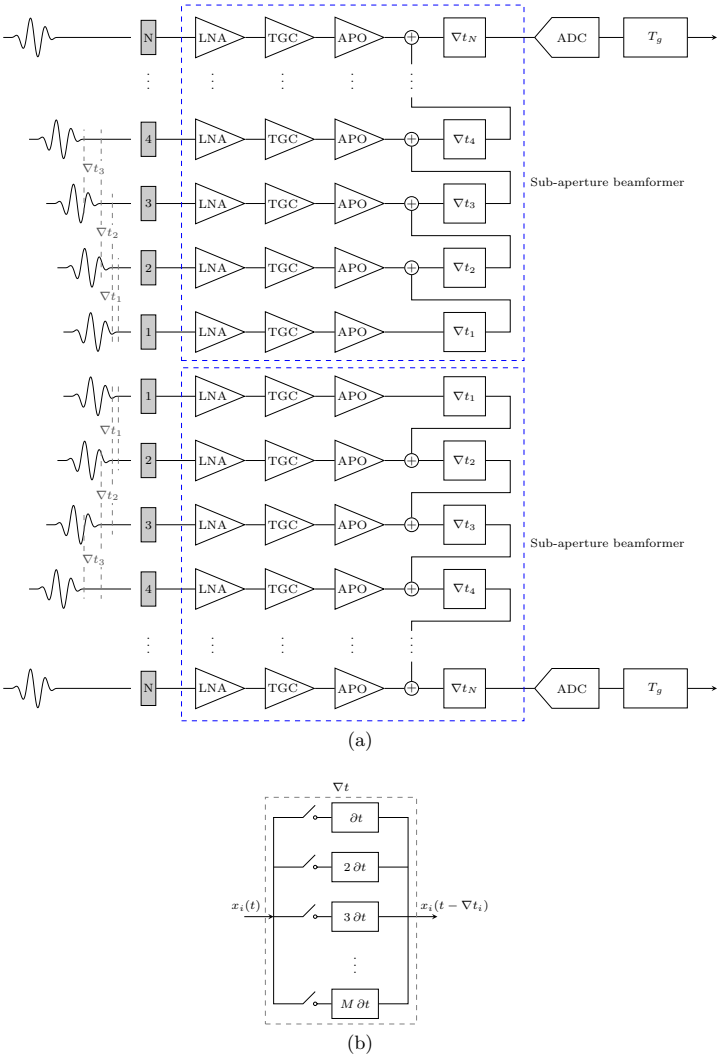

Figure 2. Schematic representation of the gradient delay beamformer system (a); conceptual implementation of the fine delay component (b).

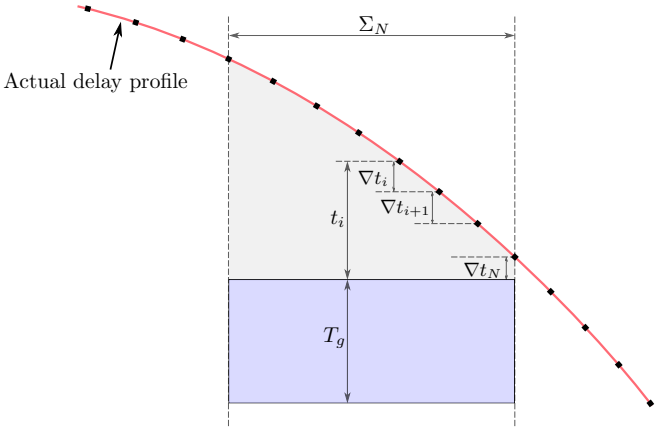

Figure 3. Gradient beamforming delay profile integration.

2.3 Simulation setup

A simulation study was performed in Field II[12,13] to evaluate the image degradation as a function of the sub-aperture size N and the quantization step size δt. Only the effect of the delay error was taken into account in the study, and other sources of image degradation were neglected. The point spread function (PSF) was simulated using a 3.75 MHz 192-element convex array transducer in a range from 10 to 130 mm in steps of 10 mm, with a fixed transmit/receive focus in 70 mm. The quantization step size was swept from 2 to 50 ns in steps of 2 ns, for $N = 2, 4, 8, 16, 32$. A sampling frequency of 60 MHz was considered for the calculation of the group delay T_g. The parameters of the simulation setup are reported in Table 1. A model of the gradient beamformer was developed in MATLAB (The MathWorks Inc., Natick, MA), and the second stage beamformer was implemented using BFT3 toolbox.[14] The high-resolution images were log-compressed after envelope detection, and finally visualized with a 60 dB dynamic range. The image quality was evaluated in terms of lateral full-width-at-half-maximum (FWHM) and -20 dB cystic resolution (CR),[15] defined as the radius ρ of a circular void centered on the PSF and providing a contrast

$$C(\rho) = 10 \log_{10} \left(1 - \frac{E_{in}(\rho)}{E_{tot}} \right) \tag{4}$$

equal to -20 dB. E_{in} and E_{tot} in Eq. (4) are the PSF energy inside the void and the total PSF energy. FWHM and CR were averaged over the simulated points and compared to the ideal non-quantized setup.

3. RESULTS

The average FWHM is shown in Fig. 4a. The resolution is close to the ideal value for quantization steps lower than 26 ns, with losses limited to 3.2% respect to the reference. A common trend is found for all the sub-aperture sizes considered in the simulation. For greater quantization steps, the resolution deteriorates and the FWHM increases with different slopes for different values of N.

As expected, the contrast is mostly affected by the delay errors even for limited quantization steps, as highlighted by the -20 dB CR in Fig. 4b. Small errors in the beamformation introduced by the quantization of the delays enhance the sidelobes level, degrading the PSF. The CR values for all the curves are close to the reference for steps smaller than 12 ns. This point provides an upper bound to the quantization step if the image quality of the ideal beamformer is to be maintained.

In Fig. 5 the PSF in 20 mm, 70 mm, and 120 mm is shown in the left and right column for the ideal non-quantized beamformer, and is compared to the one obtained using the gradient architecture with $N = 32$ and δt =12 ns in the right column. The visualized depths are chosen with the intention of showing the behaviour in the

Table 1. Simulation parameters

Transducer parameters	
Transducer	Convex array
Center frequency - f_0	3.75 MHz
Number of elements	192
Transducer element pitch	0.33 mm
Transducer element height	13 mm
Convex curvature radius	61 mm
Elevation focus	65 mm
Transmit parameters	
Excitation	2-cycle weighted sinusoid
Apodization function	Rect function
Active aperture size - M	64 elements
Virtual sources axial position	70 mm
$f\#$	3.3
Number of emissions	269
Receive parameters	
Apodization function	Hamming
Active aperture size - M	64 elements
Virtual sources axial position	70 mm
$f\#$	3.3
Second stage parameters	
Second stage apodization	Hamming

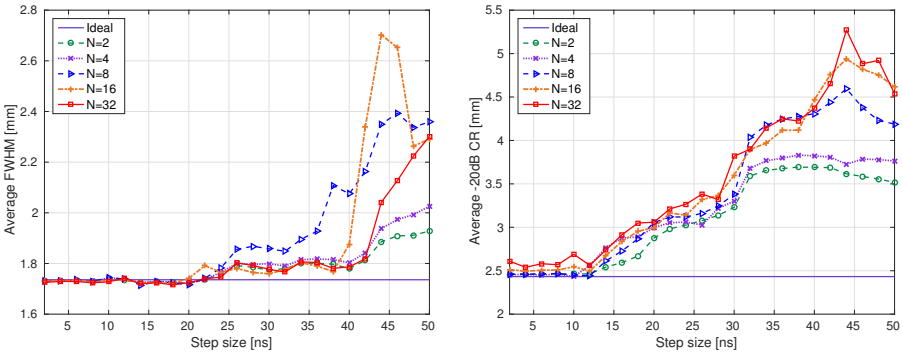

(a) (b)

Figure 4. Average FWHM (a) and -20 dB CR (b) as a function of the quantization step size for the PSF obtained with the gradient beamformer approach using sub-aperture sizes $N = 2, 4, 8, 16, 32$ and compared to the ideal setup.

near field, focal position, and far field. While the PSFs in 70 mm, and 120 mm show minimum degradation, the effect of the beamformation errors is clearly visible in the close field. In particular, the contrast is compromised as the sidelobes show higher spatial extension as well as higher intensity. For this setup, losses in average FWHM are limited to 0.25% and the average CR results degraded by less then 8.70%. It must be noted that for the setup with sub-aperture size $N = 32$, only two ADC are used for a 64-element active aperture.

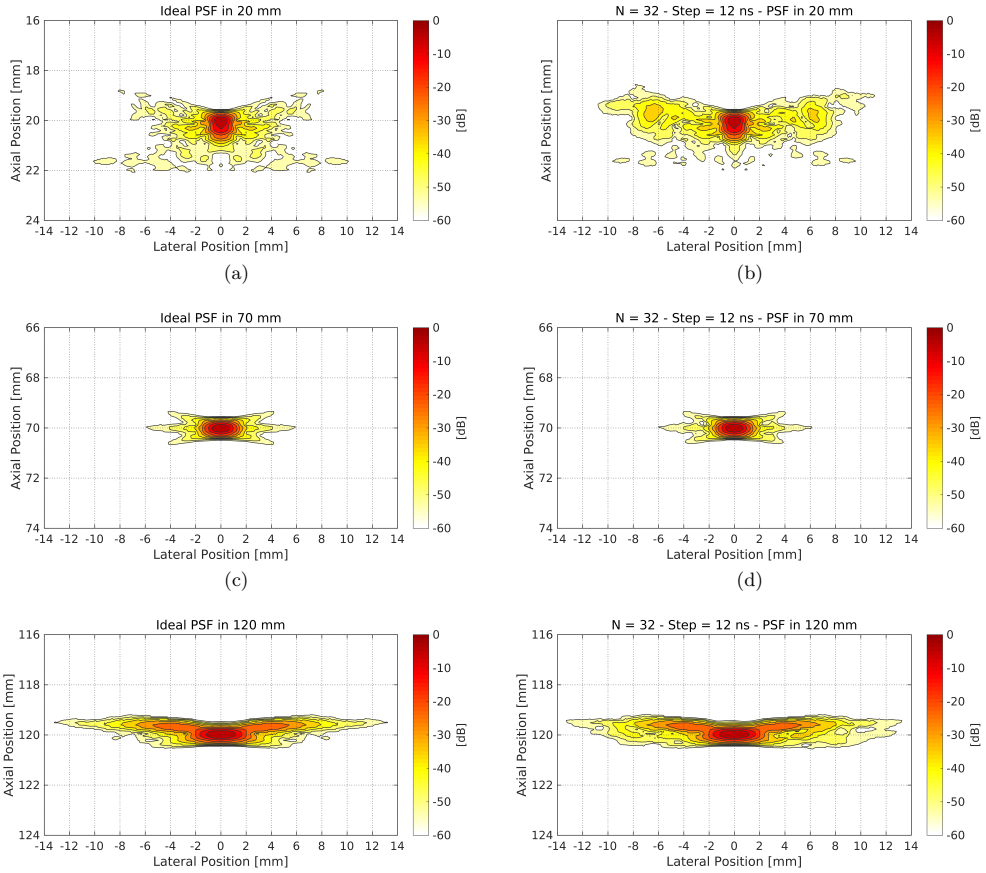

Figure 5. Simulated point spread function for the ideal beamformer (left column) and gradient beamformer with $N = 32, \delta t = 12$ ns (right column) in 20 mm (a,b); 70 mm (c,d); and 120 mm with a 3.75 MHz convex array transducer.

4. CONCLUSION

A novel analog beamformer architecture for the implementation of a low-cost wireless probe based on Synthetic Aperture Sequential Beamforming was presented and investigated in this study. The approach is based on the integration of the delay values through a series of all-pass shifting networks, and makes use of a single ADC for each sub-aperture. The actual gradient values are quantized to further reduce the system complexity, yielding a compact architecture that can be integrated in a single chip. The quantization introduces element-dependent errors in the beamformation which degrades the resolution and contrast of the imaging system. A simulation study was performed with a 3.75 MHz convex array to evaluate the image quality and obtain design constraints based on a comparison with an ideal non-quantized situation. The results show that a quantization step lower than 12 ns must be used to maintain approximately the same image quality as the ideal situation. The PSF was shown for the gradient beamformer with sub-aperture size $N = 32$ to evaluate the image degradation due to the delay errors. It turns out that the image quality is compromised in the near field, in particular for what concerns the contrast, as the sidelobes show higher intensity and spatial extension. For this configuration,

however, only two ADCs are needed for the whole active aperture. The results demonstrate that the analog gradient architecture is a suitable option for the development of a low-cost, low-power ultrasound wireless probe.

5. ACKNOWLEDGEMENTS

This work was supported by grant 82-2012-4 from the Danish National Advanced Technology Foundation and by BK Ultrasound, Herlev, Denmark.

REFERENCES

[1] Mehta, M., Jacobson, T., Peters, D., Le, E., Chadderdon, S., Allen, A. J., Caughey, A. B., and Kaul, S., "Handheld ultrasound versus physical examination in patients referred for transthoracic echocardiography for a suspected cardiac condition," *J. Am. Coll. Cardiol. Img.* **7**(10), 983–990 (2014).

[2] Sippel, S., Muruganandan, K., Levine, A., and Shah, S., "Review article: Use of ultrasound in the developing world," *Int. J. Emerg. Med.* **72** (December 2011).

[3] Poland, M. and Wilson, M., "Light weight wireless ultrasound probe." Patent US 2010/0168576 A1 (2010).

[4] Larson, III, J. D., "2-D phased array ultrasound imaging system with distributed phasing." Patent US 5229933 (July 1993).

[5] Savord, B. and Solomon, R., "Fully sampled matrix transducer for real time 3D ultrasonic imaging," in [*Proc. IEEE Ultrason. Symp.*], **1**, 945–953 (2003).

[6] Zhao, K.-Q., Bjåstad, T. G., and Kristofferson, K., "Error analysis of subaperture processing in 1-d ultrasound arrays," *IEEE Trans. Ultrason., Ferroelec., Freq. Contr.* **62**, 663–672 (April 2015).

[7] Siemens Medical Solutions USA, Inc., "Datasheet - ACUSON Freestyle^{TM} Ultrasound System - Release 3.5," (2014).

[8] Hemmsen, M. C., Kjeldsen, T., Lassen, L., Kjær, C., Tomov, B., Mosegaard, J., and Jensen, J. A., "Implementation of synthetic aperture imaging on a hand-held device," in [*Proc. IEEE Ultrason. Symp.*], 2177–2180 (2014).

[9] Hemmsen, M. C., Lassen, L., Kjeldsen, T., Mosegaard, J., and Jensen, J. A., "Implementation of real-time duplex synthetic aperture ultrasonography," in [*Proc. IEEE Ultrason. Symp.*], 1–4 (2015).

[10] Kortbek, J., Jensen, J. A., and Gammelmark, K. L., "Sequential beamforming for synthetic aperture imaging," *Ultrasonics* **53**(1), 1–16 (2013).

[11] Hemmsen, M., Hansen, P. M., Lange, T., Hansen, J. M., Hansen, K. L., Nielsen, M. B., and Jensen, J. A., "In vivo evaluation of synthetic aperture sequential beamforming," *Ultrasound Med. Biol.* **38**(4), 708–716 (2012).

[12] Jensen, J. A. and Svendsen, N. B., "Calculation of pressure fields from arbitrarily shaped, apodized, and excited ultrasound transducers," *IEEE Trans. Ultrason., Ferroelec., Freq. Contr.* **39**, 262–267 (1992).

[13] Jensen, J. A., "Field: A program for simulating ultrasound systems," *Med. Biol. Eng. Comp.* **10th Nordic-Baltic Conference on Biomedical Imaging, Vol. 4, Supplement 1, Part 1**, 351–353 (1996).

[14] Hansen, J. M., Hemmsen, M. C., and Jensen, J. A., "An object-oriented multi-threaded software beamformation toolbox," in [*Proc. SPIE Med. Imag.*], **7968**, 79680Y 1–9 (March 2011).

[15] Ranganathan, K. and Walker, W. F., "Cystic resolution: A performance metric for ultrasound imaging systems," *IEEE Trans. Ultrason., Ferroelec., Freq. Contr.* **54**(4), 782–792 (2007).

Patent I

Vector Velocity Estimation using Transverse Oscillation (TO) and Synthetic Aperture Sequential Beamforming (SASB)

Tommaso Di Ianni, Martin Christian Hemmsen, and Jørgen Arendt Jensen

Filed on August 31, 2016, with the United States Patent and Trademark Office. Number: ANA1310-US (BKM-10-7988).

Vector Velocity Estimation Using Transverse Oscillation (TO) and Synthetic Aperture Sequential Beamforming (SASB)

TECHNICAL FIELD

The following generally relates to ultrasound Vector Flow Imaging (VFI) and more particularly to estimating vector velocity for flowing structures using a combination of TO and SASB dual stage beamforming.

BACKGROUND

The visualization of blood flow dynamics is an important and effective clinical tool for the diagnosis of a number of pathological conditions. Ultrasound scanners are capable of estimating 2-D velocity vectors in real-time, allowing clinicians to extract useful information from complex flow patterns. The feasibility of a real-time duplex imaging sequence in a commercial consumer level tablet was demonstrated in Hemmsen et al., "Implementation of real-time duplex synthetic aperture ultrasonography," in Proc. IEEE Ultrason. Symp., 2015, pp. 1–4. In Hemmsen et al., the approach was based on synthetic aperture sequential beamforming (SASB). The ultrasound data were transferred wirelessly to a tablet where processing and visualization were performed. The estimation was based on directional beamforming, and the lines were cross-correlated to find the velocities. Unfortunately, this approach requires a flow angle estimation and all permutations need to be cross-correlated, which is time and computationally intensive. As such, this approach is not well-suited for fully operative real-time imaging, and there is an unresolved need for another approach.

SUMMARY

Aspects of the application address the above matters, and others.

In one aspect, an ultrasound imaging system includes a transducer array with a plurality of transducer elements configured to repeatedly emit in a predetermined pattern, a first beamformer configured to beamform echo signals received by the transducer array to produce a low resolution line of data for each emission, and a first communication interface configured to wirelessly transmit the low resolution lines of data for each

emission in series. The ultrasound imaging system further includes a second communication interface configured to for each emission in series wirelessly receive the transmitted low resolution lines of data, a second beamformer configured to beamform the received low resolution lines of data to produce high resolution ultrasound data, and a velocity processor configured to estimate vector velocity components from the high resolution ultrasound data in a lateral direction and an axial using an autocorrelation algorithm.

In another aspect, a method includes transmitting an ultrasound signal, receiving echoes generated in response to the transmitted ultrasound signal, beamforming the echoes, generating a low resolution line of data for each emission, and wirelessly transmitting the low resolution lines of data to another device. The method further includes wirelessly receiving the transmitted low resolution lines of data with the other device, beamforming the low resolution line of data, generating high resolution ultrasound image data, and estimating, using an autocorrelation algorithm, vector velocity components from the high resolution ultrasound data.

In another aspect, a non-transitory computer readable storage medium is encoded with computer readable instructions. The computer readable instructions, when executed by a processor of a computing system, cause the processor to: transmit, via a transducer array, an ultrasound signal, receive, via the transducer array, echoes generated in response to the transmitted ultrasound signal, beamform the echoes and generate a low resolution line of data for each emission, and wirelessly transmit the low resolution lines of data to another device. The computer readable instructions, when executed by the processor of the computing system, further cause the processor to: wirelessly receive the transmitted low resolution lines of data with the other device, beamform the low resolution line of data and generate high resolution ultrasound image data, and estimate, using an autocorrelation algorithm, vector velocity components from the high resolution ultrasound data.

Those skilled in the art will recognize still other aspects of the present application upon reading and understanding the attached description.

BRIEF DESCRIPTION OF THE DRAWINGS

The application is illustrated by way of example and not limited by the figures of the accompanying drawings, in which like references indicate similar elements and in which:

Figure 1 schematically illustrates an example ultrasound imaging system;

Figure 2 shows an example imaging setup with a linear transducer array;

Figure 3 schematically illustrates the example ultrasound imaging system in connection with a computing apparatus; and

Figure 4 illustrates a method in accordance with an embodiment herein.

DETAILED DESCRIPTION

The following describes an approach for VFI vector velocity estimation based on a combination of TO or DTO and SASB. In one instance, this approach allows for efficient wireless transmission of low resolution ultrasound data along with a subsequent efficient estimation of velocities therefrom. The approach is based on an autocorrelation approach, which requires a decreased amount of calculations with respect to cross-correlation. The approach makes it possible to have continuous data acquisition in the whole imaged area; therefore, high and low velocities can be estimated at once with high precision and high frame rate.

FIGURE 1 schematically illustrates an example ultrasound imaging system 100. The imaging system 100 includes a probe 102 and console 104. The probe 102 includes a probe wireless communication interface ("communication interface") 106, and the console 104 includes a console wireless communication interface ("communication interface") 108. The communication interfaces 106 and 108 are configured to wirelessly communicate over a wireless network 110.

The probe 102 includes a transducer array 112 with a plurality of transducer elements 114, which are configured to transmit ultrasound signals. The plurality of transducer elements 114 are also configured to receive echo signals and generate electrical signals indicative thereof. The echo signals are produced in response to an interaction between the ultrasound signals and the structure (e.g., flowing blood cells, organ cells, etc.).

The transducer array 112 can be a one or two-dimensional (1-D or 2-D) array. Examples of 1-D arrays include arrays with 8, 16, 32, 64, 96, 128, 512, and/or other number of elements. Examples of 2-D arrays include square, rectangular, circular, irregular, row-column addressed and/or other arrays. The transducer array 112 can be linear, curved, phased, and/or other array. The transducer array 112 can be fully populated or sparse and/or a combination thereof.

Transmit circuitry 116 generates a set of pulses that are conveyed to the transducer array 112. The set of pulses excites a set of the transducer elements 114, which causes the elements 114 to emit ultrasound signals. Receive circuitry 118 receives the electrical signals. The receive circuitry 118 may amplify, filter, convert analog signals to digital signals, etc. The transducer array 114 may have separate transmit and receive elements, and/or a switch may switch between the transmit and receive circuitry 116 and 118.

For directional transverse oscillation (DTO), a focused beam is emitted and echoes are received by all of the transducer elements 104. As described below, the echoes are beamformed using two apodized apertures separated by a distance to create a lateral oscillation. A DTO approach is described in greater detail in international application serial number PCT/IB2015/051526, filed March 3, 2015, and entitled "ULTRASOUND IMAGING FLOW VECTOR VELOCITY ESTIMATION WITH DIRECTIONAL TRANSVERSE OSCILLATION," which is incorporated herein by reference in its entirety.

The probe 102 includes a first stage (or stage 1) beamformer 120. The first stage beamformer 120 is configured to beamform the electrical signals for each emission using a fixed transmit and receive focus for continuous data acquisition in the whole image area. In one instance, the first stage beamformer 120 produces a single low-resolution line of data for each emission, which is transmitted serially by the interface 106 over the network 110 to the interface 108 at a data transfer rate commensurate with the IEEE 802.11ac (WiFi) wireless networking standard.

For example, if 25 frames per second (fps) are used for B-mode and the maximum frame rate for VFI is 480 fps at a depth of 10 cm, at full operational speed a data throughput of 320 megabits per second (Mbps) would be required. The IEEE 802.11ac (WiFi) wireless networking standard has a single-link throughput of at least 500 Mbps and a multi-station throughput of at least 1 gigabit per second (Gbps). In general, the interface

106 can transmit the low-resolution lines of data using any wireless networking standard having a data transfer rate suitable for serial transmission of the data. This includes, USB, Blue Tooth, cellular, etc.

In one instance, the first stage beamformer 120 employs an SASB algorithm to create the low-resolution lines of data. An example of a suitable SASB algorithm is described in Kortbek, et al., "Synthetic aperture sequential beamforming," in Proc. IEEE Ultrason. Symp., 2008, pp. 966–969. Another example of a suitable SASB algorithm is described in Kortbek, et al., "Sequential beamforming for synthetic aperture imaging," Ultrasonics, vol. 53, no. 1, pp. 1–16, 2013. Other algorithms, which create such low-resolution lines of data, are also contemplated herein.

The probe 102 further includes a probe controller ("controller") 122, which is configured to control the transmit circuitry 116, the receive circuitry 118, the stage 1 beamformer 120, and/or the probe wireless communication interface 106. Such control can be based on a current mode of operation (e.g., B-mode, velocity, vector velocity estimation using TO (e.g., DTO) with SASB). The probe 102 includes a user interface (UI) 122. The UI 122 may include an input device (e.g., a button, a slider, a touch surface, etc.) and/or an output device (e.g., a visual and/or audible, etc.).

The console 104 includes a second stage (stage 2) beamformer 124. The second stage beamformer 124 is configured to successively process the low-resolution lines of data, producing high resolution images. Such processing includes applying weights to create a double-oscillating field in the whole imaging region at once. The second stage beamformer 124 employs the SASB and/or other algorithms to create high resolution images.

A velocity processor 130 is configured to process the beamformed data and determine velocity components of flowing structure. This includes processing the beamformed data to determine a velocity component in the depth direction and/or in one or two directions transverse to the depth direction. As described in greater detail below, the velocity processor 130 estimates vector velocities based on a TO or DTO approach.

A display 136 displays the image and/or velocity information. Such presentation can be in an interactive graphical user interface (GUI), which allows the user to selectively rotate, scale, and/or manipulate the displayed data. Such interaction can be through a

mouse or the like, and/or a keyboard or the like, touch-screen controls and/or the like, and/or other known and/or approach for interacting with the GUI.

The console 104 further includes a console controller ("controller") 138, which is configured to control the communication interface 108, the second stage beamformer 124, and/or the velocity processor 130. Such control can be based on a current mode of operation (e.g., B-mode, velocity, vector velocity estimation using TO (e.g., DTO) with SASB). The console 104 includes a user interface (UI) 140, which may include an input device (e.g., a button, a slider, a touch surface, etc.) and/or an output device (e.g., a visual and/or audible, etc.).

It is to be appreciated that the beamformers 120 and 124, the velocity processor 130, and/or other components of the system 100 can be implemented via a processor (e.g., a microprocessor, central processing unit (CPU), graphics processing unit (GPU), etc.) executing one or more computer readable instructions encoded or embedded on a computer readable storage medium (which excludes transitory medium) such as a physical memory device. The processor can additionally or alternatively execute a computer readable carried by transitory medium such as a carrier wave, a signal, or other transitory medium. The fixed-focus first stage beamformer 120 can also be implemented using simple analog circuitry to lower the power dissipated in the probe handle.

An example of the velocity processor 130 is discussed next in connection with FIGURE 2 for a linear array 104 and a vessel 200. Virtual apertures 202 and 204 are created with virtual sources 206 and 208 emulated using the fixed-focus emissions. The illustrated example expressly shows a total of six virtual sources 206 and 208, where each of the virtual apertures 202 and 204 includes three of the virtual sources (i.e., the virtual aperture 202 includes the virtual sources 206, and the virtual aperture 204 includes the virtual sources 208). The three virtual sources 206, going from left to right, respectively insonofy regions 214, 216 and 218, and the three virtual sources 208, going from left to right, respectively insonofy regions 220, 222 and 224. The virtual apertures 202 and 204 are located in front of the transducer array 104 and are separated by a non-zero distance "D."

The first stage beamformer 120 beamforms the low-resolution lines of data using static focus points located in the same positions as the virtual sources 206 and 208. That is, for each emission, a low-resolution line of data is beamformed in receive using a fixed

focus located in the corresponding virtual source position. In general, K (an integer greater or equal to two) emissions are used to create the high-resolution image. FIGURE 2 shows at least K = 6. For each emission, a low-resolution RF line is beamformed in receive using a fixed focus located in the virtual source position. The emissions are in a predetermined order and continuously repeat, providing continuous data. Generally, 2-4 emissions can be used for lower velocities, and 20-30 emissions can be used for higher velocities.

The second stage beamformer 124 successively processes the low-resolution lines of data, applying weights to create a double-oscillating field in the whole imaging region (a region-of-interest (ROI) 210) at once. The wireless transmission of the ultrasound data from the probe 102 to the console 104 is enabled by the fact that only a single beamformed low-resolution line is transmitted for each emission, in contrast to transmitting in parallel the data from all the transducer elements. The weights weight the contributions from the low-resolution lines to create the double oscillating field in the high resolution image. The virtual sources 206 and 208 can be placed behind the transducer array 104 to increase the extent of the ROI 210 and visualize regions close to the transducer 104.

Neglecting the B-mode sequence, the pulse repetition frequency for the flow emissions is referred to as f_{prf}^{flow}. A maximum effective frame rate for the velocity estimation is therefore equal to $f_{prf-eff}^{flow} = f_{prf}^{flow}/K$. For each frame, the vector velocities are estimated in the whole ROI 210. Furthermore, the approach can be extended to high frame rate VFI by calculating a new estimate for each emission in a recursive manner, giving $f_{prf-eff}^{flow} = f_{prf}^{flow}$. This approach does not require any angle compensation of prior knowledge on the beam-to-flow angle.

The velocity processor 130, to estimate a velocity at a given point, computes a lateral signal at a corresponding location in the high-resolution image, and signals from M (wherein M is a positive integer) high-resolution images are used to estimate the velocities. A lateral signal can be determined anywhere in the ROI 210. In the illustrated example, a set of lateral signals 212 at different depths are determined within the vessel 210. Each lateral signal is a single directional signal (or line of data) for a depth of interest and is transverse to the propagation direction. Where K = 6, each line is constructed after 6 emissions.

A wavelength of the lateral oscillation is determined based on EQUATION 1:

Equation 1:

$$\lambda_x = \frac{\lambda d}{D},$$

where λ is a axial wavelength, d is the depth, D is the distance between the receiving apertures. The signal $x(n, i)$ is beamformed at the depth of interest in the direction transverse to the direction of propagation of the ultrasound beam, where n is a sample index along the lateral direction, and i is an emission index.

A quadrature signal required for the velocity estimation is determined as shown in EQUATION 2:

Equation 2:

$$y(n, i) = \mathcal{H}\{x(n, i);,$$

where $\mathcal{H}$ identifies the Hilbert transform. A complex signal r_{sq} is determined by combining the in-phase and quadrature lateral beamformed signals as shown in Equation 3:

Equation 3:

$$r_{sq}(n, i) = x(n, i) + jy(n, i),$$

where $x(n; i)$ is the real part and $y(n, i)$ is the imaginary part. A lateral wavelength for the emission i is calculated as shown in EQUATION 4:

Equation 4:

$$\frac{1}{\lambda_x(i)} = f_x(i) = \frac{\sum_{f=-\frac{N}{2}}^{\frac{N}{2}} \frac{f}{N\Delta_x} \left|R_{sq}(f, i)\right|^2}{\sum_{f=-\frac{N}{2}}^{\frac{N}{2}} \left|R_{sq}(f, i)\right|^2},$$

where $R_{sq}(f)$ is a Fourier transform of the directional signal $r_{sq}(n)$ along the lateral dimension *n*, *N* is a number of Fourier coefficients, *f* is a sample index in the Fourier domain, and Δ_x is a lateral spatial sampling period. The lateral wavelength λ_x can be averaged over a number of directional lines to improve the variance of the estimate.

Two new signals are created as shown in EQUATIONS 5 and 6:

Equation 5:

$$r_1(n,i) = r_{sq}(n,i) + jr_{sqh}(n,i),$$

and

Equation 6:

$$r_2(n,i) = r_{sq}(n,i) - jr_{sqh}(n,i).$$

where r_{sqh} denotes the Hilbert transform of the signal r_{sq} along the axial dimension. From EQUATIONS 5 and 6, lag-1 autocorrelation functions can be determined as shown in EQUATIONS 7 and 8:

Equation 7:

$$\hat{R}_1(1) = \frac{1}{MN_s}\sum_{i=0}^{M-2}\sum_{n=0}^{N_s} r_1^*(n,i)r_1(n,i+1),$$

and

Equation 8:

$$\hat{R}_2(1) = \frac{1}{MN_s}\sum_{i=0}^{M-2}\sum_{n=0}^{N_s} r_2^*(n,i)r_2(n,i+1).$$

In EQUATIONS 7 and 8, the autocorrelation estimates are averaged over the number of emissions *M* and the number of samples in the directional lines N_S along the axial direction. In addition, the autocorrelation estimates in EQUATIONS 7 and 8 can be

averaged over a number of directional lines to improve the variance of the estimate. The velocity processor 130 estimate the lateral and axial velocities respectively as shown in Equations 9 and 10:

Equation 9:

$$v_x = \frac{\lambda_x}{2\pi 2T_{prf}} = arctan\left(\frac{\Im\{R_1(1)\}\Re\{R_2(1)\} + \Im\{R_2(1)\}\Re\{R_1(1)\}}{\Re\{R_1(1)\}\Re\{R_2(1)\} - \Im\{R_1(1)\}\Im\{R_2(1)\}}\right),$$

and

Equation 10:

$$v_y = \frac{\lambda}{2\pi 4T_{prf}} = arctan\left(\frac{\Im\{R_1(1)\}\Re\{R_2(1)\} - \Im\{R_2(1)\}\Re\{R_1(1)\}}{\Re\{R_1(1)\}\Re\{R_2(1)\} + \Im\{R_1(1)\}\Im\{R_2(1)\}}\right).$$

where T_{prf} denotes the pulse repetition period, $\Im$ denotes the real part, and $\Re$ denotes the imaginary part.

By using the approach described herein, the lateral wavelength λ_x can be estimated for all the depths directly from the beamformed data, and no prediction is needed prior to the beamformation, making the approach self-calibrating. Furthermore, the approached described herein decouples the lateral oscillation wavelength from the apodization function, maintaining a low bias for the velocity estimation along the depths. Furthermore, the approach described herein only requires storing one line of data at a time so there is a reduction in the memory requirement for storing data relative to storing multiple lines of data.

Furthermore, the approach described herein provides high performance with a significant performance improvement in terms of operative time relative to cross-correlation approaches. More specifically, the autocorrelation approach described herein requires only one accumulation and no flow angle estimation. The cross-correlation approach requires a full cross-correlation of all permutations for each flow direction such that a signal with a length of N would require N accumulations times the number (e.g., 50-100) of flow directions (e.g., N*(50-100) calculations times the approached described herein). As such, the approach described herein is a technological improvement. Due to

the reduced computational complexity, the approach also enables the possibility to implement synthetic aperture vector flow imaging in general-purpose ultrasound scanners.

FIGURE 3 schematically illustrates a variation of FIGURE 1 in which the probe 102 and the console 104 interface via a hardwired connection 302 (e.g., a cable), and the console 104 wirelessly communicates the low resolution data to a computing apparatus 304, which includes the stage 2 beamformer 124 and the velocity processor 130, which process the low resolution data as described herein. In this instance, the stage 1 beamformer 120 can be in the probe 102 and/or the console 104. Where the stage 1 beamformer 120 is implemented in the probe 102 (e.g., in a handle thereof), the beamformer 120 can directly wirelessly interface to the wireless network 110 and wirelessly communicate the low resolution data directly to the computing apparatus 304.

FIGURE 4 illustrates a method for estimating a velocity vector using a combination of TO and SASB.

It is to be understood that the following acts are provided for explanatory purposes and are not limiting. As such, one or more of the acts may be omitted, one or more acts may be added, one or more acts may occur in a different order (including simultaneously with another act), etc.

At 402, an ultrasound signal is transmitted as described herein.

At 404, echoes are received and converted to electrical signals as described herein.

At 406, the electrical signals are beamformed via a first stage beamformer to produce low resolution ultrasound data as described herein.

At 408, the low resolution ultrasound data is wirelessly transmitted to another device as described herein.

At 410, the low resolution ultrasound data is beamformed via a second stage beamformer to produce high resolution ultrasound data at the other device as described herein.

At 412, vector velocity values are determined from the high resolution ultrasound data at the other device as described herein.

At 414, an image and the vector velocity values are visually presented.

The methods described herein may be implemented via one or more processors executing one or more computer readable instructions encoded or embodied on computer readable storage medium (which excludes transitory medium) such as physical

memory which causes the one or more processors to carry out the various acts and/or other functions and/or acts. Additionally, or alternatively, the one or more processors can execute instructions carried by transitory medium such as a signal or carrier wave.

The application has been described with reference to various embodiments. Modifications and alterations will occur to others upon reading the application. It is intended that the invention be construed as including all such modifications and alterations, including insofar as they come within the scope of the appended claims and the equivalents thereof.

CLAIMS

What is claimed is:

1. An ultrasound imaging system, comprising:

a transducer array including a plurality of transducer elements configured to repeatedly emit in a predetermined pattern;

a first beamformer configured to beamform echo signals received by the transducer array to produce a low resolution line of data for each emission;

a first communication interface configured to wirelessly transmit the low resolution lines of data for each emission in series;

a second communication interface configured to continuously wirelessly receive the transmitted low resolution lines of data;

a second beamformer configured to beamform the received low resolution lines of data to produce high resolution ultrasound data; and

a velocity processor configured to estimate vector velocity components from the high resolution ultrasound data in a lateral direction and an axial direction using an autocorrelation algorithm.

2. The system of claim 1, further comprising a probe, which includes the transducer array, the first beamformer, and the first communication interface are

3. The system of claim 2, further comprising a console, which includes the second communication interface, the second beamformer, and the velocity processor.

4. The system of claim 1, further comprising a probe and a console, which are in electrical communication via a hardwired path.

5. The system of claim 4, further a computing device, which includes the second communication interface, the second beamformer, and the velocity processor.

6. The system of claim 1, wherein the first communication interface transmits the low resolution ultrasound data at a rate less than 500 megabits per second.

7. The system of claim 1, wherein the ultrasound imaging system employs a combination of transverse oscillation and synthetic aperture sequential beamforming to produce to the low resolution ultrasound data, the high resolution ultrasound data, and the vector velocity estimates.

8. The system of claim 1, further comprising:

a display configured to display an ultrasound image and the vector velocity estimates.

9. The system of claim 1, wherein the vector velocity components include an axial component and a transverse component.

10. The system of claim 1, wherein the velocity processor calculates the vector velocity components directly from the high resolution ultrasound data without first determining a beam angle.

11. A method, comprising:

transmitting an ultrasound signal;

receiving echoes generated in response to the transmitted ultrasound signal;

beamforming the echoes, generating a low resolution line of data for each emission;

wirelessly transmitting the low resolution lines of data to another device;

wirelessly receiving the transmitted low resolution lines of data with the other device;

beamforming the low resolution line of data, generating high resolution ultrasound image data; and

estimating, using an autocorrelation algorithm, vector velocity components from the high resolution ultrasound data.

12. The method of claim 11, wherein the low resolution line of data is transmitted over at least one of IEEE 802.11ac, USB, Blue Tooth, or cellular.

13. The method of claim 12, wherein the low resolution line of data is wirelessly transmitted from a probe of an ultrasound imaging device to a console of the ultrasound imaging device.

14. The method of claim 12, wherein the low resolution line of data is transmitted from a console of an ultrasound imaging device to a computing system, which is not part of the ultrasound imaging device.

15. The method of claim 11, wherein the low resolution line of data is transmitted at a rate less than or equal to 500 megabits per second.

16. The method of claim 11, further comprising:

beamforming the low resolution line of data corresponding to at least two emissions.

17. The method of claim 16, further comprising:

beamforming the low resolution line of data corresponding to a first set of emissions for determining a first velocity of interest, and beamforming the low resolution line of data corresponding to a second set of emissions for determining a second velocity of interest, wherein the first set of emissions is fewer than the second set of emissions, and the first velocity if lower than the second velocity.

18. The method of claim 11, further comprising:

employing a combination of direct transverse oscillation and synthetic aperture sequential beamforming to produce to the low resolution ultrasound data, the high resolution ultrasound data, and the vector velocity estimates.

19. The method of claim 11, further comprising:

displaying an ultrasound image and the vector velocity estimates.

20. A non-transitory computer readable storage medium encoded with computer readable instructions, which, when executed by a processor of a computing system, cause the processor to:

transmit, via a transducer array, an ultrasound signal;

receive, via the transducer array, echoes generated in response to the transmitted ultrasound signal;

beamform the echoes and generate a low resolution line of data for each emission;

wirelessly transmit the low resolution lines of data to another device;

wirelessly receive the transmitted low resolution lines of data with the other device;

beamform the low resolution line of data and generate high resolution ultrasound image data; and

estimate, using an autocorrelation algorithm, vector velocity components from the high resolution ultrasound data.

ABSTRACT

An ultrasound imaging system includes a transducer array with a plurality of transducer elements configured to repeatedly emit in a predetermined pattern, a first beamformer configured to beamform echo signals received by the transducer array to produce a low resolution line of data for each emission, and a first communication interface configured to wirelessly transmit the low resolution lines of data for each emission in series. The ultrasound imaging system further includes a second communication interface configured to for each emission in series wirelessly receive the transmitted low resolution lines of data, a second beamformer configured to beamform the received low resolution lines of data to produce high resolution ultrasound data, and a velocity processor configured to estimate vector velocity components from the high resolution ultrasound data in a lateral direction and an axial using an autocorrelation algorithm.

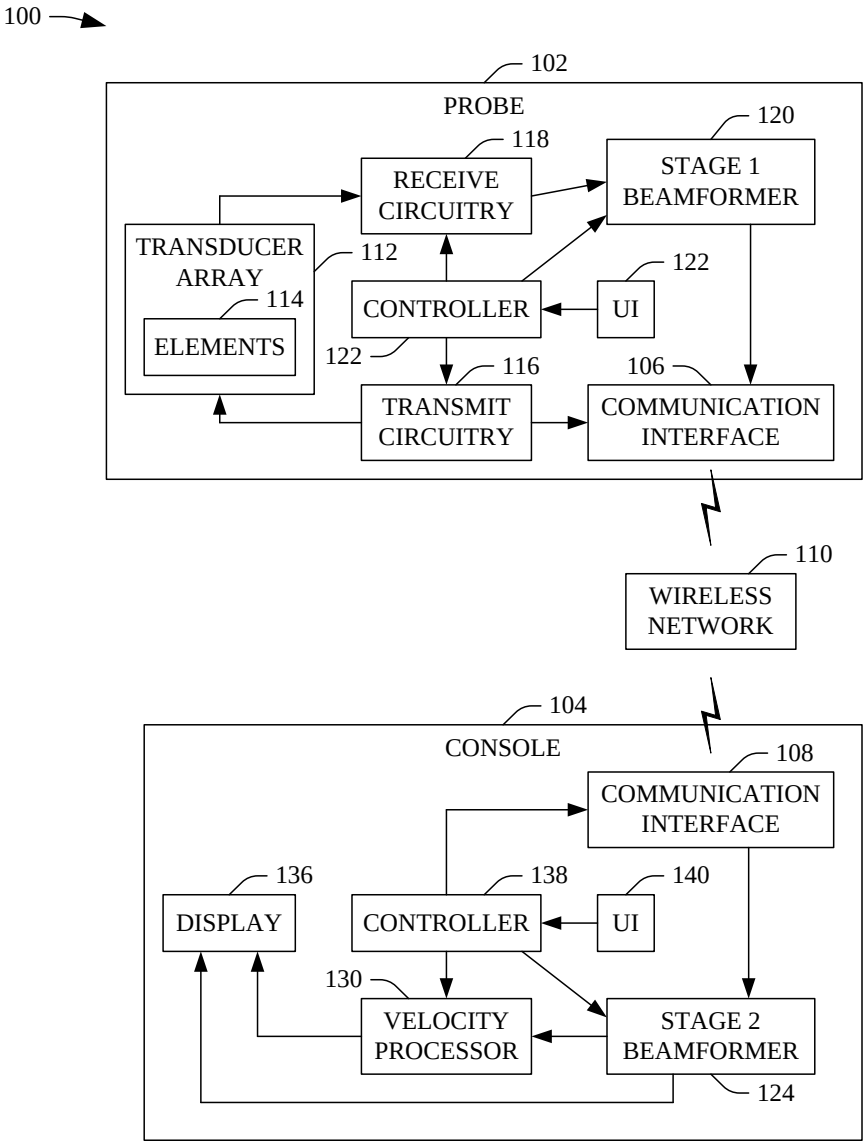
100
102
PROBE
118
RECEIVE CIRCUITRY
120
STAGE 1 BEAMFORMER
TRANSDUCER ARRAY
112
114
ELEMENTS
CONTROLLER
122
UI
122
116
106
TRANSMIT CIRCUITRY
COMMUNICATION INTERFACE
110
WIRELESS NETWORK
104
CONSOLE
108
COMMUNICATION INTERFACE
136
DISPLAY
138
CONTROLLER
140
UI
130
VELOCITY PROCESSOR
STAGE 2 BEAMFORMER
124

FIGURE 1

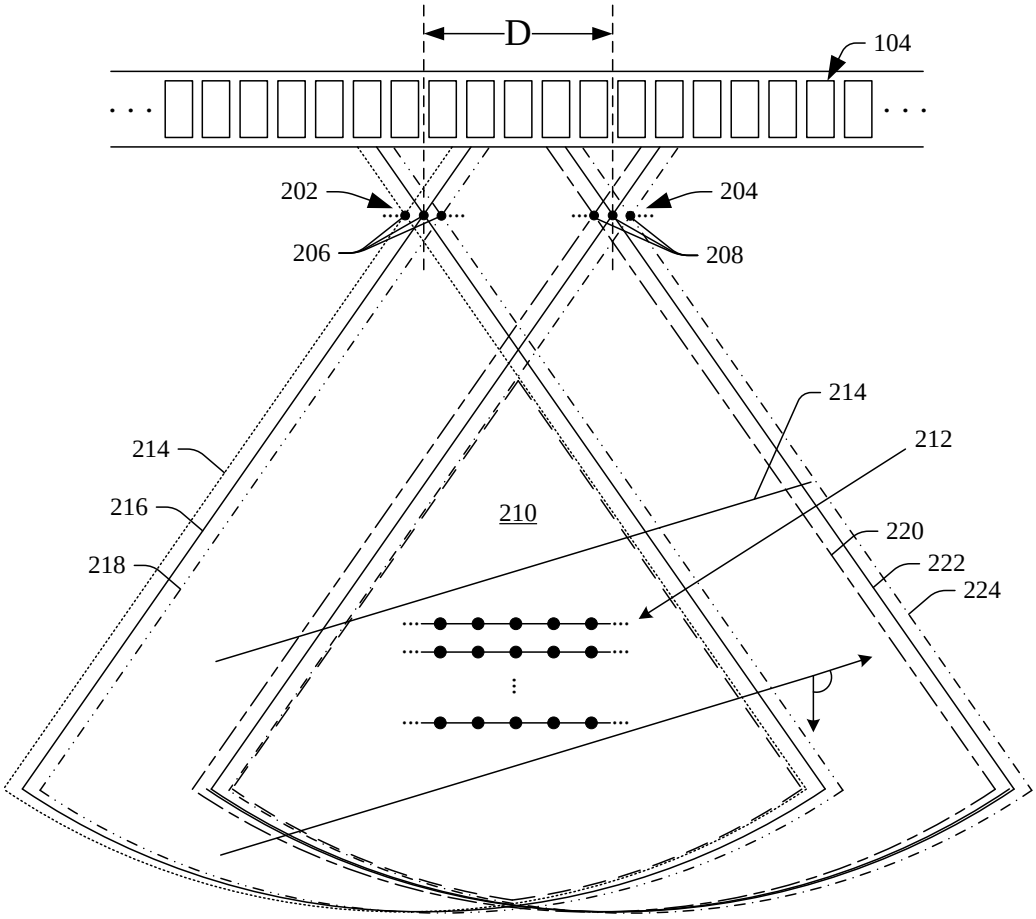

FIGURE 2

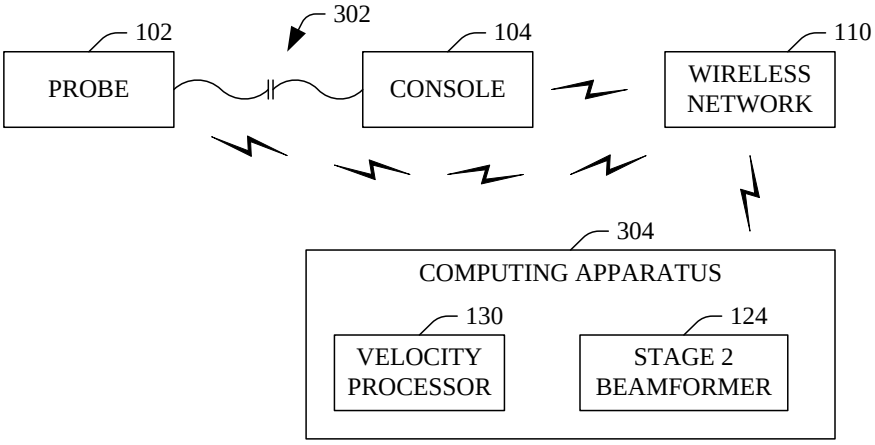

FIGURE 3

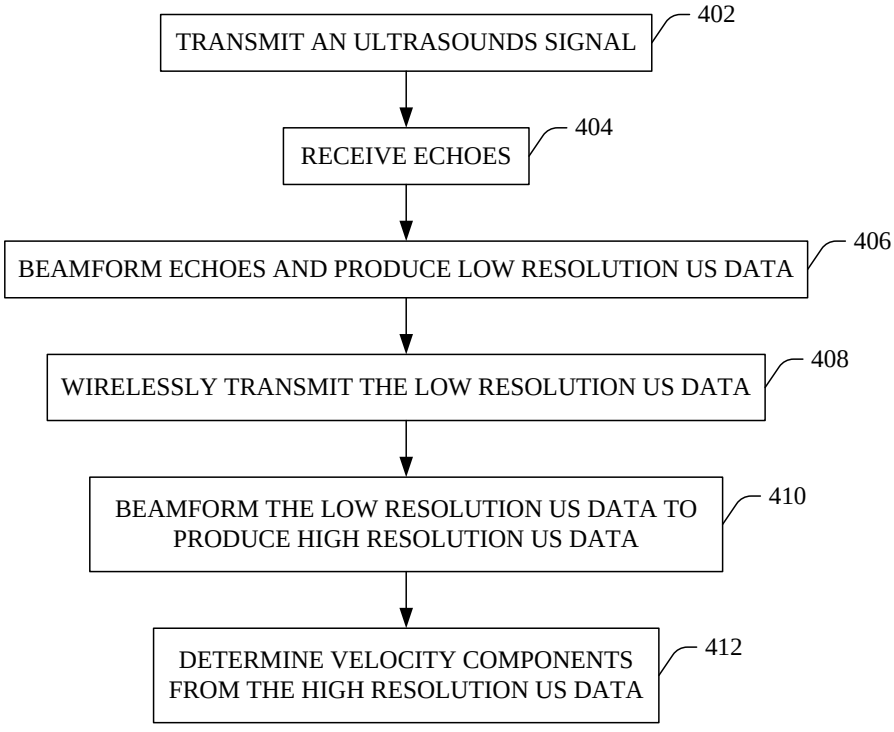

FIGURE 4